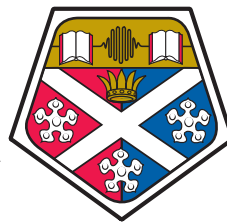


UNIVERSITY OF STRATHCLYDE  
Department of Physics

# III-Nitride LEDs and Lasers for Underwater Wireless Optical Communications

by

Georgios N. Arvanitakis



University of  
**Strathclyde**  
Glasgow

A thesis presented in fulfilment of the  
requirements for the degree of  
Doctor of Philosophy

October 2023

# Declaration of Authorship

This thesis is the result of the author's original research. It has been composed by the author and has not been previously submitted for examination which has led to the award of a degree.

The copyright of this thesis belongs to the author under the terms of the United Kingdom Copyright Acts as qualified by University of Strathclyde Regulation 3.50. Due acknowledgement must always be made of the use of any material contained in, or derived from, this thesis.

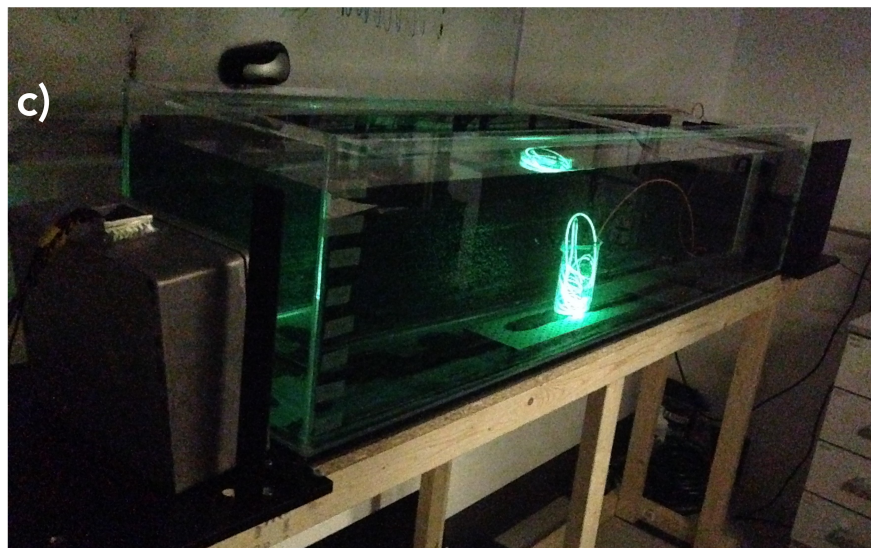
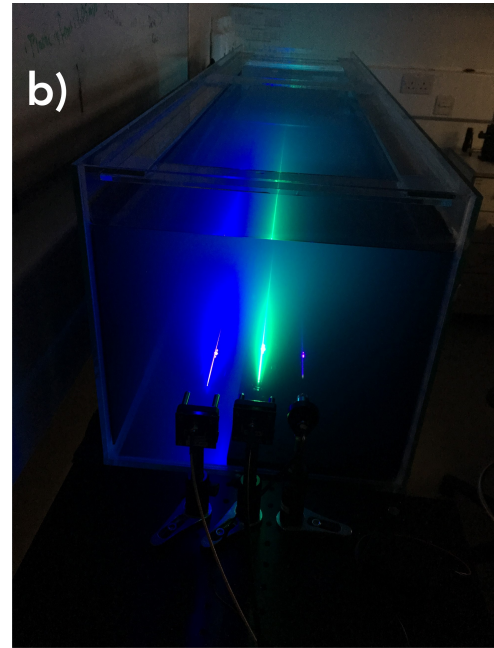
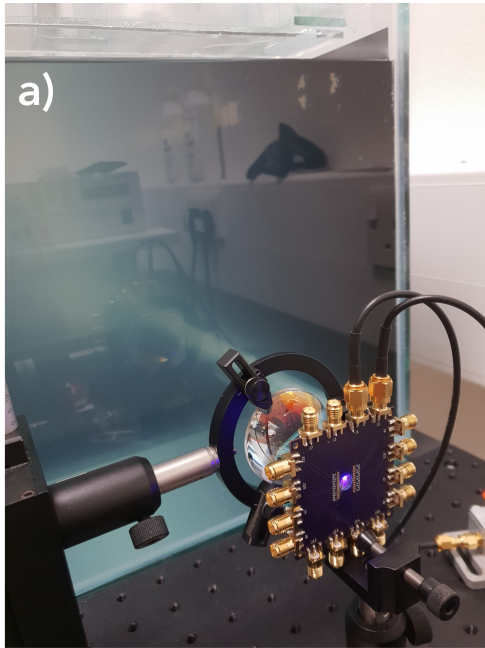
Signed: **Georgios Arvanitakis**

---

Date: **10/10/2023**

---

## Frontispiece



Optical images of the water tank showing: **a)** a violet-blue micro-LED array, developed via a transfer-printing method and used as a Transmitter (Chapter 4). **b)** Three laser diodes (violet, blue, green) used for the characterisation of various water samples (Chapter 1). **c)** The Fibrance fibre used as an underwater beacon (Chapter 5).

# *Abstract*

This thesis delves into the deployment of III-nitride micro-LED and laser-based devices for Underwater Wireless Optical Communications (UWOC), an emerging field with considerable potential for underwater data transfer. UWOC offers a compelling solution owing to the vast bandwidth available in the visible spectrum (hundreds of THz), the substantial modulation bandwidth of micro-GaN-based devices (hundreds of MHz), and the underwater “window” characterised by low light attenuation at visible wavelengths.

Throughout this thesis, extensive experiments were conducted within a 1.5 m water tank, employing various transmitters ( $T_x$ 's) and receivers ( $R_x$ 's). The results showcase error-free data transmission rates in the gigabits per second (Gb/s) and megabits per second (Mb/s) range, even in the presence of varying water turbidity levels and attenuation lengths (ALs). Notably, data rates of 4.92 Gb/s and 1.32 Gb/s were achieved using a series-connected micro-LED array of 6 pixels, spanning distances of 1.5 m and 4 m, respectively, and achieved 15 Mb/s over 5.33 ALs.

Different underwater conditions, influenced by water turbidity, lead to distinct light attenuation minima underwater. Consequently, I highlight the applicability of wavelength division multiplexing (WDM) in real UWOC scenarios. Using transfer-printed (TP) dual-colour micro-LED arrays, data rates of 200 Mb/s were demonstrated over 8.5 ALs.

In most UWOC scenarios, establishing a reliable point-to-point underwater link is challenging due to the unpredictable subsea environment and terrestrial weather conditions. To mitigate this, I introduced the deployment of a diffusing fibre coupled with a laser diode, functioning as a  $T_x$  for omnidirectional data transmission (underwater “beacon”). This approach circumvented the alignment restrictions between the  $T_x$  and  $R_x$ , and data at 5 Mb/s were successfully transmitted over 11.81 ALs, showcasing the robustness of this solution.

# Acknowledgements

Writing a PhD thesis is no small feat, and navigating through this journey during the pandemic made it feel like climbing a mountain on roller skates. Yet, here I stand at the end of this academic adventure, and I owe a world of gratitude to those who made it possible.

To my primary supervisor, Professor Martin Dawson, whose supervision was exemplary. Martin provided constant guidance from my first day at Strathclyde’s IoP and was always there when needed, providing technical, moral, and personal support, all delivered with clarity and calmness. Then, to Dr Jonathan McKendry, my “daily” supervisor, who introduced me to the fascinating field of (Underwater) Visible Light Communications. Jonathan was unconditionally by my side, even outside the lab environs (e.g., meetings at Babs or Spitfire). Without his technical wisdom, continuous feedback, and persistence, I would be drowning in a sea of confusion. Martin and Jonathan, thank you a lot for everything; your support has been a lifesaver.

I would like to express my gratitude to Dr Henry Bookey, my “industrial” supervisor from the FCAP, whose innovative ideas pushed me to think out of the box. I would also like to thank him and Martin for their support during my internship with FCAP, which allowed me to acquire valuable industrial work experience. It would be unfair if I missed Dr David Stothard from my list. David’s enthusiasm, creativity, and engineering skills were genuinely inspiring. I also thank Dr Erdan Gu for his support and advice during our catch-up meetings and Professor Harald Haas’s group for their expertise; it was a guiding light.

Within the IoP, several individuals made my life easier and filled it with funny moments, such as the days when the experiments failed, the deadlines hit hard, or when the sun was in sleep mode for months. I want to thank José Carreira for his friendship and laughs and for always being willing to support me with his knowledge in every aspect of my PhD, even after completing his dissertation and deciding to move to Lausanne (*cliché*). Chapter 4 of this thesis is *undoubtedly* dedicated to him, and I hope he realises nothing compares to Glasgow. Many thanks go to Mark Stonehouse, who tried to impart his oddly comforting “I don’t give a damn” mood to me, especially during our professional trips. I would like to thank Francesca Farell for sitting, literally, next to me throughout our PhDs and being my official translator from Scottish to understandable English. I am also grateful to Sharon Kelly and Lorraine Annand for their precious help and bureaucratic prowess.

My journey towards completing this PhD had some ups and many downs (no surprise). I was fortunate enough to share the joys with a handful of people, such as Vaios

and Demmi, Mara, Takis and Ioanna, Minas and Argyro. I am particularly grateful to Vaios and Demmi, who reminded me through several discussions (and foods) to always look on the bright side and move on when the future seemed dull and dark, and to Eirinaios, for always being ready to help, willing to share his advice remotely and make me laugh (often to tears). Talking about caring, I am forever indebted to Dracos and Marilena Vassalos, who have stood to me as a second set of parents.

Lastly, to my first set of parents, Nikos and Angela, your love, support, and life lessons have been my guiding stars. I made it, and this achievement is a testament to your love.

All of the above would be meaningless without having by my side my other half, my soulmate, my beautiful wife, Anna Maria; your unwavering support has helped me be the best version of myself.

I thank you all.

# Contents

<b>Declaration of Authorship</b>	<b>i</b>
<b>Abstract</b>	<b>iii</b>
<b>Acknowledgements</b>	<b>iv</b>
<b>List of Figures</b>	<b>viii</b>
<b>List of Tables</b>	<b>xiv</b>
<b>Abbreviations</b>	<b>xv</b>
<b>1 Introduction</b>	<b>1</b>
1.1 Introduction . . . . .	1
1.2 State-of-the-art of UWOC . . . . .	3
1.3 Technologies for underwater wireless communications . . . . .	4
1.3.1 Acoustic . . . . .	5
1.3.2 Radio frequency (RF) electromagnetic (EM) waves . . . . .	7
1.3.3 Optical waves . . . . .	8
1.3.4 Summary . . . . .	8
1.4 Optical properties of water . . . . .	9
1.4.1 Inherent optical properties of water (IOPs) . . . . .	10
1.4.1.1 Absorption . . . . .	11
1.4.1.2 Scattering . . . . .	14
1.4.2 Apparent optical properties of water (AOPs) . . . . .	18
1.5 Optical water types . . . . .	19
1.6 Laboratory-based water samples characterisation and background theory .	21
1.7 Summary . . . . .	28
<b>2 Relevant Semiconductor Device Physics and Modulation Schemes</b>	<b>33</b>
2.1 Brief overview of semiconductor physics . . . . .	33
2.1.1 Electrons in free-space . . . . .	33
2.1.2 Electrons within a crystal . . . . .	34
2.1.3 The p-n diode . . . . .	39
2.1.4 Quantum well structures . . . . .	44
2.1.5 The laser diode . . . . .	48
2.1.6 Photodetectors . . . . .	52
2.2 Modulation schemes . . . . .	61
2.2.1 On-off keying . . . . .	61
2.2.2 Orthogonal frequency division multiplexing . . . . .	62
2.3 Summary . . . . .	63

<b>3</b>	<b>Gb/s Underwater Wireless Optical Communications Using Series-Connected GaN Micro-LED Arrays</b>	<b>68</b>
3.1	Introduction . . . . .	68
3.2	Device overview . . . . .	69
3.2.1	Device design and fabrication . . . . .	69
3.2.2	Device characterisation . . . . .	70
3.3	Water sample characterisation . . . . .	75
3.4	Data transmission experimental set-up . . . . .	77
3.5	Communication performance results . . . . .	78
3.6	Summary . . . . .	82
<b>4</b>	<b>Underwater Wireless Optical Communications Using Integrated Dual-Colour Micro-LEDs</b>	<b>85</b>
4.1	Introduction . . . . .	85
4.2	Device overview . . . . .	86
4.2.1	Individually-addressable blue-violet and blue-green micro-LED arrays . . . . .	86
4.2.2	In-series connected blue-green micro-LED array . . . . .	96
4.3	Application in Underwater Wireless Optical Communications . . . . .	99
4.3.1	Experimental set-up . . . . .	99
4.3.2	Results . . . . .	102
4.4	Summary . . . . .	108
<b>5</b>	<b>Underwater Wireless Omnidirectional Optical Beacon Using Light-Diffusing Fibre</b>	<b>112</b>
5.1	Introduction . . . . .	112
5.1.1	Details of the Fibrance fibre . . . . .	114
5.2	Experimental set-up . . . . .	116
5.2.1	Set-up description . . . . .	116
5.2.2	Underwater channel characterisation . . . . .	118
5.3	Background theory and methodology . . . . .	120
5.3.1	Eye diagrams . . . . .	120
5.3.2	Methodology for calculating Bit-Error Ratios . . . . .	121
5.4	Results . . . . .	123
5.4.1	Data streams . . . . .	123
5.4.2	Eye diagram construction, histogram creation and Bit-Error Ratios calculation . . . . .	126
5.5	Wavelength Division Multiplexing simulation for the Fibrance fibre . . . . .	133
5.6	Summary . . . . .	138
<b>6</b>	<b>Conclusions</b>	<b>142</b>
6.1	Summary . . . . .	142
6.2	Future work . . . . .	145
	<b>List of Publications</b>	<b>150</b>



# List of Figures

1.1	Summary of the experimental work on UWOC showing achieved data rates from LED- and laser-based source versus distance. . . . .	4
1.2	Schematic illustration of the dominant technologies in the underwater wireless communications field, along with their nominal operational range and data rates. The background image is taken from [22]. . . . .	5
1.3	Variation of the attenuation of acoustic waves underwater in dB/km. Plot taken from [23]. . . . .	6
1.4	Variation of the attenuation of RF underwater. Plot taken from [23]. . . .	7
1.5	The available $\Delta\nu$ against range for all the background technologies that govern the UWOC domain. Image taken from [23]. . . . .	9
1.6	Schematic of how an incident light beam interacts with a small volume of water. $P_T$ : incident (or transmitted power), $P_A$ : absorbed power by the volume of water, $P_S$ : scattered power, and $P_R$ : received power. . . . .	11
1.7	Variation of the water absorption coefficient against a broad range of electromagnetic spectrum wavelengths (top). Figure taken from [34]. The water absorption coefficient variation magnified in the visible spectrum (bottom). Data taken from [37]. . . . .	12
1.8	Power losses for five visible wavelengths of an underwater channel due to pure water absorption. Data taken from [37]. . . . .	12
1.9	The absorption coefficient by pure water and the scattering coefficients of pure and sea water versus wavelength. Graphs were plotted together for comparison; scattering mostly contributes minimally to the overall attenuation. Image taken from [2]. . . . .	17
1.10	Regional distribution of the Jerlov water types. Image taken from [50]. . . .	19
1.11	The variation of the attenuation coefficient versus wavelength for all Jerlov water types. Data acquired from [51]. . . . .	20
1.12	Volume scattering functions from [11, 53, 54] for four types of ocean waters (solid curves, from top): turbid harbour, coastal ocean, clear ocean, and pure seawater. The Maalox data are presented through the dashed curve. Figure taken from [42]. . . . .	21
1.13	Optical images of the water tank and the underwater channels' characterisation of three different colours: violet, blue, and green. In <b>(a)</b> , no scattering agent is added in the water; therefore, most of the photons reach the power meter sensor almost unscattered. From <b>(b)</b> to <b>(c)</b> , a gradual increase of the Maalox content in the water occurs, and thus, attenuation effects through scattering are mainly optically observed. . . .	23
1.14	Received power vs Maalox content for 405 nm, 450 nm, and 520 nm over the 1.5 m water tank. Note the logarithmic scale in $y$ axis. . . . .	24

1.15	<b>Left:</b> The estimated attenuation coefficients of the laboratory water samples, for each wavelength of operation of the three LDs, as a function of the Maalox content with the third order polynomial fitting curves. <b>Right:</b> the variation of the attenuation coefficients for up to 3 ml of the scattering agent. Note the logarithmic scale of the $y$ axis. The measurements were carried out over the 1.5 m long water tank. . . . .	25
1.16	The variation of the number of ALs as the content of the scattering agent in the 1.5 m long water tank increases. . . . .	26
2.1	Schematic energy band diagrams for <b>(a)</b> GaN and <b>(b)</b> Si. . . . .	36
2.2	Two energy band segments of different curvatures from which it can be seen that $m_a^* > m_b^*$ . Adapted from [4]. . . . .	37
2.3	Schematic illustration of the <b>(a)</b> SRH recombination, <b>(b)</b> Auger eeh and ehh recombinations, and <b>(c)</b> radiative recombination. Taken from [10]. The vertical axis in this schematic is energy. . . . .	42
2.4	<b>(a)</b> “Vertical” (in $k$ -space) electron-hole recombinations at the edges of the conduction and valence bands and slightly above them. <b>(b)</b> Theoretical emission spectrum of an LED. Both figures taken from [12]. . . . .	44
2.5	Emission spectra of a $40 \times 40 \mu\text{m}^2$ micro-LED under different currents. Taken from [15]. . . . .	45
2.6	Schematic illustration of a forward biased <b>(a)</b> homojunction and <b>(b)</b> a QW (or DH). Both figures taken from [8]. . . . .	45
2.7	Schematic illustration of a QW structure, showing that the energy photon from the $E_{e1} \rightarrow E_{h1}$ optical transition is larger than $E_{gW}$ . $E_{e,h}$ refers to the electron and hole-confined energies. . . . .	46
2.8	Room-temperature $E_g$ and $\lambda_{em}$ versus $\alpha_0$ for an AlInGaIn alloy system. Taken from [17]. . . . .	47
2.9	Schematic illustration of a typical epitaxial structure of a UV-emitting micro-LED. The multiple QW (MQW) region is expanded and is shown on the right side of the figure (schematic not to scale). Image taken from [20] and data from [19]. . . . .	48
2.10	<i>Left</i> , an OSRAM PL520 green LD with its cap on, and <i>right</i> , the same LD with its cap off (taken from [21]). . . . .	49
2.11	The optical processes of absorption, spontaneous emission and stimulated emission of a two-energy level system with $E_1 < E_2$ . Adapted from [22]. . . . .	49
2.12	Emission spectra of a LD under different bias conditions; <b>(a)</b> current (or current density) much below threshold, <b>(b)</b> current just below threshold, <b>(c)</b> current just above threshold, <b>(d)</b> current much above threshold. Taken from [7]. . . . .	51
2.13	<b>(a)</b> A typical LI curve of a LD along with the physical processes taking place as the bias current increases (taken from [7]). <b>(b)</b> Comparison of the normalised emission spectra of a “home-made” green micro-LED (used in Chapter 4) and an OSRAM green LD (used in Section 1.6 and Chapter 5). . . . .	52
2.14	Schematic illustration of a PIN diode with a reverse bias ( $V_r$ ) applied across it. Taken from [25]. . . . .	54
2.15	<b>(a)</b> Femto Si-PIN photodiode used in Chapter 3 and <b>(b)</b> its photosensitivity versus wavelength. Taken from [26]. . . . .	55

2.16	(a) Schematic illustration of the avalanche effect generated by impact ionisation and occurring in the depletion region of a SPAD (taken from [29]). (b) Illustration of the output of a SPAD in the form of train pulses of the same amplitude, and (c) the SPAD's quenching mechanism (taken from [30]). . . . .	57
2.17	(a) Images of a sensL SiPM and the microcell structure on its surface. (b) A simplified electric circuit illustrating the array of microcells (photodiode and quench resistor) of a sensL SiPM. (c) PDE versus wavelength for a $6 \times 6 \text{ mm}^2$ sensL SiPM at different overvoltage values (2.5 V-dashed curve, 6 V-continuous curve). Taken from [30]. . . . .	58
2.18	Photograph of the Photon Torrent chip along with a plan-view photograph of the SPAD array and a simplified electric circuit illustrating the SPAD pixels. Taken from [29, 33]. . . . .	59
2.19	Bit-error ratio (BER) of a 20 kb/s UWOC link with varying the number of attenuation lengths. . . . .	60
2.20	Simplified block diagram of a VLC system. Adapted from [36]. . . . .	61
2.21	Schematic of an OOK optical transmission of a data sequence [0010110101].	62
2.22	Spectra of different OFDM sub-carriers (shown in different colours) in the frequency domain. Although their spectra overlap, the sub-carriers do not interfere with each other due to their orthogonality. Image taken from [39]. . . . .	63
3.1	(a) Schematic cross-section of two adjacent micro-LED pixels of the series-connected micro-LED array. (b) Planview optical image of six pixels from the micro-LED array at a DC bias of 1 mA. . . . .	70
3.2	Schematic of the micro-LED frequency response measurements setup. . .	71
3.3	Frequency response measurements and -6 dB (E-O) BW of LEDs operating at 450 nm of different pixel diameters. Figure taken from [9]. . . . .	72
3.4	-3 dB bandwidth plots for the in-series connected $60 \mu\text{m}$ and $80 \mu\text{m}$ micro-LEDs. . . . .	73
3.5	I-V and L-I plots for the two respective devices comprising six $60 \mu\text{m}$ and $80 \mu\text{m}$ micro-LEDs connected in-series. The $V_F$ of both arrays ( $60 \mu\text{m}$ : 21.7 V, $80 \mu\text{m}$ : 20 V) are shown at the intersection of the dashed lines and the voltage axis. . . . .	74
3.6	(a) The calculated attenuation coefficients versus the content of the scattering agent (Maalox) using a blue LD operating at 450 nm. For comparison, the typical values of six <i>Jerlov</i> ocean types are given as defined by [16]. (b) The estimated received power over 1.5 m, 3 m and 4.5 m versus the Maalox concentration for the $80 \mu\text{m}$ micro-LED array, using the optical power data showing in Figure 3.5. . . . .	76
3.7	<b>Top:</b> Illustration of the experimental set-up used for the UWOC measurements of this work. Two mirrors (M1 and M2) were placed appropriately to increase the optical link from 1.5 m to 3 m and 4.5 m. <b>Bottom:</b> Photographs from the receiver end (Fresnel lens and PiN photodetector), the water tank filled with 160 l of tap water, and the transmitter side (micro-LED array and condenser lens). . . . .	77
3.8	Measured SNR (orange) and corresponding bit loading (blue) versus OFDM carrier frequency, obtained using a $60 \mu\text{m}$ in diameter series-connected micro-LED device over 1.5 m of clear tap water. . . . .	78

3.9	BER versus data rate for the 60 $\mu\text{m}$ in diameter series-connected micro-LED device. Transmission is over 1.5 m of clear tap water ( $c(450)=0.05 \text{ m}^{-1}$ ). . . . .	79
3.10	(a) BER vs data rate for the 80 $\mu\text{m}$ in diameter series-connected micro-LED device through different water turbidities over 1.5 m. (b) BER vs data rate for the same device through different water turbidities over 3 m and 4.5 m. Note that the maximum error-free data rates were obtained at slightly different BERs. . . . .	80
3.11	The maximum data rates versus the number of attenuation lengths for all ranges examined in this work (1.5 m, 3 m, 4.5 m). . . . .	81
4.1	Simplified micro-LED epitaxial structure of the (a) violet and (b) green micro-LEDs. Dimensional values for both devices are taken from [2]. . . . .	87
4.2	Simplified micro-LED epitaxial structure of the blue micro-LED. The device's dimensional values are adapted from [2] and the image is taken from [10]. . . . .	88
4.3	Schematic illustration of the TP technique. Taken from [13]. . . . .	89
4.4	Schematic of the fabrication process of the blue micro-LED on its Si substrate before TP. Note that the device is mechanically suspended after the final step (images taken from [10]). . . . .	90
4.5	Plan view optical micrograph images of the green and blue micro-LED array (a) before and (b) after transfer-printing the blue device onto the green device's substrate (images taken from [2]). . . . .	91
4.6	Atomic force microscope image of the PSS (a) before and (b) after the SU-8 coating (images taken from [2]). . . . .	91
4.7	Plan view <i>topside</i> optical micrograph for the (a) violet (318 $\text{A}/\text{cm}^2$ ), (b) blue (15 $\text{A}/\text{cm}^2$ ) and (c) green (318 $\text{A}/\text{cm}^2$ ) micro-LEDs. Plan view <i>backside</i> optical micrograph at the same currents as the topside ones for the (d) blue-violet and (e) blue-green micro-LED arrays. . . . .	92
4.8	Normalised EL spectra of the micro-LEDs used in this work. The violet device's central wavelength is at 400 nm, the blue's at 453 nm, and the green's at 512 nm. . . . .	93
4.9	The RT voltage vs current density (JV), and optical power vs current density (LJ) plots for (a) violet (at 318 $\text{A}/\text{cm}^2$ ), (b) for blue (at 15 $\text{A}/\text{cm}^2$ ) and (c) for green (at 318 $\text{A}/\text{cm}^2$ ) micro-LEDs. The $V_F$ of the devices (violet: 3.67 V, blue: 3.26 V, green: 6.17 V) are shown at the intersection of the dashed lines and the voltage axes. . . . .	94
4.10	The -3 dB electrical-to-optical (E-O) modulation bandwidths of the violet (427 MHz), blue (134 MHz), and green (144 MHz) micro-LEDs. . . . .	95
4.11	Plan-view optical photographs of the (a) green micro-LEDs before the blue TP onto the PSS, (b) of the array after micro-TP the blue micro-LED platelets, (c) in-series connected device driven at a current of 2 mA. . . . .	97
4.12	(a) The IV and LI curves of the in-series connected blue-green micro-LED array (the $V_F = 15.8 \text{ V}$ of the array is shown at the intersection of the dashed line and the voltage axis), and (b) the -3 dB electrical-to-electrical (E-E) and electrical-to-optical (E-O) modulation bandwidths of the same device. . . . .	98

4.13	A schematic illustration of the experimental set-up used for the UWOC demonstration by deploying the individually addressable micro-LED arrays (violet-blue and blue-green). . . . .	99
4.14	Photographs of <b>(a)</b> the water tank filled with tap water and added with Maalox antacid. The $T_x$ and $R_x$ sites are also indicated. <b>(b)</b> - <b>(c)</b> The $64 \times 64$ SPADs array and the 4-inch Fresnel lens placed before the receiver. <b>(d)</b> - <b>(e)</b> The individually-addressable micro-LED array (violet-blue) under operation and the condenser lens in front of the device for beam collimation. . . . .	101
4.15	A schematic illustration of the experimental set-up used for the UWOC demonstration by deploying the in-series connected micro-LED array (blue-green). . . . .	101
4.16	BER vs attenuation coefficient and number of ALs for the individually addressable <b>(a)</b> violet-blue micro-LED array; WDM of 100 Mb/s is presented over 8.52 and 6.95 ALs for the violet and blue channel, respectively. <b>(b)</b> blue-green micro-LED array; WDM of 100 Mb/s is shown over 6.47 and 5.78 ALs for the blue and green underwater channels, respectively. . . . .	103
4.17	BER vs overall attenuation coefficient and number of ALs via deploying an AWG for the signal generation for the individually addressable <b>(a)</b> violet-blue micro-LED array; WDM of 200 Mb/s aggregate below the FEC threshold is presented over 5.85 ALs for the violet channel and 5.18 ALs for the blue. <b>(b)</b> blue-green micro-LED array; WDM of 150 Mb/s aggregate below the FEC threshold is shown over 5.71 and 5.34 ALs for the green and blue underwater channels, respectively. . . . .	105
4.18	BER values vs $c_{Maalox}$ for the in-series connected blue-green micro-LED array at 50 Mb/s. . . . .	107
5.1	Schematic illustration of the beacon concept. The Fibrance fibre could be implemented, e.g. at the hull of a surface vessel and send data omnidirectionally underwater to UUVs which are in proximity to the ship. No sophisticated optical components nor precise alignment are required. The same idea is followed for the UUVs, where optical signals of different wavelengths can be transmitted or received to other UUVs or/and the surface vessel. . . . .	113
5.2	Examples of the Fibrance's application domains in <b>(a)</b> lighting, <b>(b)</b> electronics, and <b>(c)</b> architecture. Images taken from [3]. . . . .	114
5.3	<b>(a)</b> Cross section of the Fibrance fibre; the core is divided into three regions (1, 2, 3), and the cladding area corresponds to region 4. <b>(b)</b> Optical image from glowing Fibrance fibres wrapped in spirals. . . . .	114
5.4	Graphical representation of the diffusion characteristics of the Fibrance fibre; 90% of the coupled input optical power is emitted as a diffuse output at 1 m, 5 m, and 10 m diffusion lengths, respectively. Adapted from [5, 6].	115
5.5	The experimental set-up for the underwater wireless optical communications system based on deploying the Fibrance fibre as $T_x$ . . . . .	116
5.6	<b>(a)</b> The measured EL spectrum of the LD. <b>(b)</b> IV and LI curves of the LD (adapted from [8]). . . . .	117
5.7	<b>(a)</b> Optical image of the Fibrance fibre in the glass beaker. <b>(b)</b> Optical image of the illuminated Fibrance fibre in the water tank. . . . .	118

5.8	The calculated attenuation coefficient for $\lambda = 514$ nm vs Maalox content with their second order polynomial fit and the values for $c(525$ nm) of <i>Jerlov</i> water types for reference. . . . .	119
5.9	Graphical illustration of an eye diagram. . . . .	121
5.10	Constructed eye diagram at 5 Mb/s over 0.04 ALs (0 ml of Maalox) on the right and the corresponding 1's (Upper) and 0's (Lower) normal distribution on the left. . . . .	122
5.11	The forms of the digital signal (top) sent to the LD, and (bottom) the received signal at 5 Mb/s over 0.04 ALs (0 ml of Maalox). . . . .	124
5.12	The forms of the received signals at 5 Mb/s over various water turbidities. As the water becomes more turbid due to the added scattering agent, the received signal experiences an attenuation of approximately 60% and becomes noisier. . . . .	125
5.13	Constructed eye diagram at 5 Mb/s over 0.04 ALs (0 ml of Maalox) on the left and the normal distributions histogram corresponding to the 1's (Upper) and 0's (Lower) on the right. The corresponding received signal for both diagrams is shown in Figure 5.11b. . . . .	126
5.14	The constructed eye diagrams and voltage distribution histograms for error-free underwater wireless optical communication by the Fibrance fibre over varied underwater conditions. . . . .	127
5.15	Constructed eye diagram at 5 Mb/s over 14.97 ALs (40 ml of Maalox) on the left and the corresponding to the 1's (Upper) and 0's (Lower) normal distributions histogram on the right. . . . .	128
5.16	Achieved BERs vs attenuation coefficients and number of ALs for the Maalox contents tested for this work over 1.5 m between $T_x$ - $R_x$ . . . . .	128
5.17	Depiction of the experimental set-up while moving the beaker towards the detector. . . . .	130
5.18	The constructed eye diagrams for the highest contents of the scattering agent over 1.5 m, 1.2 m, and 0.9 m between $T_x$ - $R_x$ . . . . .	132
5.19	BER vs $T_x$ - $R_x$ simulation, over <i>Jerlov</i> I, III, 9C water types at 450 nm and 525 nm. The modelling parameters are the same as with the experiment described in Section 5.2.1. . . . .	135
5.20	BER vs $T_x$ - $R_x$ simulation, over <i>Jerlov</i> I, III, 9C water types at 450 nm and 525 nm. The modelling parameters are the same as with the experiment described in Section 5.2.1 except for the transmitted power, $P_T$ , which was set to 20 mW. . . . .	136
5.21	BER vs $T_x$ - $R_x$ simulation, over <i>Jerlov</i> I, III, 9C water types at 450 nm and 525 nm. The modelling parameters are the same as with the experiment described in Section 5.2.1 except for the data rate, $P_T$ , which was set to 10 Mb/s. . . . .	137
6.1	Images of an ROV capable of demonstrating WDM underwater. The ROV can be equipped with light sources emitting at different wavelengths and coupled with the diffusing Fibrance fibre to send data omnidirectionally as an underwater beacon (see Chapter 5). The ROV's Fibrance coupled with (a) and (b) a violet and green laser diode, and (c) with a red laser diode. Images courtesy of the Fraunhofer Centre for Applied Photonics (FCAP) in Glasgow. . . . .	146
6.2	Schematic illustration of optical wireless communication links in the air-water and water-air interface. Taken from [6]. . . . .	147

# List of Tables

1.1	Comparison of the key features of the background technologies that govern the UWOC field. Data taken from [3, 28, 32]. . . . .	9
1.2	Optical properties of four ocean water types at $\lambda = 514$ nm. Data taken from [11, 54]. . . . .	22
1.3	The maximum values of the estimated attenuation coefficients and number of attenuation lengths for violet, blue, and green. . . . .	26
2.1	The temperature dependence of $E_g$ of Ge, Si, and GaAs. Data taken from [4]. . . . .	35
4.1	Summarised figures of merit for the individually addressable micro-LED arrays; violet-blue and blue-green. For the violet and green micro-LEDs, the optical powers are shown at a current density of $2.8$ kA/cm <sup>2</sup> . For the blue micro-LED, the optical power is shown at $138$ A/cm <sup>2</sup> . . . . .	96
4.2	Summarised values of interest for the in-series connected blue-green micro-LED array. The optical powers for both micro-LEDs are shown at a current of $9$ mA. . . . .	98
4.3	Summary of the FPGA results, below the FEC threshold, for the individually addressable micro-LED arrays. . . . .	104
4.4	Summary of the AWG results, below the FEC threshold, for the individually addressable micro-LED arrays. . . . .	106
5.1	Values for Maalox content and concentration, and for the respective $c(\lambda)$ and number of ALs. The values shown in this table for $c(\lambda)$ and ALs were derived from the second order polynomial fitting curve shown in Figure 5.8.120	
5.2	Summary of all the calculated values of the Fibrance fibre at $5$ Mb/s over $1.5$ m between $T_x$ - $R_x$ . Note that as the level of attenuation increases, the BER increases, as scattering prevents signal photons from reaching the $R_x$ .130	
5.3	Summary of the calculated Fibrance fibre values over various ranges, under extreme scattering conditions. Below are listed the Maalox content and the corresponding concentration, the water sample's attenuation coefficient, the distance between the beacon and the SiPM, the number of ALs, and the achieved BER. . . . .	133
5.4	Estimated values below the FEC threshold for the simulated WDM Fibrance fibre link at $P_T = 5$ mW and $5$ Mb/s. . . . .	135
5.5	Estimated values below the FEC threshold for the simulated WDM Fibrance fibre link at $P_T = 20$ mW and $5$ Mb/s. . . . .	136
5.6	Estimated values below the FEC threshold for the simulated WDM Fibrance fibre link at $P_T = 5$ mW and $10$ Mb/s. . . . .	138

# Abbreviations

<b>AC</b>	<b>A</b> lternating <b>C</b> urrent
<b>AL</b>	<b>A</b> ttenuation <b>L</b> ength
<b>AOP</b>	<b>A</b> pparent <b>O</b> ptical <b>P</b> roperty (of water)
<b>AUV</b>	<b>A</b> utonomous <b>U</b> nderwater <b>V</b> ehicle
<b>AWG</b>	<b>A</b> rbitrary <b>W</b> aveform <b>G</b> enerator
<b>BW</b>	<b>B</b> andwidth
<b>CDOM</b>	<b>C</b> oloured <b>D</b> issolved <b>O</b> rganic <b>M</b> atter
<b>CMOS</b>	<b>C</b> omplementary <b>M</b> etal- <b>O</b> xide <b>S</b> emiconductor
<b>DAC</b>	<b>D</b> igital-to- <b>A</b> nalog <b>C</b> onverter
<b>DC</b>	<b>D</b> irect <b>C</b> urrent
<b>dSiPM</b>	<b>d</b> igital <b>S</b> ilicon <b>P</b> hotomultiplier
<b>E-E</b>	<b>E</b> lectrical-to- <b>E</b> lectrical (bandwidth)
<b>EL</b>	<b>E</b> lectroluminescence
<b>ELF</b>	<b>E</b> xremely <b>L</b> ow (acoustic) <b>F</b> requency
<b>EM</b>	<b>E</b> lectromagnetic
<b>E-O</b>	<b>E</b> lectrical-to- <b>O</b> ptical (bandwidth)
<b>EQE</b>	<b>E</b> xternal <b>Q</b> uantum <b>E</b> fficiency
<b>FEC</b>	<b>F</b> orward <b>E</b> rror <b>C</b> orrection
<b>FOV</b>	<b>F</b> ield of <b>V</b> iew
<b>FPGA</b>	<b>F</b> ield <b>P</b> rogrammable <b>G</b> ate <b>A</b> rray
<b>FSO</b>	<b>F</b> ree- <b>S</b> pace <b>O</b> ptical
<b>FWHM</b>	<b>F</b> ull <b>W</b> idth at <b>H</b> alf <b>M</b> aximum
<b>ICP</b>	<b>I</b> nductively <b>C</b> oupled <b>P</b> lasma
<b>IFFT</b>	<b>I</b> nverse <b>F</b> ast <b>F</b> ourier <b>T</b> ransform
<b>IoP</b>	<b>I</b> nstitute of <b>P</b> hotonics



---

<b>IOP</b>	<b>Inherent Optical Property</b> (of water)
<b>IQE</b>	<b>Internal Quantum Efficiency</b>
<b>IR</b>	<b>Infrared</b>
<b>ISI</b>	<b>Intersymbol Interference</b>
<b>KE</b>	<b>Kinetic Energy</b>
<b>LASER</b>	<b>Light Amplification by Stimulated Emission of Radiation</b>
<b>LD</b>	<b>Laser Diode</b>
<b>LED</b>	<b>Light Emitting Diode</b>
<b>Li-Fi</b>	<b>Light-Fidelity</b>
<b>MQW(s)</b>	<b>Multiple Quantum Wells</b>
<b>NLOS</b>	<b>Non-Line-of-Sight</b>
<b>NRZ</b>	<b>Non-Return-to-Zero</b>
<b>OFDM</b>	<b>Orthogonal Frequency Divison Multiplexing</b>
<b>OOK</b>	<b>On-Off Keying</b>
<b>Pa-C</b>	<b>Parylene-C</b>
<b>PCB</b>	<b>Printed Circuit Board</b>
<b>PDE</b>	<b>Photon Detection Efficiency</b>
<b>PDMS</b>	<b>Polydimethylsiloxane</b>
<b>PE-CVD</b>	<b>Plasma-Enhanced Chemical Vapour Deposition</b>
<b>PRBS</b>	<b>Pseudo Random Bit Sequence</b>
<b>PSS</b>	<b>Periodically Patterned Surface</b>
<b>QAM</b>	<b>Quadrature Amplitude Modulation</b>
<b>QCSE</b>	<b>Quantum Confined Stark Effect</b>
<b>QE</b>	<b>Quantum Efficiency</b>
<b>QW</b>	<b>Quantum Well</b>
<b>RF</b>	<b>Radio Frequency</b>
<b>RGB</b>	<b>Red-Green-Blue</b>
<b>RIE</b>	<b>Reactive Ion Etching</b>
<b>RMS</b>	<b>Root Mean Square</b>
<b>ROV</b>	<b>Remotely Operated Vehicle</b>
<b>RT</b>	<b>Room-Temperature</b>
<b>RZ</b>	<b>Return-to-Zero</b>
<b>SiPM</b>	<b>Silicon Photomultiplier</b>

---

<b>SMaP</b>	<b>S</b> ize, <b>M</b> ass and <b>P</b> ower
<b>SNR</b>	<b>S</b> ignal-to- <b>N</b> oise <b>R</b> atio
<b>SPAD</b>	<b>S</b> ingle- <b>P</b> hoton <b>A</b> valanche <b>P</b> hotodiode
<b>SRH</b>	<b>S</b> hockley- <b>R</b> ead- <b>H</b> all
<b>SWaP</b>	<b>S</b> ize, <b>W</b> eight and <b>P</b> ower
<b>TP</b>	<b>T</b> ransfer- <b>P</b> rinting
<b>UHF</b>	<b>U</b> ltra <b>H</b> igh <b>F</b> requency
<b>UV</b>	<b>U</b> ltraviolet
<b>UWOC</b>	<b>U</b> nderwater <b>W</b> ireless <b>O</b> ptical <b>C</b> ommunications
<b>VHF</b>	<b>V</b> ery <b>H</b> igh <b>F</b> requency
<b>VLC</b>	<b>V</b> isible <b>L</b> ight <b>C</b> ommunications
<b>VLf</b>	<b>V</b> ery <b>L</b> ow <b>F</b> requency
<b>VSF</b>	<b>V</b> olume <b>S</b> cattering <b>F</b> unction
<b>WDM</b>	<b>W</b> avelength <b>D</b> ivision <b>M</b> ultiplexing
<b>XOR</b>	<b>E</b> xclusive <b>O</b> R

*To my family.*

# Chapter 1

## Introduction

### 1.1 Introduction

The content of this thesis is focused on the deployment of novel light-emitting diode (LED) and laser-based devices for high-speed underwater wireless optical communications (UWOC). Over the last decade, UWOC has attracted growing interest as an alternative or supplement to acoustic and radio frequency (RF) technologies for data transfer underwater. An increasing number of academic references has been reported in peer-reviewed journals covering different theoretical and experimental aspects of this field, the current state-of-the-art of which will be presented in Section 1.2.

Furthermore, some notable PhD theses focused on underwater beam propagation or UWOC and underwater imaging are relevant to this dissertation. For instance, in 2012, W. C. Cox from the North Carolina State University was amongst the first who simulated the underwater channel via a Monte-Carlo method for various underwater environments [1]. In 2013, B. M. Cochenour from the same US group, focused on the spatial and temporal dispersion of an underwater beam in turbid water and their implications for UWOC and imaging [2]. In 2015, L. J. Johnson from the University of Warwick detailed the optical properties of water and how the variability of these can affect an underwater communication link [3]. Although not focused on underwater data transfer, A. Maccarone's work at Heriot-Watt University demonstrated, in 2016, single-photon imaging in highly scattering water using time-of-flight and time-correlated single-photon counting techniques [4]. The expertise presented in that work was of importance for characterising laboratory-based water samples and is relevant to the experimental setups used throughout this thesis. Recently (in 2019), G. Giuliano from the University of Glasgow studied the impact of solar background in an underwater optical communication channel, proposed potential solutions to overcome it and examined the viability of a hybrid acousto-optic waveguiding system for underwater data transfer [5]. Lastly, in 2020, X.

Sun from the King Abdullah University of Science and Technology explored UWOC in non-line of sight (NLOS) configurations [6].

This thesis is divided into six chapters; Chapter 1 introduces the reader to the current state-of-the-art of the UWOC field, mentions the background technologies deployed for underwater data transfer, and describes the mechanisms of attenuation of light underwater. Then, it closes with the experimental characterisation of the laboratory-based water samples, enabling their comparison with real-world applications occurring in natural water.

Chapter 2 introduces the underlying physics of the devices used throughout this thesis as transmitters and receivers. A brief description of the modulation schemes applied in the experiments reported in the following chapters is also given.

Chapter 3 refers to deploying a novel blue gallium nitride (GaN) micro-LED array as a transmitter in a  $3 \times 2$  configuration. Both the high modulation bandwidth that a micro-LED exhibits (up to 338.5 MHz) and the increased power demonstrated due to the arrayed layout (up to 21 mW) were exploited for high-speed UWOC (on the order of Gb/s) in turbid water. In this thesis, I will call “turbid” water any water sample with added scattering agent.

The novelty in Chapter 4 is found in the deployment as transmitters of dual-colour micro-LED arrays fabricated by a transfer-printing (TP) method. Those devices were of different configurations; individually addressable violet-blue and blue-green micro-LED arrays and connected in-series blue-green micro-LED arrays. As will be shown, the flexibility of using different colours for underwater data transfer through wavelength division multiplexing (WDM) is of paramount importance as the underwater conditions (as per water turbidity) change. UWOC up to 200 Mb/s over highly turbid waters were demonstrated.

The “point-to-point” layout for an underwater link between a transmitter and receiver is lifted in Chapter 5. A diffusing fibre (Corning<sup>®</sup>Fibrance<sup>®</sup>Light-Diffusing Fibre), coupled to a green laser diode (LD), was deployed to transmit underwater data in an omnidirectional way as an underwater “beacon”. A data rate of 5 Mb/s was demonstrated over highly turbid underwater environments. Further study is presented in the last section of the chapter by simulating the potential of the beacon concept (via a concise MATLAB<sup>®</sup>script) for an increase in transmitted optical power and data rate.

Chapter 6 closes this thesis with conclusions and avenues for future work plans, and an appendix summarises the publications arising from this work.

## 1.2 State-of-the-art of UWOC

One can suggest that the basis of UWOC can be traced back to 1963, when Seibert Duntley published his famous paper entitled “*Light in the Sea*” [7]. It was the first time it was reported that the attenuation of light underwater “*varies markedly with wavelength*”. Later, in 1971, he published the results of his ten-year research on studying the optical properties of water by submerging incandescent lamps and lasers [8]. Then, in 1977 in the US, an UWOC channel was proposed from shore to a submarine using a blue-green laser [9]. Since then, and after the revolutionary work by Nakamura *et al.* on inventing efficient blue InGaN LEDs [10], the UWOC technology has matured remarkably. Upon the first UWOC Gb/s demonstration, which was reported by Hanson and Radic in 2008 [11] (1 Gb/s over a 2 m water pipe using a 532 nm laser), a plethora of research groups have reported data rates of tens of Gb/s over hundreds of metres using laser-based transmitters or tens of metres using LED-based sources.

In general, the laser-based sources can be operated with a high current density and output power. They emit coherent light of high directionality (owing to the stimulated emission of radiation) and thus with a small divergence angle ( $\approx 0.01^\circ$ ), and can exhibit high modulation bandwidth ( $> 1$  GHz). Although the former suggests that the laser-based transmitter ( $T_x$ ) should be constantly aligned with the receiver ( $R_x$ ), the later characteristic render lasers suitable for establishing high-capacity underwater optical links over relatively large distances. For instance, Chen *et al.* in [12] showed that 500 b/s can be transmitted over 144 m using a blue LD and a single-photon avalanche photodiode (SPAD). In terms of information capacity, a remarkable data rate of 30 Gb/s was reported over a 12.5 m piped underwater tap water link; the same data rate was achieved over 2.5 m in a turbid-harbour underwater environment [13].

On the other hand, the emitted light of an LED-based transmitter is divergent (owing to the LED spontaneous emission of radiation), suggesting that the alignment between  $T_x$  and  $R_x$  can be relaxed. LEDs are also cost-effective when compared to lasers, less power-demanding, and safer for the human eye. Thus, LEDs have been widely used for Li-Fi purposes [14] and are suitable for Gb/s and Mb/s UWOC over tens of metres. For example, a net data rate of 4 Gb/s over 2 m of tap water was achieved by Li *et al.* [15] using a single “mini” LED (150  $\mu\text{m}$  in dimensions) emitting at 484 nm. An LED was used in [16], operating at 470 nm, for the demonstration of 500 kb/s over 50 m, and 7.5 Mb/s over 10 m. In Chapter 3 we used an array of micro-LEDs which were in-series connected and of dimensions 60  $\mu\text{m}$  and 80  $\mu\text{m}$  and we reported data rates of up to 4.92 Gb/s, 3.22 Gb/s and 3.4 Gb/s over 1.5 m, 3 m and 4.5 m, respectively [17].

A brief summary of some of the most notable results in UWOC from academic groups, can be seen in Figure 1.1. For a more detailed survey of the domain, the reader is referred to review papers, such as [18].

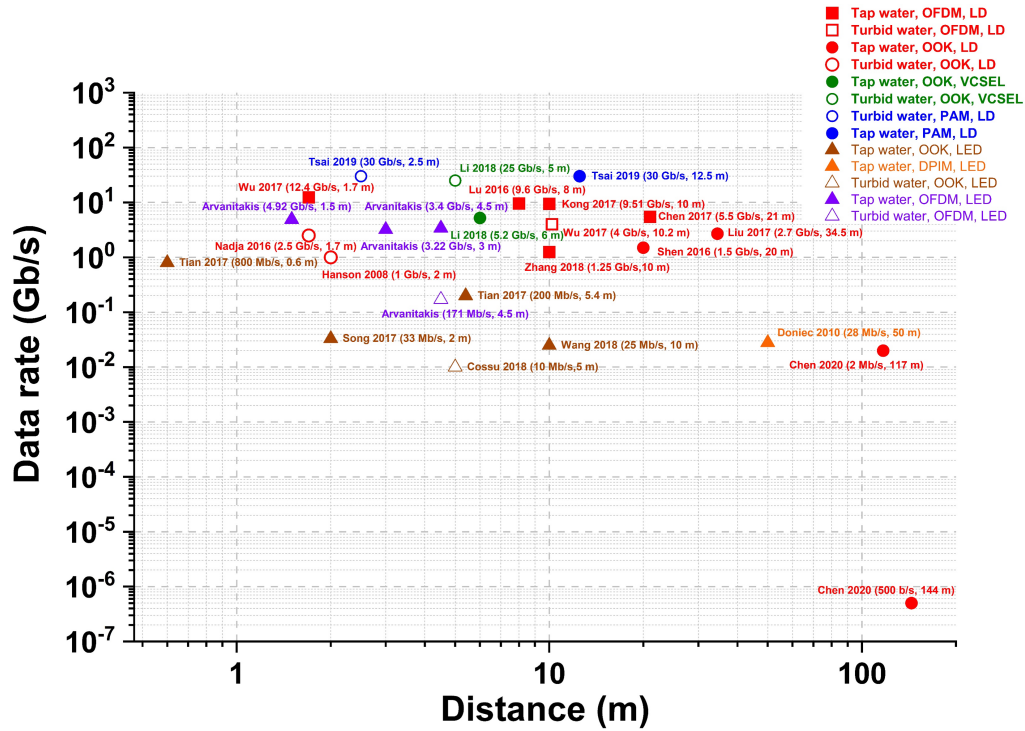


FIGURE 1.1: Summary of the experimental work on UWOC showing achieved data rates from LED- and laser-based source versus distance.

The results mentioned above refer to academic research. The need for fast underwater communications for oceanographic research, the military, or oil/gas/energy companies has increased over the last few years. The implementation and commercialisation of the UWOC technology is one of the biggest challenges the field experiences. A few companies worldwide offer commercial products using blue-green LEDs and lasers with their performances ranging from few a Mb/s over tens of metres (e.g., 2.5 to 10 Mb/s over up to 150 m, Sonardyne\*) or most recently, 1 Gb/s over 100 m in deep sea by Trimatiz Ltd [19]. Other companies focused on UWOC are BlueRobotics† and Shimadzu‡.

### 1.3 Technologies for underwater wireless communications

Wireless data transmission underwater is enabled through the deployment of primarily three types of waves: sound waves (acoustic), electromagnetic waves (EM) at RF, and

\*<https://www.sonardyne.com/products/bluecomm-200-wireless-underwater-link/>

†<https://bluerobotics.com/>

‡<https://www.shimadzu.com/underwater/index.html>

optical EM waves (Figure 1.2). When designing an underwater communication channel, two significant trade-offs are simplicity versus cost and range versus data rate. In general, the maximum bit rate of a communication link in free space or underwater can mathematically be given by the Shannon-Hartley theorem as in [20]:

$$R = \Delta\nu \log_2 \left( 1 + \frac{S}{N} \right), \quad (1.1)$$

where  $R$  is the maximum achievable data rate (in bits/sec),  $\Delta\nu$  is the channel bandwidth (in Hz),  $S$  is the average received signal power over the entire bandwidth (in Watts), and  $N$  is the total received noise over the entire bandwidth (in Watts). The  $S/N$  fraction is the signal-to-noise ratio (SNR). Equation 1.1 denotes that maximum information capacity requires high  $\Delta\nu$  and large SNR. The latter implies that the carrier wave should be propagated over the challenging underwater channel with minimum attenuation, low ambient noise and high-enough temporal fidelity so that the carrier wave can be easily demodulated at the receiver end. Equation 1.1 provides the theoretical upper limit for a given available bandwidth and SNR. It is noted that the Shannon-Hartley theorem is independent of how data is encoded in the carrier wave by the transmitter [21]. However, different modulation schemes vary in how close the maximum data rate can be achieved.

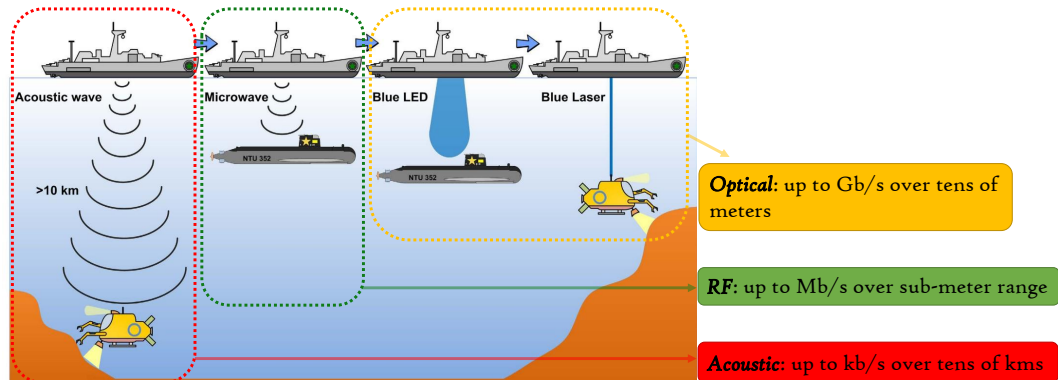


FIGURE 1.2: Schematic illustration of the dominant technologies in the underwater wireless communications field, along with their nominal operational range and data rates. The background image is taken from [22].

The following subsections will briefly describe the advantages and challenges that each of the technologies above exhibits, depending on the potential application in the underwater environment.

### 1.3.1 Acoustic

Sound waves have been the traditional mode of communication between underwater vehicles, especially for military applications. Although the acoustic channel is limited in



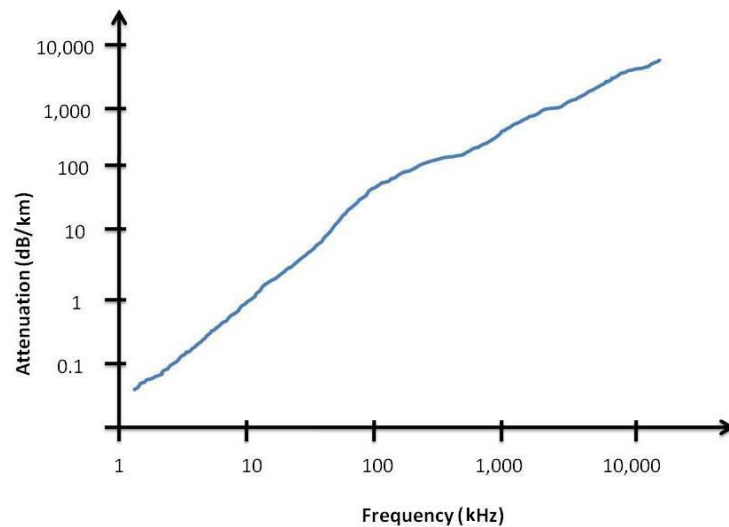


FIGURE 1.3: Variation of the attenuation of acoustic waves underwater in dB/km. Plot taken from [23].

data rate (on the order of kb/s), and thus it cannot support exchanges of large volume data in real-time (such as a high-definition video), it provides a long operational range. For instance, data transmission of 2.4 kb/s has been demonstrated over  $\approx 65$  km between an underwater vehicle and a ship on the sea surface [23].

The limitation in data rate arises from the intrinsic absorption of high acoustic frequencies ( $> 100$  kHz) via the viscous drag of the fluid and from the absorption of low frequencies (on the order of a few kHz) by specific chemicals within the seawater, such as boric acid and magnesium sulphate [24]. Both inherent attenuating features vary significantly with temperature, pressure (or depth), and salinity [21]. The attenuation (in dB/km) as a function of the acoustic wave frequency is plotted in Figure 1.3, where it is shown that in a narrow band of low frequencies ( $< 10$  kHz), the attenuation is low (less than 1 dB/km). As such, limited-bandwidth data transmissions can be enabled over large distances. However, acoustic waves are prone to multi-path propagation due to surface and bottom reflections, especially in shallow waters. The latter, along with the low speed of the acoustic carrier underwater<sup>§</sup> ( $\approx 1500$  m/s) leads to significant communication delay spreads (which can be as large as 50 – 100 ms [25]) and to inter-symbol interference (ISI). In ISI, a signal, represented by a specific data symbol, interferes with out-of-phased symbols [23, 25], rendering the demodulation of the original signal challenging.

<sup>§</sup>It is noted that underwater the speed of sound is five orders of magnitude smaller than the speed of light ( $\approx 225 \times 10^6$  m/s) in water.

### 1.3.2 Radio frequency (RF) electromagnetic (EM) waves

RF EM waves, ranging between 3 Hz - 300 GHz, dominate the communications field over free space. Typical examples include signals for satellite communications, television, radio broadcasts, Wi-Fi, mobile phones, and Bluetooth. Hence, extending RF deployment to underwater environments is rational, especially since RF EM waves propagate smoothly at the air-water interface [26]. RF waves exhibit advantages over acoustic, including faster carrier propagation velocity and higher data rates. For instance,  $>3$  Mb/s over  $<10$  m in fresh water [26].

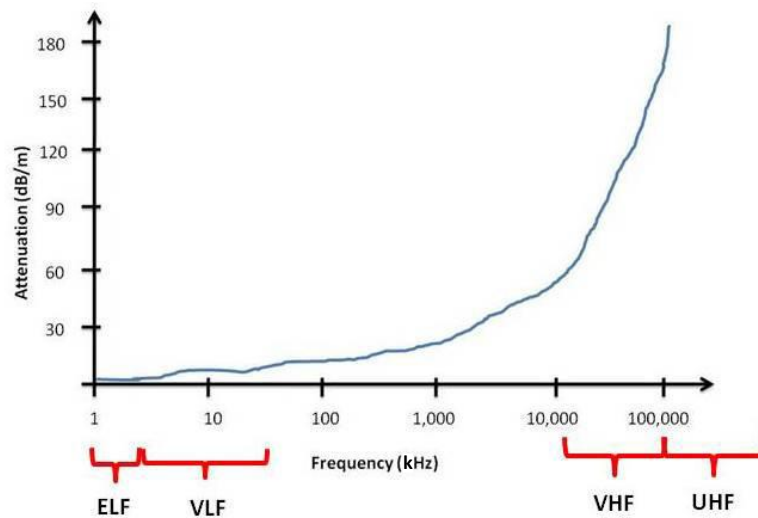


FIGURE 1.4: Variation of the attenuation of RF underwater. Plot taken from [23].

The challenges with RF emerge when considering seawater as an electrical conductor due to its salinity. Although seawater's conductivity is considerably smaller than a metal's, the EM field at RF decays exponentially with distance within a uniform conductor [21], whilst the absorption coefficient (in  $\text{m}^{-1}$ ) of seawater in the RF regime is proportional to the square root of the wave frequency<sup>¶</sup>, i.e.,  $a_{\text{seawater}} \approx \sqrt{\nu}$  [23]. Such a relation is plotted in Figure 1.4 where it is shown that the very and ultra-high frequencies (VHF and UHF, respectively) are quickly attenuated in seawater (note that the attenuation on  $y$  axis is in dB/m in contrast to dB/km for acoustic, previously). On the contrary, a narrow frequency bandwidth ( $\Delta\nu$ ) between 3 Hz - 30 kHz that lies at extremely and very low frequencies (ELF and VLF, respectively) seems adequate for long operational ranges. Still, for such use, the design and size of the antenna should be considered (note that 30 kHz corresponds to a wavelength of  $\lambda = 10$  km [28]). Additionally, according to Equation 1.1, a narrow  $\Delta\nu$  implies a limited achievable data rate.

<sup>¶</sup>Contrastingly,  $a_{\text{freshwater}}$  is essentially frequency-independent [25] and thus, RF is attractive for data transmission in, e.g., lakes if the large operational power and antenna size are ignored. For instance, a communication link was established in Loch Ness at 30 m depth between a surface vessel and a submersible vehicle at a frequency which was believed to be 150 MHz [27].

Consequently, the frequency-dependent data rates of RF render them impractical for high-speed subsea wireless communications over modest distances.

### 1.3.3 Optical waves

UWOC is considered an alternative to acoustics and RF as light attenuation in water is lowest in the visible region [29]. More precisely, the absorption coefficient in pure water is about  $0.003 \text{ m}^{-1}$  in the blue region between 460 - 480 nm [23]. The reason why a reduced attenuation is exhibited in the visible spectrum is given in detail in a later section (see Section 1.4.1.1).

For now, it is worth recalling from Section 1.3 that the large  $\Delta\nu$  (hundreds of THz) of the visible spectral region allows for data-transfer demonstrations underwater on the order of Gb/s over tens of metres (e.g. 6.6 Gb/s over 55 m of tap water [30]). Other advantages of optical waves over acoustic and RF include the reduced cost, unlicensed visible spectrum, the establishment of stealthier and high-security communications, and lower power requirements [31]. In the hundreds of THz regime, the conductivity of seawater is considered negligible [21]. Hence, the limitations for UWOC are associated with the ambient light that can saturate the receiver and the attenuation of light attributed to absorption and scattering underwater. Both phenomena considerably affect the light propagation through the aquatic medium and, eventually, limit the achievable data rate. The discussion on the challenges of light propagation underwater will be considered in Section 1.4.

### 1.3.4 Summary

A brief description of the dominant background technologies in UWOC, and the trade-off between the available  $\Delta\nu$  and range, are summarised in Figure 1.5. For reference and comparison, fibre optics are also included in the same graph as being the primary and most popular means for high-speed tethered communications around the globe. However, tethered platforms and underwater devices are impractical in the challenging underwater environment and out of the scope of this thesis. A further comparison of the key features of the background technologies is summarised in Table 1.1. Note that  $P_T$  denotes the transmitted power. As discussed, the acoustic channel and the low-frequency RF are extremely limited in bandwidth although they can have large range. The relatively low attenuation window of optical waves in the blue-green region of the EM spectrum allows for high bandwidth communications over moderate ranges (up to hundreds of metres), depending on the water and system characteristics.

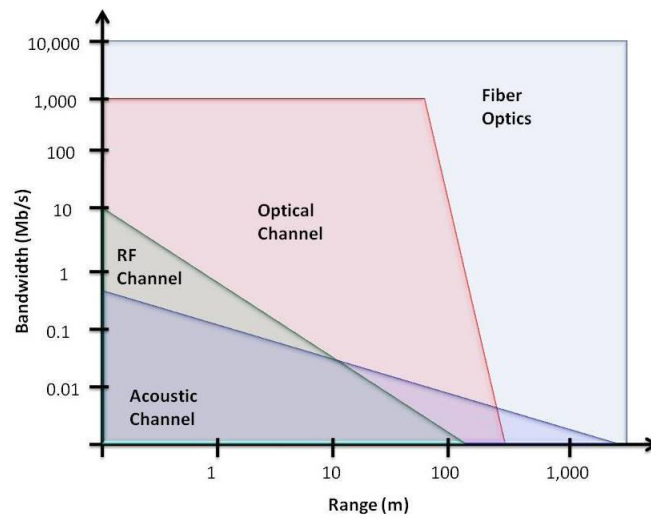


FIGURE 1.5: The available  $\Delta\nu$  against range for all the background technologies that govern the UWOC domain. Image taken from [23].

TABLE 1.1: Comparison of the key features of the background technologies that govern the UWOC field. Data taken from [3, 28, 32].

Parameters	Acoustic	RF	Optical
Data rate	kb/s	$\sim$ Mb/s	$\sim$ Gb/s
Max range	km's	tens of m's	hundreds of m's
$\Delta\nu$	1 - 100 kHz	3 Hz - 300 GHz	430 - 750 THz
$P_T$	tens of W	tens of W	mW to W
Security	low	high	high
Attenuation	<ul style="list-style-type: none"> <li>• low propagation velocity</li> <li>• temperature</li> <li>• pressure</li> <li>• salinity</li> </ul>	<ul style="list-style-type: none"> <li>• seawater conductivity</li> </ul>	<ul style="list-style-type: none"> <li>• ambient noise</li> <li>• absorption</li> <li>• scattering</li> </ul>

## 1.4 Optical properties of water

Oceanographic researchers strongly rely on marine/underwater optics to characterise water masses through their optical properties. How saline (and fresh) water ingredients interact with light significantly determines the natural waters' optical properties. Sea substances can either be dissolved organic materials, i.e., particles of diameter  $< 0.4 \mu\text{m}$ <sup>||</sup> [33], or particles of larger size of various kinds and concentrations.

<sup>||</sup> According to [33, 34], the discrimination between dissolved and particulate depends on the particle's diameter size, i.e., those of diameter size less than  $0.4 \mu\text{m}$  ( $= 400 \text{ nm}$ ) are considered dissolved but larger

C. D. Mobley, in his “*Light and Water: Radiative transfer in natural waters*” book, classified the optical properties of water into two categories [29]: *inherent* and *apparent* optical properties (IOPs and AOPs, respectively). IOPs do not depend on the ambient light field but only on the medium’s properties, whereas AOPs depend on both IOPs and the illumination’s geometrical/directional characteristics. Typical examples of IOPs are the overall attenuation coefficient ( $c(\lambda)$ , in  $\text{m}^{-1}$ ), which is given as the sum of the absorption and scattering coefficients ( $a(\lambda) + b(\lambda)$ ), and the refractive index,  $m$ , of the medium. The most common AOP is the diffuse attenuation coefficient,  $K_d$  (in  $\text{m}^{-1}$ ), which describes how the downwelling (or downward) irradiance\*\* ( $E_d$ , in  $\text{W}/\text{m}^2$ ) of the sun is attenuated underwater with depth.

Variations in the quantities mentioned above have severe implications in underwater optical propagation and, hence, in UWOC. Spatial and temporal dispersion of the beam underwater can affect the encoded signals upon the optical carrier and, eventually, degrade the bandwidth of the underwater channel. Thus, when configuring the design, modelling, and simulation of an underwater system comprising a transmitter and receiver, it is paramount to know the mechanisms that result in beam attenuation in the water. In the following sections, these mechanisms will be described.

#### 1.4.1 Inherent optical properties of water (IOPs)

As previously mentioned, absorption and scattering are the most common IOPs, as they are the main physical processes that occur when electromagnetic waves propagate through attenuating media, such as water. If  $a(\lambda)$  and  $b(\lambda)$  are known, then it is sufficient to appreciate how light interacts with the medium. To begin with, a schematic in Figure 1.6 is given in an attempt to extract simple equations that will lead to defining  $a(\lambda)$  and  $b(\lambda)$ . It is assumed that a light beam of wavelength  $\lambda$  and transmitted power  $P_T$  is incident on an elemental volume of water  $\Delta V$  with thickness  $\Delta r$ . Then, a fraction of  $P_T$  is absorbed by the medium, denoted as  $P_A$ , whilst another is scattered at an angle  $\theta$  into a solid angle  $\Delta\Omega$ , denoted as  $P_S$ . The remaining light passes through the medium unaffected, and the received power,  $P_R$ , is collected and measured by a photodetector. The energy throughout this process should be conserved, and as such,  $P_T(\lambda) = P_A(\lambda) + P_S(\lambda, \theta) + P_R(\lambda)$ . The absorption and scattering phenomena are discussed next.

---

are particulates. This dividing line is empirically set to 400 nm as it is the working minimum that can be observed through optical microscopy, i.e., via visible wavelengths.

\*\*According to Jerlov in [35], the irradiance at a point of a surface is defined as the ratio of the radiant flux (i.e., the time rate of radiant energy,  $F = Q/t$ , in Watts) and the area of the infinitesimally small surface under radiation. That is,  $E_d = dF/dA$ .

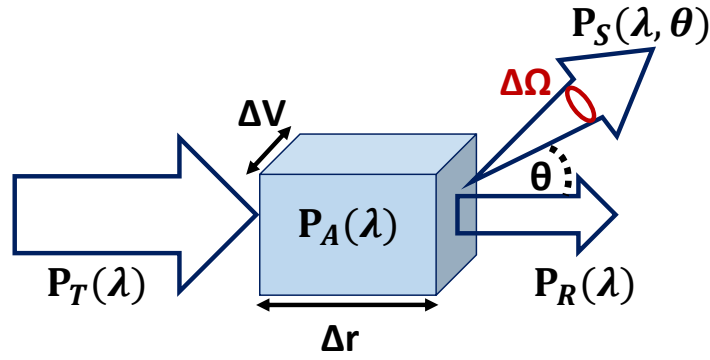


FIGURE 1.6: Schematic of how an incident light beam interacts with a small volume of water.  $P_T$ : incident (or transmitted power),  $P_A$ : absorbed power by the volume of water,  $P_S$ : scattered power, and  $P_R$ : received power.

#### 1.4.1.1 Absorption

Absorption is the physical process in which the molecules (or the atoms) that constitute the attenuating medium absorb incident photons' energy via an electronic transition in the medium. The absorbed energy can then be re-emitted radiatively or converted into a non-radiant form, such as heat or chemical energy, e.g., the formation of new chemical compounds [36]. Following the information shown in Figure 1.6, the absorptance,  $A(\lambda)$ , is defined as the ratio of the absorbed power by the medium to the incident power, i.e.,  $A(\lambda) = P_A(\lambda)/P_T(\lambda)$ . Then, the absorption coefficient per unit distance ( $\text{m}^{-1}$ ) can be calculated by taking the limit as the thickness,  $\Delta r$ , becomes infinitesimally small [28, 29]:

$$a(\lambda) = \lim_{\Delta r \rightarrow 0} \frac{\Delta A(\lambda)}{\Delta r} = \frac{dA(\lambda)}{dr}. \quad (1.2)$$

#### Absorption by pure water (molecular absorption)

Light absorption in pure water has been exhaustively studied and described in the literature (e.g. in [37, 38]). The behaviour of the pure water absorption coefficient ( $a_w$ ) as a function of the visible wavelengths is shown in Figure 1.7 (bottom).

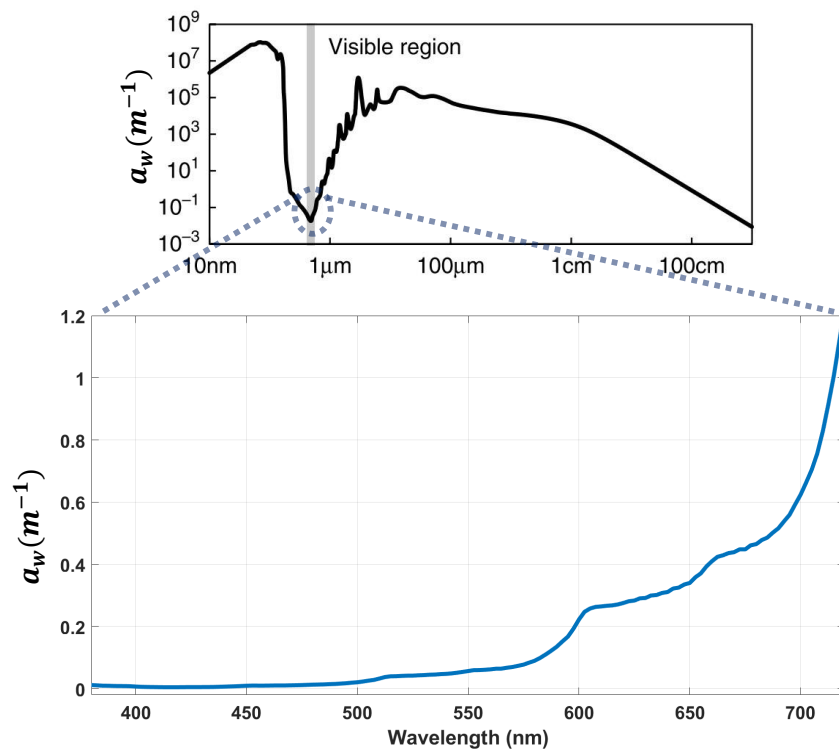


FIGURE 1.7: Variation of the water absorption coefficient against a broad range of electromagnetic spectrum wavelengths (top). Figure taken from [34]. The water absorption coefficient variation magnified in the visible spectrum (bottom). Data taken from [37].

Additionally, a representation of the power losses attributed to pure water absorption, as the wavelength of radiation increases and shifts towards the infrared (IR), is shown in Figure 1.8. Note that more than 99% of power is lost at, e.g., 30 m of propagation distance when switching from violet-blue to red wavelength.

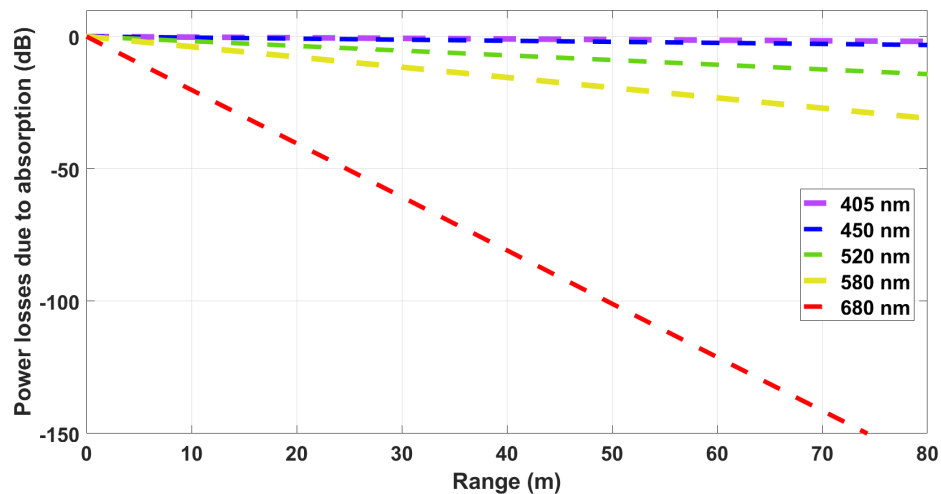


FIGURE 1.8: Power losses for five visible wavelengths of an underwater channel due to pure water absorption. Data taken from [37].

Now, by taking into account the complex form of the medium's refractive index,  $n + im$ , both quantities,  $a$  and  $\lambda$ , are mathematically related as follows [39]:

$$a = \frac{4\pi m}{\lambda}, \quad (1.3)$$

where  $m$ , is the imaginary part of the refractive index, and  $\lambda$ , the light wavelength. While the real part,  $n$ , is associated with (elastic) scattering (see Section 1.4.1.2),  $m$  is linked with the absorption coefficient. A quick investigation of Equation 1.3 shows that short wavelengths are strongly absorbed within the water.

However, how the water molecule interacts with light is far more complicated and cannot be described solely by a simple equation. The absorption bands of the medium through which electromagnetic waves pass depend primarily on the frequency of light whose electric field sets up oscillations and rotational vibrations of the molecule, ionises atoms and breaks chemical bonds. In addition, the water molecule's physical properties (i.e., electron configuration, electrical and magnetic properties) along with its geometrical parameters (i.e., the position of the atoms) should also be taken into account [38]. Details of the interactions between the water molecule and electromagnetic radiation, under the scope of atomic and molecular physics, are beyond the scope of this thesis, and the reader is advised, if interested, to refer to relevant textbooks, such as [38, 40]. Nonetheless, it is worth noting that the absorption of energetic photons in the ultraviolet (UV), at around 100 nm (corresponding  $E_{ph} = 12.4$  eV), is associated with a collective excitation of all the electrons in the water molecule [39]. Moving further within the UV regime, the dissociation of the H-OH and O-H bonds takes place at 240 nm (corresponding  $E_{ph} = 5.11$  eV) and 280 nm (corresponding  $E_{ph} = 4.4$  eV) [38], respectively. These mechanisms explain the highly peaked absorption bands of water in the UV. Similarly, the interaction of IR light with the asymmetrical structure of the water molecule results in an increased absorption in this spectral region, where vibrational and rotational transitions take place [38]. The highly peaked absorption bands in the UV and IR can be seen in Figure 1.7 (top).

The “window” of reduced attenuation due to absorption in the visible wavelengths (roughly between 300 – 700 nm) is thus attributed to the low-energetic photons within that spectral area whose energy is not sufficient to boost the water molecule electrons into higher energy levels [29].



### **Absorption by phytoplankton**

The word phytoplankton originates from the Greek words “phyto”, which means plant, and “plagktos”, which means wanderer or traveller. Indeed, phytoplankton are microscopic marine algae, most of which are buoyant and float in the upper part of the oceans, where sunlight can penetrate. Photosynthesis in phytoplankton is enabled through the absorption of sunlight by chlorophylls, the primary constituents of phytoplankton. The absorption peaks are primarily at 440 nm (blue) and secondarily at 675 nm (red) [41]. Precise measurements of absorption by phytoplankton and robust calculation of the corresponding absorption coefficient are challenging due to the varied location, depth, shape, size and concentration of the individual pigments. As a result of these variations, the minima in the absorption spectra of natural waters rich in phytoplankton are shifted towards longer wavelengths (from blue to green) within the “window” of reduced attenuation that was previously discussed [21].

### **Absorption by coloured dissolved organic matter (CDOM)**

CDOM, also known as “gelbstoff” (or yellow substance), comprises dead plant tissues and decaying marine matter. As a result, CDOM produces humic and fulvic acids whose absorption peaks are around UV and blue allowing yellow and red colours to be distinct [28]. The origin of gelbstoff can be from dissolved matter in the water or run-off soil from nearby land. Therefore, coastal waters and waters near river estuaries are expected to exhibit high concentrations of CDOM [34].

#### **1.4.1.2 Scattering**

Scattering is equally important to the absorption phenomena when predicting and describing underwater light propagation. It refers to the process whereby photons emitted by a transmitter deviate from their original path to the receiver resulting in attenuation of the optical signal. The photons’ multi-path propagation can limit the maximum data rate due to the reduction of signal levels at the receiver side and by temporal pulse stretching. This temporal dispersion is attributed to photons scattered multiple times along their way to the receiver. Hence, they have travelled longer path lengths, which requires more significant time. The time delay between the non-scattered detected photons and scattered ones induces ISI if the bit rate (or bit time) is comparable to the pulse temporal spreading [11]. The beam deflection is attributed to the suspended particles (also known as scattering centres or scatterers) in the water, whilst the intensity of the scattered light depends on the dimensions of these centres with respect to the wavelength of radiation [40].

Similarly to how absorptance was defined in Section 1.4.1.1, scatterance,  $B(\lambda, \theta)$ , is described as the ratio of the scattered to the incident power (as these quantities are shown in Figure 1.6), i.e.,  $B(\lambda, \theta) = P_S(\lambda, \theta)/P_T(\lambda)$ . Consequently, the scattering coefficient,  $b(\lambda, \theta)$  (in  $\text{m}^{-1}$ ), is given as [28, 29]:

$$b(\lambda, \theta) = \lim_{\Delta r \rightarrow 0} \frac{\Delta B(\lambda, \theta)}{\Delta r} = \frac{dB(\lambda, \theta)}{dr}. \quad (1.4)$$

A discussion on scattering would be incomplete if the angular distribution of the scattered light was not mentioned. Returning to the illustrated underwater processes in Figure 1.6, a relation which incorporates the  $P_S(\lambda, \theta)$  and  $P_T(\lambda)$  quantities along with the angular distribution of scattering, can be expressed as [42]:

$$P_S(\lambda, \theta) = P_T(\lambda)\beta(\lambda, \theta)drd\Omega \quad (1.5)$$

$$\Rightarrow \beta(\lambda, \theta) = \frac{P_S(\lambda, \theta)}{P_T(\lambda)drd\Omega}. \quad (1.6)$$

Equation 1.6 can be simplified by considering the definition of the scattered differential intensity ( $dI(\lambda, \theta)$ ), that is, the scattered power ( $P_S(\lambda, \theta)$ ) divided by the given infinitesimal solid angle,  $d\Omega$  [29, 42]. In other words,  $dI(\lambda, \theta) = P_S(\lambda, \theta)/d\Omega$  (in  $\text{W}/\text{sr}$ ). Also, by taking into account the definition of downward (or incident) irradiance that was given earlier (Section 1.4, footnote) [35], it yields that  $E_d = P_T(\lambda)/dA$  (in  $\text{W}/\text{m}^2$ ). Finally, the relations mentioned above, along with the statement that the incident beam illuminates an infinitesimal volume of water,  $dV = drdA$ , lead Equation 1.6 to a concise form as follows [29, 42]:

$$\beta(\lambda, \theta) = \frac{dI(\lambda, \theta)}{E_d dV}. \quad (1.7)$$

The angular distribution of scattering underwater is described by the form of  $\beta(\lambda, \theta)$  (in  $\text{m}^{-1} \text{sr}^{-1}$ ) in Equations 1.6 and 1.7.  $\beta(\lambda, \theta)$  is known as the volume scattering function (VSF) and, physically, it is a measure of the scattered intensity (in the scattering angle  $\theta$ ) per unit incident irradiance per unit volume of water [29, 42].

Integrating the VSF over all directions (solid angles) yields the total scattered intensity per unit irradiance per unit volume of water. More precisely, it provides a quantification of how strongly that volume of water scatters, or in other words, the water scattering coefficient,  $b(\lambda)$  (in  $\text{m}^{-1}$ ), can be calculated. That is [29]:

$$b(\lambda) = \int_0^{4\pi} \beta(\lambda, \theta) d\Omega = 2\pi \int_0^\pi \beta(\lambda, \theta) \sin(\theta) d\theta. \quad (1.8)$$

Scattering in natural waters has been categorised by Mobley based on the particulates' size in the water with respect to the wavelength of radiation. The categories are itemised as follows [29]:

- *Molecular (or Rayleigh) scattering* ( $\ll \lambda$ ): scattering attributed to molecular motions, sea salts and small-scale fluctuations in the medium's density.
- *Scattering by particles* ( $> \lambda$ ): scattering by organic and inorganic particulates whose scattering coefficient is typically ten times larger than Rayleigh scatterers.
- *Scattering by turbulence* ( $\gg \lambda$ ): scattering caused by salinity and temperature fluctuations resulting in deviations on the real part of the medium's refractive index ( $n$ ).

### **Molecular (or Rayleigh) scattering**

In molecular scattering (also known as Rayleigh or non-resonant scattering) events in pure or/and sea water, the frequency of the incoming light is not resonant to any of the atomic transitions of the molecule. As such, the photon's energy is too small to excite the molecule into a higher energy state. Despite that, the non-resonant electromagnetic field interacts with the electron cloud of the atom in the ground state by setting the cloud into vibration with a frequency equal to that of the incident light. Once the cloud starts to vibrate around the positive nucleus of the atom, an oscillating dipole is formed and immediately radiates (on the order of a femtosecond,  $10^{-15}$  s [43]) in some direction. The resulting scattered light comprises a photon carrying the same amount of energy as the incident photon. Therefore, the scattering is elastic<sup>††</sup> [45].

A quantification of the intensity of the scattered light was given by Lord Rayleigh [46]. He proposed that for the case of  $N$  atomic oscillators of size smaller than the radiation's wavelength and distributed randomly in an isotropic medium (thus, comprised of a wavelength-independent refractive index), the intensity of the scattered light varies inversely proportional to the fourth power of the incident wavelength, i.e.,  $I \sim 1/\lambda^4$ . Considering the anisotropy of the water molecules, the intensity of the elastically scattered light fluctuates more accurately according to  $\sim 1/\lambda^{4.32}$  [29]. As such, it becomes clear that the intensity of the Rayleigh scattered light increases with frequency (decreases

---

<sup>††</sup>If the scattered light consisted of a photon of energy either larger or smaller than that of the incident photon (i.e., inelastically scattered light), then the process would be described by "Raman scattering". This process occurs in a time scale of  $10^{-13}$  to  $10^{-12}$  s, on which more information can be found in [44]. Another inelastic process taking place in natural waters is fluorescence by phytoplankton, and CDOM [36] that occurs on the order of  $10^{-12}$  to  $10^{-8}$  s [43].

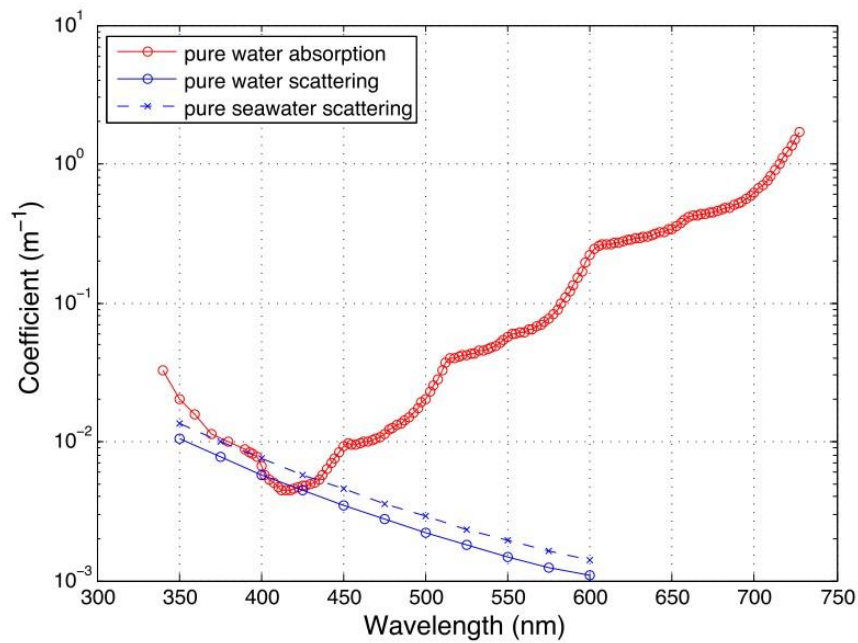


FIGURE 1.9: The absorption coefficient by pure water and the scattering coefficients of pure and sea water versus wavelength. Graphs were plotted together for comparison; scattering mostly contributes minimally to the overall attenuation. Image taken from [2].

with wavelength) and that water's atomic oscillator will respond more rigorously to the driving frequency as this approaches the UV (where the water molecule's electronic resonances are [39]).

Closing this section, it is worth noting that scattering from the sea and pure water is similar but slightly increased in seawater due to the presence of sea ions (e.g.,  $\text{Cl}^-$ ,  $\text{Na}^+$ , etc.) [42], as is shown in Figure 1.9 (blue curves) [2]. However, the contribution of molecular scattering (either by pure or seawater) to the overall attenuation, when compared to the molecular absorption (red curve), is minimal at visible wavelengths as can be seen in the same figure.

### Scattering by particles

The previous description of molecular scattering was mainly based on the interaction between the incident radiation and the water molecules on a submicroscopic scale. It was also assumed that the medium (i.e., saline or pure water) was homogeneous, so the small fluctuations in  $n$  due to random molecular motions were negligible, and practically  $n$  could be considered constant.

However, the water-particle interface becomes substantial when discussing scattering by large particles (of typical sizes larger than  $2 \mu\text{m}$ ) of organic or inorganic matter. The inhomogeneities that light encounters when meeting the particle or passing through it

allow the scattering process to be described macroscopically, i.e., via classical optics. Scattered light by large particles can be linked to surface reflection, refraction, multiple internal reflections, and diffraction [40]. Although diffraction is independent of the particles' composition, reflection and refraction are strongly determined by the particles' refractive index [47], and both phenomena are well defined by Snell's law. Thereby, the real part of the water's refractive index (i.e.,  $n$ ) that was introduced in the molecular absorption description (Section 1.4.1.1) is associated with elastic scattering [45].

### Scattering by turbulence

In free space, variations in  $n$  of the atmosphere due to temperature fluctuations or/and the motion of the air due to winds and convection are known as turbulence. Atmospheric turbulence in, e.g., astronomy makes stars twinkle. At the same time, in long-range free-space optical communication links, it can cause the beam to wander at the receiver end, which in turn can result in significant degradation of the channel.

By transferring the above concept underwater, it is noticed that although small variations in water's  $n$  are unimportant, when it comes to judging the robustness of a UWOC link over several tens of meters, the fluctuations in water's  $n$  should be considered [36, 42]. The turbulence-induced scattering is owned to water temperature and salinity variations [29]. Measurements on  $n$  of seawater samples as a function of wavelength, salinity, temperature, and pressure, were performed by the authors in [48]. Their conclusions can be summarised as follows;  $n$  decreases as the wavelength and temperature increase, and it increases while increasing salinity or pressure. Despite this evidence, turbulence-induced scattering will be considered negligible for this thesis, as the refractive index variation due to turbulence can be on the order of  $10^{-6}$  [49].

### 1.4.2 Apparent optical properties of water (AOPs)

Section 1.4 stated that the AOPs of water differ from the IOPs in terms of the ambient light field and the directional structure of the light rays. For instance, a radiometric quantity, such as irradiance, can dramatically change in magnitude within a short period when, e.g., the sun is instantly covered by a cloud on a sunny day. Ideally, though, an AOP alters slowly with external environmental changes [29]. Such an AOP can be a radiometric quantity that changes "smoothly" with depth variation. To be characterised, various variables need to be considered [42], namely the atmospheric conditions, irradiance distribution on the surface, angle of incidence, etc.

As mentioned before (Section 1.4), one of the AOPs of interest is the diffuse attenuation coefficient,  $K_d$  (in  $\text{m}^{-1}$ ), which indicates how the downward irradiance ( $E_d$ ) diffuses as a function of depth ( $\zeta$ , in m) and wavelength. According to [29],  $K_d$  is given as:

$$K_d(\zeta, \lambda) = -\frac{1}{E_d(\zeta, \lambda)} \frac{dE_d(\zeta, \lambda)}{d\zeta}. \quad (1.9)$$

$K_d(\zeta, \lambda)$ , as an AOP, is similar to  $c(\lambda)$  from the IOPs, as both variables quantify power losses within a water volume. Their distinct difference, though, is that  $c(\lambda)$  refers mostly to a narrow, collimated beam propagating underwater, whereas  $K_d(\zeta, \lambda)$  regards ambient downward irradiance that originates from all directions and strongly depends on the directional structure of the ambient light field [29]. This is to say that  $c(\lambda)$  fits well with point-to-point or line-of-sight (LOS) links, whilst  $K_d(\zeta, \lambda)$  is more suitable in non-line-of-sight configurations [42].

## 1.5 Optical water types

It was previously stated that the nature and concentration of suspended matter in water shifts the minimum light attenuation towards longer wavelengths (see Section 1.4.1.1). This observation has an impact on UWOC that should not be overlooked, as the robustness and reliability of an UWOC system depend strongly on whether the encoded data are transmitted through water with minimum losses. As such, selecting the optimum transmission wavelength is highly desirable when configuring what type of transmitter and receiver should be used in the underwater channel. For instance, Chapter 4 is inspired by the previous observation and is devoted to deploying a versatile dual-colour device that enables data transmissions of up to 200 Mb/s via WDM over turbid waters.

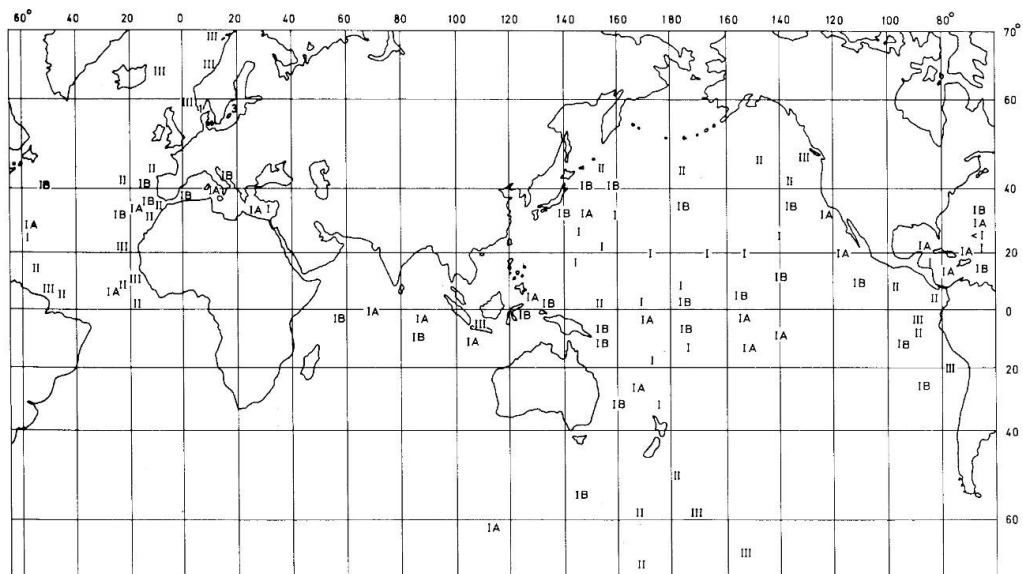


FIGURE 1.10: Regional distribution of the Jerlov water types. Image taken from [50].

For convenience, N. G. Jerlov classified natural waters into individual groups based on their optical properties, as these can be quantified by  $K_d(\zeta, \lambda)$  of each body of water [50]. The classification scheme includes the open ocean waters where power losses due to absorption by phytoplankton are dominant. These types are labelled as *I* for the clearest type of open ocean water, *IA*, *IB*, and *III* for the most turbid ones. On the other hand, coastal waters (where DCOM and inorganic particles account for the beam degradation) are categorised as *1*, for the clearest type, up to *9* for the murkiest. The regional distribution of the optical water types is illustrated in Figure 1.10.

Although the Jerlov classification was based on  $K_d(\zeta, \lambda)$  (that is an AOP), Solenko and Mobley in [51] calculated the  $c(\lambda)$  (that is an IOP) of all Jerlov water types as a function of the light wavelength. They also showed in Figure 1.11 the variation of those water bodies'  $c(\lambda)$  minima as the water turbidity increases.

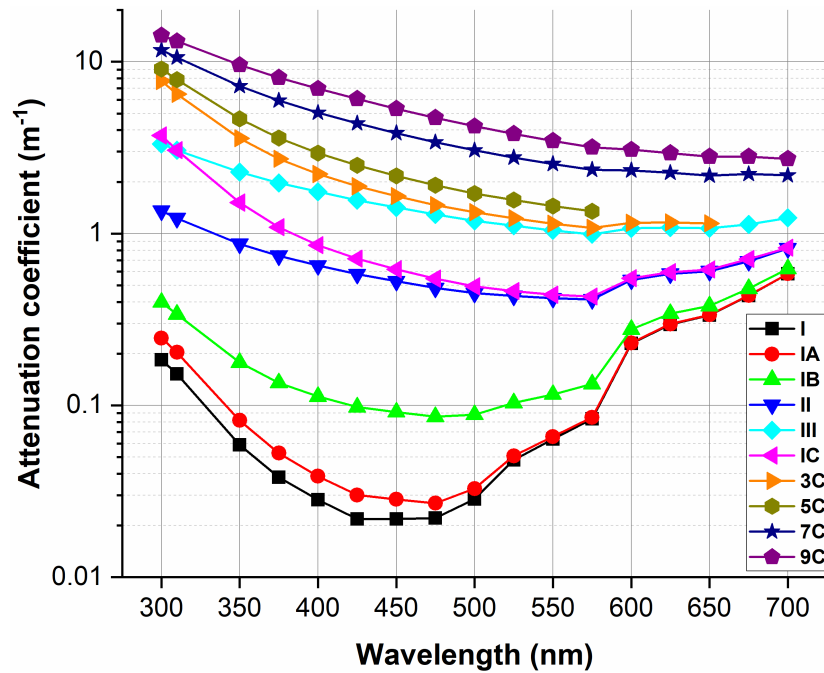


FIGURE 1.11: The variation of the attenuation coefficient versus wavelength for all Jerlov water types. Data acquired from [51].

Inspired by Solenko and Mobley's work, the following section details the characterisation of the laboratory-based water samples used in this thesis by estimating their attenuation coefficient.

## 1.6 Laboratory-based water samples characterisation and background theory

The feasibility of UWOC depends on the optical properties of the body of water over which a communication link is established. As such, the first step before any UWOC demonstration in our research was to characterise the laboratory-based water samples of various turbidities used throughout this thesis. The characterisation was based on estimating the  $c(\lambda)$  (in  $\text{m}^{-1}$ ) of those water samples.

The following process was based on replicating methods used in past references, where commercial antacid was used to simulate the scattering properties of natural ocean waters. More precisely, Maalox<sup>®</sup> antacid, whose particulate size is around  $11 \mu\text{m}$  [52] and which comprises aluminum hydroxide ( $\text{Al}(\text{OH})_3$ ) and magnesium hydroxide ( $\text{Mg}(\text{OH})_2$ ), has been extensively reported as the most common simulated scattering agent. It has been shown that the forward portion of its VSF, i.e., the angular distribution of scattering at very small angles (less than  $10^\circ$ ), is remarkably comparable to that of natural waters [8, 53]. This statement is confirmed by examining Figure 1.12 where the VSFs of four ocean water types (turbid harbour, coastal ocean, clear ocean and pure sea water) are plotted along with Maalox antacid's VSF at  $\lambda = 514 \text{ nm}$ <sup>‡‡</sup>. Table 1.2 summarises the optical properties of the water bodies shown in Figure 1.12.

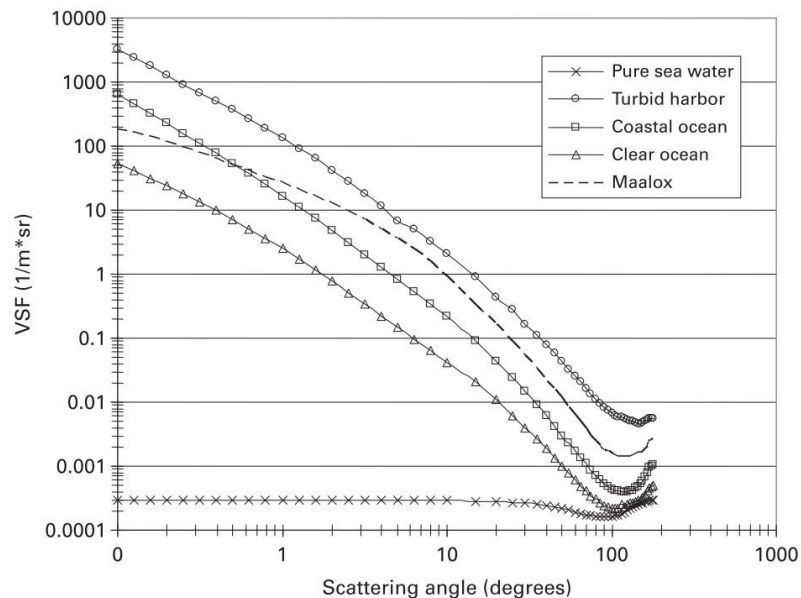


FIGURE 1.12: Volume scattering functions from [11, 53, 54] for four types of ocean waters (solid curves, from top): turbid harbour, coastal ocean, clear ocean, and pure seawater. The Maalox data are presented through the dashed curve. Figure taken from [42].

<sup>‡‡</sup>In this work, S. Duntley reported that the attenuation in light's optical power due to Maalox over an underwater beam propagation of 5.5 m was estimated to be 98.3% of the initial optical power [8].



TABLE 1.2: Optical properties of four ocean water types at  $\lambda = 514$  nm. Data taken from [11, 54].

Water type	$a$ ( $\text{m}^{-1}$ )	$b$ ( $\text{m}^{-1}$ )	$c$ ( $\text{m}^{-1}$ )
Pure sea water	0.0405	0.0025	0.043
Clear ocean <sup>§§</sup>	0.114	0.037	0.151
Coastal ocean <sup>¶¶</sup>	0.179	0.219	0.298
Turbid harbour <sup>***</sup>	0.266	1.824	2.19

For reference the corresponding *Jerlov* water types (at  $\lambda = 525$  nm) to Table 1.2's pure sea water and turbid harbour are *Jerlov* I and 7C, respectively, whilst clear and coastal ocean fall between *Jerlov* IB and II [51]. It can be seen that while pure sea water exhibits a relatively uniform VSF (due to the limited presence of scatterers in the water), the angular dependence of the other three ocean types is highly peaked at very small angles, although the magnitudes range over almost a factor of 100. The large forward peak suggests that scattered photons are most likely to scatter into very small angles relative to their propagation direction prior to scattering.

Three off-the-shelf laser diodes (LDs) were used to characterise the laboratory-based water samples. These devices respectively operated at three different wavelengths, i.e., 405 nm (violet, LD-F405E04), 450 nm (blue, OSRAM, PL450B), and 520 nm (green, OSRAM, PL520). These colours were the same as the nominal central wavelengths of this thesis's LED- and laser-based devices. The in-house constructed laboratory-based water tank, over which the LD beams were propagated, was of dimensions  $1.5 \times 0.35 \times 0.35$  m<sup>3</sup> and filled with 160 l of tap water. The water tank was the main component for all the experiments presented in this dissertation. Its walls were fitted with high transmittance (91%) Pilkington Optiwhite<sup>TM</sup> glass, which was used in recent studies for single-photon imaging in highly scattering underwater environments [4]. Furthermore, matt black plastic sheets were placed at the bottom and around its walls to prevent reflections coming from the tank's walls, which would not occur in open waters and may lead to signal distortion due to multipath beam propagation. The beams of the blue and green LDs were collimated by two plastic aspheric lenses (Thorlabs, CAY033) placed in front of the devices, whilst the violet was acquired with an embedded collimating lens. On the other side of the tank, a power meter sensor of  $9.7 \times 9.7$  mm<sup>2</sup> area (Thorlabs, S121C) connected to a power meter (Thorlabs, PM100D) collected the transmitted powers of each LD through different water turbidities induced by varying the Maalox content (or concentration) in the water. Optical images of the underwater channels' characterisation

---

<sup>§§</sup>Bahamas (station 8, Tongue of the ocean, 1.6 km deep)

<sup>¶¶</sup>Catalina channel (station 11)

<sup>\*\*\*</sup>San Diego harbour (station 2040)

are shown in Figure 1.13, where from 1.13a (clear tap water, no Maalox added) to 1.13c (turbid water), there is a gradual increase of the scattering agent in the water and thus, the beam attenuation becomes evident.

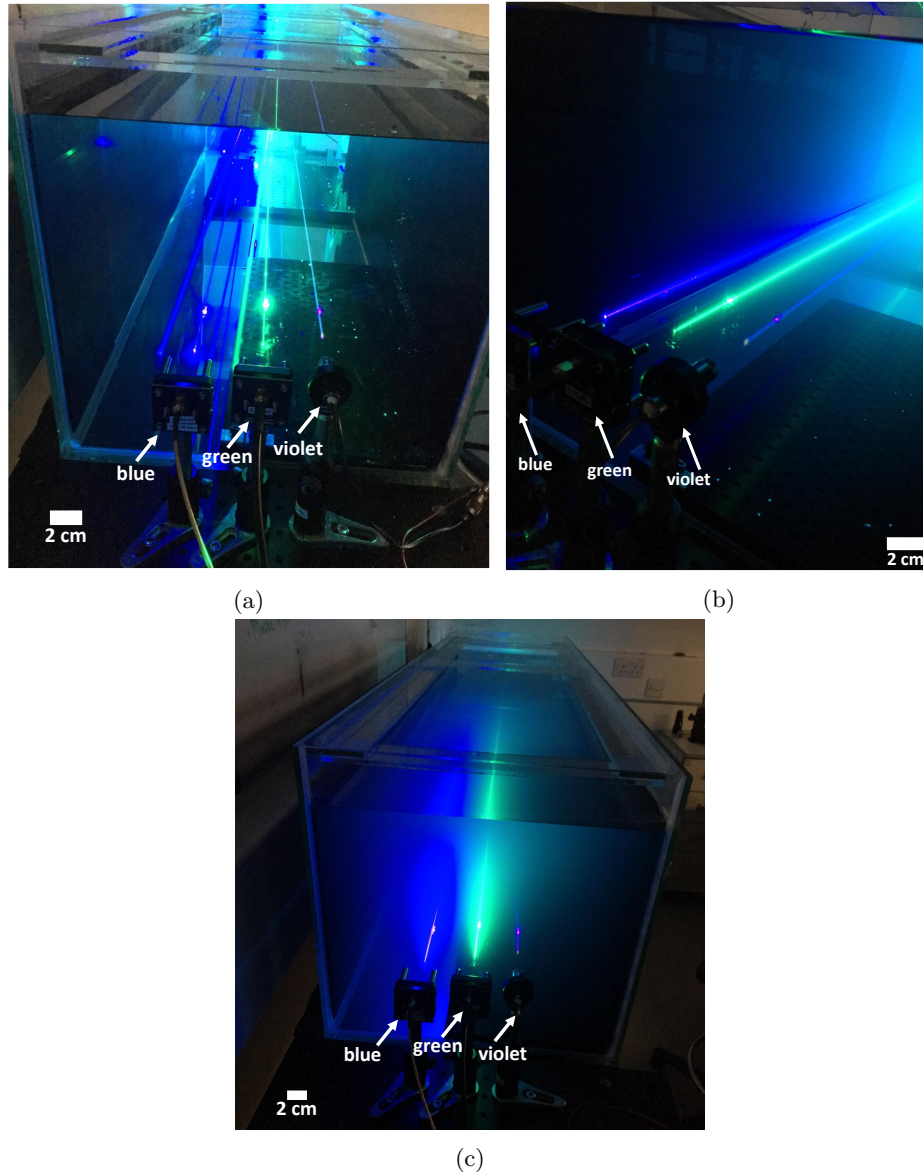


FIGURE 1.13: Optical images of the water tank and the underwater channels' characterisation of three different colours: violet, blue, and green. In (a), no scattering agent is added in the water; therefore, most of the photons reach the power meter sensor almost unscattered. From (b) to (c), a gradual increase of the Maalox content in the water occurs, and thus, attenuation effects through scattering are mainly optically observed.

The variation in the received power ( $P_R$ ) in mW for each wavelength, as a function of the scattering agent content in 160 l of tap water, is shown in Figure 1.14. The Maalox content ranged from 0 ml (clear tap water) to maxima of 20 ml (or 0.0125% by volume), 19 ml (or 0.0118%), and 18 ml (or 0.0112%) for the green, blue, and violet

colours, respectively. It is demonstrated below that for Maalox contents  $\leq 14$  ml, the natural logarithm of  $P_R$  attenuates linearly with turbidity. At larger Maalox contents, that linearity “breaks” as the power sensor collects multiple-scattered light, resulting in light attenuation at a slower rate as the water turbidity increases. This observation will be later analysed and explained.

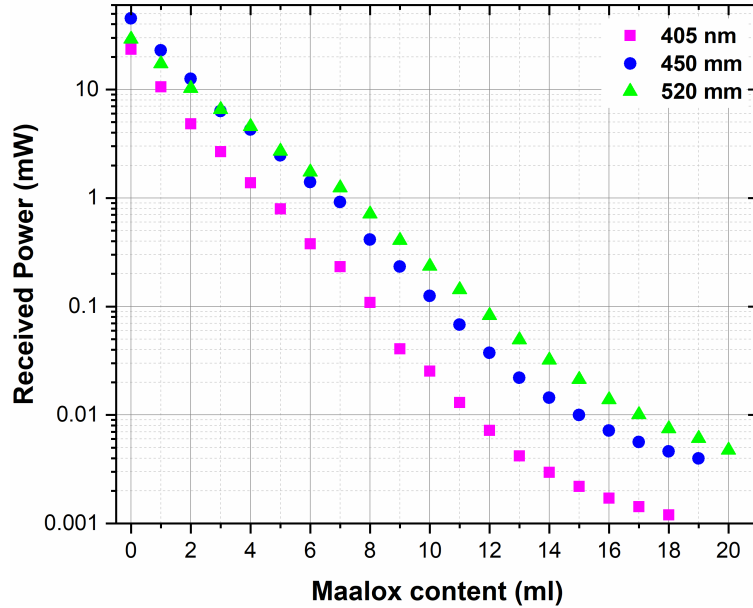


FIGURE 1.14: Received power vs Maalox content for 405 nm, 450 nm, and 520 nm over the 1.5 m water tank. Note the logarithmic scale in  $y$  axis.

It is also worth commenting that the 405 nm beam undergoes heavier power losses for all Maalox contents than those at 450 nm and 520 nm. A qualitative explanation of this observation can be given through Rayleigh scattering, as the 405 nm light experiences heavier scattering due to the inverse proportionality of the intensity of the scattered light from water particles to the (fourth power of) the wavelength (see Section 1.4.1.2) [40, 55]. Therefore, shorter wavelengths (e.g. 405 nm, violet) undergo stronger scattering than longer ones (450 nm, blue, and 520 nm, green).

Another quantity here introduced is the unitless number of attenuation lengths (ALs). That is the product of  $c(\lambda)$  and the propagation distance,  $z$ , in m (i.e.,  $c(\lambda) \cdot z$ )<sup>†††</sup>. For the sake of the measurements of this section, the propagation distance equals the length of the water tank ( $z = 1.5$  m). Physically, 1 AL means that the the  $P_R$  (in Watts) falls to  $1/e$  ( $\approx 0.37$ ) of the transmitted power ( $P_T$ ). For instance, assuming  $P_T = 100$  W, then at 1 AL, the received power would be  $P_R \approx 37$  W (or  $-4.34$  dB power losses). At 2 ALs, the received power would be dropped to the  $1/e^2$  of the  $P_T$ , i.e.,  $P_R \approx 13$  W (or  $-8.86$

<sup>†††</sup>It should be clarified that the *number* of ALs differs from the definition of the attenuation length ( $d_{atten}$ , in m).  $d_{atten}$  is defined as the *propagation distance* at which the  $P_R$  has fallen to  $1/e$  of  $P_T$ , and as such, from Equation 1.10 which is given later it can be derived that  $d_{atten} = 1/c(\lambda)$ .

dB power losses), and so on. The AL term is commonly used in the UWOC community as it allows the direct comparison of different system performances over various distances and water qualities [56].

Figure 1.15 and 1.16 show the estimated attenuation coefficients for the optical beams of the three LDs and the number of ALs as a function of the Maalox content, respectively. As with the power loss measurements (Figure 1.14), we observe an increase of  $c(\lambda)$  (and, hence, in ALs) as the turbidity of the water increases. The linearity “break” that is also shown here at Maalox content above  $\approx 14$  ml, allowed for a third order polynomial (instead of a linear) fit to be performed for the curves in Figure 1.15, as this, empirically, reflects more accurately the variations in  $c(\lambda)$ . As previously explained, shorter wavelengths (405 nm) experience stronger attenuation. Also, as the water turbidity increases, the maxima of the estimated attenuation coefficients and the number of ALs (see Table 1.3) are larger for the violet colour and become smaller as the colour of operation shifts towards longer wavelengths (blue and green).

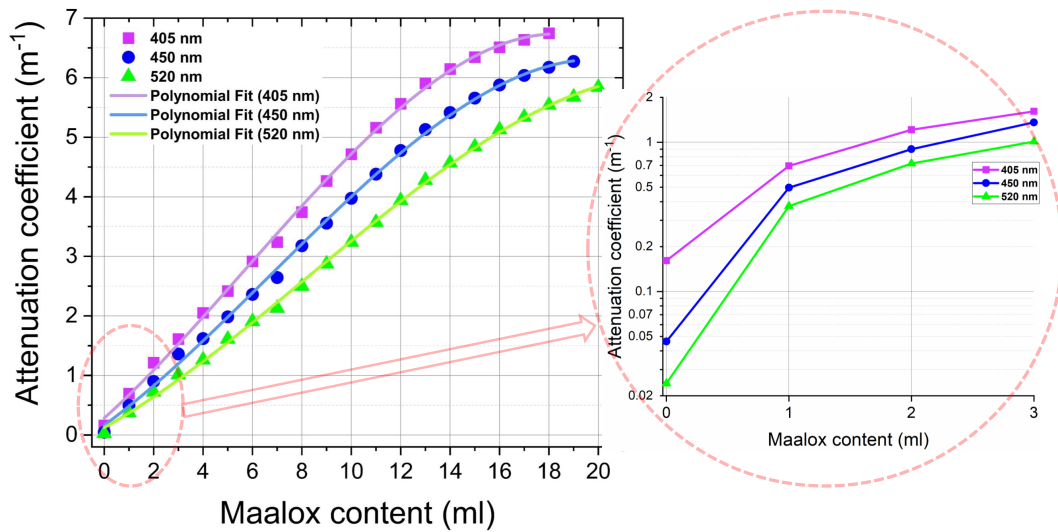


FIGURE 1.15: **Left:** The estimated attenuation coefficients of the laboratory water samples, for each wavelength of operation of the three LDs, as a function of the Maalox content with the third order polynomial fitting curves. **Right:** the variation of the attenuation coefficients for up to 3 ml of the scattering agent. Note the logarithmic scale of the  $y$  axis. The measurements were carried out over the 1.5 m long water tank.

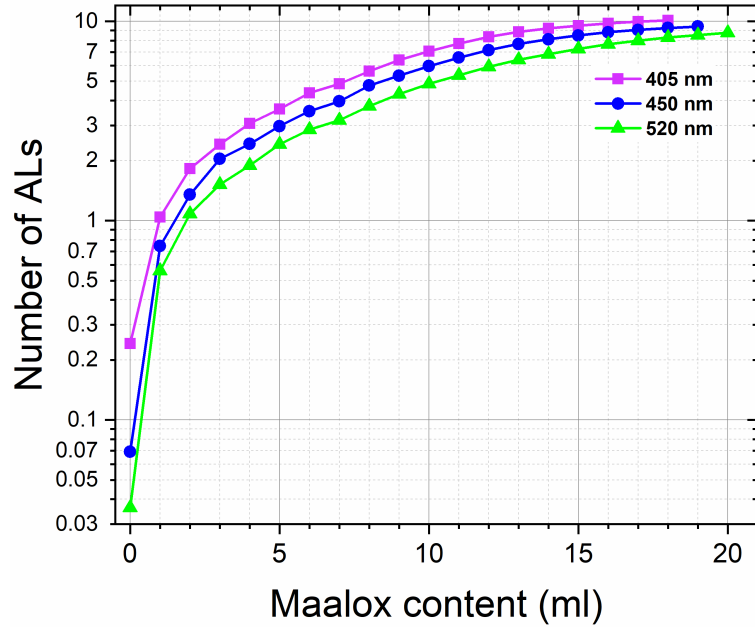


FIGURE 1.16: The variation of the number of ALs as the content of the scattering agent in the 1.5 m long water tank increases.

TABLE 1.3: The maximum values of the estimated attenuation coefficients and number of attenuation lengths for violet, blue, and green.

Wavelength (nm)	max $c(\lambda)$ ( $\text{m}^{-1}$ )	max number of ALs
405	6.74	10.12
450	6.27	9.41
520	5.84	8.76

All the calculations above were made by considering only the IOPs of water, i.e., absorption and scattering or the attenuation coefficient,  $c(\lambda)$ . Then, the quantification of the power losses of the underwater optical link for a given wavelength was estimated following Beer's law, where  $P_R$ ,  $P_T$ ,  $c(\lambda)$ , and  $z$  are combined in Equation 1.10<sup>†††</sup>:

$$P_R(z) = P_T(z)e^{-c(\lambda)z}. \quad (1.10)$$

At this point, it is worth noting that previous reports related to underwater beam scattering due to Maalox have demonstrated that Equation 1.10 is valid under two scenarios [57–60]: firstly, it is assumed that the alignment between transmitter and receiver is perfect, and secondly, the detected photons are unscattered. More precisely,

<sup>†††</sup>Beer's law expression is a solution to the differential equation which describes the differential path loss (in power or intensity) an optical beam undergoes while propagating through a medium of length  $z$ ,  $dP/dz = -cP$ . Then, by integrating both sides over  $P_T$  to  $P_R$ , and 0 to  $z$ , respectively, Equation 1.10 yields:  $\int_{P_T}^{P_R} dP/P = -c \int_0^z dz \Rightarrow \ln(P_R/P_T) = -cz \Rightarrow P_R = P_T e^{-cz}$ .

the latter is met in waters of  $< 10$  ALs where the detected signal attenuates as the non-scattered light would [59], i.e., according to  $\sim e^{-cz}$ .

In more turbid underwater environments, such as of ALs  $> 15$ , the beam largely diverges and is spatially distributed such that its scattering profile approaches that of a diffuse source [57]. Consequently, as the turbidity of the water increases and scattering becomes the dominant reason for power losses,  $P_R$  attenuates at a slower rate as the multiple-scattered photons make their way back into the receiver's field of view (FOV), leading to a positive contribution to the overall received signal [42]. Thus, for the multiple-scattering-dominated regimes, the calculation of  $P_R$  via Equation 1.10 would lead to an overestimation of the power losses and, therefore, to an underestimation of the achievable range [57]. As such, Equation 1.10 needs to be reconsidered to account for the collection of scattered light, and therefore, it can be rewritten as [59]:

$$P_R(cz) = P_T(cz)e^{-\gamma z}, \quad (1.11)$$

where  $\gamma = a + (1 - \eta)b$ , is the so-called system attenuation coefficient, or  $k_{sys}$  [42, 57].

In the above expression for  $\gamma$ , the Greek letter  $\eta$  is defined as the scattering factor ( $0 \leq \eta \leq 1$ ), which shows the percentage of the received scattered light relative to all of the scattered light on its way to the receiver. Therefore,  $\eta$  is a complex function encompassing the IOPs of water and system parameters (e.g. receiver FOV, aperture, beam divergence and radius). Now, by briefly investigating  $\gamma$ , it can be seen that if  $\eta \rightarrow 0$ , the received signal is dominated by non-scattered light. Thus, optical losses can be quantified through Equation 1.10. On the other hand, when  $\eta \rightarrow 1$ , it is implied that, practically, all of the scattered light is collected and  $P_R$  is attenuated by the absorption coefficient,  $a$ . It is convenient, then, to introduce to Equation 1.11 the scattering albedo ( $\omega = b/c$ ) along with the number of ALs ( $c \cdot z$ ). Then, Equation 1.12 is as<sup>§§§</sup> [59]:

$$P_R(cz) = P_T(cz)e^{(1-\omega)cz}. \quad (1.12)$$

It can now be deduced that a light beam's attenuation through water is exponential by  $c$  and  $\gamma$  in low and multiple scattering regimes, respectively [42].

---

<sup>§§§</sup> $\gamma = a + (1 - \eta)b \Rightarrow \gamma = a + b - \eta b \xrightarrow{c=a+b} \gamma = c - \eta b \xrightarrow{b=\omega c} \gamma = c - \eta \omega c \Rightarrow \gamma z = (1 - \eta \omega)cz \xrightarrow{\eta \rightarrow 1} \gamma z = (1 - \omega)cz.$

## 1.7 Summary

This chapter provided a general introduction to the background technologies suitable for underwater wireless communications: acoustic, radio frequencies, and optical waves. It was discussed that although acoustic is the dominant technology due to the extensive range it can achieve, the limitations in data rates render the optical waves an ideal supplementary technology that can offer data rates up to Gbs/s over tens of metres. A brief introduction to marine optics was then given, where the optical properties of water and how these affect underwater beam propagation were discussed. The chapter closed by categorising the natural water bodies into Jerlov water types and the characterisation of the laboratory-based water samples (based on their attenuation coefficient) that will be used throughout this thesis.

## References

- [1] William C. Cox. *PhD Thesis. Simulation, Modeling, and Design of Underwater Optical Communication Systems*. North Carolina State University, 2012.
- [2] Brandon M. Cochenour. *PhD Thesis. Experimental Measurements of Temporal Dispersion for Underwater Laser Communications and Imaging*. North Carolina State University, 2013.
- [3] Laura J. Johnson. *PhD Thesis. Optical property variability in the underwater optical wireless channel*. University of Warwick, 2015.
- [4] Aurora Maccarone. *PhD Thesis. Single-photon Detection Techniques for Underwater Imaging*. Heriot-Watt University, 2016.
- [5] Giovanni Giuliano. *PhD Thesis. Underwater optical communications systems*. University of Glasgow, 2019.
- [6] Xiaobin Sun. *PhD Thesis. Ultraviolet Based Underwater Wireless Optical Communication*. King Abdullah University of Science and Technology, 2020.
- [7] Seibert Q. Duntley. Light in the Sea\*. *Journal of the Optical Society of America*, 53(2):214, feb 1963.
- [8] S. Duntley. Chapter 7. In *Underwater Lighting by Submerged Lasers and Incandescent Sources*. Scripps Institution of Oceanography Visibility Laboratory, 1971.
- [9] M. Callaham. Submarine communications. *IEEE Communications Magazine*, 19(6):16–25, nov 1981.
- [10] Shuji Nakamura, Takashi Mukai, and Masayuki Senoh. Candela-class high-brightness InGaN/AlGaIn double-heterostructure blue-light-emitting diodes. *Applied Physics Letters*, 64(13):1687–1689, mar 1994.
- [11] Frank Hanson and Stojan Radic. High bandwidth underwater optical communication. *Applied Optics*, 47(2):277, 2008.
- [12] Honglan Chen, Xinwei Chen, Jie Lu, Xiaoyan Liu, Jiarong Shi, Lirong Zheng, Ran Liu, Xiaolin Zhou, and Pengfei Tian. Toward long-distance underwater wireless optical communication based on a high-sensitivity single photon avalanche diode. *IEEE Photonics Journal*, 12(3):1–10, 2020.
- [13] Wen-Shing Tsai, Hai-Han Lu, Hsiao-Wen Wu, Chung-Wei Su, and Yong-Cheng Huang. A 30 Gb/s PAM4 underwater wireless laser transmission system with optical beam reducer/expander. *Scientific Reports*, 9(1):8605, jun 2019.
- [14] TED Talks. Wireless data from every light bulb. [https://www.ted.com/talks/harald\\_haas\\_wireless\\_data\\_from\\_every\\_light\\_bulb](https://www.ted.com/talks/harald_haas_wireless_data_from_every_light_bulb).
- [15] Xueyang Li, Chen Cheng, Chao Zhang, Zixian Wei, Lai Wang, H. Y. Fu, and Yanfu Yang. Net 4 Gb/s underwater optical wireless communication system over 2 m using a single-pixel GaN-based blue mini-LED and linear equalization. *Optics Letters*, 47(8):1976, apr 2022.
- [16] Tao Liu, Hongming Zhang, Yufei Zhang, and Jian Song. Experimental Demonstration of LED Based Underwater Wireless Optical Communication. In *2017 4th International Conference on Information Science and Control Engineering (ICISCE)*, pages 1501–1504. IEEE, jul 2017.



- 
- [17] G. N. Arvanitakis, R. Bian, J. J. D. McKendry, C. Cheng, E. Xie, X. He, G. Yang, M. S. Islim, A. A. Purwita, E. Gu, H. Haas, and M. D. Dawson. Gb/s underwater wireless optical communications using series-connected gan micro-led arrays. *IEEE Photonics Journal*, 12(2):1–10, 2020.
- [18] Shijie Zhu, Xinwei Chen, Xiaoyan Liu, Guoqi Zhang, and Pengfei Tian. Recent progress in and perspectives of underwater wireless optical communication. *Progress in Quantum Electronics*, 73(July):100274, sep 2020.
- [19] Shojiro Ishibashi and Ken-Ichi Susuki. 1Gbps x 100m Underwater Optical Wireless Communication Using Laser Module in Deep Sea. In *OCEANS 2022, Hampton Roads*, volume 2022-October, pages 1–7. IEEE, oct 2022.
- [20] C. E. Shannon. A mathematical theory of communication. *The Bell System Technical Journal*, 27(4):623–656, 1948.
- [21] Philip Lacovara. High-Bandwidth Underwater Communications. *Marine Technology Society Journal*, 42(1):93–102, 2008.
- [22] Tsai Chen Wu, Yu Chieh Chi, Huai Yung Wang, Cheng Ting Tsai, and Gong Ru Lin. Blue laser diode enables underwater communication at 12.4 gbps. *Scientific Reports*, 7:40480, 2017.
- [23] Marco Lanzagorta. Underwater Communications. *Synthesis Lectures on Communications*, 5(2):1–129, 2012.
- [24] Michael A. Ainslie and James G. McColm. A simplified formula for viscous and chemical absorption in sea water. *The Journal of the Acoustical Society of America*, 103(3):1671–1672, 1998.
- [25] Liu Lanbo, Zhou Shengli, and Cui Jun-Hong. Prospects and problems of wireless communication for underwater sensor networks. *Wireless Communications and Mobile Computing*, 8(8):977–994, 2008.
- [26] Xianhui Che, Ian Wells, Gordon Dickers, Paul Kear, and Xiaochun Gong. Re-evaluation of RF electromagnetic communication in underwater sensor networks. *IEEE Communications Magazine*, 48(12):143–151, 2010.
- [27] I.S. Bogie. Conduction and magnetic signalling in the sea a background review. *Radio and Electronic Engineer*, 42:447–452(5), October 1972.
- [28] Hemani Kaushal and Georges Kaddoum. Underwater Optical Wireless Communication. *IEEE Access*, 4:1518–1547, 2016.
- [29] Curtis D. Mobley. L & W (PI-C03): Optical Properties of Water. In *Light and Water: Radiative transfer in natural waters*. 1994.
- [30] Chao Fei, Xiaojian Hong, Guowu Zhang, Ji Du, Yu Gong, Julian Evans, and Sailing He. 16.6 Gbps data rate for underwater wireless optical transmission with single laser diode achieved with discrete multi-tone and post nonlinear equalization. *Optics Express*, 26(26):34060, 2018.
- [31] Hassan M. Oubei, Chao Shen, Abla Kammoun, Emna Zedini, Ki Hong Park, Xiaobin Sun, Guangyu Liu, Chun Hong Kang, Tien Khee Ng, Mohamed Slim Alouini, and Boon S. Ooi. Light based underwater wireless communications. *Japanese Journal of Applied Physics*, 57(8), 2018.
- [32] Giuseppe Schirripa Spagnolo, Lorenzo Cozzella, and Fabio Leccese. Underwater optical wireless communications: Overview. *Sensors (Switzerland)*, 20(8), 2020.

- 
- [33] C. D. Mobley. Introduction to Optical Constituents of the Ocean. <http://www.oceanopticsbook.info/view/optical-constituents-of-the-ocean/introduction-to-optical-constituents-of-the-ocean>.
- [34] Laura J Johnson, Faezah Jasman, Roger J Green, and Mark S Leeson. Recent advances in underwater optical wireless communications. *Underwater Technology: International Journal of the Society for Underwater*, 32(3):167–175, nov 2014.
- [35] Chapter 1 Introduction. In N.G. Jerlov, editor, *Optical Oceanography*, volume 5 of *Elsevier Oceanography Series*, pages 1–12. Elsevier, 1968.
- [36] Curtis D. Mobley. L & W (PII-C05): Within the Water. In *Light and Water: Radiative transfer in natural waters*. 1994.
- [37] Robin M. Pope and Edward S. Fry. Absorption spectrum (380–700 nm) of pure water. II. Integrating cavity measurements. *Appl. Opt.*, 36(33):8710–8723, Nov 1997.
- [38] Bogdan Wozniak and Jerzy Dera. *Light Absorption in Sea Water*, pages 11–81. Springer New York, New York, NY, first edition, 2007.
- [39] Curtis D. Mobley. Introduction to Optical Constituents of the Ocean: Water. <https://www.oceanopticsbook.info/view/optical-constituents-of-the-ocean/water>.
- [40] Jerzy Dera. *Marine Physics*. Elsevier Oceanography Series, first edition, 1992.
- [41] Curtis D. Mobley. Introduction to Optical Constituents of the Ocean: Phytoplankton. <https://www.oceanopticsbook.info/view/optical-constituents-of-the-ocean/phytoplankton>.
- [42] Brandon Cochenour and Linda Mullen. *Free-space optical communications underwater*, page 201–239. Cambridge University Press, 2012.
- [43] Curtis D. Mobley. Radiative Transfer of Energy: The SRTE:Heuristic Development. <https://www.oceanopticsbook.info/view/radiative-transfer-theory/the-srte-heuristic-development>.
- [44] Curtis D. Mobley. Scattering: Raman Scattering. <https://www.oceanopticsbook.info/view/scattering/level-2/raman-scattering>.
- [45] Eugene Hecht. *Optics*. Fifth edition, 2017.
- [46] Hon. J.W. Strutt. On the scattering of light by small particles. *The London, Edinburgh, and Dublin Philosophical Magazine and Journal of Science*, 41(275):447–454, 1871.
- [47] Chapter 2 Scattering. In N.G. Jerlov, editor, *Optical Oceanography*, volume 5 of *Elsevier Oceanography Series*, pages 15–46. Elsevier, 1968.
- [48] R. W Austin and G. Halikas. The index of refraction of seawater. *UC San Diego: Library-Scripps Digital Collection*, 1976.
- [49] Zahra Vali, Asghar Gholami, Zabih Ghassemlooy, Masood Omoomi, and David G. Michelson. Experimental study of the turbulence effect on underwater optical wireless communications. *Applied Optics*, 57(28):8314, oct 2018.
- [50] N. G. Jerlov. Chapter 10 irradiance. In *Optical Oceanography*, volume 5 of *Elsevier Oceanography Series*, pages 115 – 132. Elsevier, 1968.

- 
- [51] Michael G. Solonenko and Curtis D. Mobley. Inherent optical properties of Jerlov water types. *Applied Optics*, 54(17):5392, 2015.
- [52] B. Johnson, D. Scroggins, B. Kamgar-Parsi, D. Folds, and E. Belcher. 3-d acoustic imaging with a thin lens. In *Proceedings of OCEANS '93*, pages III444–III449 vol.3, 1993.
- [53] T. Petzold. Volume Scattering Functions for Selected Ocean Waters. *Scripps Inst. Oceanogr.*, (3):SIO Ref. 72–78, 1972.
- [54] Linda Mullen. Optical propagation in the underwater environment. In *Atmospheric Propagation VI*, volume 7324, pages 64 – 72. International Society for Optics and Photonics, SPIE, 2009.
- [55] Xiaobin Sun, Wenqi Cai, Omar Alkhazragi, Ee-Ning Ooi, Hongsen He, Anas Chaaban, Chao Shen, Hassan Makine Oubei, Mohammed Zahed Mustafa Khan, Tien Khee Ng, Mohamed-Slim Alouini, and Boon S. Ooi. 375-nm ultraviolet-laser based non-line-of-sight underwater optical communication. *Optics Express*, 26(10):12870, May 2018.
- [56] William Cox and John Muth. Simulating channel losses in an underwater optical communication system. *Journal of the Optical Society of America A*, 31(5):920, 2014.
- [57] Brandon M. Cochenour, Linda J. Mullen, and Allan E. Laux. Characterization of the beam-spread function for underwater wireless optical communications links. *IEEE Journal of Oceanic Engineering*, 33(4):513–521, 2008.
- [58] Brandon Cochenour, Linda Mullen, and Alan Laux. Spatial and temporal dispersion in high bandwidth underwater laser communication links. *Proceedings - IEEE Military Communications Conference MILCOM*, 2008.
- [59] Brandon Cochenour, Linda Mullen, and John Muth. Effect of scattering albedo on attenuation and polarization of light underwater. *Optics Letters*, 35(12):2088–2090, 2010.
- [60] Linda Mullen, Derek Alley, and Brandon Cochenour. Investigation of the effect of scattering agent and scattering albedo on modulated light propagation in water. *Applied Optics*, 50(10):1396–1404, 2011.

## Chapter 2

# Relevant Semiconductor Device Physics and Modulation Schemes

This chapter is dedicated to exploring the underlying physics of the transmitters (GaN micro-LEDs and laser diodes, LDs) and receivers (e.g., a PIN photodiode, a Si photomultiplier (SiPM), and a single-photon avalanche diode (SPAD) array) employed throughout this thesis. Since most of these devices are based on semiconductors, a brief review of relevant semiconductor physics will be given. The “backbone” of every semiconductor diode, and as such of the GaN LEDs and LDs, is the p-n junction. A description of its operational principles will therefore be mentioned. Finally, the modulation schemes applied for encoding data on the optical carrier will be discussed, which were utilised in the experiments presented in the following chapters. The modulation schemes predominantly used were on-off keying (OOK) and orthogonal frequency division multiplexing (OFDM).

### 2.1 Brief overview of semiconductor physics

#### 2.1.1 Electrons in free-space

From quantum mechanics, it is fundamentally known that the energy atomic electrons can take is quantised. That being said, and by recalling the wave-particle duality, their energy and momentum over free space can be expressed as [1]:

$$E = hf = h\frac{\omega}{2\pi} = \hbar\omega, \text{ and } p = \frac{h}{\lambda} = \frac{2\pi\hbar}{\lambda} = \hbar k, \quad (2.1)$$

where  $k = 2\pi/\lambda$  is the wavenumber. Another useful expression that defines the energy of a free electron and by considering the electron's kinetic energy ( $E = \frac{1}{2}mv^2$ , where  $m = m_e = 9.01 \times 10^{-28}$  gr) and Equation 2.1 is:

$$E = \frac{p^2}{2m} = \frac{\hbar^2 k^2}{2m}. \quad (2.2)$$

Since electrons exhibit both particle and wave characteristics, they can be described via a travelling wave through a wavefunction,  $\Psi(x, t)$ , which is a solution to Schrödinger's equation. It is noted that  $\Psi(x, t)$  is a complex function, and as such, it cannot represent a real physical quantity. However, Max Born in 1926 postulated that the  $|\Psi(x, t)|^2 dx$  provides the probability of finding the electron within the  $x$  and  $x + dx$  range at a given time. In other words,  $|\Psi(x, t)|^2$  is a probability density function [2].

When discussing the behaviour of an electron within a semiconductor crystal, it is important first to mention the quantisation of its energy. For instance, in the isolated hydrogen atom, the quantised electron energy is given as [1]:

$$E_n = -\frac{13.6}{n^2} eV, \quad (2.3)$$

where  $n$  is a positive integer ( $n = 1, 2, 3, \dots$ ), also known as the quantum number. Equation 2.3 implies that the electron's energy can only have particular discrete values according to  $n$ . A similar result can be acquired when solving Schrödinger's equation for the problem of a particle in the infinite potential well of width  $L$  in which the solutions are wavefunctions representing standing waves. The total energy of the electron can then be written as [2]:

$$E_n = \frac{\hbar^2 n^2 \pi^2}{2mL^2}, \quad (2.4)$$

indicating, once again, the quantisation of energy according to  $n$ .

### 2.1.2 Electrons within a crystal

#### Energy band diagrams and energy gap

Within a crystal, a vast number of atoms (on the order of  $10^{22}$  in  $1 \text{ cm}^3$ ) are in close proximity (on the order of few Å). Consequently, the wavefunctions of their electrons overlap, and the result of the electrons' interaction is the splitting of their initial quantised energy level into allowed and forbidden energy bands [2]. It should be noted, though, that within an allowed band, no more than two electrons can occupy an energy

level due to Pauli's exclusion principle. The discrete energy levels within a band should be large enough to accommodate the large number of electrons. The energy difference between them is very small (on the order of  $10^{-19}$  eV), so that the energy distribution through the energy band can be considered quasi-continuous. At  $T = 0$  K, the lowest energy state is fully occupied by electrons in the lower band (the valence band), whilst the upper band (the conduction band) is empty. The energy gap ( $E_g$ ) between the top of the valence band and the bottom of the conduction band equals the width of the forbidden energy band.

The width of the  $E_g$  (in eV) essentially defines the material's electrical and optical properties and enables their categorisation into *insulators* and *semiconductors* (assuming that *metals* fall into the latter). Generally, if a material's  $E_g$  is more than 3.5 eV, it is customary to call the crystal an insulator. If the gap is less than 3.5 eV, the material is usually characterised as a semiconductor [3]. The temperature dependency of the  $E_g$  is elucidated as follows; a temperature decrease results in a contraction of the crystal lattice that strengthens the interatomic bonds between the crystal atoms, and as such, the gap increases [4]. On the other hand, as the temperature increases, the crystal lattice expands, and the interatomic bonds become weaker. Therefore, less energy (smaller  $E_g$ ) is required for an electron to be transitioned to the conduction band. Typical values of the  $E_g$  of three important semiconductors (Ge, Si, GaAs) at room temperature (300 K) and 0 K are shown in Table 2.1. The energy of the emitted photon upon radiative transition from the conduction to the valence band is given as [1]:

$$E_g = \frac{hc}{\lambda} \approx \frac{1240}{\lambda}, \quad (2.5)$$

where the energy and the wavelength are in eV and nm, respectively.

TABLE 2.1: The temperature dependence of  $E_g$  of Ge, Si, and GaAs. Data taken from [4].

Material	$E_g$ (300 K) (eV)	$E_g$ (0 K) (eV)
Ge	0.67	0.75
Si	1.12	1.17
GaAs	1.42	1.51

Semiconductor materials can be divided into two categories based on their band structure. These are semiconductors of direct and indirect bandgap. In the former case, the conduction band minimum occurs at the same point (in  $k$ -space) as the valence band maximum, which results in a high probability for a band-to-band radiative transition upon absorption of a photon since the crystal momentum is conserved [5]. Due to this

behaviour, direct bandgap semiconductors (such as GaAs and GaN) are suitable for developing efficient LEDs and laser diodes [2]. On the other hand, in indirect bandgap materials, the minima and maxima occur in different points in  $k$ -space and therefore, a phonon (the quasiparticle of the crystal lattice vibrations) must be absorbed to supply the missing crystal momentum [6]. Consequently, the probability for a band-to-band transition in indirect bandgap materials (such as Si and Ge) is significantly low [5]. Figures 2.1a and 2.1b depict simplified schematics of the energy band structures of GaN (direct semiconductor of  $E_g = 3.2$  eV [5]) and Si (indirect semiconductor of  $E_g = 1.12$  eV [6]), respectively.

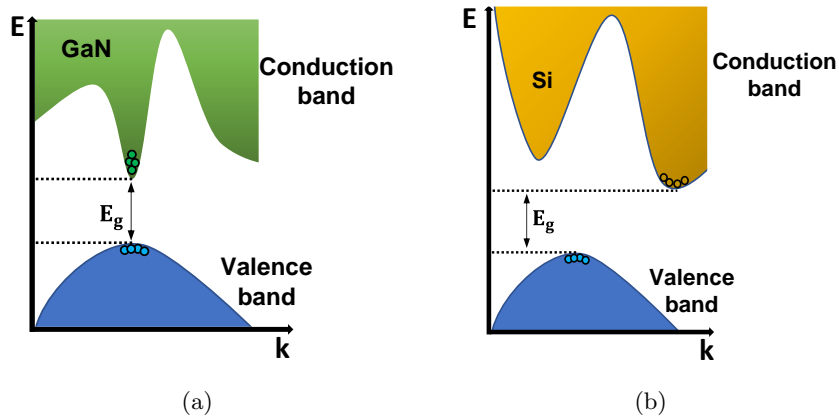


FIGURE 2.1: Schematic energy band diagrams for (a) GaN and (b) Si.

### Effective mass

Another important quantity when discussing the motion of an electron within a band is the effective mass ( $m^*$ ).  $m^*$  can be approximated through Newtonian principles if the electron's motion is likened to a travelling wavepacket within the crystal. Then, its group velocity is given as  $v_g = \frac{dx}{dt} = \frac{d\omega}{dk}$ , and by considering the  $\omega = E/\hbar$  relation in Equation 2.1, the wavepacket group velocity is formed as [4]:

$$v_g = \frac{1}{\hbar} \frac{dE}{dk}, \quad (2.6)$$

where it is shown that the first derivative of energy with respect to the wavenumber is related to the velocity of the wavepacket (or the particle).

A force due to an externally applied electric field or dopant ions in the crystal can be considered an “external” force,  $F_{ext}$ . Its impact on the wavepacket's momentum over  $dt$  is described as:

$$F_{ext} = \frac{dp}{dt} = \frac{d(\hbar k)}{dt}. \quad (2.7)$$

Since an expression for  $F_{ext}$  and  $v_g$  has now been acquired (Equations 2.6 and 2.7), the next step towards defining  $m^*$  is to take into account Newton's 2<sup>nd</sup> law ( $\sum F_{ext} = m^* \frac{dv_g}{dt}$ ) and derive the group velocity in Equation 2.6 in time. As such:

$$\frac{dv_g}{dt} = \frac{1}{\hbar} \underbrace{\frac{d}{dt} \left( \frac{dE}{dk} \right)}_{\frac{d^2 E}{dk^2} \frac{dk^*}{dt}} = \frac{1}{\hbar^2} \frac{d^2 E}{dk^2} \underbrace{\frac{d(\hbar k)}{dt}}_{F_{ext}}. \quad (2.8)$$

From Equations 2.7 and 2.8, this yields:

$$F_{ext} = \left( \frac{1}{\hbar^2} \frac{d^2 E}{dk^2} \right)^{-1} \frac{dv_g}{dt} = m^* \frac{dv_g}{dt}. \quad (2.9)$$

From the above, it becomes evident that the second derivative of the energy with respect to the wavenumber is inversely proportional to the effective mass of the wavepacket (or the particle), i.e.:

$$\frac{1}{\hbar^2} \frac{d^2 E}{dk^2} = \frac{1}{m^*}. \quad (2.10)$$

By inspecting Equation 2.10, one can deduce the relative masses of the carrier(s) in the crystal. For instance, in Figure 2.2 we illustrate two speculative energy band segments of different curvatures. It can be seen that in the vicinity of the energy minima, the curvature of  $b$  is larger than that of  $a$ , and thus,  $(d^2 E/dk^2)_b > (d^2 E/dk^2)_a \Rightarrow m_a^* > m_b^*$ .

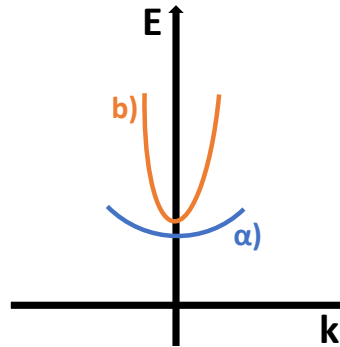


FIGURE 2.2: Two energy band segments of different curvatures from which it can be seen that  $m_a^* > m_b^*$ . Adapted from [4].

It is noted that although the above-simplified description is adequate to explain the  $m^*$  concept qualitatively, it concerns the one-dimensional  $E$ - $k$  diagram. Within a three-dimensional crystal (described by 3  $k$ -vectors), though, further complications arise as

\*  $\frac{d^2 E}{dk^2} = \frac{d}{dk} \left( \frac{dE}{dk} \right) = \frac{d}{dt} \frac{dt}{dk} \left( \frac{dE}{dk} \right) = \frac{dt}{dk} \frac{d}{dt} \left( \frac{dE}{dk} \right) \Rightarrow \frac{d}{dt} \left( \frac{dE}{dk} \right) = \frac{d^2 E}{dk^2} \frac{dk}{dt}$ .



the curvatures at the conduction band minimum may not be the same, and the carriers'  $m^*$  must be expressed as a tensor [7].

### Carrier concentration

In a previous section (Section 2.1.2), we briefly mentioned the radiative transition of an electron (upon thermally excitation or absorption of a photon of  $E_{ph} > E_g$ ) from the conduction to the valence band in a semiconductor. At this point, it is worth introducing the notion of the hole, which can be conceived as a positively charged empty state created when a valence electron is elevated into the conduction band [2]. The conductivity of a semiconductor is, therefore, attributed to the drift of both electrons and holes.

A semiconductor can either be intrinsic, i.e., the number of thermally generated electrons in the conduction band equals the number of holes in the valence band, or extrinsic. The latter designates the variation of the semiconductor's conductivity through doping, i.e., the intentional addition of different types and concentrations of impurities (or "foreign" atoms) in the crystal. Extrinsic semiconductors can either be  $n$ - or  $p$ -type depending on whether their dopant atoms are donors ( $N_D$ ) or acceptors ( $N_A$ ), respectively. For instance, a group-V element, such as phosphorus (5 valence electrons), is a donor impurity to group-IV elements, such as silicon (4 valence electrons). The fifth valence electron of phosphorus acts as a donor electron weakly bound to the phosphorus atom and can be easily freed into the conduction band upon thermal energy absorption. Similarly, group-III elements as boron (3 valence electrons), act as acceptors in silicon. Boron accepts an electron from an adjacent Si-Si bond to complete its own bond scheme. Thereby, a hole is created that exists and wanders in the valence band [4].

The next step is determining the concentration or the number of carriers per unit energy,  $N(E)$ , available for conduction. As discussed above, electrons can occupy energy levels of quantised energy within the crystal. Determining the allowed density of states as a function of energy will allow calculating the electrons' (and holes') concentration. The density of states,  $g(E)$ , is given in terms of states per unit energy per unit volume and for the conduction and valence bands, it is proportional to  $g_c(E) \propto \sqrt{E - E_c}$  and  $g_v(E) \propto \sqrt{E_v - E}$ , respectively [2]. The Fermi-Dirac probability function,  $f(E)$ , gives the probability that an electron occupies a quantum state, i.e.:

$$f(E) = \frac{N(E)}{g(E)} = \frac{1}{1 + e^{\frac{E - E_f}{kT}}}. \quad (2.11)$$

Here,  $E_f$  is the Fermi energy that does not have to correspond to an allowed energy level and determines the electrons' statistical distribution. The mathematical derivation of

both quantities,  $g(E)$  and  $f(E)$ , is a challenging task and can be found in any solid-state physics/semiconductor devices textbook, such as Neamen's [2].

Under thermal equilibrium, the electrons ( $n$ ) and holes ( $p$ ) concentrations are given by [4]:

$$\begin{aligned} n &= \int_{E_c}^{\infty} g_c(E)f(E)dE, \\ p &= \int_{-\infty}^{E_v} g_v(E)[1 - f(E)]dE. \end{aligned} \quad (2.12)$$

Equations 2.12 can be rewritten upon approximations in more convenient and readily used forms:

$$\begin{aligned} n &= N_c e^{(E_f - E_c)/kT}, \\ p &= N_v e^{(E_v - E_f)/kT}, \end{aligned} \quad (2.13)$$

where  $N_c$  and  $N_v$  are the effective density of states functions in the conduction and valence bands<sup>†</sup>, respectively. As mentioned before,  $n = p = n_i$  for an intrinsic semiconductor, and therefore  $np = n_i^2$ . Equations 2.13 can now be further approximated and written as [2]:

$$n_i^2 = N_c N_v e^{\frac{-(E_c - E_v)}{kT}} = N_c N_v e^{\frac{-E_g}{kT}}. \quad (2.14)$$

### 2.1.3 The p-n diode

A light-emitting diode (LED) is a structure formed by a p-n diode, and this section will summarise some of its electrical and optical characteristics.

#### Electrical characteristics

A p-n diode comprises adjacent layers of heavily doped p- and n-type material and can consist of either the same semiconductor material, i.e., a homojunction, or different semiconductor materials, i.e., a heterojunction. When the junction is formed, the majority carrier electrons from the n-region will start diffusing into the p-region and recombining

---

<sup>†</sup>  $N_c = 2 \left( \frac{2\pi m_n^* kT}{h^2} \right)^{3/2}$  and  $N_v = 2 \left( \frac{2\pi m_p^* kT}{h^2} \right)^{3/2}$ . At  $T = 300$  K both quantities,  $N_c$  and  $N_v$ , are on the order of  $10^{19} \text{ cm}^{-3}$  for most semiconductors [2].

with excess holes, leaving positively charged donor ions ( $N_D^+$ ) behind. Similarly, the majority carrier holes from the p-region will begin diffusing into the n-region, recombining with excess electrons and leaving negatively charged acceptor ions ( $N_A^-$ ) behind.

The charge density created by the net positive and negative charged ions implies the existence of an electric field (Gauss's law) and, therefore, a potential difference right at the junction between the p- and n-type material. Its direction is from the positive (n-region) to the negative charge (p-region). The "built-in" electric field causes some electrons and holes to move in the opposite direction to the flow caused by diffusion. In thermal equilibrium (no applied voltage or external electric field, nor light shining on the device), the opposing flows from diffusion and electric field balance each other, depleting the junction region of free charge carriers and, as such, it is called the "depletion region".

The depletion region is highly resistive, and its resistance can be modified by applying an external electric field. Suppose the external electric field is in the opposite direction to that of the built-in field (forward bias), the resistance of the depletion region becomes smaller. In contrast, if the external electric field is applied in the same direction as the built-in field (reverse bias), then the resistance becomes larger. The built-in voltage ( $V_{bi}$ ) produced across the depletion region is the voltage that must be overcome before the diode conducts current. In other words,  $V_{bi}$  is the potential barrier the electrons of the conduction band in the n-region see when trying to move into the conduction band of the p-region and the potential barrier the holes in the valence band of the p-region see when trying to move into the valence band of the n-region. Mathematically,  $V_{bi}$  is given by Equation 2.15 as [8]:

$$V_{bi} = \frac{kT}{e} \ln \left( \frac{N_A N_D}{n_i^2} \right), \quad (2.15)$$

where  $k$  is the Boltzmann constant,  $T$  is the temperature (in Kelvin),  $e$  is the elementary charge,  $N_A$  and  $N_D$  are the concentrations of acceptors and donors, respectively, and  $n_i$  is the intrinsic carrier concentration of the semiconductor.

The total current of an ideal p-n diode of area  $A$  is given by the Shockley diode equation as:

$$I = I_s \left( e^{eV/kT} - 1 \right), \quad (2.16)$$

where the reverse saturation current,  $I_s$ , of Equation 2.16 has been defined as:

$$I_s = eA \left( \sqrt{\frac{D_p}{\tau_p} \frac{n_i^2}{N_D}} + \sqrt{\frac{D_n}{\tau_n} \frac{n_i^2}{N_A}} \right). \quad (2.17)$$

Here,  $D_{p,n}$  and  $\tau_{p,n}$  are the hole and electron diffusion constants and the hole and electron minority-carrier lifetimes, respectively, and  $V$  is the applied voltage.

Under forward bias, the p- and n-type materials are connected to the positive and negative bias, respectively. The potential barrier is reduced, allowing the injection of the majority carrier electrons from the n-side across the depletion region into the p-material, and the majority carrier holes from the p-side are injected across the depletion region to the n-material. The applied voltage is much larger than the thermal voltage ( $V \gg kT/e$ ), and Equations 2.16 and 2.17 can now be rewritten as [8]:

$$I = eA \left( \sqrt{\frac{D_p}{\tau_p} N_A} + \sqrt{\frac{D_n}{\tau_n} N_D} \right) e^{e(V-V_{bi})/kT}. \quad (2.18)$$

The exponential part of Equation 2.18 denotes that when the applied voltage approaches the built-in voltage, the current of the junction rapidly increases. The voltage at which the exponential increase in current occurs is known as the turn-on voltage or threshold voltage,  $V_{th}$ . For an ideal junction (where every electron that recombines with a hole in the depletion region generates a photon),  $V_{th}$  can be approximated by the ratio of the bandgap energy of the semiconductor and the elementary charge, i.e.:

$$V_{th} \approx \frac{E_g}{e}. \quad (2.19)$$

Practically, LEDs and micro-LEDs (LEDs of diameter/dimensions  $\leq 100 \mu\text{m}$ ) exhibit parasitic resistances that result in deviation from the ideal Shockley equation. The parasitic resistance can be either series ( $R_s$ ) or parallel resistance ( $R_p$ ). E.g., in GaN devices, the parasitic resistance can be attributed to factors including bandgap discontinuities, low p-type GaN conductivity and poor Ohmic contacts. If  $R_s$  and  $R_p$  are taken into account then Equation 2.18 (in forward bias) becomes [8]:

$$I - \frac{V - IR_s}{R_p} = I_s e^{e(V-IR_s)/(nkT)}. \quad (2.20)$$

For the Shockley equation it was assumed that  $R_p \rightarrow \infty$ ,  $R_s \rightarrow 0$  and  $n = 1$ .

Under reverse bias, a positive voltage is applied to the n-region of the diode and a negative voltage to the p-type material. As a result, the  $V_{bi}$  and the width of the depletion region increase, limiting the diffusion of the majority carrier electrons and

holes. However, a small negative current is observed attributed to the drift currents of the thermally generated minority carrier electrons in the p-region and the minority carrier holes on the n-region. In the absence of parallel resistance, the drift current component is essentially independent of  $V_{bi}$  and is so small that it can be considered negligible [9].

### Optical characteristics

Electrons and holes in an LED-based device can recombine either radiatively or non-radiatively. The former is clearly preferred (Figure 2.3c) and can be quantitatively expressed by the bimolecular rate equation as [10]:

$$R = -\frac{dn}{dt} = -\frac{dp}{dt} = Bnp, \quad (2.21)$$

where  $R$  denotes recombination,  $B$  is the bimolecular recombination coefficient<sup>‡</sup> (in  $\text{cm}^3/\text{s}$ ) that is material dependent and  $n$ ,  $p$  are the electrons and holes concentrations, respectively. Thus, the intensity of luminescence is proportional to the recombination rate or the carrier concentration.

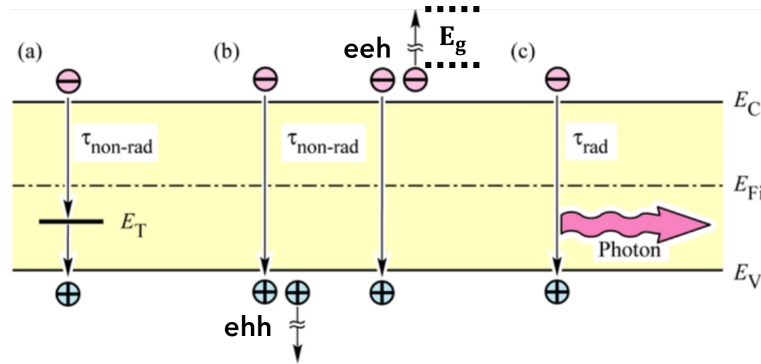


FIGURE 2.3: Schematic illustration of the (a) SRH recombination, (b) Auger eeh and ehh recombinations, and (c) radiative recombination. Taken from [10]. The vertical axis in this schematic is energy.

In the unwanted non-radiative recombination processes, the energy released during the electron-hole recombination is converted to heat (phonons). This is attributed to defects in the crystal lattice, such as unwanted foreign atoms, dislocations, native defects, etc., which generate energy levels within the bandgap, acting as traps (or deep levels). The recombination via deep levels is known as Shockley-Read-Hall (SRH) recombination and is illustrated in Figure 2.3 as process (a). SRH recombination can also occur at the surface of the semiconductor. Surfaces can be considered as abrupt discontinuities from

<sup>‡</sup>Typical values of  $B$  in GaN micro-LEDs: for a 44  $\mu\text{m}$  diameter 450 nm emitting device,  $B_{450} = (0.33 - 1.5) \times 10^{-11} \text{ cm}^3/\text{s}$ , whereas for a 54  $\mu\text{m}$  diameter 520 nm emitting device,  $B_{520} = (0.4 - 2) \times 10^{-12} \text{ cm}^3/\text{s}$  [11].

the crystal lattice periodicity that result in the addition of electronic states within the crystal's bandgap [10].

Another non-radiative process is Auger recombination, as shown in Figure 2.3b. Two types of Auger recombination are considered; one involves two electrons and a hole (eeh), and the other involves an electron and two holes (ehh). During the former process, the energy from an electron-hole recombination is dissipated to a free electron in the conduction band (“hot” electron). In the latter, a hole is excited deep in the valence band (“hot” hole). Subsequently, the hot electrons and holes lose their energy via multiple phonon emission [10].

Radiative recombination can be characterised by its efficiency. Ideally, an LED would emit a photon per injected electron. In reality, however, some photons emitted from the active region do not leave the semiconductor die due to internal reflection or/and reabsorption effects by the LED substrate and metallic contact. Two important optical properties of the LED-based devices that define their efficiency are internal quantum efficiency (IQE) and external quantum efficiency (EQE). IQE can be defined as the ratio of the generated photons in the active region per second to the number of electrons injected into LED per second, i.e. [12]:

$$IQE = \frac{P_{int}/(hf)}{I/e}, \quad (2.22)$$

where  $P_{int}$  is the optical power emitted from the active region and  $I$  is the injected current. The EQE gives the ratio of the number of photons emitted into free space per second to the number of electrons injected into LED per second, i.e. [12]:

$$EQE = \frac{P/(hf)}{I/e}, \quad (2.23)$$

where  $P$  is the optical power emitted into free space. Examples of IQE and EQE values for GaN-based micro-LEDs have been reported in the literature and can reach peaks up to 74% for IQE [13] and usually below 15% for EQE [14].

The spectral characteristics of an LED are strongly dependent on the spontaneous emission of a photon upon “vertical” (in  $k$ -space) electron-hole recombination, as was previously shown in Figures 2.1a and 2.3c. In practice, for  $T > 0$  K, the photon energy is not exactly equal to  $E_g$  since electrons and holes also have thermal energy that forces them to reside slightly above and below their band edges,  $E_c$  and  $E_v$ , as shown in Figure 2.4a. Consequently, the emitted photon energy will be slightly larger than  $E_g$ .

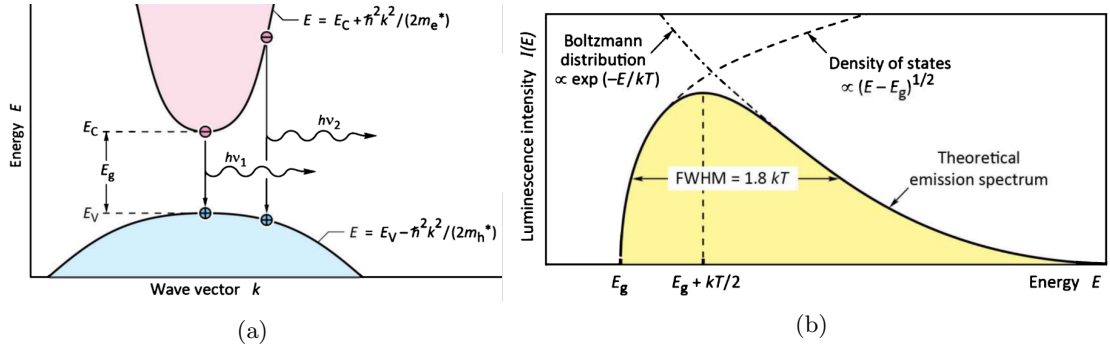


FIGURE 2.4: (a) “Vertical” (in  $k$ -space) electron-hole recombinations at the edges of the conduction and valence bands and slightly above them. (b) Theoretical emission spectrum of an LED. Both figures taken from [12].

The emission intensity of an LED (or the spontaneous emission rate) is given theoretically by the product of the density of states,  $g(E)$  (proportional to  $\sqrt{E - E_g}$  in a 1D case, see Section 2.1.2) and the probability these states being occupied by a carrier (given by the Fermi-Dirac distribution,  $f(E)$ , as discussed in Section 2.1.2). The result of the product is shown schematically in Figure 2.4b where  $f(E)$  has been approximated by the Boltzmann distribution for simplicity. The spectrum of spontaneous emission features an energy threshold of  $E_g$ , a peak of  $E_g + (kT/2)$  and an energy full-width at half-maximum (FWHM) of  $\Delta E = 1.8 kT$ , or a wavelength FWHM of [7, 12]:

$$\Delta\lambda = \frac{1.8 kT \lambda^2}{hc}. \quad (2.24)$$

Practically, the emission spectrum of a real LED device differs from the above theoretical idealisation. Emission spectra of a  $40 \times 40 \mu\text{m}^2$  micro-LED with a central emission wavelength at  $\approx 435 \text{ nm}$ , acquired by R. Ferreira in [15] and shown in Figure 2.5, reveal a different behaviour that is not predicted above. As the injection current slightly increases (up to 20 mA), there is a blue-shift of  $\lambda_{peak}$  due to crystal lattice defects, piezoelectric effects or/and energy band misalignments. However, at  $I \geq 40 \text{ mA}$ ,  $\lambda_{peak}$  shifts towards longer wavelengths (red-shift) due to the  $E_g$  decrease as the junction temperature increases. Finally, the temperature rise increases  $\Delta\lambda$ , which agrees with Equation 2.24.

#### 2.1.4 Quantum well structures

What has been discussed in the previous section referred to p-n diodes whose minority carriers recombine radiatively (and non-radiatively) after diffusion in the opposite conductivity type of the junction. In the case of homojunctions (or homostructures, see Figure 2.6a), the mean distance a minority carrier diffuses before recombination (i.e.,

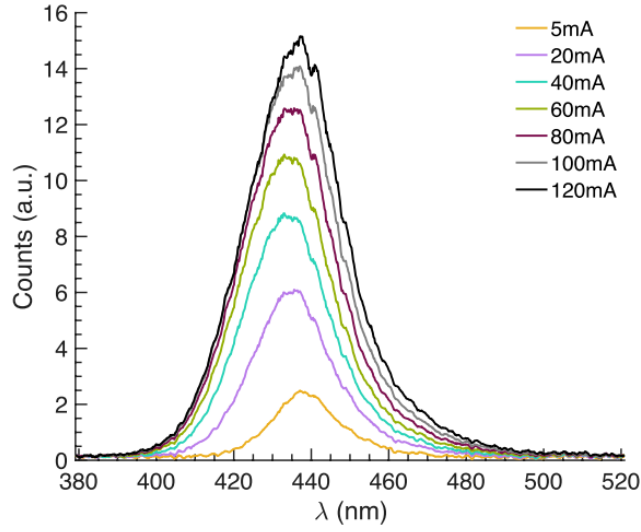


FIGURE 2.5: Emission spectra of a  $40 \times 40 \mu\text{m}^2$  micro-LED under different currents. Taken from [15].

the diffusion length,  $L_{n,p}$ ) can be significant (on the order of several  $\mu\text{m}$ 's) limiting the carrier concentration, and thus, the radiative efficiency of an LED (see Equation 2.21).

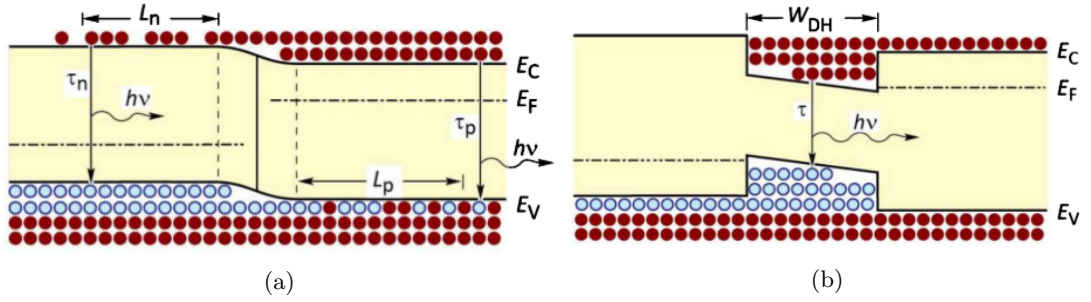


FIGURE 2.6: Schematic illustration of a forward biased (a) homojunction and (b) a QW (or DH). Both figures taken from [8].

The latter can be mitigated using quantum wells (QWs or double heterostructures, DHs). A single QW is formed by three layers of materials in such a way that the intrinsic (i-type) middle layer of thickness  $W_{DH}$  has a smaller  $E_g$  than the surrounding layers (see Figure 2.6b). The outer layers can be doped for electrical injection. This bandgap difference creates potential barriers where charge carriers are confined for recombination in the intrinsic material. The width of the narrow i-region, where recombination occurs (also known as active region), can be engineered down to a few nm's and be comparable to or smaller than the de Broglie wavelength [16]:

$$W_{DH} \lesssim \lambda_{deB} = \frac{h}{p(z)} = \frac{h}{\sqrt{2m^*E}} = \frac{h}{\sqrt{2m^*kT}}. \quad (2.25)$$



In such a situation, the quantisation of the carrier energy in discrete values must be taken into account<sup>§</sup>.  $p(z)$  in Equation 2.25 corresponds to the carrier momentum in the growth,  $z$ , direction where the carriers are confined (free motion in the  $x, y$  plane).

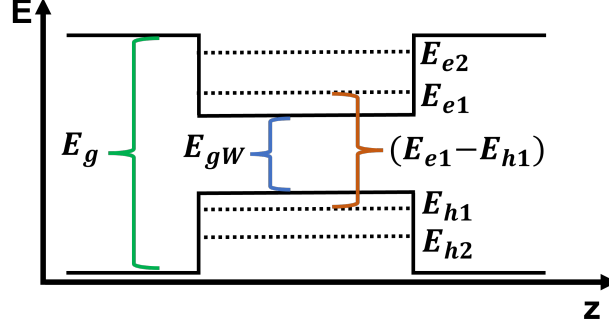


FIGURE 2.7: Schematic illustration of a QW structure, showing that the energy photon from the  $E_{e1} \rightarrow E_{h1}$  optical transition is larger than  $E_{gW}$ .  $E_{e,h}$  refers to the electron and hole-confined energies.

A confined carrier in a QW can be approximated with the quantum mechanics problem of a particle within an infinite potential well<sup>¶</sup> (see in Section 2.1.1, Equation 2.4). By solving Schrödinger's equation for a QW of width  $W_{DH}$ , the energy of the carriers is provided in integer multiples:

$$E_n = \frac{\hbar^2 n^2 \pi^2}{2m^* W_{DH}^2} = \frac{h^2 n^2}{8m^* W_{DH}^2}, \quad \text{where } n = 1, 2, 3, \dots \quad (2.26)$$

By examining Equation 2.26 and Figure 2.7, it is deduced that as the width of the QW decreases and becomes narrower, the energy level separation increases resulting in emitted photons of shorter wavelengths from the active region of the QW. Thus, wavelength tuning of an LED can be achieved by carefully engineering the width of its active region. Additionally, the carriers' confinement in a QW improves its radiative efficiency. This explains why highly efficient LEDs are structured by multiple QWs (i.e., a QW structure repeated multiple times in the growth ( $z$ ) direction).

<sup>§</sup>The  $\lambda_{deB}$  for GaN is  $\approx 17$  nm, given that  $m^* = 2m_e$  which means that for a GaN active layer of  $\lesssim 17$  nm quantum effects can be observed.

<sup>¶</sup>It is noted that although the QW of an LED can be approximated with an infinite potential well for simplicity, it will lead to an overestimation of the confinement energy of the carriers. In reality, a QW's barriers are finite; thus, a finite potential well is a closer approximation to a real LED. This approximation allows the wavefunction to spread out due to quantum tunnelling effects, thereby reducing the confinement energy [16].

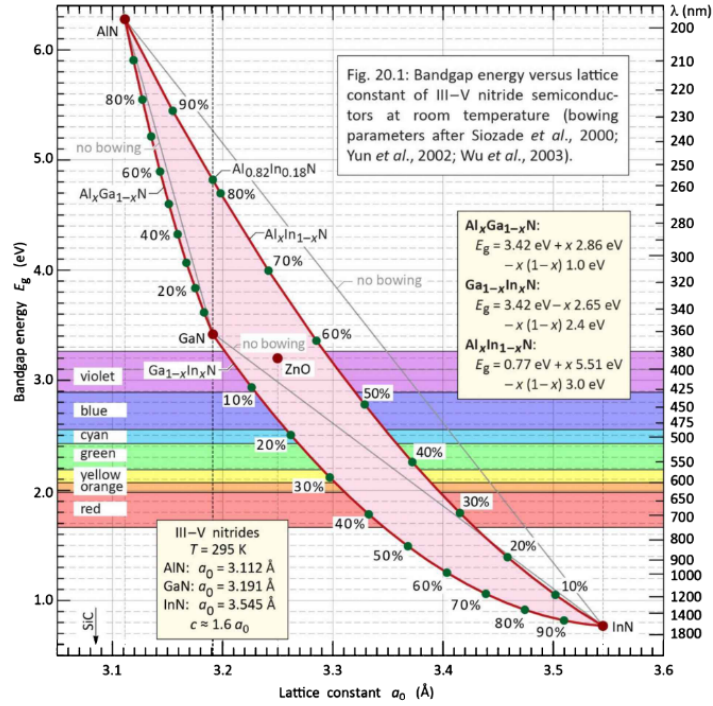


FIGURE 2.8: Room-temperature  $E_g$  and  $\lambda_{em}$  versus  $\alpha_0$  for an AlInGaN alloy system. Taken from [17].

Another way to engineer the wavelength tuning of a QW is to change the composition of its layer and, thus, its bandgap energy. For instance, in III-V nitride alloys and more particularly in InGaN/GaN and AlInN/InN QWs, the emission wavelength ( $\lambda_{em}$ ) can be changed from violet to red in the visible by varying the In and Al content, respectively. This is shown in Figure 2.8 where room-temperature  $E_g$  and  $\lambda_{em}$  versus lattice constant ( $\alpha_0$ ) are illustrated for the AlInGaN alloy system. The subscript notation denotes the relative composition of an alloy, e.g.,  $\text{In}_{0.1}\text{Ga}_{0.9}\text{N}$  means that this alloy comprises 10% InN and 90% GaN. In “real-world”  $\text{In}_x\text{Ga}_{1-x}\text{N}$  alloy systems, violet is emitted when the In composition equals to  $x = 9\%$ , blue when  $x = 17\%$ , and green for  $x = 30\%$  [18].

An example of the epitaxial structure of such a micro-LED emitting at  $\approx 370\text{nm}$  [19], can be seen in Figure 2.9. A 25 nm thick buffer layer of undoped GaN is grown on a c-plane sapphire substrate, followed by 2.3  $\mu\text{m}$  of undoped GaN, 1.4  $\mu\text{m}$  of Si-doped  $n$ -type GaN and then a multi-quantum well (MQW) region approximately 50 nm in thickness. The MQW is capped with a 100 nm thick magnesium (Mg)-doped AlGaIn cladding layer, or “electron-blocking” layer, which is intended to provide a potential barrier to prevent electrons overflowing and escaping the active region. The structure is finally capped with a 20 nm thick Mg-doped GaN contact layer. The MQW region consists of seven  $\text{In}_{0.05}\text{Ga}_{0.95}\text{N}$  quantum wells, each of 2 nm thickness, with 10 nm thick  $\text{Al}_{0.2}\text{Ga}_{0.8}\text{N}$  barriers. Thin quantum well structures are favoured for growth in c-plane sapphire as they minimise the spatial charge separation due to built in strain fields that

can result in reduced radiative rates due to a separation and reduced overlap of the electron and hole wavefunctions, a phenomenon known as the “quantum confined Stark effect” (QCSE). This structure is fairly representative of the epitaxial structure of the micro-LEDs discussed in this thesis, and of InGaN-based LEDs in general [20].

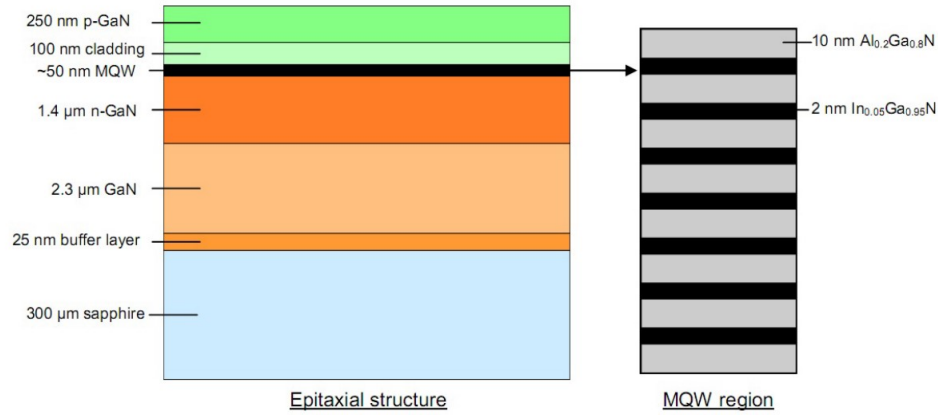


FIGURE 2.9: Schematic illustration of a typical epitaxial structure of a UV-emitting micro-LED. The multiple QW (MQW) region is expanded and is shown on the right side of the figure (schematic not to scale). Image taken from [20] and data from [19].

### 2.1.5 The laser diode

Off-the-shelf laser diodes (LDs) have been employed throughout this thesis, either for the characterisation of the turbidity of the water samples (see Section 1.6) or for the underwater wireless data transmission by using the Fibrance<sup>®</sup> Light-Diffusing Fibre (see Chapter 5).

A LD is related to an LED in that both devices comprise a p-n junction, and their energy source is an electric current injected into the p-n junction (see Figure 2.10). The LD operational principle, though, differs from an LED’s. As shown in the previous sections, the photon output of an LED is random in space and time (incoherent) due to the spontaneous and radiative recombination of an electron-hole pair. On the other hand, as the acronym of “laser” suggests (**L**ight **A**mplification by **S**timulated **E**mission of **R**adiation), the output photon of a LD is due to stimulated emission. In this process, an already excited atom is stimulated by a photon of energy  $\geq E_g$  and forces it back to its ground state by the emission of a second photon of the same wavelength and phase as the incident one. Thereby, the output light comprises two photons (i.e., optical gain or amplification) that are in phase; therefore, the laser light is coherent.

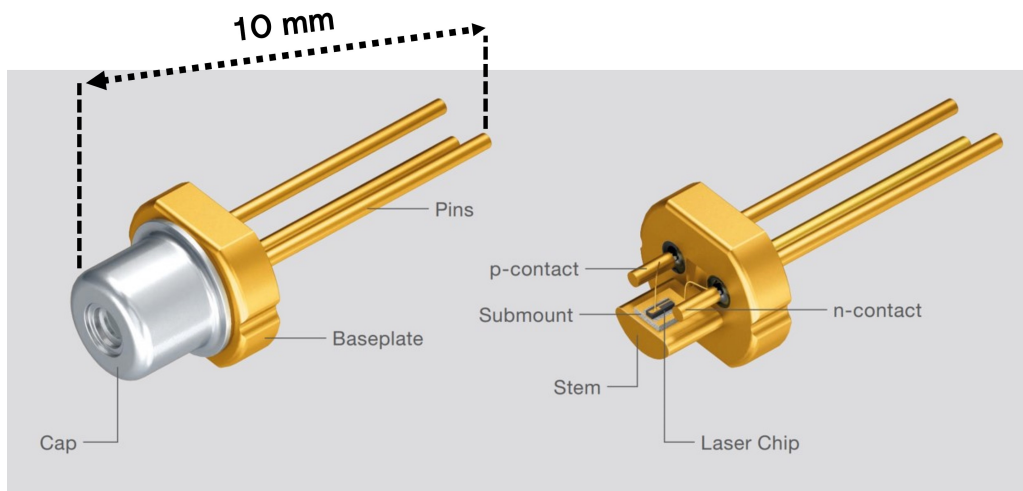


FIGURE 2.10: *Left*, an OSRAM PL520 green LD with its cap on, and *right*, the same LD with its cap off (taken from [21]).

One of the conditions to achieve lasing is the population inversion that can be briefly explained as follows; moving away from the energy bands picture of solids for simplicity, we now assume a system of two energy levels, as shown in Figure 2.11,  $E_1$  (ground state) and  $E_2$  (excited state) that are populated by electron concentrations of  $N_1$  and  $N_2$ , respectively.

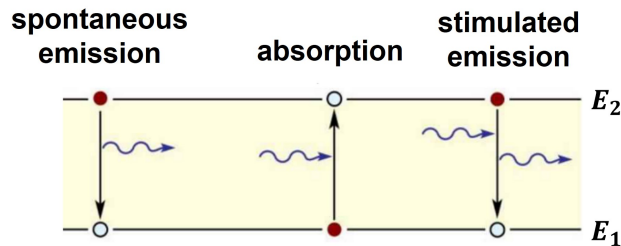


FIGURE 2.11: The optical processes of absorption, spontaneous emission and stimulated emission of a two-energy level system with  $E_1 < E_2$ . Adapted from [22].

When light of intensity  $\phi$  is incident on the two-energy level system, the occurring optical processes are absorption, spontaneous emission and stimulated emission. The transition rates of these processes can be described as [7]:

$$\begin{aligned}
 R_{ab} &= B_{12} N_1 \phi, \\
 R_{sp} &= A_{21} N_2, \\
 R_{st} &= B_{21} N_2 \phi.
 \end{aligned}
 \tag{2.27}$$

Here,  $B_{12}$ ,  $A_{21}$ , and  $B_{21}$  are the Einstein coefficients for absorption, spontaneous emission, and stimulated emission, respectively, that have dimension  $[\text{time}]^{-1}$ . If spontaneous emission is ignored and  $B_{12} = B_{21}$ , the net optical output of a laser is given by:

$$R_{st} - R_{ab} = (N_2 - N_1) B_{21} \phi. \quad (2.28)$$

Population inversion occurs when the laser system is pumped (i.e., the p-n junction is forward biased) so that  $N_2 > N_1$  and the net optical gain of the laser from Equation 2.28 is positive.

The second lasing condition involves a structural requirement. An optical resonator (or optical cavity) placed in the direction of the light output ( $z$ -direction) serves to trap the light inside and build up the light intensity. The resonator consists of two perfectly parallel mirror-like walls (perpendicular to the junction), one of which can be partially reflecting so that a portion of light can come out only from one side whilst the other is (nominally) totally reflecting. The optical cavity of length  $L$  can support those resonant frequencies (longitudinal modes) for which the following formula is satisfied:

$$N \left( \frac{\lambda}{2} \right) = L, \quad (2.29)$$

i.e., the length of the cavity must be an integral number ( $N$ ) of half wavelengths [2]. The longitudinal modes are separated by  $\Delta\lambda = \frac{\lambda^2}{2L} \Delta N$ . It is therefore deduced that by reducing  $L$ ,  $\Delta\lambda$  increases, and the output of the LD can be led to a single dominant mode with a very narrow bandwidth [2].

If the optical gain due to stimulated emission is denoted as  $g$  and the optical losses due to absorption are denoted as  $a$ , the net gain/losses formula is given by [7]:

$$\phi(z) \propto e^{(g-a)z}. \quad (2.30)$$

Optical losses also occur due to the partially reflecting mirror of the cavity. If  $R_1$  and  $R_2$  are the mirrors' reflectivities, then after one round trip through the cavity,  $R_1$ ,  $R_2$  and  $a$  are fixed and  $g$  is the only parameter that varies the overall gain for a given system. To sustain a lasing action, the overall gain must be positive as losses are typically represented by a factor less than unity. This can be expressed by the formula [7]:

$$R_1 R_2 e^{(g-a)2L} > 1. \quad (2.31)$$

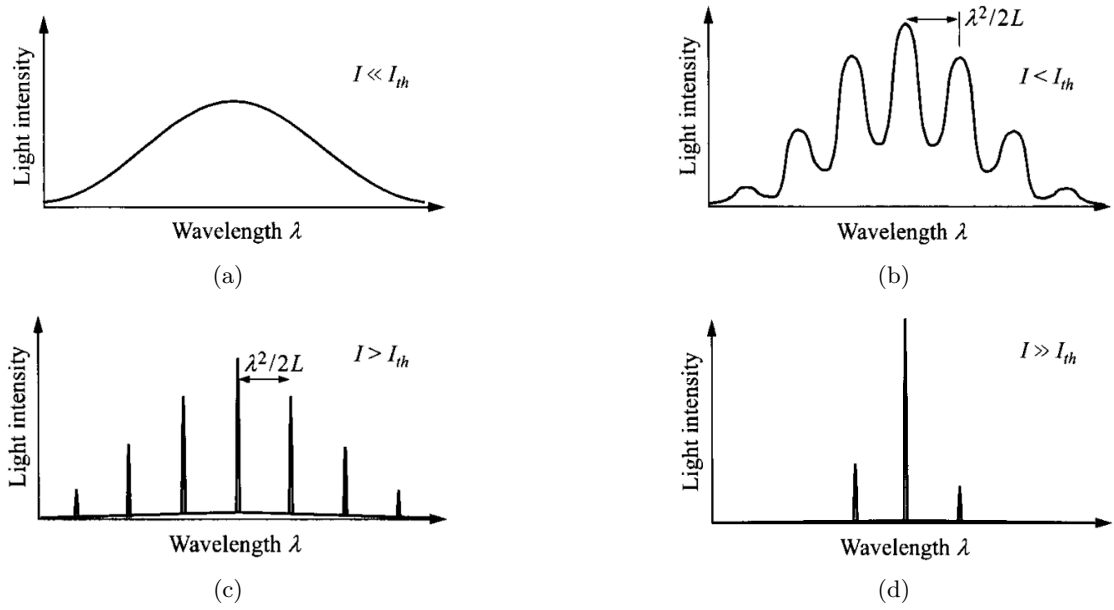


FIGURE 2.12: Emission spectra of a LD under different bias conditions; (a) current (or current density) much below threshold, (b) current just below threshold, (c) current just above threshold, (d) current much above threshold. Taken from [7].

The condition being greater than unity ensures that the amplification of light exceeds losses and is capable of sustaining lasing in the laser cavity. From Equation 2.31 the threshold gain,  $g_{th}$ , yields as [2, 7]:

$$g_{th} = a + \frac{1}{2L} \ln \left( \frac{1}{R_1 R_2} \right). \quad (2.32)$$

The optical gain of a LD is proportional to the current applied across the p-n junction; at low current densities ( $J$ , in  $\text{A}/\text{cm}^2$ ), spontaneous emission is the dominant process, and the output light comprises a broad spectrum (like an LED's, see Figure 2.12a). As the current density increases, so does  $g$ , and light intensity peaks start to appear that correspond to the modes (or standing waves) the optical cavity can support (Figure 2.12b). When a current density value is above threshold ( $J_{th}$ ),  $g$  is now expressed by Equation 2.32 and is larger than optical losses (i.e., lasing, Figure 2.12c). The threshold current density is given by [2]:

$$J_{th} = \frac{1}{\beta} \left[ a + \frac{1}{2L} \ln \left( \frac{1}{R_1 R_2} \right) \right]. \quad (2.33)$$

$\beta$  can be determined either experimentally or theoretically. The number of modes can be reduced by further increasing the applied current density (Figure 2.12d), which complements the previous discussion on reducing the optical cavity's length (see Equation 2.29).

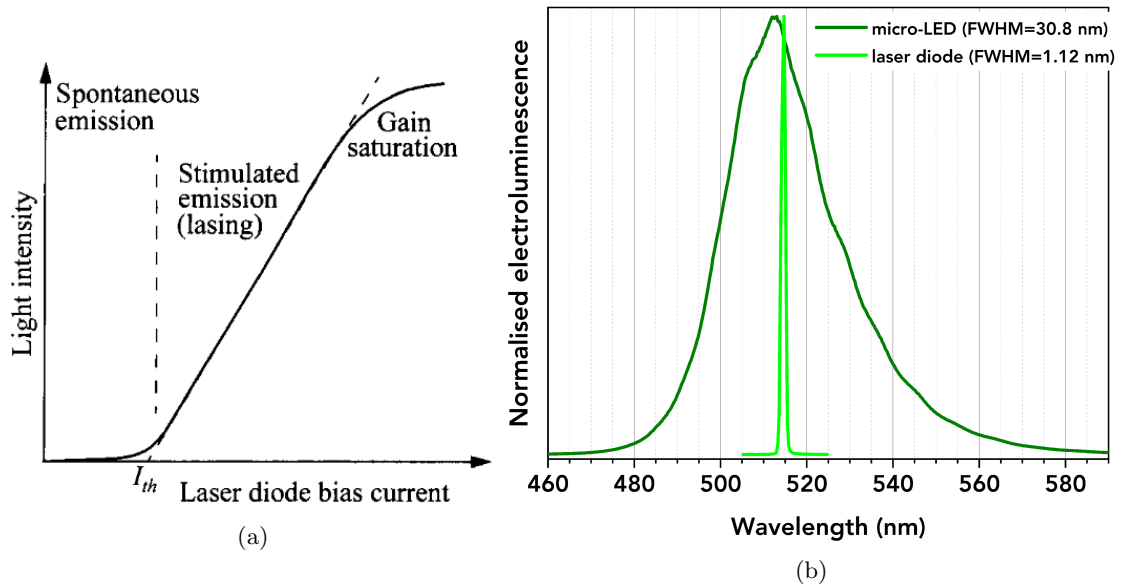


FIGURE 2.13: **(a)** A typical LI curve of a LD along with the physical processes taking place as the bias current increases (taken from [7]). **(b)** Comparison of the normalised emission spectra of a “home-made” green micro-LED (used in Chapter 4) and an OSRAM green LD (used in Section 1.6 and Chapter 5).

A typical curve of a LD that shows the output light versus the input current (LI curve) is shown in Figure 2.13a, where the processes of spontaneous and stimulated emission, as previously discussed, have been indicated. Gain saturation arises when the stimulated emission rate is so high that the population inversion can no longer be sustained.

For comparison, Figure 2.13b shows the normalised emission spectra of two devices used in this thesis, along with their FWHM values. The broad spectrum (dark green curve) corresponds to a green micro-LED with a central emission peak at 512 nm, developed at the University of Strathclyde’s Institute of Photonics (IoP) by José Carreira and utilised in Chapter 4. The narrow spectrum (light green curve) corresponds to the OSRAM green LD (as shown in Figure 2.10) with a central emission peak at 514 nm and was used extensively in Chapters 1 (Section 1.6) and 5. The difference in their FWHM (30.8 nm for the micro-LED and 1.12 nm for the LD) of both devices is attributed to the isotropic incoherent output light of the micro-LED due to spontaneous emission and the coherent amplified output light of the LD due to stimulated emission.

### 2.1.6 Photodetectors

In this thesis, various photodetectors were utilised. These are summarised as a PIN photodiode in Chapter 3, a “Photon Torrent” single photon avalanche photodiode (SPAD) array (developed by Professor Robert Henderson’s group at the University of Edinburgh)

in Chapter 4, and a sensL Si photomultiplier (SiPM) in Chapter 5. The basic operational principles of these photodetectors are discussed in the following subsections.

By definition, photodetectors are devices that convert optical signals into electrical signals. Some of their important general characteristics are the quantum efficiency (QE) which must be high at the operating wavelengths, the response speed, and the device noise, which must be kept low so the output signal can be better discriminated from the background noise. These features are briefly outlined below.

### Quantum efficiency

The QE ( $\eta$ ) of a photodetector represents the probability an output signal is generated upon the absorption of an incident photon. It is defined as the number of carriers (electrons or holes) produced per number of incident photons, i.e. [7]:

$$\eta = \frac{I_{ph}}{\Phi} = \frac{S \times 1240}{\lambda}, \quad (2.34)$$

where  $I_{ph}$  is the photocurrent,  $\Phi$  is the photon flux ( $= P_{opt}/hf$ , with  $P_{opt}$  being the optical power),  $S$  is the photosensitivity ( $= I_{ph}/P_{opt}$ ), a metric that is similar to QE, and  $\lambda$  is the wavelength of the incident light (in Å). QE is usually expressed as a percentage; thus, an ideal photodetector will have  $\eta = 100\%$ . In practice, though,  $\eta$  is always lower due to various factors that lead to photon losses, such as absorption, scattering or reflection from the air-semiconductor interface. The absorption of a photon is also strongly dependent on the photodetector's material and design. It is worth noting that a photon absorbed successfully by the device will not always result in an electrical output signal [23].

### Response speed

A photodetector's response speed ( $\tau$ ) expresses the time it takes to extract the generated carriers in an output signal. The response speed can be limited by a combination of three factors, namely  $\tau_1$ ,  $\tau_2$ , and  $\tau_3$  [7, 24].

$\tau_1$  is proportional to the  $R_L C_j$  time constant, where  $R_L$  is the load resistance of the junction and  $C_j$  is its capacitance.  $C_j$  is proportional to the area of the depletion region (or the photosensitive area),  $W$ , of the photodetector; thus, the device's depletion layer must not be too wide. On the other hand, by decreasing  $W$ ,  $R_L$  increases and therefore, a compromise on the area of the depletion layer must be considered.

$\tau_2$  is associated with the diffusion time of the carriers generated outside the depletion layer when the surrounding area of the photosensitive region and the substrate below the



depletion layer absorb light. The depletion layer should be formed close to the surface to minimise  $\tau_2$ .

$\tau_3$  refers to the time it takes for the carriers to diffuse in the depletion layer. Minimising the depletion layer's thickness minimises  $\tau_3$ . However, as previously mentioned, the decrease of  $W$  leads inevitably to an increase of  $\tau_1$ .

All the factors mentioned above combine to determine the response speed of a photodetector, whose formula is finally given by [24]:

$$\tau = \sqrt{\tau_1^2 + \tau_2^2 + \tau_3^2}. \quad (2.35)$$

### Device noise

Besides a significant output signal, low noise is highly desirable in photodetectors technology as it determines the minimum detectable “useful” signal. The signal-to-noise (SNR) ratio is a metric that compares the level of the output signal to the level of the background noise, and it is defined as the ratio of the signal power to the noise power. The origin of the noise is found in various factors. Some of these include the “dark” noise, i.e., the triggering of an output signal when the photodetector is biased but no incident light is present. Thermal noise can also be met when  $kT > E_g$ , or when the carriers are thermally agitated in any resistive device (“Johnson” noise). Another noise source is the “shot” noise linked to the single events of the photoelectric effect, and it is more pronounced when the signal level is comparable to it<sup>†</sup>. Surface traps due to imperfections of the photodetector's material can also be considered as noise sources (“flicker” noise) that lead to unwanted random generation-recombination events [7].

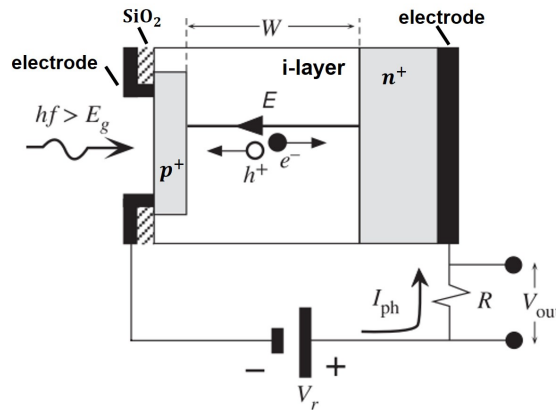


FIGURE 2.14: Schematic illustration of a PIN diode with a reverse bias ( $V_r$ ) applied across it. Taken from [25].

<sup>†</sup>The SNR according to Poisson statistics is  $SNR = \frac{S}{\sqrt{N}}$ . For a minimum detectable signal, the SNR should be set equal to a minimum threshold value, i.e.,  $SNR = 1$ . Therefore, the minimum detectable signal is  $S = \sqrt{N}$ .

### PIN photodiode

As introduced in Section 2.1.4, a PIN photodiode is formed by a p-n junction with an i-layer (intrinsic) between the p and n materials (see Figure 2.14). The i-layer of width  $W$  can be intrinsic or lightly doped compared to the heavily doped p- and n-regions.

The advantages of a PIN photodiode over a p-n photodiode can be summarised as follows [25]; firstly, the purpose of the i-layer is to increase the photosensitivity of the PIN device as its width is much larger when compared to that of a simple p-n junction and the PIN structure is designed so that the photon absorption takes place primarily within the i-layer. It should be noted that by designing PIN devices with large  $W$ , more photons can be absorbed, which leads to an increased output signal, but the speed of response of the devices is slowed as the carriers' transit time becomes longer.

Secondly, the  $W$  in a PIN photodiode is fixed by the structure; thus, it is independent of the applied voltage. The latter makes the PIN devices suitable for applications requiring high reverse voltage.

Thirdly, the capacitance of the depletion layer is very small (on the order of picofarads) and inversely proportional to  $W$ . As discussed, small  $C$  leads to small  $RC$  time constants rendering the PIN photodiode suitable for high modulation frequency signal photodetection.

The PIN silicon photodiode used in Chapter 3 (Femto, HSA-X-S-1G4-SI, Figure 2.15a) has a time response of typically  $\approx 250$  ps [26]. In contrast, a silicon photomultiplier's time response, for instance, can be on the order of ns or  $\mu$ s. Some additional information on the Femto PIN photodiode is the device's upper cut-off frequency at 1.4 GHz and its maximum spectral response or sensitivity of 0.51 A/W at 760 nm [26] (Figure 2.15b).

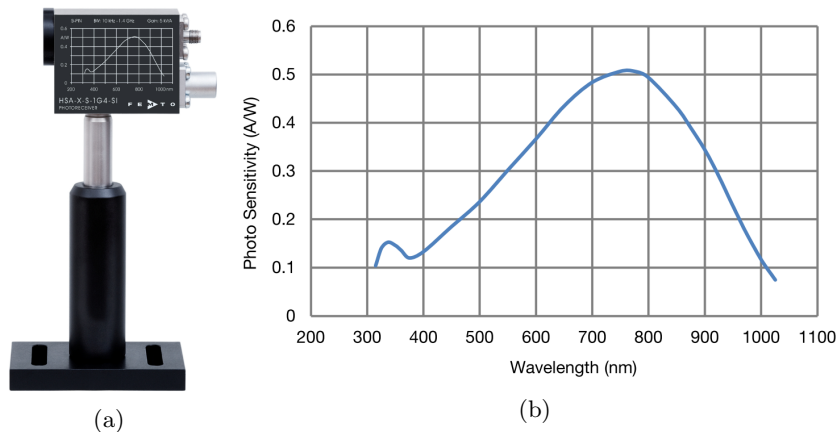


FIGURE 2.15: (a) Femto Si-PIN photodiode used in Chapter 3 and (b) its photosensitivity versus wavelength. Taken from [26].

### Single-photon avalanche diode

A single-photon avalanche diode (SPAD) is essentially a p-n diode in which the applied reverse voltage is well above the breakdown voltage ( $V_{bd}$ ), a mode of operation known as Geiger mode. At this bias, the electric field is so high ( $> 5 \times 10^5$  V/cm) in the depletion region that an electron drifting within it can gain sufficient kinetic energy (KE) to ionise a host crystal atom by bombardment (impact ionisation). For the impact ionisation to occur, the electron's KE should be larger than  $E_g$  (that is equivalent to exciting an electron from the valence band to the conduction band) and thus, an electron-hole pair is created [25]. The electron-hole pairs generated by impact ionisation can now be accelerated by the electric field that will give rise to further ionising collisions triggering an avalanche effect (Figure 2.16a), leading to a fast discharge of the device's depletion capacitance. It is worth noting that the internal amplification (gain) due to the avalanche effect in a SPAD can be of up to  $10^8$ , contrary to conventional p-n and PIN photodiodes whose gain is 1, rendering SPADs as an attractive candidate for photon-limited underwater links [27].

The output of a SPAD comprises a train of sharp current pulses of the same amplitude that indicate the arrival times of the photons at the sensor (Figure 2.16b). Since the received pulses are of the same amplitude, intensity information can be provided by recording the number of the obtained pulses or measuring the mean time interval between subsequent pulses [28].

Once a current is flowing, the avalanche should be quenched to avoid complete damage of the diode. This is achieved by an external circuit that temporarily lowers the bias voltage below  $V_{bd}$ . Thus the electric field in the p-n junction can no longer sustain impact ionisation, and the avalanche stops. The SPAD is then charged back gradually, and eventually, the bias voltage goes above  $V_{bd}$ . Then, the SPAD is fully light-sensitive again. This process is depicted in Figure 2.16c. The time it takes to quench the avalanche and recharge the diode (up to  $\approx 90\%$ ) is defined as the dead time that is usually on the order of ns. As a result of the above, a SPAD operates in a “binary” on/off mode where “on” corresponds to the signal detection of one photon, regardless of the number of photons interacting with the diode.

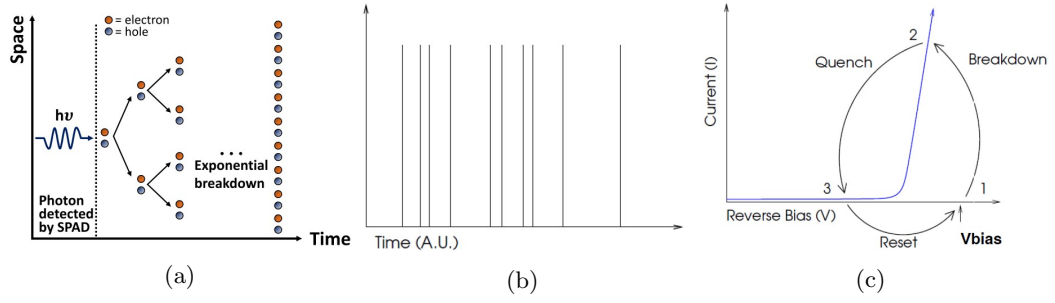


FIGURE 2.16: (a) Schematic illustration of the avalanche effect generated by impact ionisation and occurring in the depletion region of a SPAD (taken from [29]). (b) Illustration of the output of a SPAD in the form of train pulses of the same amplitude, and (c) the SPAD's quenching mechanism (taken from [30]).

### The silicon photomultiplier

A silicon photomultiplier (SiPM, used in Chapter 5) can be employed to overcome the disproportion between the incident photon flux and output signal mentioned previously. A SiPM is essentially an array of independent SPADs (microcells, Figure 2.17a), each with its own quenching mechanism. This means that when a photon is detected by a microcell independently, a Geiger avalanche is triggered and confined to the single microcell it was initiated in (along with the quenching process that follows, as described above). During the recovery time of the triggered microdevice, all other microcells of the SiPM remain charged and ready for photon detection. The sum of the photocurrents from each microcell is combined to form an output signal of the SPAD (see Figure 2.17b) in a quasi-analog form, and therefore, information on the magnitude of the incident photon flux can be acquired. An important performance parameter of a SiPM is its spectral response, i.e., its photon detection efficiency (PDE). PDE is the probability an incident photon to generate an avalanche and is defined as [30, 31]:

$$PDE(\lambda, V) = \eta(\lambda) \cdot \epsilon(V) \cdot F_{fill} = \eta(\lambda)_{PDP} \cdot F_{fill}. \quad (2.36)$$

Here,  $\eta(\lambda)$  is the device quantum efficiency and  $\epsilon(V)$  is the avalanche initiation probability. Their product,  $\eta(\lambda)_{PDP}$ , is the photon detection probability and  $F_{fill}$  the device fill factor, i.e., the percentage of the SiPM area that is sensitive to light. The PDE of the  $6 \times 6 \text{ mm}^2$  sensL SiPM used in this thesis, versus wavelength, can be seen in Figure 2.17c. The  $PDE_{max}$  is 51% at 420 nm at 6 V overvoltage (i.e., the applied voltage above  $V_{bd}$ ).

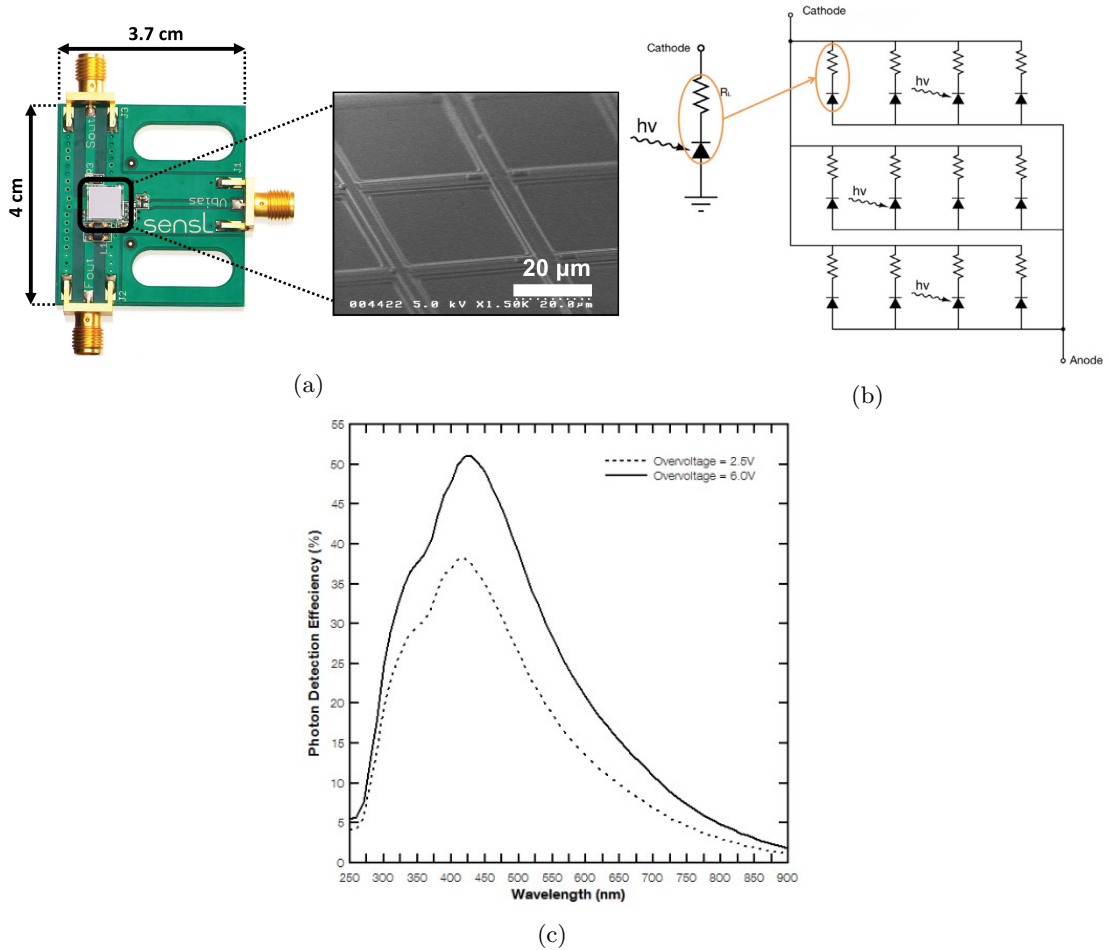


FIGURE 2.17: **(a)** Images of a sensL SiPM and the microcell structure on its surface. **(b)** A simplified electric circuit illustrating the array of microcells (photodiode and quench resistor) of a sensL SiPM. **(c)** PDE versus wavelength for a  $6 \times 6 \text{ mm}^2$  sensL SiPM at different overvoltage values (2.5 V-dashed curve, 6 V-continuous curve). Taken from [30].

$F_{fill}$  has its importance in SiPMs as each microcell needs to be separated from its neighbour for electrical purposes, such as space required for the quench resistor and signal tracks, and optical purposes, such as the avoidance of noise in the form of afterpulsing and optical crosstalk. The former regards trapped carriers in Si defects that can be released after a delay of several ns, triggering an avalanche and eventually creating an afterpulse in the same microcell. Afterpulsing can be negligible when occurring within the device dead time but impactful when occurring at longer delays. Optical crosstalk is an additional source of unwanted noise for a SiPM. It refers to the probability a microcell is triggered by a neighbouring avalanching microcell that results in higher signal generation than a single photon's level. Crosstalk is overvoltage and fill factor-dependent. Thus a trade-off between the two parameters should be considered to minimise it. A high fill factor (larger microcells) will result in higher PDE. But also in higher noise levels and, eventually, a lower dynamic range. A lower fill factor (smaller microcells)

will result in lower PDE but higher dynamic range due to lower capacitances and faster recovery times [30].

SiPMs are nowadays well-recognised photodetectors thanks to their high gain, low operating voltage, compactness, exceptional photon detection capability and single photon resolution. These advantages of SiPMs over other devices, such as PIN photodiodes, render them attractive candidates for applications where UWOC and SWaP (Size, Weight and Power) or SMaP (Size, Mass and Power) portable devices can be successfully combined.

### The “Photon Torrent” SPAD array

The Photon Torrent chip (used in Chapter 4) is essentially a bespoke SPAD array that combines the single-photon sensitivity of a SPAD with the speed of a conventional photodetector. The output of the array is combined using XOR trees so that the device operates as a digital Si photomultiplier (dSiPM) [32] with a single output of photons at given sample rates of 100 MHz, 200 MHz, 400 MHz, and 800 MHz (Figure 2.18) [33].

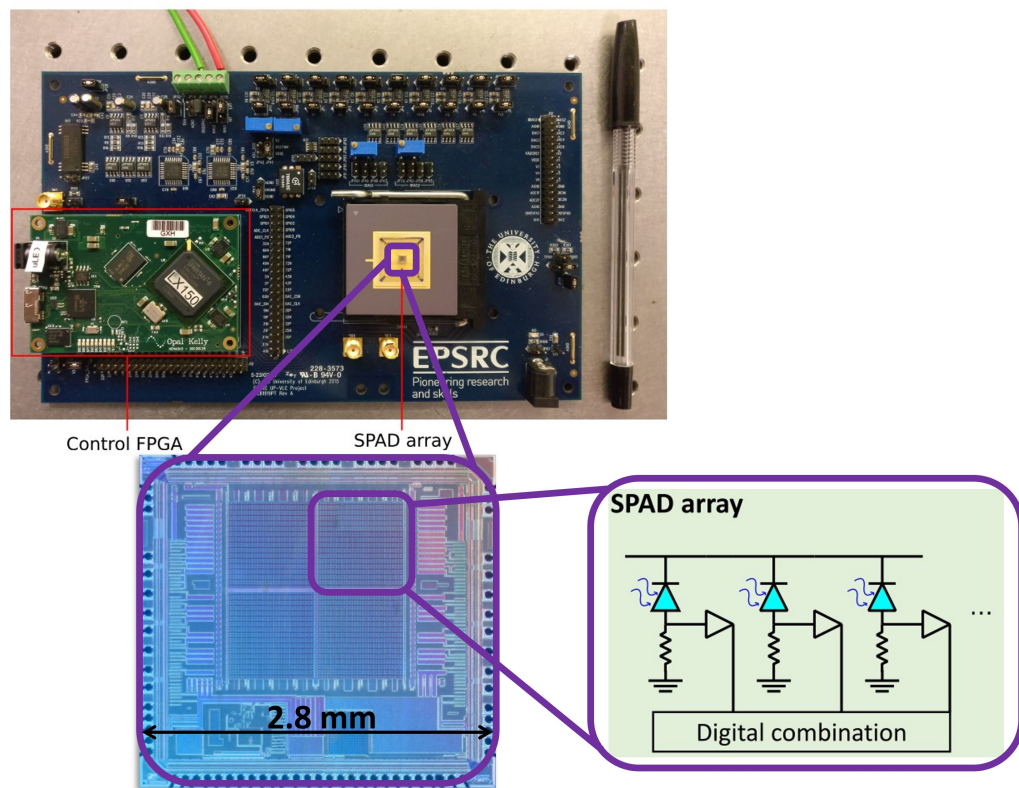


FIGURE 2.18: Photograph of the Photon Torrent chip along with a plan-view photograph of the SPAD array and a simplified electric circuit illustrating the SPAD pixels. Taken from [29, 33].

The device consists of  $64 \times 64$  pixels giving 4096 Si SPADs on a  $21 \mu\text{m}$  pitch, with a fill factor of  $F_{fill} = 43\%$ . The chip dimensions are  $2.6 \times 2.8 \text{ mm}^2$  (including the surrounding

electronics), and it is packaged to interface with a Printed Circuit Board (PCB). The chip is controlled and powered via a Field Programmable Gate Array (FPGA), and an external bias of 15.2 V is applied to the SPAD pixels. The individual pixels have  $\eta_{PDP} = 37\%$  at 450 nm ( $PDE_{chip} \approx 16\%$ ) and a dead time of 12 ns [34].

Strathclyde University’s IoP has extensively used the chip in free-space optical (FSO) communication links. For instance, Griffiths *et al.* in [31] demonstrated data rates of up to 20 Mb/s over 750 m in a “real-world” scenario with a micro-LED source. Further Photon Torrent applications of exceptionally high sensitivity levels can be found in [33] where data rates of 50 kb/s and optical received power in the picowatt range have been demonstrated.

The latter can be highly applicable in underwater environments where scattering and/or absorption are dominant, resulting in high light attenuation and, thereby, establishing a UWOC link is challenging. Preliminary results using a micro-LED array emitting at 450 nm and the Photon Torrent as a receiver over the water tank (the same experimental set-up as introduced in Section 1.6) showed that 20 kb/s can be transmitted “error-free” (bit-error ratio  $\leq 1 \times 10^{-3}$ )\*\* over 7.5 ALs (Figure 2.19). This number of ALs practically means that 99.94 % of the light propagated over the water tank is lost. The practicality of the Photon Torrent in UWOC applications is marked since even under a significant degree of light attenuation, data transmission is achievable without needing a high-power optical transmitter.

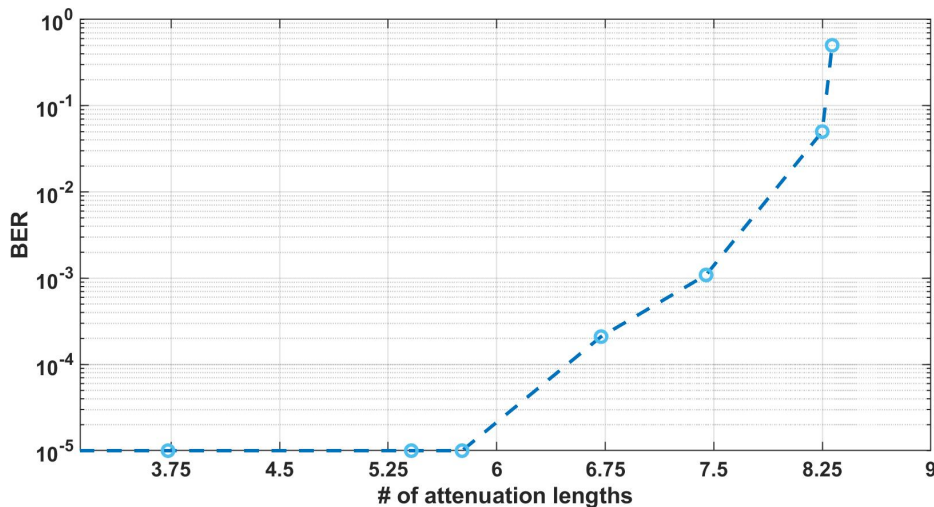


FIGURE 2.19: Bit-error ratio (BER) of a 20 kb/s UWOC link with varying the number of attenuation lengths.

\*\*The ratio of the incorrectly decoded bits to the total transmitted bits is the bit-error ratio (BER) and BER values below  $1 \times 10^{-3}$  can be corrected with forward error correction (FEC) algorithms [35].

## 2.2 Modulation schemes

In (underwater) visible light communications (VLC) using LEDs and most schemes involving LDs, the information to be transmitted is encoded to the instantaneous intensity of the optical carrier<sup>††</sup>. A simplified depiction of the modulation process of, e.g., an LED device is summarised in the block diagram shown in Figure 2.20.

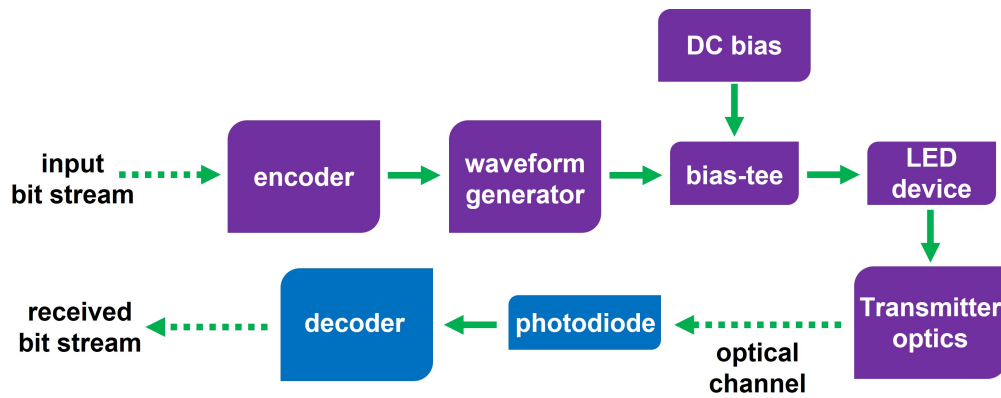


FIGURE 2.20: Simplified block diagram of a VLC system. Adapted from [36].

The input bit stream, in digital form, is firstly encoded using the chosen modulation scheme. A digital-to-analog converter (DAC) or a waveform generator converts the digital signal to a voltage signal (analog) that will modulate the LED device. This signal is then combined via a bias-tee with a DC bias. The DC bias drives the LED device above its threshold voltage ( $V_{th}$ , see Section 2.1.3) in the regime where the luminosity-voltage curve (L-V) or luminosity-current curve (L-I) is quasi-linear [36, 37]. The optical output of the LED is then modulated by the AC signal coming from the waveform generator following the LED’s L-V or L-I curve. The optical signal is propagated over the optical channel via optics to the receiver end. At the receiver side, a photodiode converts the optical signal into an electrical signal and the input bit stream is ideally fully recovered by the decoder electronics.

### 2.2.1 On-off keying

On-off keying (OOK) was used in the experiments presented in Chapters 4 and 5 and is considered the simplest (in terms of hardware and concept) method of transmitting data. The information is in this case encoded in the intensity of output pulses modulated between two levels, representing binary values of “0” and “1”. For the LED- and laser-based devices used in this thesis, the two intensity levels are often below and above the DC bias, combined with the AC modulated signal and provided by a bias-tee (see above). OOK can either be Non-Return-to-Zero (NRZ), in which a transmitted pulse

<sup>††</sup>For LDs the information could also be encoded, e.g., in polarisation or orbital angular momentum.



has a pulse duration equal to the bit duration, and thus the pulse intensity remains constant, or Return-to-Zero (RZ), where the pulse duration equals a portion of the pulse bit and returns to “zero” state [36, 38]. A schematic illustration of an OOK data stream is shown in Figure 2.21.

Decoding the transmitted data at the receiver end requires a threshold to determine the transmitted bit. As the modulation rate increases, the two intensity levels will become closer, making the distinction between them difficult. This results in binary symbols being decoded incorrectly, i.e., in bit errors or ISI.

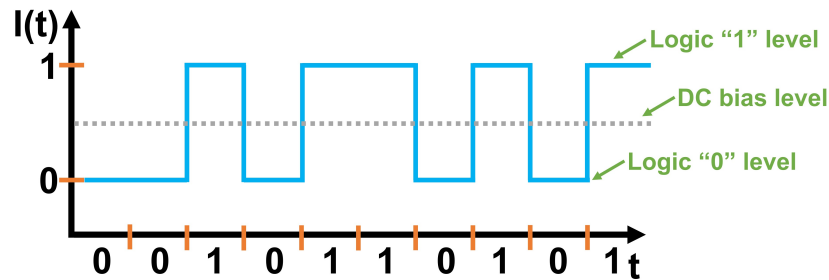


FIGURE 2.21: Schematic of an OOK optical transmission of a data sequence [0010110101].

To mitigate these effects, other modulation schemes that are tolerant to, e.g. ISI and offer higher spectral efficiency can be considered. The higher the spectral efficiency, the more data (higher data rates) can be transmitted over the available system bandwidth [36]. Such a scheme is orthogonal frequency division multiplexing (OFDM) and will be presented in the subsequent section.

### 2.2.2 Orthogonal frequency division multiplexing

OFDM effectively utilises the available frequency bandwidth by dividing it into sub-carriers, each representing sinusoidal signals with distinct frequencies. Unlike OOK, where data is sent one bit at a time, OFDM enables the transmission of multiple data streams concurrently. The key concept in OFDM is using sub-carriers, which are essentially individual carriers dedicated to specific frequencies within the allocated bandwidth (Figure 2.22). These sub-carriers can be encoded by alternating their amplitude and/or phase using a modulation scheme such as Quadrature Amplitude Modulation (QAM).

The frequencies of the modulated sub-carriers are chosen to be mathematically orthogonal among them, which is the main idea in OFDM. Orthogonality implies that the inner product of any two distinct sub-carriers is zero, essentially making them independent. In the context of OFDM, the sub-carriers are designed to be orthogonal, meaning their waveforms are aligned so their peaks and troughs do not coincide. This unique

property allows the simultaneous transmission of multiple sub-carriers in a confined frequency space without causing interference among them. Consequently, this inherent orthogonality is a fundamental reason why OFDM is highly resilient against ISI. Following modulation, the subcarriers are combined using the Inverse Fast Fourier Transform (IFFT) to synthesise waveforms in the time domain, ready for transmission.

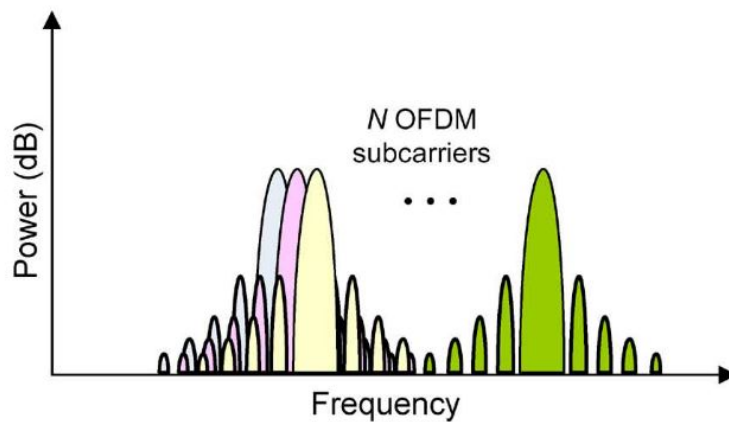


FIGURE 2.22: Spectra of different OFDM sub-carriers (shown in different colours) in the frequency domain. Although their spectra overlap, the sub-carriers do not interfere with each other due to their orthogonality. Image taken from [39].

Although OFDM has been extensively used in free-space optical wireless communications for the demonstration of data rates on the order of Gb/s (e.g., 11.74 Gb/s by Xie *et al.* in 2020 [40]), it can require complex hardware or can be computationally heavy (thus, power-hungry). This can potentially make the implementation of OFDM impractical in natural underwater environments. However, it shows the full capability of high-speed data transfer underwater when compared with other technologies, such as acoustic and radio frequency. Two representative examples of OFDM in high-speed UWOC can be found in Chapter 3, where 4.92 Gb/s over 1.5 m of tap water were demonstrated by using a blue micro-LED array as a transmitter [41], and in [42], by Huang *et al.*, where 14.8 Gb/s were reported over 1.7 m of seawater, by using a blue GaN LD.

## 2.3 Summary

This chapter first briefly explained the underlying physics of the semiconductor devices used throughout this thesis. Some introductory terms of semiconductor physics were analysed, such as energy band diagrams, carrier concentrations and effective mass. In the following chapters, the devices for UWOC are LED- and laser-based devices, and therefore, the operation principles of a p-n junction were detailed along with those of the laser diode. A brief summary of the features of the photodetectors used in this dissertation was also reported: a PIN photodiode, an array of SPADs (SiPM), and the

Photon Torrent chip. Lastly, it was given a simplified description of OOK and OFDM, the two modulation schemes (i.e., the process of encoding data onto light) used in the following chapters.

## References

- [1] Stefanos Trachanas. *An introduction to quantum physics: a first course for physicists, chemists, materials scientists, and engineers*. Wiley-VCH, 2017.
- [2] Donald A. Neamen. *Semiconductor Physics and Devices: Basic Principles*. McGraw-Hill, 2012.
- [3] Eleftherios N. Economou. *The Physics of Solids: Essentials and Beyond*. Springer, Berlin, Heidelberg, 1st edition, 2010.
- [4] Robert F. Pierret. *Advanced Semiconductor Fundamentals*. Modular Series on Solid State Devices, second edition, 2003.
- [5] S. F. Chichibu and S. Nakamura. *Introduction to Nitride Semiconductor Blue Lasers and Light Emitting Diodes*. CRC Press, 2000.
- [6] N. W. Ashcroft and N. D. Mermin. *Solid State Physics*. Holt-Saunders, 1976.
- [7] S.M. Sze and Kwok K. Ng. *Physics of Semiconductor Devices*, volume 10. John Wiley & Sons, Inc., Hoboken, NJ, USA, oct 2006.
- [8] E. F. Schubert. *Light-Emitting Diodes. Chapter 4: LED basics: electrical properties*, page 59–85. Cambridge University Press, 2nd edition, 2006.
- [9] Gerold W. Neudeck. *The PN Junction Diode*. Addison-Wesley, second edition, 1989.
- [10] E. F. Schubert. *Light-Emitting Diodes. Chapter 2: Radiative and non-radiative recombination*, pages 27–47. Cambridge University Press, 2nd edition, 2006.
- [11] Richard P. Green, Jonathan J D McKendry, David Massoubre, Erdan Gu, Martin D. Dawson, and A. E. Kelly. Modulation bandwidth studies of recombination processes in blue and green InGaN quantum well micro-light-emitting diodes. *Applied Physics Letters*, 102(9):1–5, 2013.
- [12] E. F. Schubert. *Light-Emitting Diodes. Chapter 5: LED basics: Optical properties*, pages 86–100. Cambridge University Press, 2nd edition, 2006.
- [13] Han Youl Ryu, Ki Seong Jeon, Jun Ho Sung, Min Woo Lee, Euna Lee, Hooyoung Song, Min Gu Kang, Yoonho Choi, and Jeong Soo Lee. Internal quantum efficiency of GaN-based light-emitting diodes grown on silicon substrates determined from rate equation analyses. *Current Applied Physics*, 13(8):1600–1603, 2013.
- [14] Sheng Hang, Chia-Ming Chuang, Yonghui Zhang, Chunshuang Chu, Kangkai Tian, Quan Zheng, Tingzhu Wu, Zhaojun Liu, Zi-Hui Zhang, Qing Li, and Hao-Chung Kuo. A review on the low external quantum efficiency and the remedies for GaN-based micro-LEDs. *Journal of Physics D: Applied Physics*, 54(15):153002, apr 2021.
- [15] Ricardo Ferreira. *Gallium nitride light-emitting diode enabled visible light communications*. PhD thesis, University of Strathclyde, Department of Physics, 2017.
- [16] Fox Mark. *Optical Properties of Solids.*, volume Second edition of *Condensed Matter Physics*. OUP Oxford, 2010.
- [17] E. F. Schubert. *Light-Emitting Diodes. Chapter 13: The AlGaInN material system and ultraviolet emitters*, page 222–238. Cambridge University Press, 2nd edition, 2006.

- 
- [18] Jaehee Cho, E. Fred Schubert, and Jong Kyu Kim. Efficiency droop in light-emitting diodes: Challenges and counter measures, may 2013.
- [19] C.-W. Jeon, H.W. Choi, Erdan Gu, and M.D. Dawson. High-Density Matrix-Addressable AlInGaN-Based 368-nm Microarray Light-Emitting Diodes. *IEEE Photonics Technology Letters*, 16(11):2421–2423, nov 2004.
- [20] Jonathan McKendry. *Micro-pixelated AlInGaN light-emitting diode arrays for optical communications and time-resolved fluorescence lifetime measurements*. PhD thesis, University of Strathclyde, Department of Physics, 2011.
- [21] Osram Opto Semiconductors. Green Laser Diode in TO38 ICut Package. Technical Report Version 1.1, February 2016.
- [22] E. F. Schubert. *Light-Emitting Diodes. Chapter 3: Theory of radiative recombination*, page 48–58. Cambridge University Press, 2nd edition, 2006.
- [23] Dmitry V. Morozov, Alessandro Casaburi, and Robert H. Hadfield. Superconducting photon detectors. *Contemporary Physics*, pages 1–23, mar 2022.
- [24] Hamamatsu Photonics K.K. Si photodiodes. Technical report, 05 2022.
- [25] S. O. Kasap. *Principles of Electronic Materials & Devices*. McGraw-Hill Education, fourth edition, 2018.
- [26] FEMTO Messtechnik GmbH. Ultra High Speed Photoreceiver with Si-PIN Photodiode. Technical report, FEMTO Messtechnik GmbH, Berlin, mar 2022.
- [27] P. Leon, F. Roland, L. Brignone, J. Opderbecke, J. Greer, M. A. Khalighi, T. Hamza, S. Bourenane, and M. Bigand. A new underwater optical modem based on highly sensitive silicon photomultipliers. In *OCEANS 2017 - Aberdeen*, pages 1–6, 2017.
- [28] Cristiano Niclass, Maximilian Sergio, and Edoardo Charbon. A Single Photon Avalanche Diode Array Fabricated in Deep-Submicron CMOS Technology. In *Proceedings of the Design Automation & Test in Europe Conference*, volume 1, pages 1–6. IEEE, 2006.
- [29] Jose F.C. Carreira. *Hybrid micro-LED devices enabled by elastomeric micro-transfer printing*. PhD thesis, University of Strathclyde, Department of Physics, 2020.
- [30] Semiconductor Components Industries. Introduction to the Silicon Photomultiplier (SiPM). Technical report, onsemi-sensL, July 2021.
- [31] Alexander D. Griffiths, Johannes Herrnsdorf, Robert K. Henderson, Michael J. Strain, and Martin D. Dawson. High-sensitivity inter-satellite optical communications using chip-scale led and single-photon detector hardware. *Opt. Express*, 29(7):10749–10768, Mar 2021.
- [32] Salvatore Gnecci, Neale A. W. Dutton, Luca Parmesan, Bruce R. Rae, Sara Pellegrini, Stuart J. McLeod, Lindsay A. Grant, and Robert K. Henderson. Digital silicon photomultipliers with or/xor pulse combining techniques. *IEEE Transactions on Electron Devices*, 63(3):1105–1110, 2016.
- [33] Alexander D. Griffiths. *Novel optical communications and imaging enabled by CMOS interfaced LED technology*. PhD thesis, University of Strathclyde, Department of Physics, 2018.

- 
- [34] John Kosman, Oscar Almer, Tarek Al Abbas, Neale Dutton, Richard Walker, Stefan Videv, Kevin Moore, Harald Haas, and Robert Henderson. 29.7 a 500mb/s -46.1dbm cmos spad receiver for laser diode visible-light communications. In *2019 IEEE International Solid- State Circuits Conference - (ISSCC)*, pages 468–470, 2019.
- [35] International Telecommunication Union. Forward error correction for high bit-rate DWDM submarine systems. *ITU, Geneva, Switzerland, Tech. Rep. ITU-T G.975.1*, Nov 2013.
- [36] P. Tian, Jonathan J.D. McKendry, J. Herrnsdorf, S. Zhu, Erdan Gu, Nicolas Laurand, and Martin D. Dawson. Chapter nine - micro-led based optical wireless communications systems. In *Micro LEDs*, volume 106 of *Semiconductors and Semimetals*, pages 281–321. Elsevier, 2021.
- [37] A. D. Griffiths, J. Herrnsdorf, J. J. D. McKendry, M. J. Strain, and M. D. Dawson. Gallium nitride micro-light-emitting diode structured light sources for multi-modal optical wireless communications systems. *Philosophical Transactions of the Royal Society A: Mathematical, Physical and Engineering Sciences*, 378(2169):20190185, apr 2020.
- [38] Z. Ghassemlooy, W. Popoola, and S. Rajbhandari. *Optical Wireless Communications: System and Channel Modelling with MATLAB*. CRC Press, 1st edition, 2013.
- [39] Jean Armstrong. OFDM for Optical Communications. *Journal of Lightwave Technology*, 27(3):189–204, 2009.
- [40] Enyuan Xie, Rui Bian, Xiangyu He, Mohamed Sufyan Islim, Cheng Chen, Jonathan J. D. McKendry, Erdan Gu, Harald Haas, and Martin D. Dawson. Over 10 Gbps VLC for Long-Distance Applications Using a GaN-Based Series-Biased Micro-LED Array. *IEEE Photonics Technology Letters*, 32(9):499–502, 2020.
- [41] Georgios N. Arvanitakis, Rui Bian, Jonathan J. D. McKendry, Chen Cheng, Enyuan Xie, Xiangyu He, Gang Yang, Mohamed S. Islim, Ardimas A. Purwita, Erdan Gu, Harald Haas, and Martin D. Dawson. Gb/s Underwater Wireless Optical Communications Using Series-Connected GaN Micro-LED Arrays. *IEEE Photonics Journal*, 12(2):1–10, 2020.
- [42] Yu-Fang Huang, Chen-Ting Tsai, Yu-Chieh Chi, Ding-Wei Huang, and Gong-Ru Lin. Filtered Multicarrier OFDM Encoding on Blue Laser Diode for 14.8-Gbps Seawater Transmission. *Journal of Lightwave Technology*, 36(9):1739–1745, 2018.

## Chapter 3

# Gb/s Underwater Wireless Optical Communications Using Series-Connected GaN Micro-LED Arrays

The work in this chapter was published in: G. N. Arvanitakis *et al.*, IEEE Photonics Journal, 12(2), 1-10, 2020 [1].

### 3.1 Introduction

As discussed in the introductory chapters, LED-based devices have attracted a great deal of attention in recent years for use as light-fidelity (Li-Fi) transmitters, where LED luminaires are used to provide both general-purpose lighting and Mb/s or Gb/s optical wireless links. LEDs have also been used as transmitters in underwater optical links. For instance, recent results by Zhou *et al.* demonstrated 15.17 Gb/s over 1.2 m of clear tap water using 5 LEDs of primary colours [2]. A single (green) LED operating at 521 nm was used by Wang *et al.* to show 2.175 Gb/s through 1.2 m of clear tap water [3]. In general, LEDs are relatively simple and cost-effective compared to laser-based sources. However, standard off-the-shelf LEDs have limited modulation bandwidth (typically  $\approx 20$  MHz) due to the large capacitance of standard large area LED dies, which limits the achievable data rates.

On the other hand, micro-sized LEDs (micro-LEDs) have much smaller dimensions ( $\leq 100 \mu\text{m}$ ), and therefore, their bandwidths are not limited by the device's capacitance. Micro-LEDs have been used quite extensively over free space for visible light applications

and to some extent recently in the UWOC domain. For example, Tian *et al.* reported 800 Mb/s over 0.6 m and 200 Mb/s over 5.4 m of clear tap water using a single micro-LED at 450 nm [4]. However, the small active area of a single micro-LED unavoidably results in a relatively low output power ( $< 5$  mW), which may be insufficient for practical UWOC due to light attenuation in the underwater environment.

To mitigate this, we here detail the deployment of series-connected micro-LED arrays operating at 450 nm for UWOC. These devices consist of 6 connected micro-LED pixels, each 60 or 80  $\mu\text{m}$  in diameter. The in-series connection configuration allows the device to achieve higher optical power than a single micro-LED pixel while retaining the characteristic high modulation bandwidth of the micro-LEDs as a result of the same high current density flowing through each. These devices thus offer the high output powers of a standard LED die but with the high modulation bandwidth of micro-LEDs. Of course, the drive voltage required for such a design increases according to the number of the series pixels. Strathclyde University's IoP recently first developed and used such a micro-LED array. Using OFDM, a GaN-based micro-LED array in series-biased format was used to demonstrate free space optical wireless data rates of 10.11 Gb/s over 5 m and 1.61 Gb/s over 20 m.

By applying OFDM for UWOC with such a device, this chapter reports data rates of up to 4.92 Gb/s, 3.22 Gb/s and 3.4 Gb/s over 1.5 m, 3 m and 4.5 m, respectively. In clear tap water, the corresponding bit error ratios (BERs) were  $1.5 \times 10^{-3}$ ,  $1.1 \times 10^{-3}$  and  $3.1 \times 10^{-3}$ . Furthermore, the performance of these optical links over varying turbidities was explored by adding Maalox antacid (scattering agent) to clear tap water. Mb/s data transmission was demonstrated over 5.33 ALs. These results show that these series-connected micro-LEDs' relatively high bandwidth and output power can be used to achieve high data rates and mitigate the effects of signal attenuation.

## 3.2 Device overview

### 3.2.1 Device design and fabrication

The micro-LEDs reported in this work were fabricated from commercial blue-emitting III-nitride LED wafers grown on a 2" c-plane sapphire substrate with a periodically patterned surface (PSS). The fabrication procedure has been described in previous works reported by the IoP group (e.g., in [5]) and is summarised as follows (Figure 3.1a). Inductively coupled plasma (ICP) etching was used to etch the micro-LED elements down to the *n*-type GaN layer and defined the disk-shaped micro-LEDs pixels. A second ICP etch step to the sapphire substrate enabled the electrical isolation of each micro-LED



element and the definition of individual  $140 \times 140 \mu\text{m}^2$  mesas, with a  $70 \mu\text{m}$  spacing between adjacent mesas to reduce potential photon absorption by neighbouring micro-LED elements (see Figure 3.1b). Also, a uniform current spreading is thus guaranteed as each micro-LED element is at the centre of its corresponding GaN mesa. Subsequently, an ohmic contact on the  $p$ -GaN was formed by a  $100 \text{ nm}$  Pd metal layer through evaporation and further annealing at  $300^\circ\text{C}$  in an  $\text{N}_2$  environment. The  $n$ -GaN metallisation was achieved by the deposition of Ti/Au ( $50 \text{ nm}/200 \text{ nm}$ ) bilayer. The pixels' insulation concludes the fabrication process via a  $300 \text{ nm}$   $\text{SiO}_2$  layer and the metal interconnection for the series-connection configuration via another Ti/Au metal bilayer.

A schematic cross-section of two adjacent micro-LED pixels of the array is shown in Figure 3.1a. The epitaxial structure of the micro-LEDs comprised a) an undoped GaN buffer layer of  $3.4 \mu\text{m}$  in thickness, b) a  $2.6 \mu\text{m}$  thick  $n$ -type GaN layer, c) an  $84.3 \text{ nm}$  active layer which comprised eleven periods of InGaN ( $2.8 \text{ nm}$ ) and GaN ( $13.5 \text{ nm}$ ) quantum wells emitting at  $450 \text{ nm}$ , d) a  $30 \text{ nm}$  thick AlGaIn cladding layer, and e) an  $160 \text{ nm}$  thick  $p$ -type GaN layer. As shown in Figure 3.1a, metal tracks connecting one pixel's cathode to a neighbouring pixel's anode were used to create the series connection.

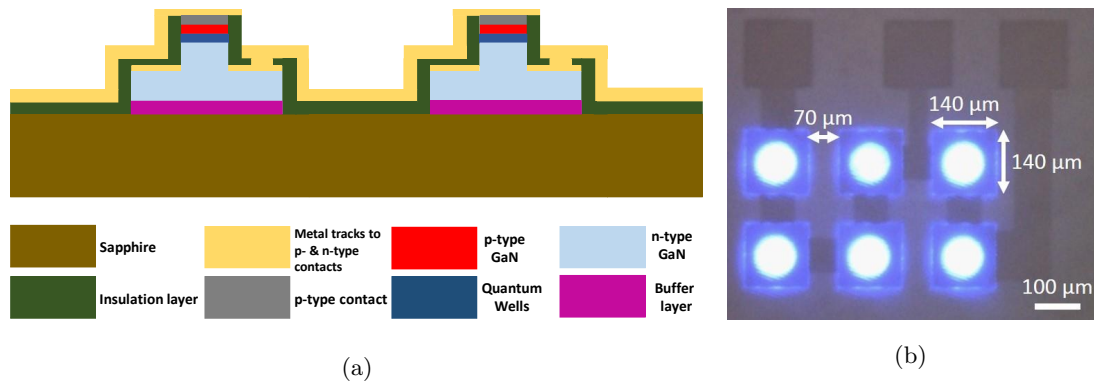


FIGURE 3.1: **(a)** Schematic cross-section of two adjacent micro-LED pixels of the series-connected micro-LED array. **(b)** Planview optical image of six pixels from the micro-LED array at a DC bias of  $1 \text{ mA}$ .

Each micro-LED shown here is of  $60 \mu\text{m}$  or  $80 \mu\text{m}$  in diameter (for two different devices) while the operational wavelength is  $\approx 450 \text{ nm}$  for all the devices. Figure 3.1b shows that each device consists of 6 micro-LED pixels arranged in a  $3 \times 2$  array. All 6 pixels were simultaneously biased in series to maximise the output optical power.

### 3.2.2 Device characterisation

#### Modulation bandwidth and frequency response measurements

An LED's modulation bandwidth (BW) measures how fast the LED responds to an input signal that varies with time. The modulation BW is valuable in optical communications

applications as it is proportional to the maximum data rate at which a modulated device can be operated (recall the Shannon-Hartley theorem, Section 1.3). The modulation BW can be defined as the frequency at which the detected electrical power ( $P_{elec}$ ) is reduced to 50% (-3 dB) of its maximum value and can be recorded by finding the point on the frequency response curve where the response has fallen by -3 dB.  $f_{3dB}$  is also known as the *electrical-to-electrical* BW (E-E BW), and mathematically is given by the following expression [6]:

$$f_{3dB} = \frac{\sqrt{3}}{2\pi\tau}, \quad (3.1)$$

where  $\tau = RC$  is the resistance  $\times$  capacitance time constant of the LED element or the carrier lifetime. Micro-LEDs have a small RC constant due to their small area (C is proportional to area). This behaviour has been reported in detail in, e.g., [7]. Therefore, as discussed below, the carrier lifetime limits the BW of a micro-LED. In this thesis, the BWs of all the micro-LED-based devices were measured using the experimental setup shown in Figure 3.2.

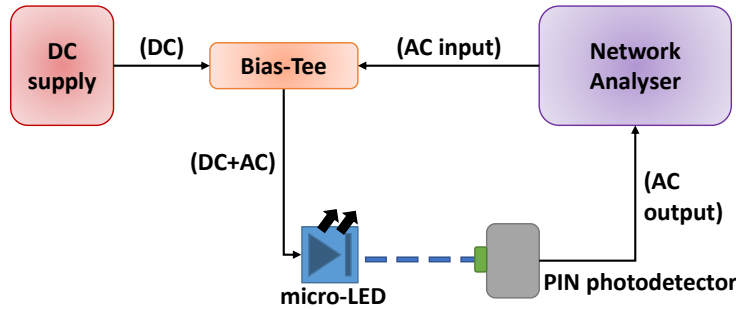


FIGURE 3.2: Schematic of the micro-LED frequency response measurements setup.

In Figure 3.2, the micro-LED pixels were driven by an electrical signal comprising both a DC and an AC component. The DC component was provided by a DC supply (Yokogawa, GS610) and the AC by a network analyser (HP8753ES). The optical output of the micro-LEDs was collected via a fast PiN photodetector (Femto, HAS-X-S-1G4-SI) of 1.4 GHz BW\*. The photodetector output was returned to the input of the network analyser, which displayed the received  $P_{elec}$  at the photodetector as a function of frequency. When light is incident on the PiN photodetector, the photocurrent,  $I$ , that the PiN generates is proportional to the incident optical power ( $P_{opt} \propto I$ ) as, ideally, each photon generates a single charge carrier. The *electrical-to-optical* BW (E-O BW)

\*It is important to note that the BW of the receiver and all other components (e.g., cables, bias tee) are much higher than that of the LED. This means that their response should be “flat” across the measured frequency response, so what is measured is the response of the LED and not a convolution of the LED’s response, plus the receiver’s response, plus the cable’s response, etc.

is defined as the frequency at which the optical power received by the PiN has dropped by half. By taking into account that  $P_{elec} = VI = I^2R$ , it is seen that when  $P_{opt}$  is reduced by half,  $P_{elec}$ , is reduced to a quarter due to the  $I^2$  term. As such, -6 dB on the  $P_{elec}$  curve displayed by the network analyser corresponds to the -3 dB of the  $P_{opt}$  value [8]. It is also worth noting that the power drop (or loss,  $L_P$ ) in dB is given by:

$$L_P = 10 \log_{10} \left( \frac{P}{P_0} \right), \quad (3.2)$$

where  $P$  is the measured power and  $P_0$  is the reference (starting) power.

An example of such a frequency response measurement is shown in Figure 3.3 where was measured the E-O BW (or -6 dB) of LEDs of different pixel sizes (40  $\mu\text{m}$ , 150  $\mu\text{m}$ , and 500  $\mu\text{m}$ ) [9]. The points at which the grey -6 dB line meets the respective devices' frequency response denote their E-O modulation BW. Figure 3.3 also shows a dependency between the pixel size of the LEDs and the BW; that is, the BW increases as the pixel size decreases.

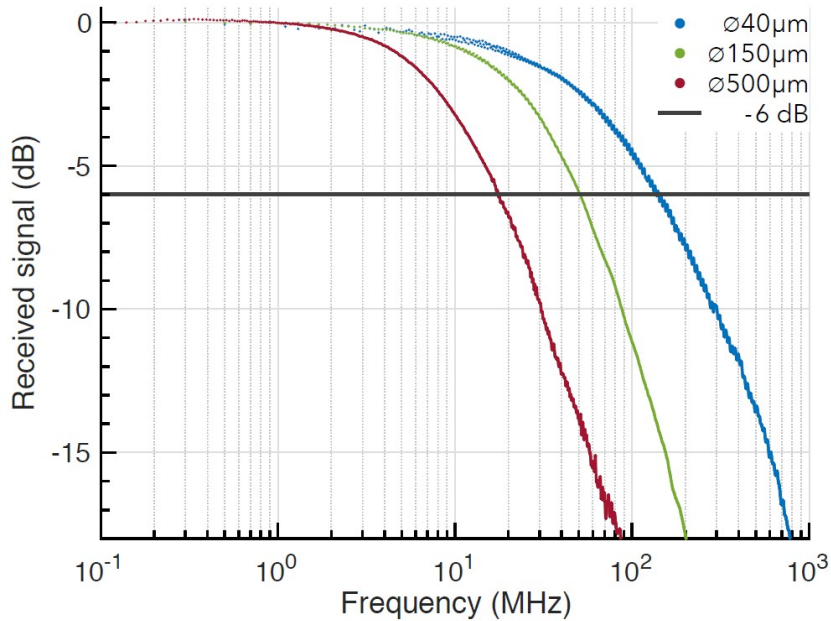


FIGURE 3.3: Frequency response measurements and -6 dB (E-O) BW of LEDs operating at 450 nm of different pixel diameters. Figure taken from [9].

When an alternating applied electrical signal modulates an LED, the time it takes for the device to reach a steady state is mainly governed by its capacitance and carrier recombination time (or differential carrier lifetime). Conventional, broad area LEDs of pixel size larger than, e.g. 200  $\mu\text{m}$ , and primarily used for lighting applications, can be modulated up to tens of MHz [10] as their switching speeds are mainly limited by their

RC time constant [11]. On the other hand, previous works from the IoP group have reported that micro-LEDs (of typical pixel size smaller than  $100 \mu\text{m}$ ) can be driven at higher injected current densities than conventional LEDs. The increased carrier concentration results in faster radiative recombinations within the micro-LED's active region, leading to smaller area micro-LEDs exhibiting large modulation BW [7], approaching values close to 1 GHz [12]. The latter can be mathematically estimated by examining Equation 3.1, where a decrease in  $\tau$  results in an increase of  $f_{3dB}$  and a more precise mathematical relation, the *ABC* model, has been proposed to describe the relationship between the carrier lifetimes and carrier density ( $N$ ) [11, 13]:

$$\tau(N) = \frac{1}{A + 2BN + 3CN^2}. \quad (3.3)$$

Here,  $A$  and  $B$  are the Shockley-Read-Hall (SRH) non-radiative recombination and radiative recombination coefficients, respectively, whilst the  $C$  parameter is a non-radiative recombination coefficient usually associated with Auger recombination. From Equation 3.3, it is clear that the carrier lifetime decreases by increasing  $N$  (by injecting higher current).

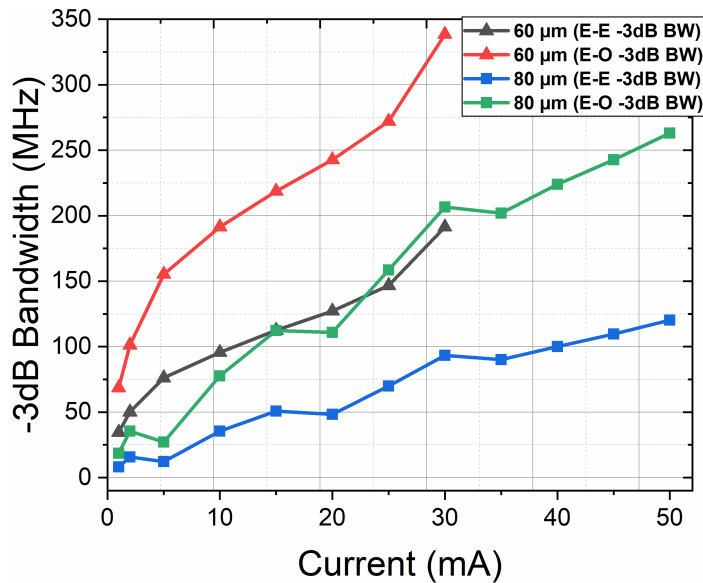


FIGURE 3.4: -3 dB bandwidth plots for the in-series connected  $60 \mu\text{m}$  and  $80 \mu\text{m}$  micro-LEDs.

The BW values (-3 dB E-E and E-O) of the in-series connected micro-LEDs of this chapter, of  $60 \mu\text{m}$  and  $80 \mu\text{m}$  pixels diameter, are shown in Figure 3.4. As previously described, the BWs were measured by applying a DC bias and an AC signal generated by a network analyser to modulate the micro-LED arrays at different current points. The optical response of the devices was collected via a 1.4 GHz PiN photodetector. Figure

3.4 shows that the maximum E-O bandwidth for the 60  $\mu\text{m}$  in diameter series-connected micro-LED array is 338.5 MHz at 30 mA, whilst for the 80  $\mu\text{m}$  device, it is 263 MHz at 50 mA. These results agree with previous works (e.g., in [7]), where it was demonstrated that as the pixel diameter of a micro-LED element decreases, the corresponding E-O bandwidth increases.

### Electrical and optical characterisation

Figure 3.5 shows the current versus voltage (I-V) and the output optical power versus current (L-I) for the in series-connected devices with, respectively, 60  $\mu\text{m}$  or 80  $\mu\text{m}$  pixels. It should be noted that the optical power is the forward detected power. It was measured by placing the micro-LEDs close to a calibrated Si photodiode (Thorlabs, S121C) connected to a power meter (Thorlabs, PM100D). This measurement calibrates the “useful” optical power that can be directed into a beam for applications and is not the full extracted power that would be measured in an integrating sphere. The turn-on voltage ( $V_F$ ) for each device can be calculated by performing a linear fit in the “linear” part of the IV curves, as shown in Figure 3.5, and seeing the intersection of the fitting curve with the y-axis. As such, the  $V_F$  at 1 mA for the 60  $\mu\text{m}$  in diameter device is 21.7 V, corresponding to about 3.6 V for each micro-LED element, whereas for the 80  $\mu\text{m}$  device, the  $V_F$  is 20 V corresponding to approximately 3.3 V for each micro-LED pixel. Additionally, both devices can be operated at a current beyond 50 mA and demonstrate an optical power before thermal rollover of over 21 mW and 15 mW for the 80  $\mu\text{m}$  and 60  $\mu\text{m}$  device, respectively.

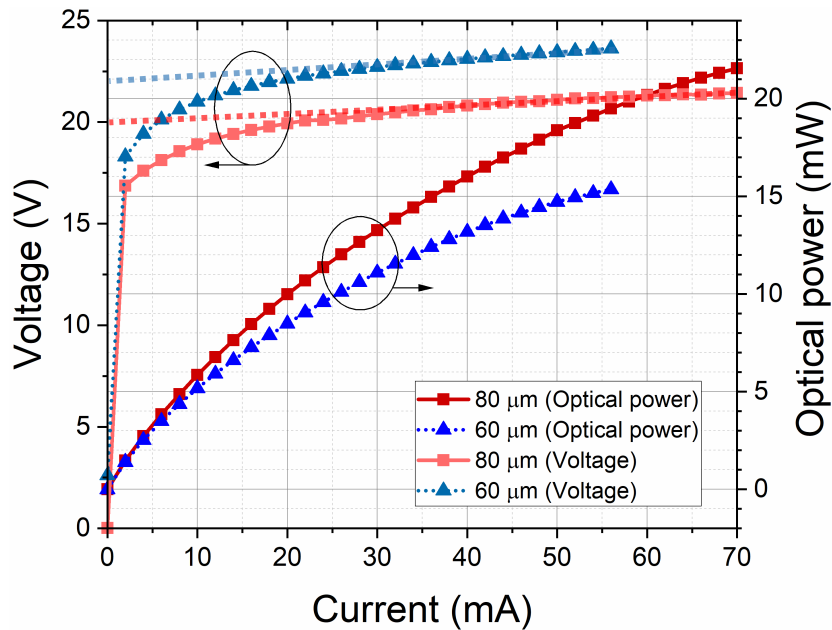


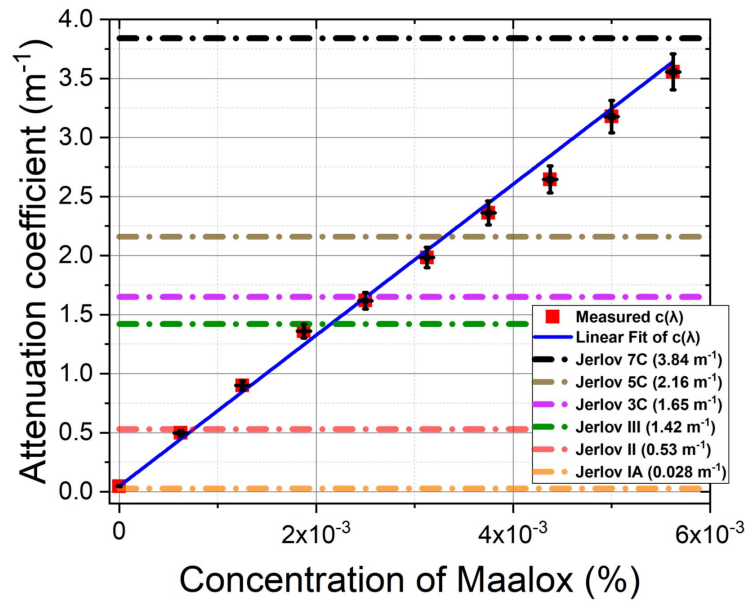
FIGURE 3.5: I-V and L-I plots for the two respective devices comprising six 60  $\mu\text{m}$  and 80  $\mu\text{m}$  micro-LEDs connected in-series. The  $V_F$  of both arrays (60  $\mu\text{m}$ : 21.7 V, 80  $\mu\text{m}$ : 20 V) are shown at the intersection of the dashed lines and the voltage axis.

### 3.3 Water sample characterisation

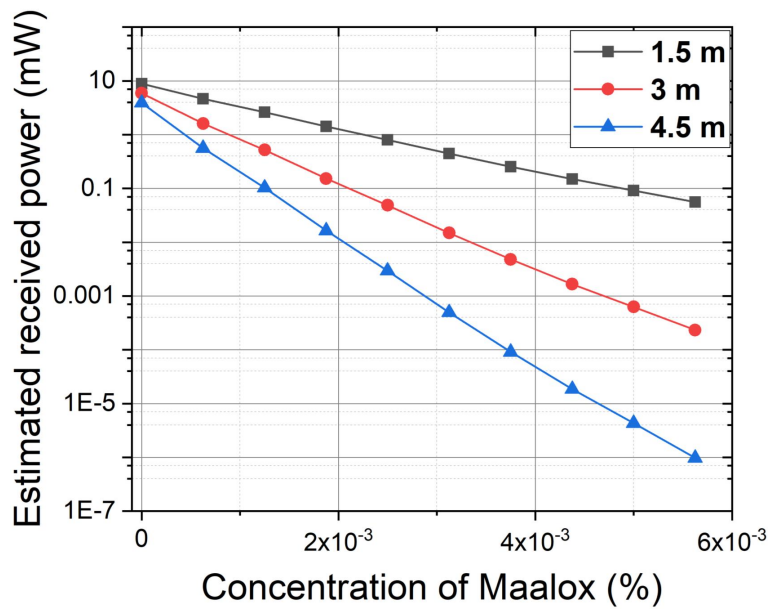
A detailed description of the underwater channel's characterisation can be found in Section 1.6. In summary, the variation of the underwater attenuation was controlled by adding Maalox antacid to 160 l of tap water in a water tank (dimensions  $1.5 \times 0.35 \times 0.35$  m<sup>3</sup>), following a method commonly reported in previous references [14].

A blue LD (OSRAM, PL450B) operating at the same nominal central wavelength as the micro-LEDs (450 nm) was employed for the estimation of the water sample's attenuation coefficient ( $c(\lambda)$  with units of m<sup>-1</sup>) at each Maalox concentration. Nine different concentrations of the scattering agent were examined, ranging from 0.0006% (1 ml of Maalox in 160 l of tap water) to 0.0056% (9 ml of Maalox). A laser was chosen for these measurements as the divergence of the micro-LED emission would make an accurate estimation of  $c(\lambda)$  difficult. A plastic aspheric lens (Thorlabs, CAY033) was placed in front of the laser diode to collimate the beam, which was subsequently focused onto a power meter sensor (Thorlabs, 121C) at the other side of the tank. At each concentration, the received optical power,  $P_R$ , was measured over the optical path,  $z$  (equal to 1.5 m). Using these values for  $P_R$  along with the Beer's law equation [15],  $P_R(z) = P_T(z)e^{-c(\lambda)z}$ , and the measured transmitted power of  $P_T$ , the corresponding attenuation coefficients for each water sample were calculated and are shown in Figure 3.6a. It can be seen that the minimum measured attenuation coefficient, which corresponds to clear tap water (no scattering agent added), is  $0.05 \text{ m}^{-1}$ , a value relatively close to that of *Jerlov IA* open ocean water type which is  $0.028 \text{ m}^{-1}$  [16]. For the samples with added Maalox, the maximum measured attenuation coefficient was  $3.56 \text{ m}^{-1}$  for 0.0056% (9 ml) of Maalox and is close to the *Jerlov 7C* coastal ocean type where  $c(450)=3.84 \text{ m}^{-1}$  [16].

Figure 3.6b illustrates the estimated received power for the  $80 \mu\text{m}$  in diameter series-connected micro-LED array for each concentration of the scattering agent at 1.5 m, 3 m and 4.5 m. The estimated received power,  $P_R$ , was calculated through Beer's law equation and by taking into account that the estimated transmitted power,  $P_T$ , was 13.27 mW at 30 mA, based on the L-I measurements in Figure 3.5.



(a)



(b)

FIGURE 3.6: (a) The calculated attenuation coefficients versus the content of the scattering agent (Maalox) using a blue LD operating at 450 nm. For comparison, the typical values of six *Jerlov* ocean types are given as defined by [16]. (b) The estimated received power over 1.5 m, 3 m and 4.5 m versus the Maalox concentration for the 80  $\mu$ m micro-LED array, using the optical power data showing in Figure 3.5.

### 3.4 Data transmission experimental set-up

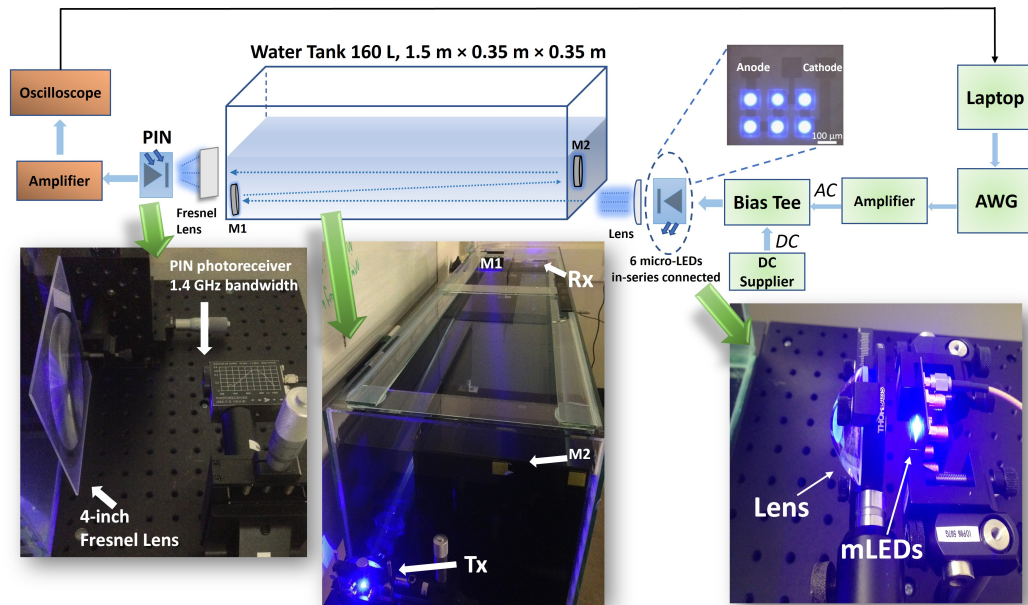


FIGURE 3.7: **Top:** Illustration of the experimental set-up used for the UWOC measurements of this work. Two mirrors (M1 and M2) were placed appropriately to increase the optical link from 1.5 m to 3 m and 4.5 m. **Bottom:** Photographs from the receiver end (Fresnel lens and PiN photodetector), the water tank filled with 160 l of tap water, and the transmitter side (micro-LED array and condenser lens).

Figure 3.7 depicts the set-up used for this work. The digital data signal to be transmitted was generated and processed in MATLAB<sup>®</sup>. Afterwards, this optimised signal was converted to an analog one through an arbitrary waveform generator (AWG, Agilent, 81180A) and amplified (SHF Communication Technologies AG S126A). The AC signal from the AWG was combined with a DC of 30 mA via a DC supply (Yokogawa, GS610) through a bias tee (Tektronix, PSPL5575A) to drive the micro-LED arrays. A condenser lens (Thorlabs, ACL50832U-A) was used to collimate the beam to be optically transmitted through the 1.5 m length water tank and over 160 l of tap water. For the longer range data transmissions, two 100 mm diameter mirrors (M1 and M2 in Figure 3.7) were mounted in the tank to increase the optical path up to 3 m and 4.5 m by retro-reflecting the primary beam to make one or two additional passes through the length of the tank. At the receiver end, a 4-inch diameter Fresnel lens (Edmund Optics, #46-614) was used to focus the collimated beam onto the PiN photodetector of 1.4 GHz BW. The received signal was processed through an amplifier (Mini-Circuits, ZHL-6A-S+) and captured through an oscilloscope of 1 GHz BW and a maximum sample rate of 4 GSa/s (Agilent, MSO 7104B). The received signal was processed and demodulated offline in MATLAB<sup>®</sup>. At this stage, the transmitted and received data are compared to identify any incorrectly



transmitted bits, allowing the BER to be calculated. It should be noted that OFDM is robust against multi-path effects experienced in underwater environments.

### 3.5 Communication performance results

In conjunction with the communication capabilities of GaN micro-LEDs, OFDM has been extensively investigated by the IoP group. Following a similar methodology as for our previous works, e.g. in [12, 17], an adaptive bit and energy loading scheme was used to allow different Quadrature Amplitude Modulation (QAM) levels to be loaded onto the OFDM subcarriers based on the measured SNR of each carrier. The higher the carrier SNR, the higher the QAM level that could be used; thus, more bits could be loaded onto that channel. This is illustrated in Figure 3.8 where an example of the measured SNR and the corresponding number of transmitted bits per OFDM carrier frequency is shown for a transmission measurement using a 60  $\mu\text{m}$  in diameter series-connected micro-LED device over 1.5 m of clear tap water.

Figure 3.9 shows the measured BER against various transmission data rates using the 60  $\mu\text{m}$  in diameter series-connected micro-LEDs as a transmitter through 1.5 m of clear water. The orange dashed line indicates the BER target of  $3.8 \times 10^{-3}$  [18], below which “error-free” data transmission can be achieved using Forward Error Correction (FEC) with a 7% overhead of the gross data rate. The maximum achieved data rate that met this criterion was 4.92 Gb/s, corresponding to a net data rate of 4.58 Gb/s after FEC, though it should be pointed out that FEC was not actually used in this work.

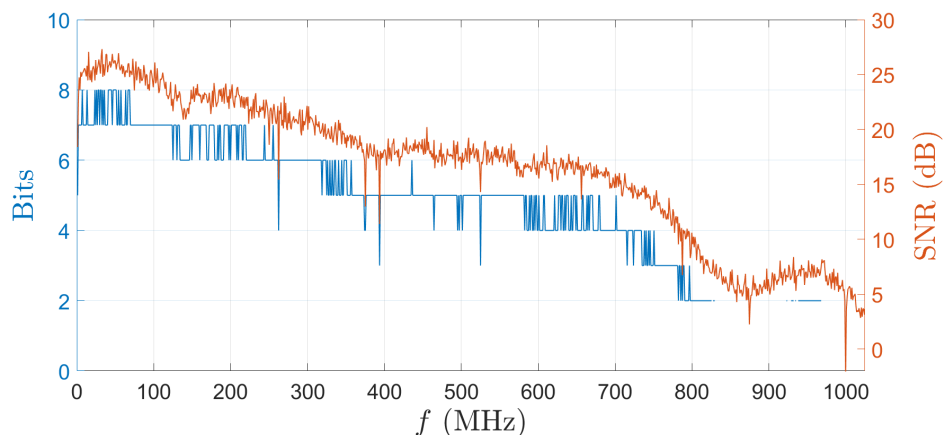


FIGURE 3.8: Measured SNR (orange) and corresponding bit loading (blue) versus OFDM carrier frequency, obtained using a 60  $\mu\text{m}$  in diameter series-connected micro-LED device over 1.5 m of clear tap water.

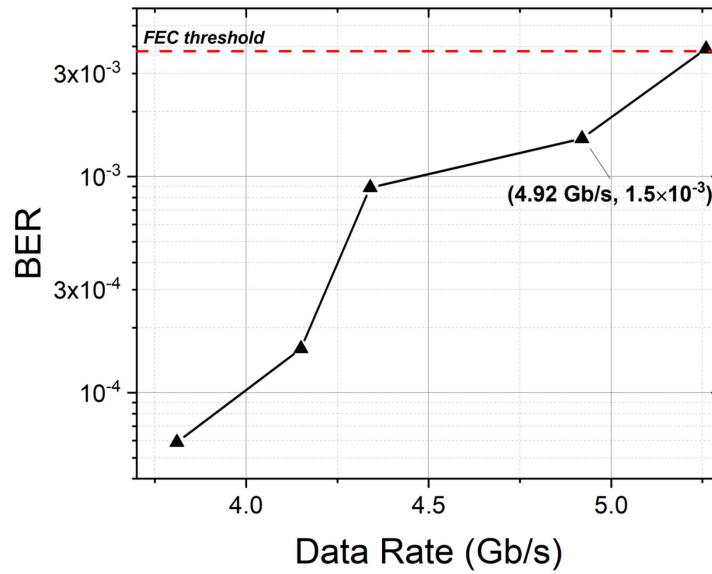
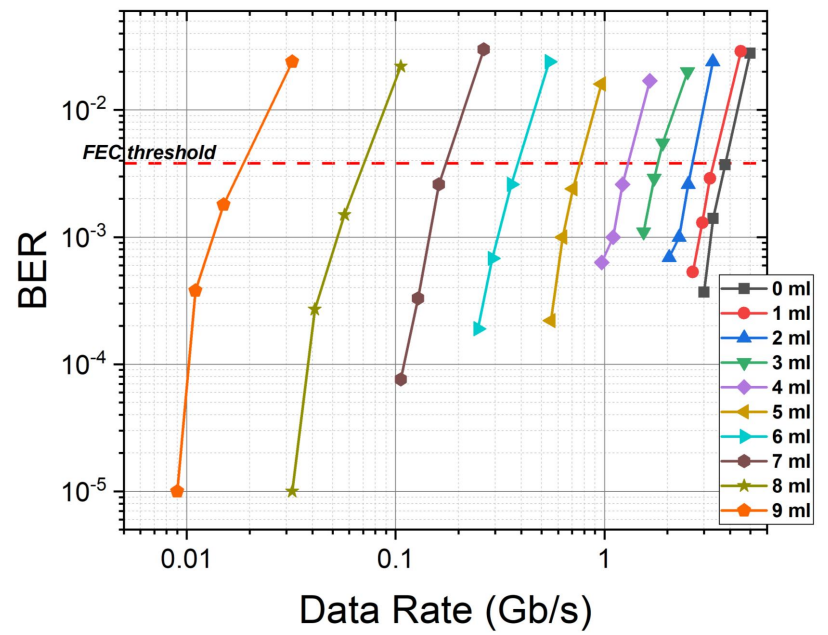


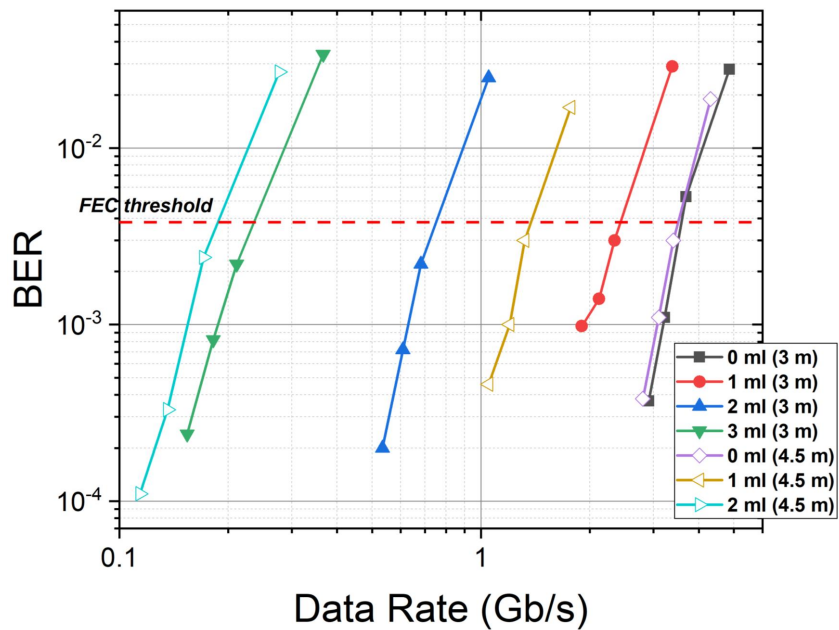
FIGURE 3.9: BER versus data rate for the 60  $\mu\text{m}$  in diameter series-connected micro-LED device. Transmission is over 1.5 m of clear tap water ( $c(450)=0.05 \text{ m}^{-1}$ ).

Figure 3.10a shows the BER versus data rates for the 80  $\mu\text{m}$  in diameter series-connected micro-LED device through different water turbidities over 1.5 m. The maximum data rate through clear tap water is 3.78 Gb/s at a BER of  $3.7 \times 10^{-3}$ , and it can be shown that the increase in water turbidity leads to attenuated transmission power levels collected by the detector and causes a lower overall SNR level. With a lower SNR level, fewer bits are loaded on each subcarrier, and the achievable data rate decreases. In extreme water turbidities ( $c(450)=3.56 \text{ m}^{-1}$ ) a data rate up to 15 Mb/s was demonstrated over 5.33 ALs.

Figure 3.10b presents the BER versus data rate for the same device at 3 m and 4.5 m through different concentrations of Maalox. At 3 m, the maximum data rate through clear tap water is 3.22 Gb/s with a BER of  $1.1 \times 10^{-3}$  while at 4.5 m, a larger BER of  $3.1 \times 10^{-3}$  is indicated for 3.4 Gb/s (corresponding  $c(450)=0.05 \text{ m}^{-1}$  for both ranges). As the Maalox concentration increases, the maximum data rate drops to 211 Mb/s at 3 m over 4.08 ALs with a BER of  $2.3 \times 10^{-3}$  (corresponding  $c(450)=1.36 \text{ m}^{-1}$ ) and 171 Mb/s at 4.5 m over 4.05 ALs with a BER of  $2.5 \times 10^{-3}$  (corresponding  $c(450)=0.90 \text{ m}^{-1}$ ).



(a)



(b)

FIGURE 3.10: (a) BER vs data rate for the  $80 \mu\text{m}$  in diameter series-connected micro-LED device through different water turbidities over 1.5 m. (b) BER vs data rate for the same device through different water turbidities over 3 m and 4.5 m. Note that the maximum error-free data rates were obtained at slightly different BERs.

The drop in data rate at all ranges can be explained by taking into account the Shannon-Hartley theorem,

$$D = B \log_2(1 + S/N), \quad (3.4)$$

where  $D$  is the maximum data transmission rate in bits/sec,  $B$  is the channel bandwidth in Hz,  $S$  is the average signal power over the entire bandwidth in Watts, and  $S/N$  is the SNR. The degradation of the received SNR and the received optical power due to increased attenuation result in a decrease in the achievable data rates.

Figure 3.11 shows the error-free maximum data rates versus the number of ALs for all transmission distances. It can be observed that the maximum data rate decreases with an increase in the number of ALs, for all path lengths. This can be understood as increased signal attenuation results in a lower SNR. It can also be seen that similar data rates are obtained when the number of ALs is similar. However, the curves do not overlap exactly because each maximum data rate was obtained at a slightly different BER, as shown in Figures 3.10a and 3.10b.

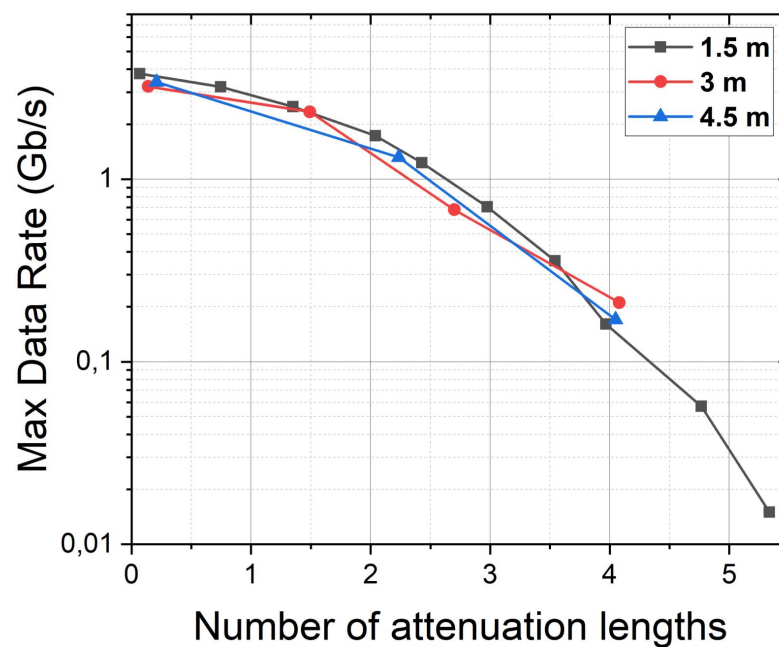


FIGURE 3.11: The maximum data rates versus the number of attenuation lengths for all ranges examined in this work (1.5 m, 3 m, 4.5 m).

These results indicate that the relatively high power and bandwidth from series-connected micro-LEDs can enable UWOC at Mb/s and Gb/s, even through turbid water samples. Further improvements to the achievable data rates and link lengths could be obtained by, for instance, increasing the transmitted power by adding additional LEDs, narrowing the optical beam profile, or applying multiplexing techniques such as wavelength division multiplexing (WDM), which was implemented for the work of the next chapter.

### 3.6 Summary

In this chapter, the high output power and modulation bandwidth of micro-LED arrays, consisting respectively of 6 series-connected pixels of diameter 60  $\mu\text{m}$  or 80  $\mu\text{m}$ , enabled Gb/s underwater optical wireless data transmissions using OFDM as modulation scheme over three underwater distances of 1.5 m, 3 m and 4.5 m. A BER of  $1.5 \times 10^{-3}$  was achieved for a maximum data rate of 4.92 Gb/s through 1.5 m of clear tap water whose attenuation coefficient was  $c(450) = 0.05 \text{ m}^{-1}$ . Further underwater wireless optical transmissions were performed through different water turbidities: 2.34 Gb/s were demonstrated for an attenuation coefficient of  $0.5 \text{ m}^{-1}$  which is close to *Jerlov* II open ocean type ( $0.53 \text{ m}^{-1}$ ) over 3 m, whereas 1.32 Gb/s were shown over 4.5 m. With an attenuation coefficient of  $3.56 \text{ m}^{-1}$  and over 5.33 ALs, a data rate of 15 Mb/s was achieved through 1.5 m. Our approach is compatible with the multi-wavelength operation of WDM, and the realisation of this concept is presented in Chapter 4.

The results of this work show the potential implementation of series-connected micro-LEDs to enable high-speed underwater wireless communications through various water turbidities.

## References

- [1] G. N. Arvanitakis, R. Bian, J. J. D. McKendry, C. Cheng, E. Xie, X. He, G. Yang, M. S. Islam, A. A. Purwita, E. Gu, H. Haas, and M. D. Dawson. Gb/s underwater wireless optical communications using series-connected gan micro-led arrays. *IEEE Photonics Journal*, 12(2):1–10, 2020.
- [2] Yingjun Zhou, Xin Zhu, Fangchen Hu, Jianyang Shi, Fumin Wang, Peng Zou, Junlin Liu, Fengyi Jiang, and Nan Chi. Common-anode LED on Si substrate for beyond 15 Gbit/s underwater visible light communication. *Photonics Research*, 7(9), 2019.
- [3] Fumin Wang, Yuanfan Liu, Fengyi Jiang, and Nan Chi. High speed underwater visible light communication system based on LED employing maximum ratio combination with multi-PIN reception. *Optics Communications*, 425(December 2017):106–112, 2018.
- [4] Pengfei Tian, Xiaoyan Liu, Suyu Yi, Yuxin Huang, Shuailong Zhang, Xiaolin Zhou, Laigui Hu, Lirong Zheng, and Ran Liu. High-speed underwater optical wireless communication using a blue GaN-based micro-LED. *Optics Express*, 25(2):1193, 2017.
- [5] Enyuan Xie, Xiangyu He, Mohamed Sufyan Islam, Ardimas Andi Purwita, Jonathan J.D. McKendry, Erdan Gu, Harald Haas, and Martin D. Dawson. High-Speed Visible Light Communication Based on a III-Nitride Series-Biased Micro-LED Array. *Journal of Lightwave Technology*, 37(4):1180–1186, 2019.
- [6] E. Fred Schubert. *Light-Emitting Diodes. Chapter 24: LED modulation characteristics*, page 393–403. Cambridge University Press, 2nd edition, 2006.
- [7] Jonathan J.D. McKendry, David Massoubre, Shuailong Zhang, Bruce R. Rae, Richard P. Green, Erdan Gu, Robert K. Henderson, A. E. Kelly, and Martin D. Dawson. Visible-light communications using a CMOS-controlled micro-light-emitting-diode array. *Journal of Lightwave Technology*, 30(1):61–67, 2012.
- [8] Ques10.com. Optical bandwidth and electrical bandwidth. <http://www.ques10.com/p/5363/short-note-optical-bandwidth-and-electrical-band-2/#>.
- [9] Ricardo Ferreira. *Gallium nitride light-emitting diode enabled visible light communications*. PhD thesis, University of Strathclyde, Department of Physics, 2017.
- [10] D. Karunatilaka, F. Zafar, V. Kalavally, and R. Parthiban. Led based indoor visible light communications: State of the art. *IEEE Communications Surveys Tutorials*, 17(3):1649–1678, 2015.
- [11] Sujan Rajbhandari, Jonathan J.D. McKendry, Johannes Herrnsdorf, Hyunchoe Chun, Grahame Faulkner, Harald Haas, Ian M. Watson, Dominic O’Brien, and Martin D. Dawson. A review of gallium nitride LEDs for multi-gigabit-per-second visible light data communications. *Semiconductor Science and Technology*, 32(2), 2017.
- [12] Ricardo X G Ferreira, Enyuan Xie, Jonathan J D McKendry, Sujan Rajbhandari, Hyunchoe Chun, Grahame Faulkner, Scott Watson, Anthony E. Kelly, Erdan Gu, Richard V. Penty, Ian H. White, Dominic C. O’Brien, and Martin D. Dawson. High Bandwidth GaN-Based Micro-LEDs for Multi-Gb/s Visible Light Communications. *IEEE Photonics Technology Letters*, 28(19):2023–2026, 2016.
- [13] Richard P. Green, Jonathan J D McKendry, David Massoubre, Erdan Gu, Martin D. Dawson, and A. E. Kelly. Modulation bandwidth studies of recombination processes in blue and green InGaN quantum well micro-light-emitting diodes. *Applied Physics Letters*, 102(9):1–5, 2013.

- 
- [14] Brandon Cochenour, Linda Mullen, and John Muth. Effect of scattering albedo on attenuation and polarization of light underwater. *Optics Letters*, 35(12):2088–2090, 2010.
  - [15] William Cox and John Muth. Simulating channel losses in an underwater optical communication system. *Journal of the Optical Society of America A*, 31(5):920, 2014.
  - [16] Michael G. Solonenko and Curtis D. Mobley. Inherent optical properties of Jerlov water types. *Applied Optics*, 54(17):5392, 2015.
  - [17] Dobroslav Tsonev, Hyunchae Chun, Sujan Rajbhandari, Jonathan J D McKendry, Stefan Videv, Erdan Gu, Mohsin Haji, Scott Watson, Anthony E. Kelly, Grahame Faulkner, Martin D. Dawson, Harald Haas, and Dominic O’Brien. A 3-Gb/s single-LED OFDM-based wireless VLC link using a gallium nitride micro-LED. *IEEE Photonics Technology Letters*, 26(7):637–640, 2014.
  - [18] International Telecommunication Union. Forward error correction for high bit-rate DWDM submarine systems. *ITU, Geneva, Switzerland, Tech. Rep. ITU-T G.975.1*, Nov 2013.

## Chapter 4

# Underwater Wireless Optical Communications Using Integrated Dual-Colour Micro-LEDs

### 4.1 Introduction

This chapter presents the development of integrated dual-colour micro-LED arrays for UWOC applications over various *Jerlov* water types [1]. The micro-LED arrays comprised a GaN-violet or green micro-LED grown on a sapphire substrate (the “host” substrate) and a GaN-blue micro-LED grown on a silicon (Si) substrate, which was deposited onto the “host” array via a transfer-printing (TP) method. The arrays were designed in two different layouts: individually addressable for blue-violet/blue-green and in-series connected for blue-green micro-LED arrays. The individually addressable device achieved an aggregated data rate when driven via an FPGA of 100 Mb/s over 8.52 ALs in a 1.5 m long water tank. Higher-speed UWOC of 200 Mb/s (aggregated) over 5.85 ALs were demonstrated from the same device, using an arbitrary waveform generator (AWG) that replaced the FPGA. The same TP micro-LED arrays were used in previous work over free space by Carreira *et al.* [2]. Demonstrating WDM VLC, an aggregate error-free data rate of 3.35 Gb/s was reported for the violet-blue micro-LED array and 1.79 Gb/s for the blue-green device. In this chapter, underwater WDM is reported, and multiple colours were used to increase the aggregate data rate.

The term SWaP (Size, Weight and Power) or SMaP (Size, Mass and Power) is commonly used when discussing portable devices. For instance, in previous works from



the IoP, micro-LED arrays and high-sensitivity receivers have been proposed for optical communications between CubeSats [3, 4]. Low-SWaP components would benefit UWOC in remotely-operated and autonomous underwater vehicles (ROVs and AUVs) due to their limited payload/battery power. Therefore, the concept of the two on-chip dual-colour micro-LED arrays presented here would be applicable in real-world scenarios. For instance, in an ROV they could be used for underwater data acquisition, data transmission and/or reception from/to other unmanned underwater vehicles (UUVs), divers and surface vessels.

As shown earlier (Section 1.4), the attenuation of light underwater is wavelength dependent. Moreover, it has been reported that as the water becomes more turbid due to the presence of a large number of scattering particles, its lowest overall attenuation point shifts towards longer wavelengths (from blue-green for *Jerlov* oceanic types I-III, to yellow-red for *Jerlov* coastal types 1-9) [5, 6]. Thus, the operation of a wavelength adaptive device, which would enable choice of the optimum data transmission wavelength depending on the water type, would be highly practical. Ito *et al.* [7] reported the employment of red, green, and blue (RGB) off-the-shelf LEDs and investigated their wavelength-dependent communication performance at 100 kb/s over turbid waters in a 1 m long water tank. However, the TP method used in this work allowed the development of transmitters of different colours on the same chip to demonstrate high-speed WDM in turbid underwater environments. The reliable communication performance of the TP micro-LEDs showed that our proposed system could be implemented in a low-SWaP device at a low cost.

## 4.2 Device overview

### 4.2.1 Individually-addressable blue-violet and blue-green micro-LED arrays

#### Violet and green micro-LEDs based on GaN-on-sapphire epitaxy

Micro-LEDs, in a flip-chip configuration, at violet (400 nm) and green (512 nm) wavelengths were fabricated from commercial InGaN epistuctures grown on a c-plane patterned sapphire substrate (PSS). Schematic illustrations of the epitaxial structures for both micro-LEDs can be seen in Figure 4.1. More precisely, the violet device consisted of [2]: a) a 4.5  $\mu\text{m}$  GaN buffer layer, b) a 1.8  $\mu\text{m}$  thick *n*-doped GaN, c) an 116 nm thick active layer, d) an 85 nm magnesium-doped aluminium gallium nitride (AlGaN:Mg) cladding layer, and e) a 25 nm thick *p*-doped GaN layer (see Figure 4.1a).

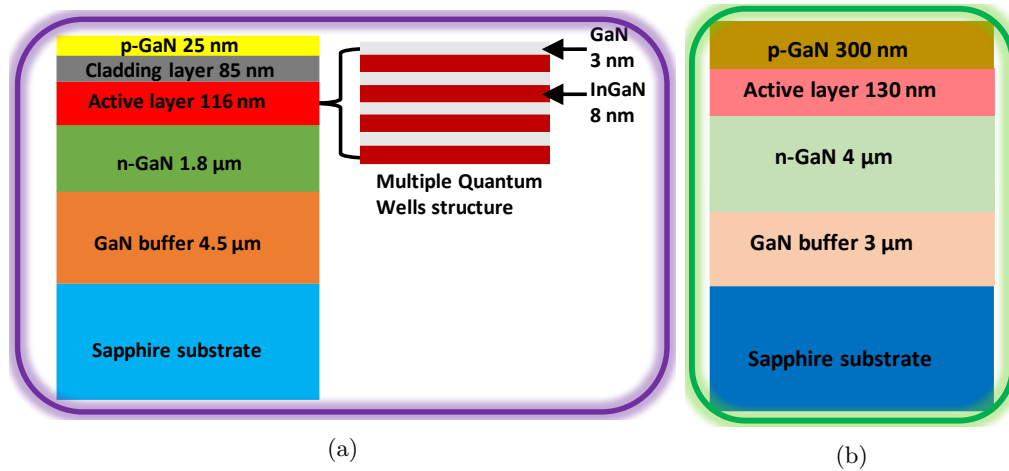


FIGURE 4.1: Simplified micro-LED epitaxial structure of the (a) violet and (b) green micro-LEDs. Dimensional values for both devices are taken from [2].

The epitaxial structure of the green micro-LED comprised a) a  $3 \mu\text{m}$  undoped GaN buffer layer, b)  $4 \mu\text{m}$  of  $n$ -doped GaN, c) a 130 nm thick active layer and finally was topped with d) a 300 nm thick  $p$ -doped GaN layer (see Figure 4.1b).

Although a similar device fabrication procedure is described in [8], the fabrication process for the violet and green micro-LEDs is described briefly as follows: a  $p$ -GaN metal contact consisting of palladium (Pd) of 100 nm thickness, was electron-beam deposited, lithographically patterned, and annealed at  $300^\circ\text{C}$  in a nitrogen environment. The underlying  $n$ -GaN layer was exposed via inductively coupled plasma (ICP) etching which defined a  $20 \mu\text{m}$  diameter pixel of  $3.15 \times 10^{-6} \text{ cm}^2$  active area for both LEDs. Another ICP step then took place, defining a  $90 \mu\text{m}$  side square mesa down to the PSS, which resulted in further reduction of the micro-LEDs capacitance [9]. Furthermore, a metal-sputter deposition of titanium (Ti) and gold (Au) of 20 nm and 200 nm, respectively, in thickness, defined the  $n$ -GaN metal contact layer. Then, plasma-enhanced chemical vapour deposition (PE-CVD) was used for the deposition of 300 nm silicon dioxide ( $\text{SiO}_2$ ). A  $\text{SiO}_2$  aperture on top of the  $p$ -GaN was defined by reactive ion etching (RIE). The final step involved defining the metal track by a second Ti/Au metallisation.

### Blue GaN micro-LEDs grown on silicon (Si) substrate

Commercial InGaN epistuctures were utilised to fabricate the blue micro-LED platelets in a flip-chip configuration, emitting at 453 nm and grown on a silicon (Si) 111-orientated substrate. A schematic illustration of the blue micro-LED's epitaxial structure can be seen in Figure 4.2 and consisted of [2]: a) a 200 nm thick aluminium nitride (AlN) layer, followed by b) a 650 nm Al-graded GaN buffer layer, c) a 300 nm non-intentionally (nid) doped GaN layer, d) an 800 nm thick  $n$ -doped GaN, e) an 100 nm thick active

layer, and f) an 140 nm thick *p*-doped GaN layer. To compensate for the lower optical output power density of the blue micro-LEDs, they were chosen to be larger than their violet and green counterparts. This is because the growth on silicon is non-optimised compared to that on sapphire.

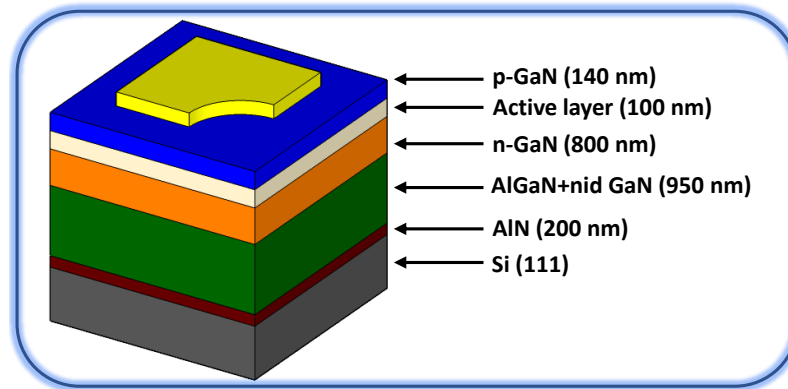


FIGURE 4.2: Simplified micro-LED epitaxial structure of the blue micro-LED. The device's dimensional values are adapted from [2] and the image is taken from [10].

As such, an L-shaped pixel of an active area of  $6.5 \times 10^{-5} \text{ cm}^2$  and a  $100 \mu\text{m}$  squared mesa were defined following similar processes as described in section 4.2.1 with a few modifications that will be described next.

### Integration of dual-colour micro-LED arrays by transfer printing

TP at the micron scale ( $\mu\text{TP}$ ) is a technique for heterogeneous assembly that allows the integration of optoelectronic devices onto non-native substrates. John Rogers' group (then) at the University of Illinois first developed this technique at the microfabrication and semiconductor level [11, 12]. The basis of TP is found in the soft elastomeric polydimethylsiloxane (PDMS) stamps, which are used to “pick and place” appropriately prepared micro/nano-scale devices from their native (“donor”) growth substrate onto a dissimilar “host” (or receiver) substrate. Usually, the devices to be printed are prepared in the form of suspended membranes, often achieved by under-etching. In this way, devices and structures from diverse materials that can not be grown together through conventional methods (e.g. epitaxial growth) are assembled to comprise a hybrid optoelectronic structure. A qualitative illustration of the process is presented in Figure 4.3; the retrieval of the object to be TP is achieved through the downward force mechanically exerted by the stamp. The retraction must be rapid to maximise the adhesion strength between the object and the stamp. On the other hand, when it comes to “releasing” the object onto the host substrate, the retraction needs to be slow to minimise the adhesion strength, and thereby, the object is transferred, and the TP process is completed.

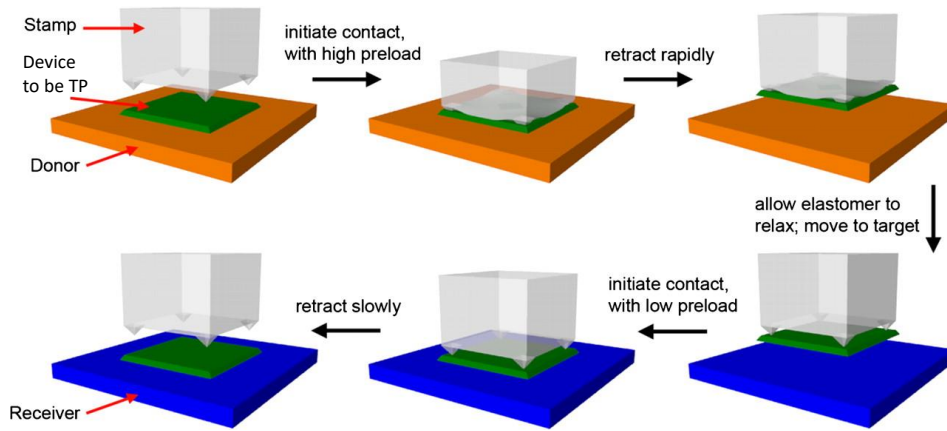


FIGURE 4.3: Schematic illustration of the TP technique. Taken from [13].

Over the last decade, the University of Strathclyde’s IoP has further explored and developed  $\mu$ TP by examining and exploiting the technique’s reliability and capabilities. For instance, Trindade *et al.* in [14] demonstrated TP at nano-scale accuracy of GaN-based micro-LEDs onto mechanically flexible substrates, whilst in [15] they reported TP of blue micro-LEDs on diamond and silica substrates for enhanced thermal management. Most recently, Carreira *et al.* in [10] demonstrated via  $\mu$ TP the integration of an  $8 \times 8$  blue micro-LED array onto a Si complementary metal-oxide-semiconductor (Si-CMOS) drive chip showing a potential pathway to realising a full-colour complementary metal-oxide semiconductor (CMOS)-controlled micro-LED array. On the drive chip, the same SPAD array used for this chapter’s work was also integrated for the photon detection, and the device allowed for VLC at a data rate of up to 1 Mb/s [10].

The TP method, as described above, was applied to integrate the blue micro-LED platelets (donor substrate) onto the sapphire substrate (host substrate) of respective violet and green micro-LEDs. More precisely, supporting “anchors” were defined during the ICP mesa etching as shown in Figure 4.4, which tether the micro-LED platelet to the growth Si substrate. The exposure of the chemically preferentially etched Si(110) planes was achieved via an additional etching step. Then, the Si(110) planes underneath the micro-LED platelets were removed by the implementation of wet etching using a 30% potassium hydroxide (KOH) solution at 80°C. Upon completion of the underetch step, the blue-micro LED platelets were held suspended, above an air gap of 2  $\mu$ m, by the two diagonally opposed sacrificial anchors [14].

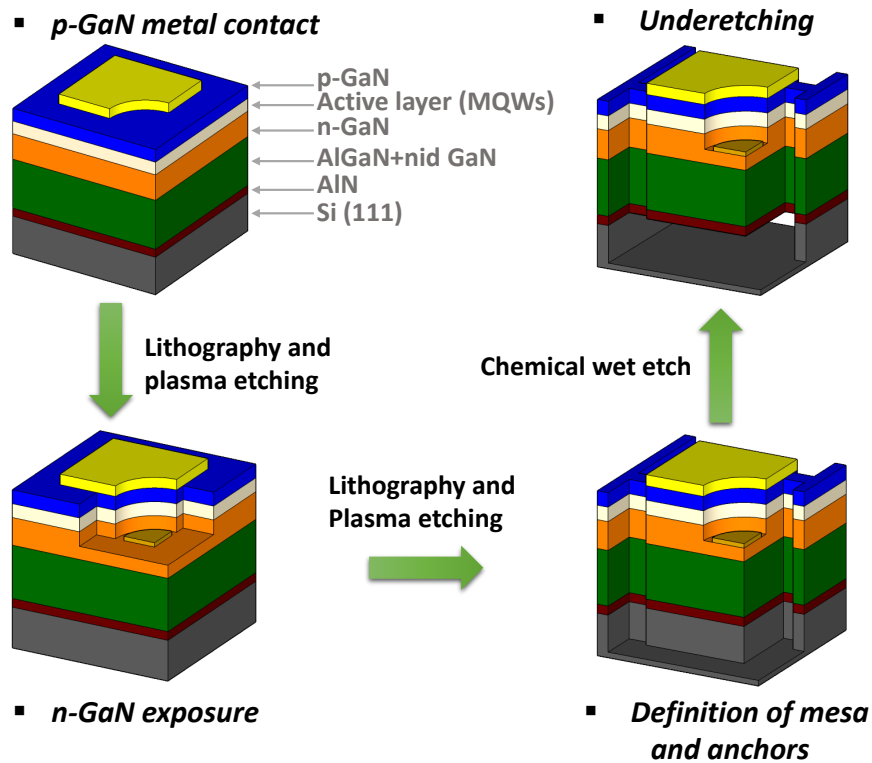


FIGURE 4.4: Schematic of the fabrication process of the blue micro-LED on its Si substrate before TP. Note that the device is mechanically suspended after the final step (images taken from [10]).

The employment of a PDMS elastomeric stamp enabled the pick up of the suspended blue micro-LED platelets from their Si substrate and their transfer printing onto the green and violet sapphire substrate (PSS). The blue micro-LED was placed  $50 \mu\text{m}$  apart from the violet or green micro-LED mesa. For this operation to be successful, the adhesion force between the blue micro-LED platelet backside and the PSS receiving substrate must be larger than the adhesion force between the micro-LED platelet and the stamp. Figures 4.5a and 4.5b show plan view optical photographs of the blue-green micro-LED array before and after TP of the blue micro-LED platelet, respectively. The electrical layout of this array is at an individually-addressable anode and a shared common cathode. The blue-violet micro-LED array follows the same layout.

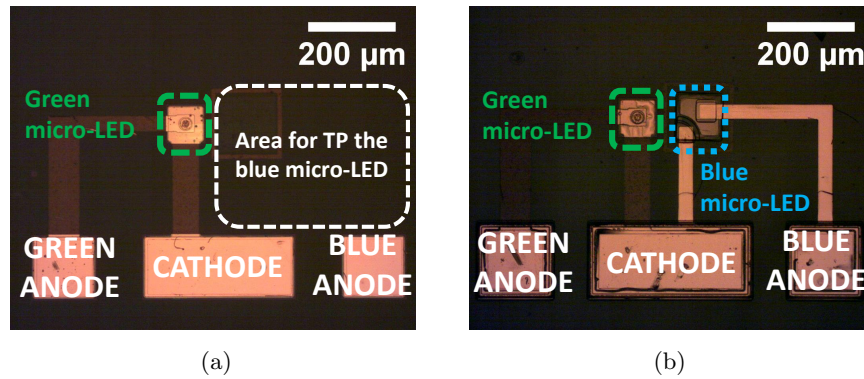


FIGURE 4.5: Plan view optical micrograph images of the green and blue micro-LED array (a) before and (b) after transfer-printing the blue device onto the green device's substrate (images taken from [2]).

However, the TP process is not a trivial task. Firstly, the concave curvature of the micro-LED platelet attributed to strain effects on its release, as investigated by Trindade *et al.* [15], prevents efficient electrical insulation of the pixel by thin layers, e.g.  $\text{SiO}_2$ . Secondly, the highly dense cone-shaped periodic pattern of the PSS, as shown in Figure 4.6a as obtained via an atomic force microscope (AFM)\*, reduces the effective contact area of the micro-LED platelet backside with the receiving substrate, rendering the release of the micro-LED platelet from the stamp quite challenging.

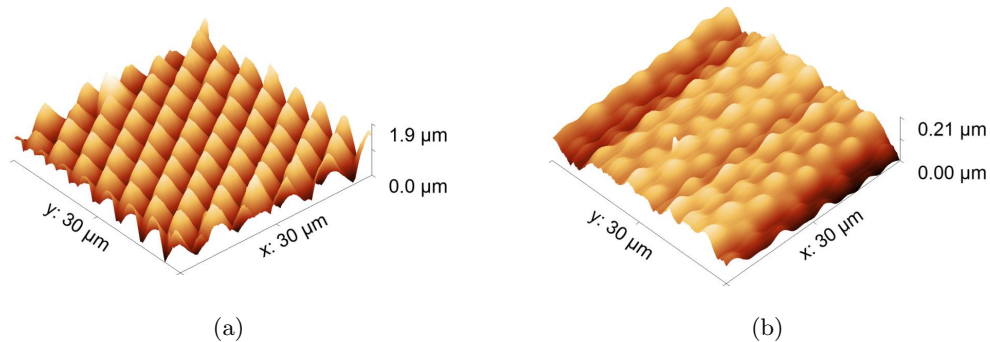


FIGURE 4.6: Atomic force microscope image of the PSS (a) before and (b) after the SU-8 coating (images taken from [2]).

The PSS exhibits a root-mean-square (RMS) roughness of 342 nm and a maximum height feature of 1.9  $\mu\text{m}$ . To assist the release of the micro-LED platelet, an adhesion-enhancing layer of SU-8 epoxy-based photoresist [16] of 4.5  $\mu\text{m}$  thick was chosen to coat the PSS of the violet/green micro-LEDs. SU-8 was selected due to its excellent planarising and coating properties and the mechanical and chemical stability it exhibits [17]. Figure 4.6b shows that the SU-8 layer effectively planarises the PSS as the PSS

\*The images were taken by a Park Systems AFM.

RMS roughness and maximum height feature were decreased to 16.9 nm and 0.18  $\mu\text{m}$ , respectively.

The pixel insulation after TP was completed by depositing a 4.5  $\mu\text{m}$  thick Parylene-C (Pa-C) layer. Pa-C was chosen due to its excellent electrical insulation properties, chemical stability and exceptional conformity [18]. The latter is attributed to the chemical vapour deposition through which Pa-C is deposited at room temperature [19]. This results in stress-free films, whereas other thick polymers used for pixel encapsulation (e.g. SU-8) are applied by spin-coating techniques, which may cause non-uniformity due to devices' displacement that is not strongly bonded to their receiving substrate. The pixel metallisation concludes the final fabrication step as 40  $\mu\text{m}$  wide metal tracks of Ti/Au and 50 nm/200 nm thick were lithographically defined for contacting the micro-LED platelet through apertures in the Pa-C.

In Figures 4.7a - 4.7c are shown plan view *topside* optical photographs of the respective individually-addressable micro-LEDs, driven at 318  $\text{A}/\text{cm}^2$  (or 1 mA) for the violet and green devices and at 15  $\text{A}/\text{cm}^2$  (or 0.975 mA) for the blue. Plan view *backside* optical photographs from the blue-violet (Figure 4.7d) and blue-green (Figure 4.7e) post-printing micro-LED two-colour devices, simultaneously driven at 318  $\text{A}/\text{cm}^2$  and 15  $\text{A}/\text{cm}^2$  for the violet/green and blue devices, respectively, can also be seen.

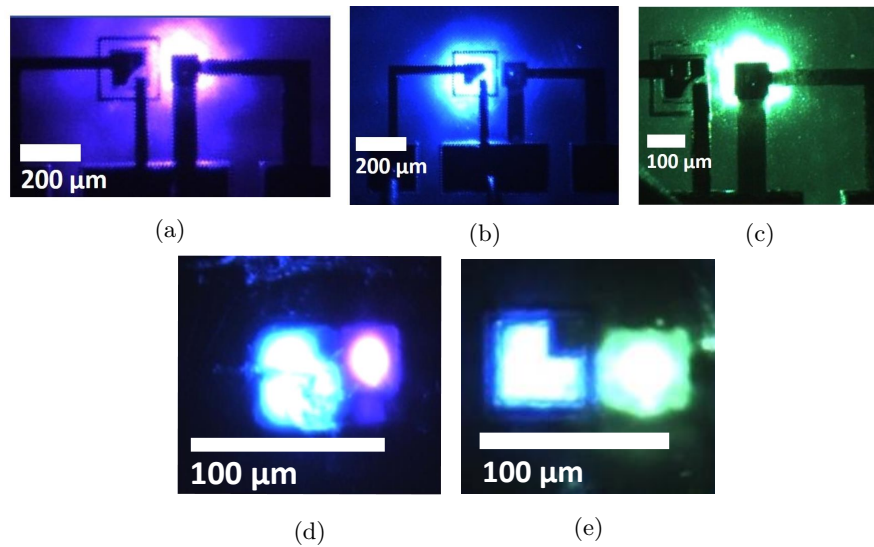


FIGURE 4.7: Plan view *topside* optical micrograph for the (a) violet (318  $\text{A}/\text{cm}^2$ ), (b) blue (15  $\text{A}/\text{cm}^2$ ) and (c) green (318  $\text{A}/\text{cm}^2$ ) micro-LEDs. Plan view *backside* optical micrograph at the same currents as the topside ones for the (d) blue-violet and (e) blue-green micro-LED arrays.

### Micro-LEDs electrical, optical and modulation performance

The electroluminescence (EL) spectra of all the micro-LED devices are shown in Figure 4.8 and were obtained through an optical fibre-coupled spectrometer (Avantes, AvaSpec-2048L) at current densities of 318 A/cm<sup>2</sup> (or 1 mA) and 15 A/cm<sup>2</sup> (or 0.975 mA) for the violet/green and blue devices, respectively, whilst the central wavelength for violet is at 400 nm, for blue at 453 nm, and for green at 512 nm.

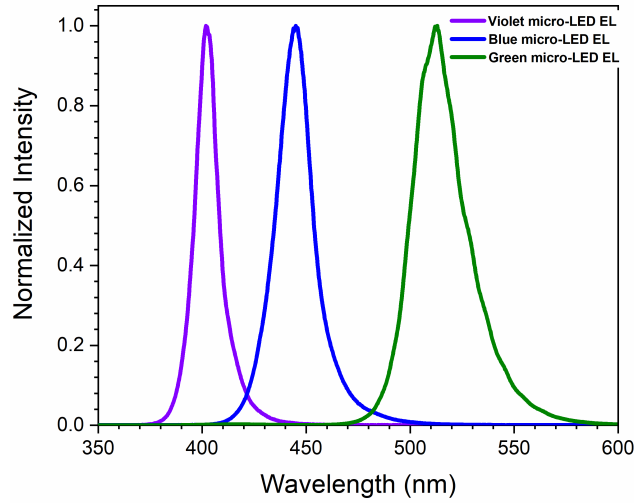


FIGURE 4.8: Normalised EL spectra of the micro-LEDs used in this work. The violet device’s central wavelength is at 400 nm, the blue’s at 453 nm, and the green’s at 512 nm.

The corresponding values for the full width at half maximum (FWHM or  $\Delta\lambda$ ) are for the violet device 13.98 nm, 20.95 nm for the blue device, and 29.78 nm for the green device. The broadening in EL curves results from the increasing indium (In) content from the violet to green devices’ active region. In general, by varying the fraction Ga/In in the micro-LED’s QWs, the material’s  $E_g$  is affected. In our case, the  $E_g$  from violet to green is being narrowed, and thus, the emitted photons upon radiative recombination are of a longer wavelength. The FWHM of the emission spectrum is proportional to the wavelength squared ( $\Delta\lambda \propto \lambda^2$ ) of the emitted photons [20] and since  $\lambda_{green} > \lambda_{blue} > \lambda_{violet}$ , then  $\Delta\lambda_{green} > \Delta\lambda_{blue} > \Delta\lambda_{violet}$ .

Further electrical and optical characteristics of the violet, blue, and green micro-LEDs are depicted in Figure 4.9. The room-temperature (RT) voltage vs current density (JV) for each micro-LED was measured by scanning each data point under the operation of a direct current (DC) source (Yokogawa, GS610 Source Measure Unit). By performing a linear fit to the “linear” part of the JV curves, the turn-on voltage ( $V_F$ ) was extracted for each micro-LED: 3.67 V, 3.26 V, and 6.17 V for the violet, blue and green micro-LED, respectively. The larger (than expected)  $V_F$  for green is attributed to a possible misalignment during the metallisation of the *p*-GaN contact. The optical power vs



current density (LJ) was collected through a calibrated Si photodiode power sensor of area  $9.7 \times 9.7 \text{ mm}^2$  (Thorlabs, S121C) in proximity to the backside of the micro-LEDs and connected to a power meter (Thorlabs, PM100D). The violet and green micro-LEDs exhibit optical powers of 0.85 mW and 0.34 mW, respectively, at  $2.8 \text{ kA/cm}^2$  (or 8.8 mA), whilst the blue micro-LED presents an optical power of 1.04 mW at  $138 \text{ A/cm}^2$  (or 9 mA). The lower current density operation of the TP blue micro-LED is attributed to its larger pixel size. It should also be noted that under dark conditions, a reverse leakage current of 350 nA at -3 V is observed for the blue micro-LED, which is lower than values from similar devices coated with SU-8 as an insulation layer. This indicates the importance of insulating the TP micro-LEDs with Pa-C for this work, whereas the low reverse current leakage shows a very good JV performance of the devices [2].

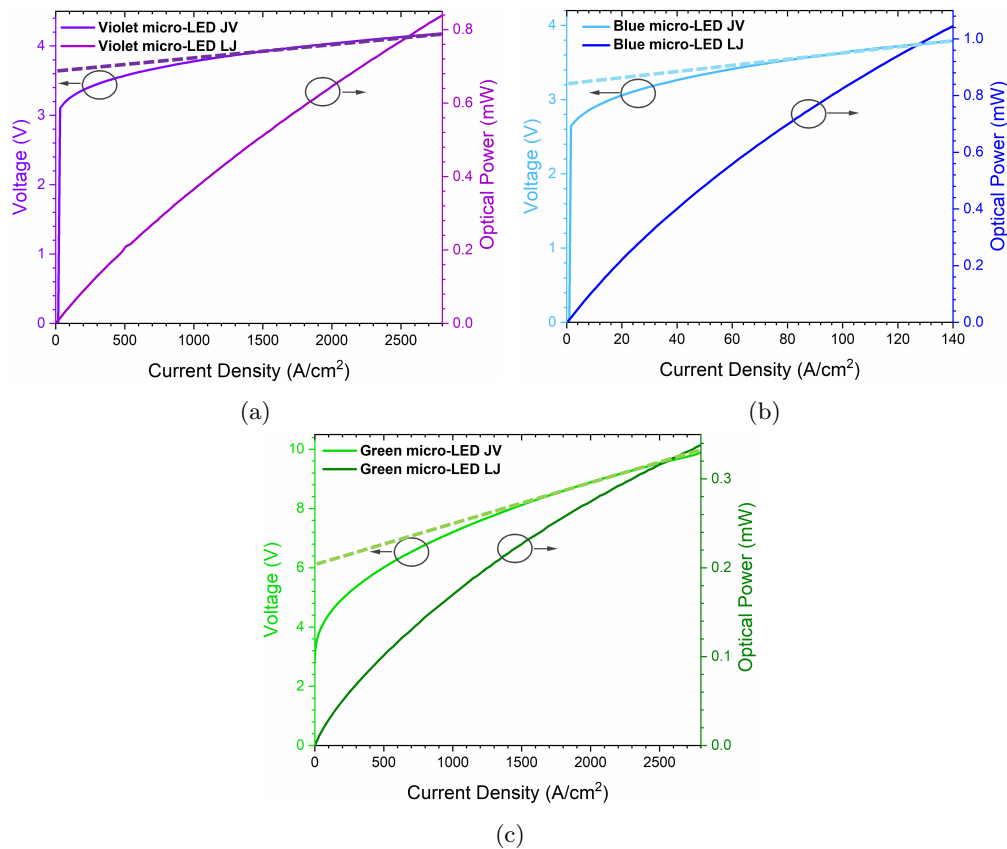


FIGURE 4.9: The RT voltage vs current density (JV), and optical power vs current density (LJ) plots for **(a)** violet (at  $318 \text{ A/cm}^2$ ), **(b)** for blue (at  $15 \text{ A/cm}^2$ ) and **(c)** for green (at  $318 \text{ A/cm}^2$ ) micro-LEDs. The  $V_F$  of the devices (violet: 3.67 V, blue: 3.26 V, green: 6.17 V) are shown at the intersection of the dashed lines and the voltage axes.

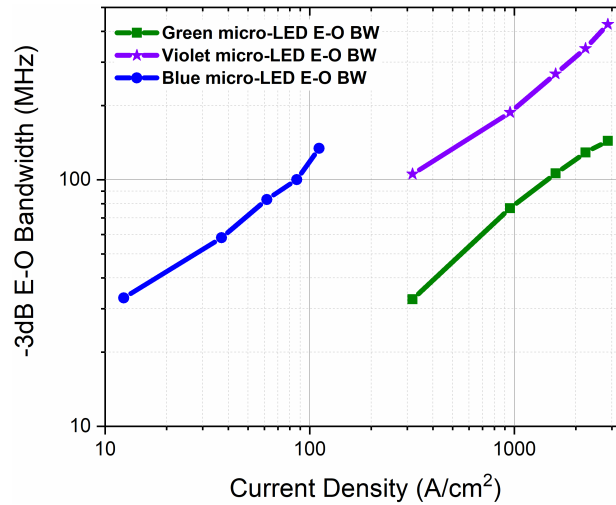


FIGURE 4.10: The -3 dB electrical-to-optical (E-O) modulation bandwidths of the violet (427 MHz), blue (134 MHz), and green (144 MHz) micro-LEDs.

The RT -3 dB E-O BWs (or the -6 dB E-E BWs) of each micro-LED are shown in Figure 4.10. As with previous identical measurements (Section 3.2.2), these were acquired by applying a DC bias and an AC signal generated by a network analyser (HP8753ES) to modulate the micro-LEDs at different current density points. The optical power output from the micro-LEDs was collected by a lens system and focused onto a PiN photoreceiver of 1.4 GHz bandwidth (Femto, HAS-X-S-1G4-SI). As can be seen from Figure 4.10, the violet and green micro-LEDs exhibit an E-O BW of 427 MHz and 144 MHz, respectively. Compared to the violet device, the low E-O BW of the green micro-LED can be explained as follows: as mentioned in Section 4.2.1, the green micro-LED was grown on a sapphire substrate. Although this is the most commonly used substrate material, there is a lattice mismatch between sapphire and GaN, which results in strain effects in the GaN barrier. Subsequently, strain induces a piezoelectric field within the material layers. That field significantly affects the compressively strained InGaN MQWs of the LED, as it causes separation and a reduced overlap of the electron-hole wavefunctions. This phenomenon is known as the quantum confined Stark effect (QCSE) [21] and was briefly mentioned in Section 2.1.4. QCSE can lead to reduced radiative recombination rates limiting the LED's modulation BW [22]. For the micro-LEDs of this work, the higher composition of In is found in green's active region, as previously mentioned. This means larger strain-induced piezoelectric fields in the InGaN QWs and, thus, stronger QCSE [23]. The blue micro-LED has a -3 dB E-O BW of 134 MHz, and its lower value can be attributed to its larger pixel size, thus lower current density operation. It can also be observed that blue micro-LED's operating current density is lower than those of the violet and green devices. This can be attributed to the layer of Pa-C that the device sits on, resulting in inadequate heat-sinking and preventing it

from being driven to high current density. All values of interest, as addressed above for the individually addressable micro-LEDs, are summarised in Table 4.1.

TABLE 4.1: Summarised figures of merit for the individually addressable micro-LED arrays; violet-blue and blue-green. For the violet and green micro-LEDs, the optical powers are shown at a current density of 2.8 kA/cm<sup>2</sup>. For the blue micro-LED, the optical power is shown at 138 A/cm<sup>2</sup>.

	<i>Violet</i>	<i>Blue</i>	<i>Green</i>
$\lambda$ (nm)	400	453	512
Active area (cm <sup>2</sup> )	$3.14 \times 10^{-6}$	$6.5 \times 10^{-5}$	$3.14 \times 10^{-6}$
$V_F$ (V)	3.67	3.26	6.17
Optical power (mW)	0.85	1.04	0.34
E-O BW (MHz)	427	134	144

### 4.2.2 In-series connected blue-green micro-LED array

#### Device development

As mentioned earlier, the devices for the UWOC applications were developed in two different layouts: individually-addressable, discussed in Section 4.2.1, and in-series connected, which will be presented here. The fabrication process for the in-series connected blue-green micro-LED array is similar to that followed for the individually-addressable micro-LED arrays, with some exceptions.

For the optical power to be increased, the pixel diameter of the green micro-LED was increased from 20  $\mu\text{m}$  to 30  $\mu\text{m}$  resulting in an increased active area of  $7.07 \times 10^{-6}$  cm<sup>2</sup> from  $3.15 \times 10^{-6}$  cm<sup>2</sup>. As shown in Figure 4.11a, a common anode and cathode were defined during the ICP etching to the PSS before TP the blue micro-LED platelet, whilst the metallisation of the pixel's *n*-GaN layer by Ti/Au of 50/200 nm in thickness, concluded the green micro-LED fabrication.

For the in-series connecting layout, the L-shaped pixel developed for the blue individually-addressable micro-LED, as described in Section 4.2.1, would not be practical. Therefore, a  $60 \times 60$   $\mu\text{m}^2$  central square pixel was defined during the blue micro-LED's ICP step to expose the *n*-GaN layer and a square-shaped *n*-contact metal ring of Ti/Au, 50/200 nm thick, was deposited via metal sputtering. Underetching in KOH solution at 80°C followed, for the suspension of the blue micro-LED platelets.

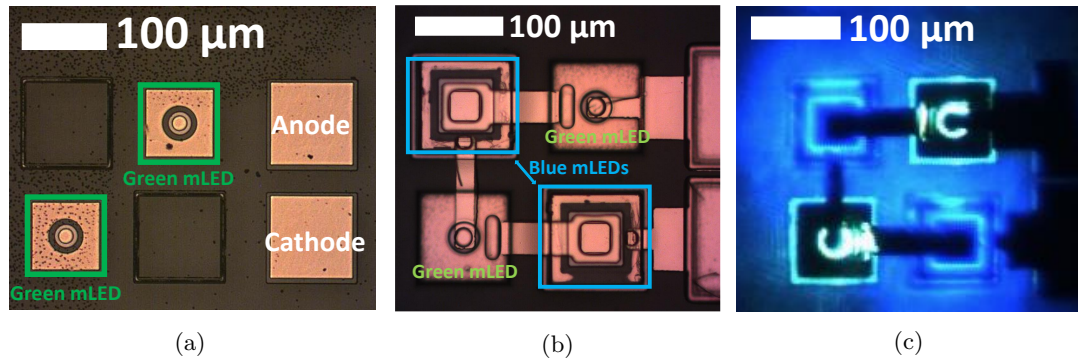


FIGURE 4.11: Plan-view optical photographs of the (a) green micro-LEDs before the blue TP onto the PSS, (b) of the array after micro-TP the blue micro-LED platelets, (c) in-series connected device driven at a current of 2 mA.

Micro-TP enabled the heterogeneous integration of the blue micro-LED platelets onto the PSS of the green micro-LEDs, coated with SU-8 (see Figure 4.11b). The electrical insulation of the micro-LEDs was achieved by depositing a  $4.5 \mu\text{m}$  thick Pa-C film. The final fabrication step involved defining the metal tracks by Ti/Au, which connected the pixels in-series. Figure 4.11c shows a plan-view photograph of the in-series connected micro-LED array driven at 2 mA, corresponding to a current density of  $55 \text{ A/cm}^2$  and  $283 \text{ A/cm}^2$  for the blue and green micro-LEDs, respectively. The current values will be presented in current intensity (in mA) for the “in-series connected devices” section rather than current density for convenience.

### Electrical, optical and modulation performance of the in-series connected micro-LED array

The IV and LI curves of the in-series connected blue-green device are depicted in Figure 4.12a. The room temperature IV characteristics were measured, as previously mentioned in Section 4.2.1, by scanning each data point under the operation of a direct current (DC) source (Yokogawa, GS610). As with the individually addressable devices, a linear fit was performed in the “linear” part of the IV curve, and a turn-on voltage of 15.8 V was extracted. Taking into account that the single blue and green micro-LEDs  $V_F$  values were 3.26 V and 6.17 V, respectively (see Section 4.2.1), a “theoretical”  $V_F$  for the in-series connected device would be 18.86 V. Thus, it can be deduced that the ohmic contact between the *p*-GaN layer and the metal contacts of the in-series device is of good quality when the value of the calculated  $V_F$  (15.8 V) is compared to the “theoretical” one (18.86 V). The LI characteristics were acquired using a calibrated Si photodiode power sensor (Thorlabs, S121C) positioned near the backside of the micro-LEDs and connected to a power meter (Thorlabs, PM100D). Since the micro-LEDs are connected in-series, the LI measurement could not be carried out for each pixel individually. As such, the optical power was acquired by changing the power meter’s relative spectral

responsivity to be aligned with the peak emission wavelength of each micro-LED, i.e. 453 nm for blue and 512 nm for green. The in-series connected blue micro-LEDs exhibit optical power of 1.58 mW, whereas for the green device it was 1.37 mW at 9 mA.

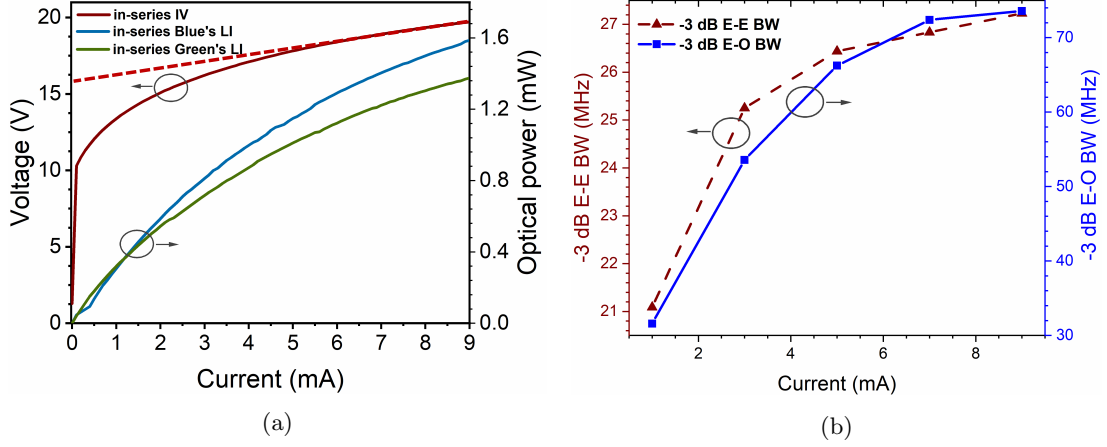


FIGURE 4.12: **(a)** The IV and LI curves of the in-series connected blue-green micro-LED array (the  $V_F = 15.8$  V of the array is shown at the intersection of the dashed line and the voltage axis), and **(b)** the -3 dB electrical-to-electrical (E-E) and electrical-to-optical (E-O) modulation bandwidths of the same device.

Regarding the RT -3 dB BWs of the array, it can be seen from Figure 4.12b that the E-E and E-O BWs are 27.23 MHz and 73.6 MHz, respectively, at 9 mA. The process for measuring the modulation BWs of the in-series connected micro-LED array was the same as described in Section 4.2.1, where a combined DC bias and an AC signal from a network analyser (HP8753ES) modulated the micro-LEDs at different current points. The optical response of the micro-LED array was measured through a 1.4 GHz PiN photodetector (Femto, HAS-X-S-1G4-SI). The in-series connected micro-LED array's parameters are summarised in Table 4.2.

TABLE 4.2: Summarised values of interest for the in-series connected blue-green micro-LED array. The optical powers for both micro-LEDs are shown at a current of 9 mA.

	<i>Blue</i>	<i>Green</i>
Active area (cm <sup>2</sup> )	$3.6 \times 10^{-5}$	$7.07 \times 10^{-6}$
$V_F$ (V)	15.8	
Optical power (mW)	1.58	1.37
E-O BW (MHz)	73.6	

### 4.3 Application in Underwater Wireless Optical Communications

#### 4.3.1 Experimental set-up

The first series of measurements refers to deploying the individually addressable violet-blue and blue-green micro-LED arrays discussed in Section 4.2.1. The experimental setup is depicted in Figure 4.13. As with previous chapters, a water tank of dimensions  $1.5 \times 0.35 \times 0.35 \text{ m}^3$  was filled with 160 l of tap water. The water tank walls were fitted with high transmittance (91%) Pilkington Optiwhite™ glass which has been utilised in recent studies for single-photon imaging in highly scattered underwater environments [24].

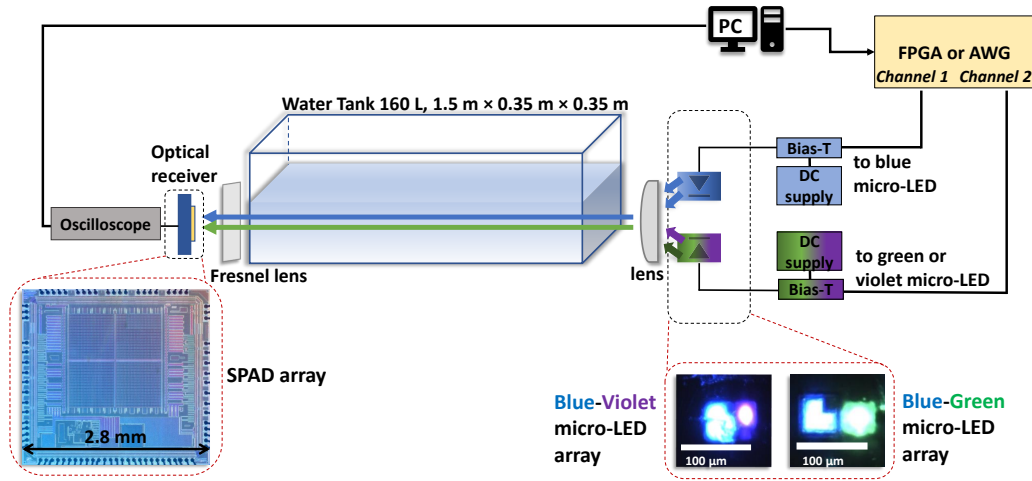


FIGURE 4.13: A schematic illustration of the experimental set-up used for the UWOC demonstration by deploying the individually addressable micro-LED arrays (violet-blue and blue-green).

The transmitter site ( $T_x$ ) consisted of the individually addressable blue-green (or violet-blue) micro-LED array. An OOK data signal was generated by an FPGA (Opal Kelly, XEM6310-LX45) or an AWG (Keysight, M8190A) that modulated the micro-LEDs. It should be noted that for real-world applications, an FPGA would be advantageous due to its compactness and practical weight. As such, it could be easily implemented in a AUV without further constraints. However, the FPGA prevented the devices from achieving high data rates as it limited the modulation depth or peak-to-peak modulation voltage ( $V_{pp}$  ranged from 1.5 V to 2.4 V) of the micro-LEDs due to its limited clock speed (or rise/fall times). An AWG was deployed to further expand the devices' modulation depth, enabling the demonstration of larger data rates underwater as the devices'  $V_{pp}$ 's ranged from 4.3 V to 15 V.

The OOK data signal, generated by the FPGA or the AWG, was combined with a DC bias (from Yokogawa, GS610) through a bias-tee (Mini-Circuits, ZFBT-4R2G+). Two channels from the FPGA/AWG were used, one for each micro-LED, through SMA connectors. From both channels, a sequence of length  $2^{15}$  bits was optically transmitted through the water tank (Figure 4.14a), consisting of a wide synchronisation pulse and a pseudo-random bit sequence as the blue-green (or blue-violet) pixels were operated simultaneously. However, it should be mentioned that each colour carried a different data stream. For the FPGA measurements, RF attenuators were connected between the arrays and the FPGA to prevent the FPGA and the micro-LEDs from damage. For the AWG measurements, an external amplifier (Mini-Circuits, ZHL-1A-S+) was connected to the AWG's output to assess the micro-LEDs' full dynamic range. The micro-LEDs' emission was collected and collimated by a condenser lens (Thorlabs, ACL50832U-A) (Figure 4.14 d - e), propagated through the water tank and then focused onto the receiver by a 4-inch diameter Fresnel lens (Edmund, #46-614) (Figure 4.14c). The collection of each data stream was enabled by placing bandpass filters (Laser 2000, FF01-392-23/25 for the violet, FF01-445-20/25 for the blue, and FF01-525-45/25 for the green) before the receiver ( $R_x$ ).

The  $R_x$  comprises the Photon Torrent chip (Figure 4.14b), as introduced in Section 2.1.6, a  $64 \times 64$  array of 4096 Si single photon avalanche diodes (SPADs) (details can be found in [25]). The SPAD array has a fill factor of  $F_{fill} = 43\%$ , the chip's dimensions are  $2.6 \times 2.8 \text{ mm}^2$ , including the surrounding electronics whilst the photon detection probability ( $\eta_{PDP}$ ) of the individual pixels is  $\eta_{PDP} = 26\%$  at 450 nm and of 20 ns dead time ( $\tau_d$ ) [4]. The arrayed nature of the Photon Torrent chip masks the dead time of a single SPAD, which can be 35-45 ns for commercial products (e.g. Thorlabs, SPCM20A and SPCM50A) [26]. Thus, more photons can be detected, achieving higher data rates. The photon counts were summed over a time window of 5 ns, and the count values were outputted through a digital-to-analog converter (DAC). The DAC signal was captured with an active oscilloscope probe and transferred to MATLAB<sup>®</sup> for offline processing to determine the BER. As with previous measurements, the turbidity of the water sample was varied by adding Maalox<sup>®</sup> antacid to tap water, a method widely used (e.g. in [27]) to mimic different natural water analogues in a laboratory set-up.

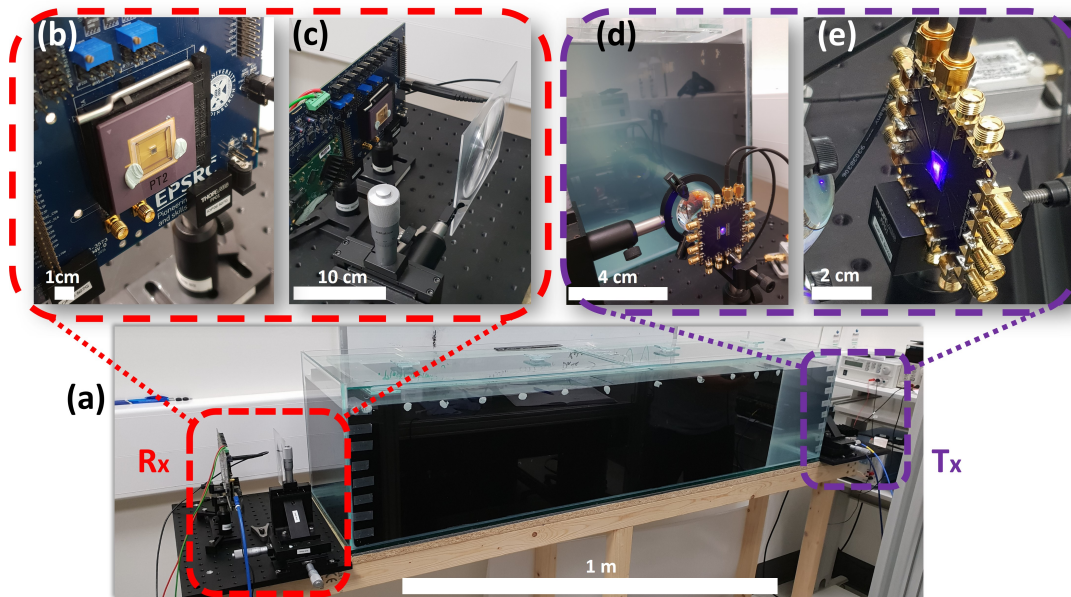


FIGURE 4.14: Photographs of (a) the water tank filled with tap water and added with Maalox antacid. The  $T_x$  and  $R_x$  sites are also indicated. (b)-(c) The  $64 \times 64$  SPADs array and the 4-inch Fresnel lens placed before the receiver. (d)-(e) The individually-addressable micro-LED array (violet-blue) under operation and the condenser lens in front of the device for beam collimation.

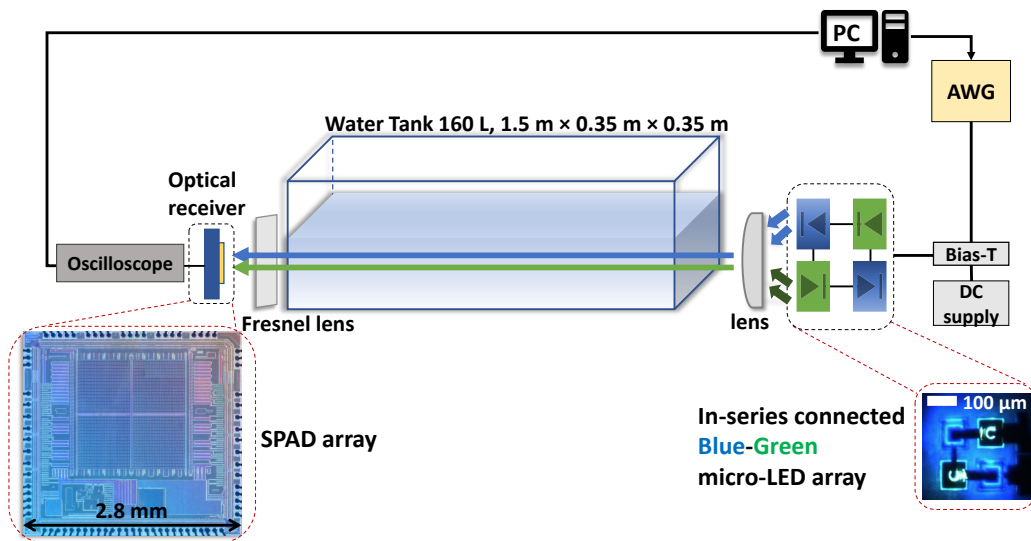


FIGURE 4.15: A schematic illustration of the experimental set-up used for the UWOC demonstration by deploying the in-series connected micro-LED array (blue-green).

The second series of measurements addresses the deployment of the in-series connected blue-green micro-LED array discussed in Section 4.2.2. The experimental set-up is depicted in Figure 4.15 and was the same as used previously for the individually-addressable devices with a few exceptions; the in-series connected blue-green micro-LED array was used as  $T_x$  and the device was modulated only by the AWG.



### 4.3.2 Results

#### Individually-addressable devices

##### FPGA results

The integrated violet-blue and blue-green micro-LED arrays were operated as dual-wavelength WDM transmitters. The underwater WDM results acquired via the FPGA are summarised in Figures 4.16a and 4.16b. The violet-blue micro-LED array ( $DC_{violet} = 3.3$  V, violet's  $V_{pp} = 1.5$  V; and  $DC_{blue} = 2.6$  V, blue's  $V_{pp} = 1.5$  V), achieved 100 Mb/s aggregate data rate (50 Mb/s for each colour), below the FEC threshold (Figure 4.16a). These data rates were demonstrated over 8.52 ALs and 6.95 ALs for the violet and blue pixels at 0.0081% (or 13 ml of Maalox in 160 l of tap water) and 0.0075% of the scattering agent concentration (or 12 ml of Maalox in 160 l of tap water), respectively. The number of ALs and the calculated attenuation coefficients for each wavelength were calculated via the method described in Section 1.6. For reference, in the same graph, short vertical dotted lines depict the attenuation coefficients of the most turbid *Jerlov* coastal waters (*Jerlov* 7C and 9C).

As for the blue-green micro-LED array ( $DC_{blue} = 2.8$  V, blue's  $V_{pp} = 1.5$  V,  $DC_{green} = 7$  V, green's  $V_{pp} = 1.5$  V), an aggregate data rate of 100 Mb/s (50 Mb/s for each wavelength) was achieved, below the FEC threshold (Figure 4.16b). The maximum number of attenuation lengths over which those transmissions were demonstrated were 6.47 ALs at  $c_{Maalox} = 0.0068\%$  (or 11 ml in 160 l of tap water) and 5.78 ALs at  $c_{Maalox} = 0.0075\%$  (or 12 ml in 160 l of tap water) for the blue and green micro-LED arrays, respectively. As before, the *Jerlov* 7C and 9C attenuation coefficients are also shown at wavelengths close to the colour of operation of the micro-LED devices.

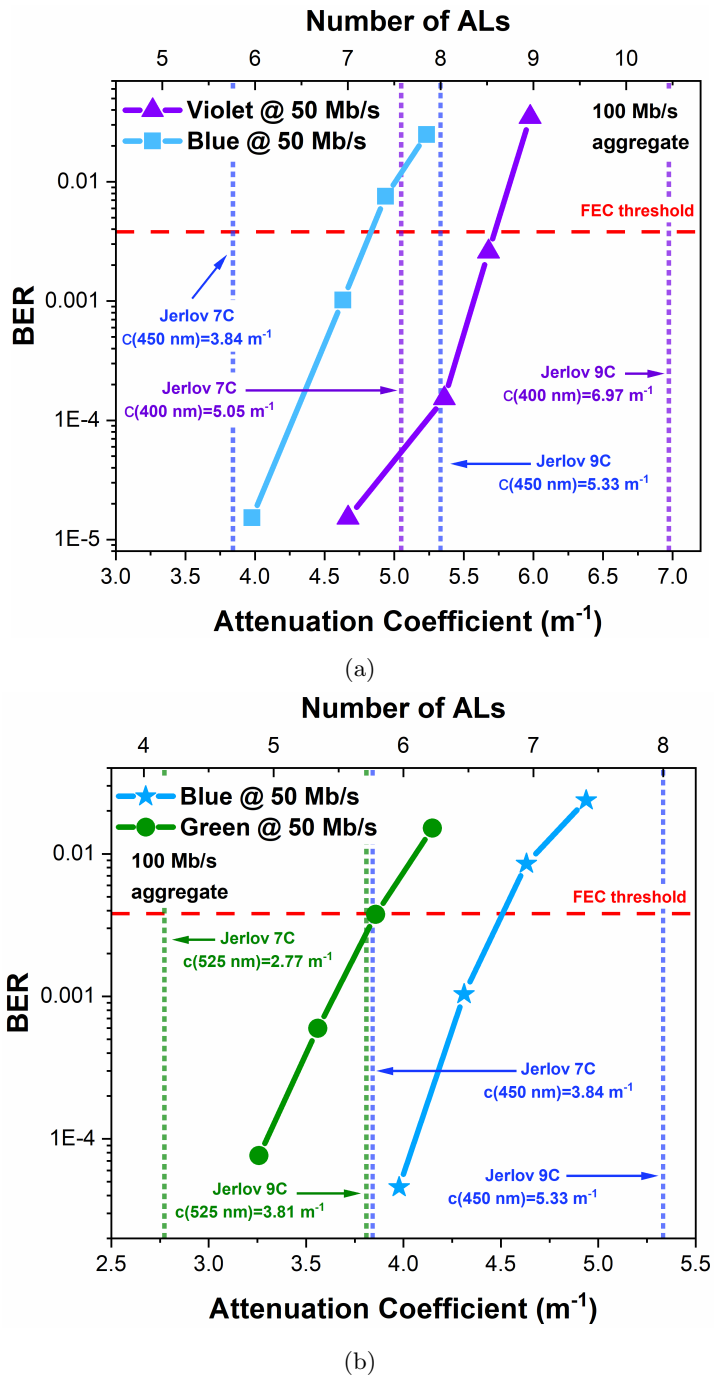


FIGURE 4.16: BER vs attenuation coefficient and number of ALs for the individually addressable (a) violet-blue micro-LED array; WDM of 100 Mb/s is presented over 8.52 and 6.95 ALs for the violet and blue channel, respectively. (b) blue-green micro-LED array; WDM of 100 Mb/s is shown over 6.47 and 5.78 ALs for the blue and green underwater channels, respectively.

As all signals propagated over the same distance (1.5 m), the violet signal (the shortest wavelength of the three) experiences higher attenuation than blue and green as the concentration of the scattering agent increases. This explains why the violet device's data stream corresponds to a more significant number of ALs when compared to those of

the blue and green devices. Figure 4.16a also shows that the violet micro-LED achieves a similar BER to the blue for a higher number of ALs. This is possibly attributed to the violet device's larger E-O BW (see Table 4.1) that allows the device to modulate faster. As for the blue-green micro-LED array, Figure 4.16b shows that the blue signal propagates over a more significant number of ALs (when compared to the green). Both micro-LEDs exhibit similar BER, despite the slight difference in their E-O BWs. Therefore, the blue device's larger optical power output (see Table 4.1) allows propagation over a larger number of ALs. A summary of the above-discussed results is shown in Table 4.3.

TABLE 4.3: Summary of the FPGA results, below the FEC threshold, for the individually addressable micro-LED arrays.

<b>FPGA results</b>				
micro-LED array	DR (Mb/s)	WDM (Mb/s)	ALs	$c_{Maalox}$ (%)
Violet	50	100	8.52	0.0081
Blue	50		6.95	0.0075
Blue	50	100	6.47	0.0068
Green	50		5.78	0.0075

### AWG results

As previously mentioned, an AWG replaced the FPGA to aim for higher data rates from the same devices. It is worth noting that the Keysight M8190A AWG can support modulation frequencies of up to 5 GHz [28] whereas the FPGA can sustain frequencies  $\approx 100$  MHz. As such, optical signals of faster rise and fall times can be generated, thus demonstrating higher data rates.

Indeed, the results acquired via the AWG's modulation are shown in Figures 4.17a and 4.17b, and indicate WDM demonstration of 200 Mb/s for the violet-blue device and 150 Mb/s for the blue-green (below FEC), compared to 100 Mb/s for the FPGA results shown in the previous section.

With regards to the violet-blue micro-LED array ( $DC_{violet} = 1$  V, violet's  $V_{pp} = 5$  V; and  $DC_{blue} = 1.5$  V, blue's  $V_{pp} = 4.3$  V), 100 Mb/s were achieved for each wavelength over 5.85 ALs for the violet at  $c_{Maalox} = 0.0050\%$  (or 8 ml of the scattering agent in 160 l of tap water) and 5.18 ALs for the blue at  $c_{Maalox} = 0.0053\%$  (or 8.5 ml in 160 l of tap water).

The blue-green device ( $DC_{blue} = 1.5$  V, blue's  $V_{pp} = 4.3$  V,  $DC_{green} = 1$  V, green's  $V_{pp} = 15$  V) achieved WDM of 150 Mb/s; 100 Mb/s were demonstrated through the blue channel over 5.71 ALs at  $c_{Maalox} = 0.0059\%$  (or 9.5 ml of Maalox in 160 l of tap

water) and 50 Mb/s through the green over 5.34 ALs at  $c_{Maalox} = 0.0068\%$  (or 11 ml of Maalox in 160 l of tap water). A summary of the results mentioned above is shown in Table 4.4.

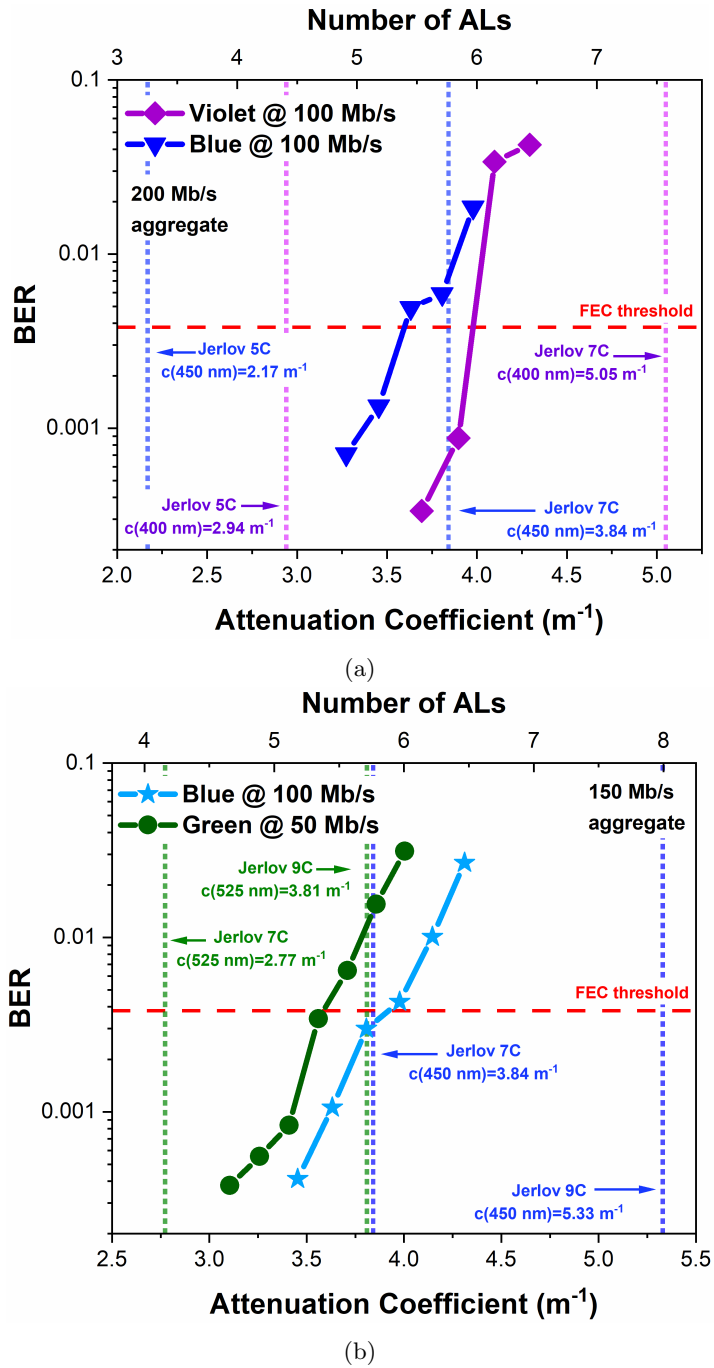


FIGURE 4.17: BER vs overall attenuation coefficient and number of ALs via deploying an AWG for the signal generation for the individually addressable (a) violet-blue micro-LED array; WDM of 200 Mb/s aggregate below the FEC threshold is presented over 5.85 ALs for the violet channel and 5.18 ALs for the blue. (b) blue-green micro-LED array; WDM of 150 Mb/s aggregate below the FEC threshold is shown over 5.71 and 5.34 ALs for the green and blue underwater channels, respectively.

TABLE 4.4: Summary of the AWG results, below the FEC threshold, for the individually addressable micro-LED arrays.

AWG results				
micro-LED array	DR (Mb/s)	WDM (Mb/s)	ALs	$c_{Maalox}$ (%)
Violet	100	200	5.85	0.0050
Blue	100		5.18	0.0053
Blue	100	150	5.71	0.0059
Green	50		5.34	0.0068

As with the FPGA measurements, the large number of ALs of the violet channel indicates that the lowest wavelength (violet) attenuates more than blue and green as the water turbidity increases.

Moreover, it can be seen that as the data rate increases (e.g. from 50 Mb/s via the FPGA to 100 Mb/s through the AWG), violet attenuates faster as error-free underwater data transmission is achievable at 8 ml of Maalox via the AWG, whereas error-free data transmission was feasible at 13 ml of Maalox via the FPGA. The latter is observed not only for the violet channel but also for the blue and green. This can be attributed, firstly, to the “trade-off” between high data rates and optical power losses for the device; as the bit period (equals to  $\frac{1}{\text{data rate}}$ ) decreases, the micro-LEDs are forced to follow the fast logic transitions between 1’s and 0’s imposed by the AWG, resulting in reduced emitted optical power. Optical power loss is translated to fewer emitted photons which, eventually, “survive” the turbid underwater environment and reach the  $R_x$ . Secondly, the  $R_x$ ’s  $\tau_d$  (=20 ns) significantly limits the distinguishability of 1’s and 0’s as the data rate increases, resulting in a decreased SNR. Thirdly, the bias conditions between the FPGA and AWG measurements were different. For instance, it is reminded that the violet micro-LED was biased with  $DC_{violet} = 3.3$  V and  $V_{pp} = 1.5$  V for the FPGA data set, and  $DC_{violet} = 1$  V and  $V_{pp} = 5$  V for the AWG data set. A higher DC makes the LEDs “faster” (as higher DC means higher BW). A higher  $V_{pp}$  (as previously stated) increases the LED’s modulation depth, making it easier to distinguish 1’s and 0’s. However, a high DC bias and a  $V_{pp}$  can lead to signal distortion due to the non-linear output of the LEDs.

It is also worth mentioning that the blue-green micro-LED array presented resilience to the increase in data rate and water turbidity, as the data transmissions were demonstrated over a similar number of ALs either the device was modulated by the FPGA or the AWG. However, the limited E-O BW of the green micro-LED (144 MHz, Table 4.1) could explain why a higher data rate was not feasible for the green micro-LED pixel.

### In-series connected device

#### AWG results

The in-series connected device was tested for UWOC under various scattering conditions, following the same procedures described in the previous Section. Figure 4.18 shows the BER values vs the concentration of Maalox. The micro-LED array was DC-biased at 4.5 V, and the modulation depth or  $V_{pp}$  was set at 20 V. A data rate of 50 Mb/s was achieved at  $c_{Maalox} = 0.0068\%$  (or 11 ml of the scattering agent in 160 l of tap water). The latter underwater conditions correspond to 6.46 ALs for the blue channel and 5.34 ALs for the green, similar to the ALs of the individually-addressable blue-green device. It is also outlined that these data transmissions can be feasible through turbid *Jerlov* coastal waters (7C and 9C). The lower data rate (50 Mb/s), when compared to the blue-green micro-LED arrays of different layouts, is attributed to the relatively low E-O BW of the in-series connected device ( $\approx 74$  MHz, Table 4.2). However, the in-series connected device's flexibility in terms of connectivity renders it practical for real-world scenarios as it can be controlled and biased without the deployment of heavy electronic equipment.

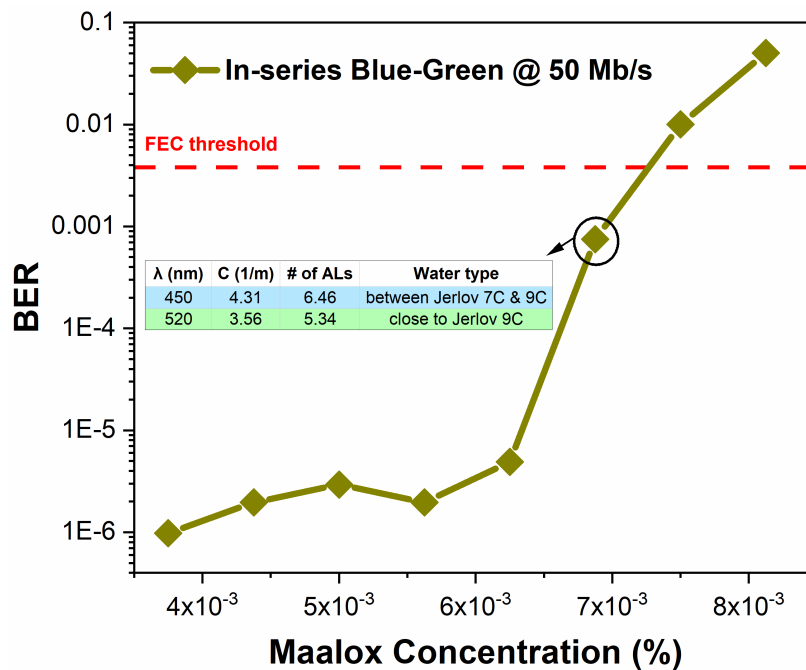


FIGURE 4.18: BER values vs  $c_{Maalox}$  for the in-series connected blue-green micro-LED array at 50 Mb/s.

## 4.4 Summary

The above results denote the practicality of the concept of this work as introduced in Section 4.1; high-speed UWOC (up to 200 Mb/s using OOK) are achievable through WDM over an adequate number of ALs ( $\approx 5$  to 8.5) through various underwater turbidities. The analogy to natural waters is aligned with Jerlov coastal waters (5C, 7C and 9C). The TP method implemented for developing the micro-LED arrays (individually addressable and in-series connected) enabled the simultaneous operation of different colours of micro-LED pixels sitting on the same substrate (sapphire). As the attenuation that an optical signal undergoes underwater is heavily wavelength dependent, one comprehends that the colour tuning of the  $T_x$  and implementing WDM are highly applicable to real-case scenarios. As for the  $R_x$ , a SPAD-array was utilised, suitable for low light level data transmissions, enabling photon detection even under high scattering underwater environments.

More precisely, the maximum data rate of 200 Mb/s was achieved using individually addressable micro-LED arrays: 100 Mb/s through a violet micro-LED (over 5.85 ALs) and 100 Mb/s via a blue micro-LED (over 5.18 ALs) that was transfer-printed onto the violet's substrate. An AWG modulated both devices; a lower (aggregate) data rate of 100 Mb/s (50 Mb/s via each wavelength over 8.52 ALs for the violet and 6.95 ALs for the blue) was achieved when an FPGA modulated the devices.

The array consisting of the blue-green micro-LEDs achieved an aggregate data rate of 150 Mb/s (100 Mb/s via the blue channel over 5.71 ALs and 50 Mb/s via the green channel over 5.34 ALs) when modulated by an AWG. As for the FPGA results, 100 Mb/s were demonstrated: 50 Mb/s for each wavelength, over 6.47 ALs for the blue and 5.78 ALs for the green.

The practicality of an in-series connected micro-LED array consisting of two blue pixels and two green pixels was also examined. The in-series blue-green micro-LED array was modulated by an AWG and achieved 50 Mb/s over 6.46 ALs for the blue wavelength and 5.34 ALs for the green wavelength.

The preliminary results of this work were published and presented in: J. F. C. Carreira *et al.*, "Underwater Wireless Optical Communications at 100 Mb/s using Integrated Dual-Color Micro-LEDs," 2019 IEEE Photonics Conf. IPC 2019 - Proc., pp. 1–2, 2019.

## References

- [1] N. G. Jerlov. Chapter 10 irradiance. In *Optical Oceanography*, volume 5 of *Elsevier Oceanography Series*, pages 115 – 132. Elsevier, 1968.
- [2] J. F. C. Carreira, E. Xie, R. Bian, C. Chen, J. J. D. McKendry, B. Guilhabert, H. Haas, E. Gu, and M. D. Dawson. On-chip GaN-based dual-color micro-LED arrays and their application in visible light communication. *Optics Express*, 27(20):A1517, 2019.
- [3] Alexander Griffiths, Johannes Herrnsdorf, Michael Strain, and Martin Dawson. High sensitivity inter-satellite optical communications using leds and single photon receivers. In *SPACOMM 2019*, United States, 3 2019. IARIA.
- [4] Alexander D. Griffiths, Johannes Herrnsdorf, Oscar Almer, Robert K. Henderson, Michael J. Strain, and Martin D. Dawson. High-sensitivity free space optical communications using low size, weight and power hardware. Workingpaper, 2 2019.
- [5] Marco Lanzagorta. *Underwater Communications*, volume 5. Morgan and Claypool Publishers, 2012.
- [6] Philip Lacovara. High-Bandwidth Underwater Communications. *Marine Technology Society Journal*, 42(1):93 – 102, 2008.
- [7] Yousuke Ito, Shinichiro Haruyama, and Masao Nakagawa. Short-range underwater wireless communication using visible light LEDs. *WSEAS Trans. Commun*, 9:525–552, 2010.
- [8] Mohamed Sufyan Islim, Ricardo X. Ferreira, Xiangyu He, Enyuan Xie, Stefan Videv, Shaun Viola, Scott Watson, Nikolaos Bamiedakis, Richard V. Penty, Ian H. White, Anthony E. Kelly, Erdan Gu, Harald Haas, and Martin D. Dawson. Towards 10 Gb/s orthogonal frequency division multiplexing-based visible light communication using a GaN violet micro-LED. *Photonics Research*, 5(2):A35, 2017.
- [9] Ricardo X G Ferreira, Enyuan Xie, Jonathan J D McKendry, Sujun Rajbhandari, Hyunhae Chun, Grahame Faulkner, Scott Watson, Anthony E. Kelly, Erdan Gu, Richard V. Penty, Ian H. White, Dominic C. O’Brien, and Martin D. Dawson. High Bandwidth GaN-Based Micro-LEDs for Multi-Gb/s Visible Light Communications. *IEEE Photonics Technology Letters*, 28(19):2023–2026, 2016.
- [10] J. F. C. Carreira, A. D. Griffiths, E. Xie, B. J. E. Guilhabert, J. Herrnsdorf, R. K. Henderson, E. Gu, M. J. Strain, and M. D. Dawson. Direct integration of micro-LEDs and a SPAD detector on a silicon CMOS chip for data communications and time-of-flight ranging. *Opt. Express*, 28(5):6909 – 6917, Mar 2020.
- [11] E. Menard, K. J. Lee, D.-Y. Khang, R. G. Nuzzo, and J. A. Rogers. A printable form of silicon for high performance thin film transistors on plastic substrates. *Applied Physics Letters*, 84(26):5398–5400, 2004.
- [12] Matthew A. Meitl, Zheng Tao Zhu, Vipin Kumar, Keon Jae Lee, Xue Feng, Yonggang Y. Huang, Ilesanmi Adesida, Ralph G. Nuzzo, and John A. Rogers. Transfer printing by kinetic control of adhesion to an elastomeric stamp. *Nature Materials*, 5(1):33–38, 2006.
- [13] Seok Kim, Jian Wu, Andrew Carlson, Sung Hun Jin, Anton Kovalsky, Paul Glass, Zhuangjian Liu, Numair Ahmed, Steven L. Elgan, Weiqiu Chen, Placid M. Ferreira, Metin Sitti, Yonggang Huang,



- and John A. Rogers. Microstructured elastomeric surfaces with reversible adhesion and examples of their use in deterministic assembly by transfer printing. *Proceedings of the National Academy of Sciences*, 107(40):17095–17100, 2010.
- [14] A. J. Trindade, B. Guilhabert, D. Massoubre, D. Zhu, N. Laurand, E. Gu, I. M. Watson, C. J. Humphreys, and M. D. Dawson. Nanoscale-accuracy transfer printing of ultra-thin AlInGaN light-emitting diodes onto mechanically flexible substrates. *Applied Physics Letters*, 103(25), 2013.
- [15] A. J. Trindade, B. Guilhabert, E. Y. Xie, R. Ferreira, J. J. D. McKendry, D. Zhu, N. Laurand, E. Gu, D. J. Wallis, I. M. Watson, C. J. Humphreys, and M. D. Dawson. Heterogeneous integration of gallium nitride light-emitting diodes on diamond and silica by transfer printing. *Optics Express*, 23(7):9329, 2015.
- [16] MicroChem. SU-8 2000 Permanent Epoxy Negative Photoresist, Processing guidelines for: SU-8 2000.5, SU-8 2002, SU-8 2005, SU-8 2007, SU-8 2010 and SU-8 2015. [http://www.micro-resist.de/daten/mcc/su\\_8\\_2000\\_5\\_2015.pdf](http://www.micro-resist.de/daten/mcc/su_8_2000_5_2015.pdf).
- [17] A del Campo and C Greiner. SU-8: a photoresist for high-aspect-ratio and 3d submicron lithography. *Journal of Micromechanics and Microengineering*, 17(6):R81–R95, may 2007.
- [18] D. Kang, A. Standley, J. H. Chang, Y. Liu, and Y. Tai. Effects of deposition temperature on Parylene-C properties. In *2013 IEEE 26th International Conference on Micro Electro Mechanical Systems (MEMS)*, pages 389–390, 2013.
- [19] Brian J. Kim and Ellis Meng. Micromachining of Parylene C for bioMEMS. *Polymers for Advanced Technologies*, 27(5):564 – 576, 2016.
- [20] E. Fred Schubert. *Light Emitting Diodes - Ch. 5 LED basics: Optical properties*, page 86–100. Cambridge University Press, 2 edition, 2006.
- [21] Sujan Rajbhandari, Jonathan J.D. McKendry, Johannes Herrnsdorf, Hyunchae Chun, Grahame Faulkner, Harald Haas, Ian M. Watson, Dominic O’Brien, and Martin D. Dawson. A review of gallium nitride LEDs for multi-gigabit-per-second visible light data communications. *Semiconductor Science and Technology*, 32(2), 2017.
- [22] Mary H. Crawford. LEDs for solid-state lighting: Performance challenges and recent advances. *IEEE Journal on Selected Topics in Quantum Electronics*, 15(4):1028–1040, 2009.
- [23] J. Ryou, P. D. Yoder, J. Liu, Z. Lochner, H. Kim, S. Choi, H. J. Kim, and R. D. Dupuis. Control of Quantum-Confined Stark Effect in InGaN-Based Quantum Wells. *IEEE Journal of Selected Topics in Quantum Electronics*, 15(4):1080 – 1091, July 2009.
- [24] A. Maccarone. *Single-photon Detection Techniques for Underwater Imaging*. Heriot-Watt University, 2016.
- [25] J. Kosman, O. Almer, T. A. Abbas, N. Dutton, R. Walker, S. Videv, K. Moore, H. Haas, and R. Henderson. 29.7 A 500Mb/s -46.1dBm CMOS SPAD Receiver for Laser Diode Visible-Light Communications. In *2019 IEEE International Solid- State Circuits Conference - (ISSCC)*, pages 468–470, 2019.
- [26] Thorlabs. Operational Manual of the SPCMxxA Single Photon Counting Module. <https://www.thorlabs.com/thorproduct.cfm?partnumber=SPCM20A/MS>.

- 
- [27] Brandon Cochenour, Linda Mullen, and John Muth. Effect of scattering albedo on attenuation and polarization of light underwater. *Optics Letters*, 35(12):2088–2090, 2010.
- [28] Keysight. M8190A Arbitrary Waveform Generator. Data Sheet. <https://www.keysight.com/gb/en/assets/7018-02903/data-sheets/5990-7516.pdf>.

## Chapter 5

# Underwater Wireless Omnidirectional Optical Beacon Using Light-Diffusing Fibre

### 5.1 Introduction

The work presented in previous chapters, along with the UWOC links that have been widely reported in the literature, refer to typically “point-to-point” links, where a single  $T_x$  addresses a single  $R_x$ . This suggests that the optimal optical alignment between  $T_x$  and  $R_x$  is continuously preserved. However, as discussed in Chapter 1, the optical channel is affected and compromised by the inherent optical properties (IOP) of water, molecular absorption and molecular scattering due to small temperature and density fluctuations, and macroscopic absorption and scattering due to organic and inorganic particles which can significantly decrease the signal quality and/or limit the optical link range. In addition, the external diverse environmental conditions in the open ocean, such as heavy winds, can result in stormy waters and severe underwater currents, which would render the maintenance of the optical alignment between  $T_x$  and  $R_x$  quite challenging or in some cases implausible. Furthermore, tethered links can be expensive and impractical in the challenging underwater environment.

To mitigate the alignment restrictions in an underwater channel, this chapter reports the deployment of the Corning®Fibrance®Light-Diffusing Fibre [1] as an underwater omnidirectional “beacon”. For convenience, the fibre will be referred as “Fibrance fibre” for the rest of the chapter. A detailed description of the critical features of the Fibrance fibre will be given in Section 5.1.1. However, it is worth mentioning that this fibre exhibits the property of scattering light uniformly along its length instead of delivering

it from point to point over long distances. In this way, a simple and cost-effective omnidirectional beacon is realised with no moving or complex optical and mechanical parts or precise underwater alignment. The Fibrance fibre could establish a wireless link within a volume of water covered by the beacon, such as a ship broadcasting to multiple divers or ROVs and UUVs that are in proximity to the ship. In contrast, tracking and aligning each link separately with point-to-point cases would be necessary. Another scenario could be that an ROV employs the beacon concept to communicate to a surface vessel without continuously tracking and optically aligning the data link. As discussed previously, optical wireless data links can remove the need for tethered communications, significantly increasing mobility and functionality and reducing costs. A conceptual illustration of how the Fibrance fibre concept could be implemented in real-world applications is shown in Figure 5.1.

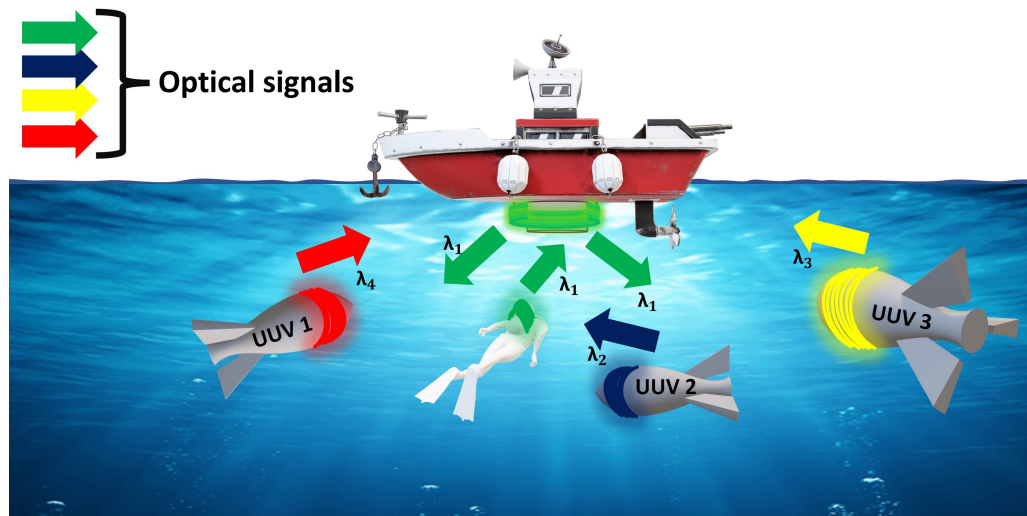


FIGURE 5.1: Schematic illustration of the beacon concept. The Fibrance fibre could be implemented, e.g. at the hull of a surface vessel and send data omnidirectionally underwater to UUVs which are in proximity to the ship. No sophisticated optical components nor precise alignment are required. The same idea is followed for the UUVs, where optical signals of different wavelengths can be transmitted or received to other UUVs or/and the surface vessel.

The omnidirectional beacon is here placed at the ship's hull and coupled to a light source located, e.g. on the vessel's deck, thereby transmitting wireless underwater data to UUVs. Following appropriate engineering, the Fibrance fibre could be wrapped around a UUV and send the collected data to the surface vessel, such as high-definition video or pictures from the seabed. In this way, the time-consuming and costly procedures of pulling the unmanned vehicle out, placing it on the ship's deck, unloading data, and putting it back in the water are significantly avoided. Depending on the underwater conditions, different wavelengths of optical signals can also be deployed to different multiplex receivers, as suggested by Figure 5.1, and as further examined in Section 5.5.

### 5.1.1 Details of the Fibrance fibre

The Fibrance fibre is a patented product [2], invented by Corning Inc. Some of the Fibrance fibre's main application domains are depicted in Figure 5.2 and involve use in speciality lighting, signage and display purposes [3].

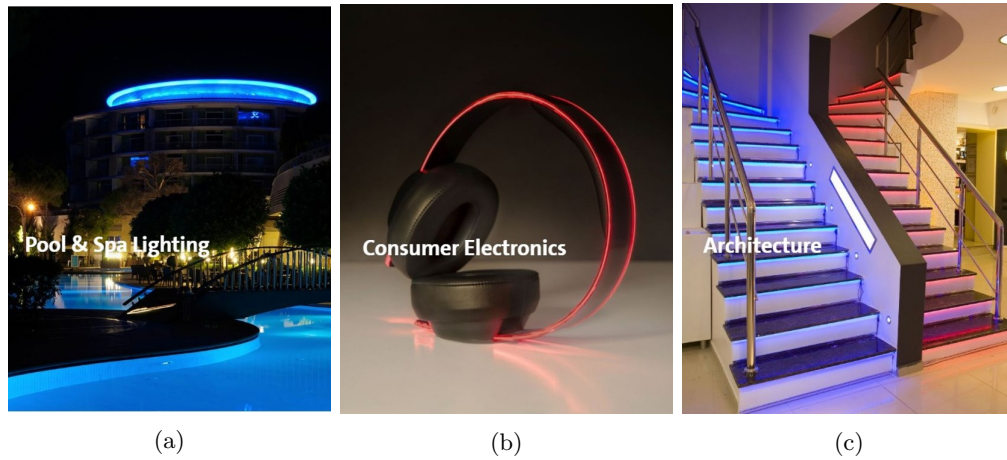


FIGURE 5.2: Examples of the Fibrance's application domains in (a) lighting, (b) electronics, and (c) architecture. Images taken from [3].

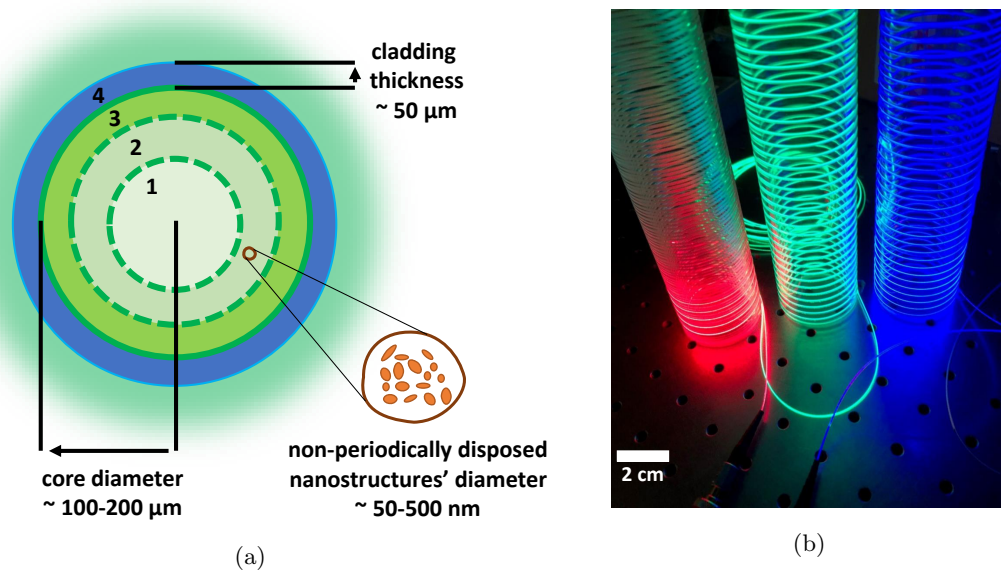


FIGURE 5.3: (a) Cross section of the Fibrance fibre; the core is divided into three regions (1, 2, 3), and the cladding area corresponds to region 4. (b) Optical image from glowing Fibrance fibres wrapped in spirals.

The glass core of the Fibrance fibre, whose diameter is between  $100\text{-}200\ \mu\text{m}$ , consists of pure or fluorine-doped silica and is divided into three regions; 1, 2, and 3, as shown in Figure 5.3a, where a cross-section of the Fibrance is illustrated. Section 1 and section 3 refer to the solid central and outer solid regions, respectively. Section 2 comprises a

ring-shaped area (“*inner annular core region*”), where has been placed non-periodically disposed nano-sized structures, reported as voids filled with gas [2, 4]. The cladding, which corresponds to section 4 in Figure 5.3a, is approximately  $50\ \mu\text{m}$  thick and consists of a low refractive index material, such as acrylate- or silicone-based polymer. The uniqueness of this thin and flexible fibre lies in the aforementioned nano-sized scattering centres, which scatter the coupled light (from an LED- or laser-based device) away from the core and towards the outer surface of the fibre. Then, the light is diffused through the sides of the fibre and is emitted along the Fibrance fibre’s length. This “glowing” effect can be easily seen in Figure 5.3b, where three Fibrance fibres were coupled to off-the-shelf LDs of different operational wavelengths and wrapped around three tubes for demonstration purposes. The magnitude of the scattered light can be changed by adjusting the size of the scattering centres whose diameter varies from 50-500 nm [2].

Different offerings of Fibrance fibres are identified by the light-diffusion lengths; 1 m, 5 m, and 10 m, whereas custom fibre diffusion lengths are also available [5]. According to Corning Inc., a diffusion length is defined as the point along the length of the Fibrance fibre at which the optical power of the emitted light through the fibre’s outer cladding is reduced to 1/10 of the initial optical power coupled into the fibre at the input facet ( $P = P_0/10$ ) [6], following an exponential decay, as shown graphically in Figure 5.4 [5, 6]. Hence, assuming that the cumulative emitted optical power right after the fibre coupler is maximum, after 1 m, i.e. at the opposite end of the fibre, the emitted optical power will have been decreased by 90%. The same consideration apply to the fibres of 5 m and 10 m diffusion length.

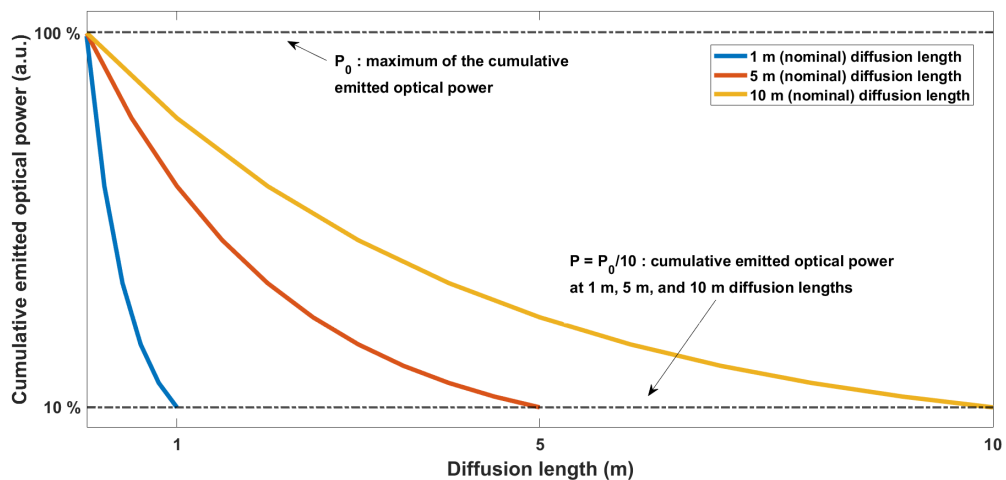


FIGURE 5.4: Graphical representation of the diffusion characteristics of the Fibrance fibre; 90% of the coupled input optical power is emitted as a diffuse output at 1 m, 5 m, and 10 m diffusion lengths, respectively. Adapted from [5, 6].

The scattering properties of the Fibrance fibre, along with its flexibility and affordability, have attracted interest for several potential applications. For instance, by exploiting the Fibrance fibre’s diffusing properties and coupling short-wavelength light into Fibrance, light can be delivered into areas which other bulky light sources cannot easily access for applications such as polymer photo-curing and/or stimulation of biological material by photoreaction [4]. The same concept can be applied in medical applications, e.g. in photodynamic therapy, where a photochemical drug is activated by targeted radiation of a specific wavelength and thus, cancer cells and tissues can be destroyed [7]. However, little has been reported in the communications field regarding the deployment of Fibrance fibre. The following sections will analyse how the light-diffusion fibre enabled omnidirectional wireless underwater data transmission over clear and turbid waters.

## 5.2 Experimental set-up

### 5.2.1 Set-up description

The experimental set-up for this work is depicted in Figure 5.5. As previously mentioned, the Fibrance fibre was deployed as  $T_x$ , in the form of an underwater beacon, to send data omnidirectionally without the need for precise alignment with respect to the  $R_x$  nor optical and mechanical components.

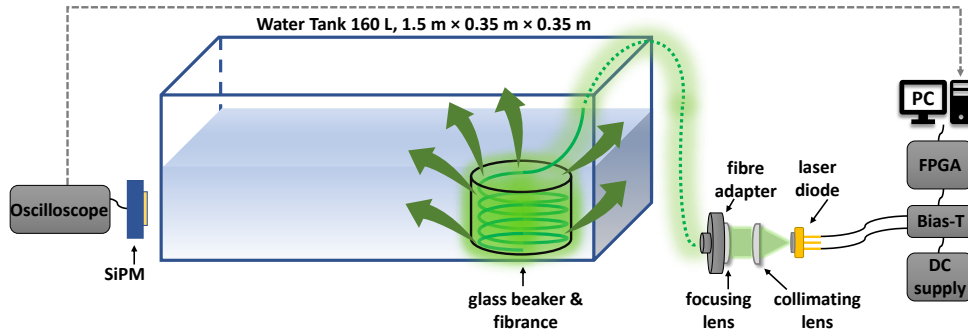


FIGURE 5.5: The experimental set-up for the underwater wireless optical communications system based on deploying the Fibrance fibre as  $T_x$ .

The 5 m long Fibrance fibre was coupled with an off-the-shelf InGaN LD (Osram, PL520), whose actual wavelength of operation is approximately 514 nm and which has a linewidth of 1.13 nm FWHM at 90 mA. The electroluminescence (EL) spectrum of the LD, shown in Figure 5.6a, was obtained through an optical fibre-coupled spectrometer (Avantes, AvaSpec-2048L) at the same current value (90 mA). The LI and the IV curves, are plotted in Figure 5.6b, where it can be noticed that the emitted optical power of the LD at 90 mA is approximately 32 mW. The forward detected output optical power of

the beam upon collimation through an aspheric lens (Thorlabs, C240TME-A) was about 5 mW as measured via a calibrated Si photodiode power sensor of area  $9.7 \times 9.7 \text{ mm}^2$  (Thorlabs, S121C) and connected to a power meter (Thorlabs, PM100A). This light was then focused by an identical aspheric lens as previously (Thorlabs, C240TME-A) and coupled through a fibre adapter plate (Thorlabs, SM1ST) to the Fibrance fibre.

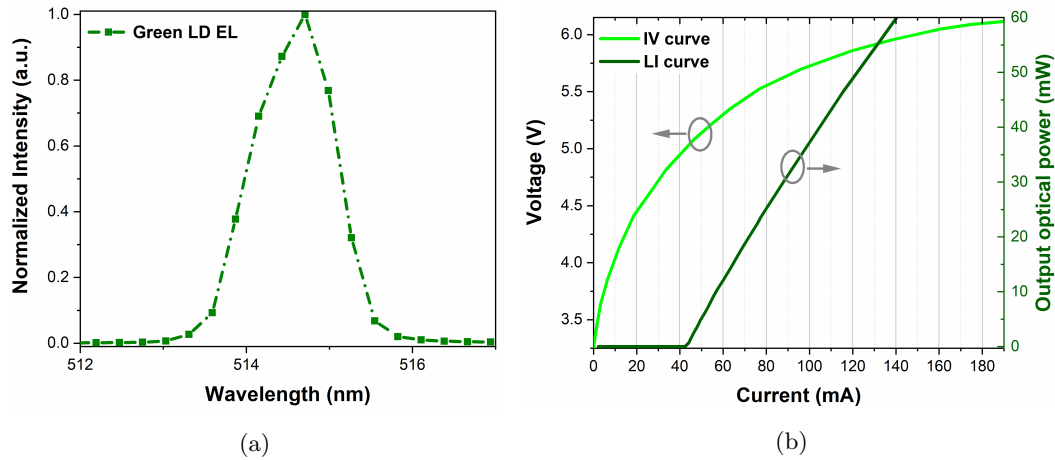


FIGURE 5.6: (a) The measured EL spectrum of the LD. (b) IV and LI curves of the LD (adapted from [8]).

The Fibrance fibre was placed inside a glass beaker (see Figure 5.7a), and the beaker positioned at the bottom of the 1.5 m long water tank (see Figure 5.7b), filled with 160 l of tap water. To prevent reflections from the tank's walls that would not occur in open waters and may lead to multipath signal distortions, matt black plastic sheets were placed at the bottom and around its walls. The OOK modulation scheme (see Section 2.2.1) was used for generating a pseudo-random bit sequence (PRBS) of 127 bits via an FPGA (Opal Kelly, XEM3010). The FPGA data output and DC supply (Yokogawa, GS610) of 6.5 V were combined to drive the LD via a bias tee (Mini-Circuits, ZFBT-4R2G+). A MATLAB<sup>®</sup> script ran the FPGA through a PC, whereas the modulation data rate was 5 Mb/s. Following the same process as in previous chapters, the turbidity of the water was varied by adding Maalox<sup>®</sup> antacid in the water tank, starting from 0 ml of the scattering agent to 160 l of tap water and finishing up to 40 ml that corresponds to a concentration of 0.025% at the same volume of water.



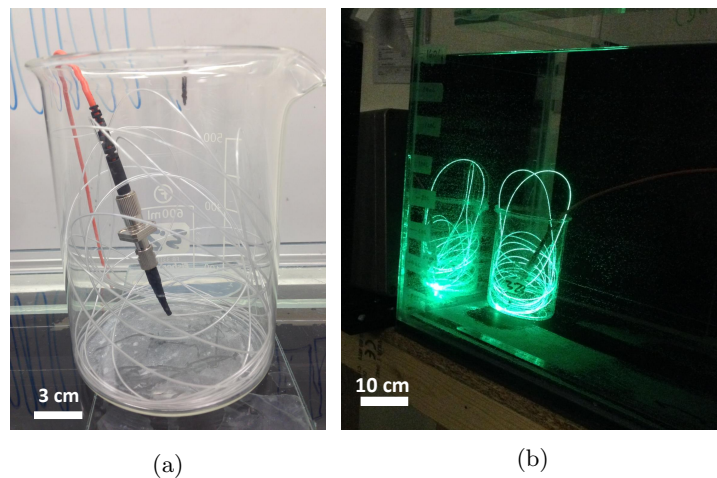


FIGURE 5.7: (a) Optical image of the Fibrance fibre in the glass beaker. (b) Optical image of the illuminated Fibrance fibre in the water tank.

As for the  $R_x$ , a  $6 \times 6 \text{ mm}^2$  SiPM (SensL J-Series, 60035) was placed at the other side of the tank, approximately aligned with the Fibrance fibre which was sufficient enough to collect part of the signal propagated through water (no receiver optics were used), either scattered due to Maalox or not. The SiPM was connected to an oscilloscope for monitoring the captured signal, and the data were transferred back to the PC for further offline analysis. For the majority of the measurements, the distance between  $T_x$  and  $R_x$  was fixed to the maximum possible 1.5 m. However, for high scattering conditions (above 11 ALs) and beyond 24 ml, or 0.015% in concentration, of the scattering agent), the distance was decreased by moving the beaker in the water tank closer to the SiPM, which resulted in a captured signal of better quality but of reduced number of ALs. This can be easily explained as the number of ALs is given by the product  $c \cdot z$ , where  $c$  is the attenuation coefficient of the water sample, and  $z$  gives the propagation distance of the captured optical signal. Small  $z$  results in a low number of ALs.

### 5.2.2 Underwater channel characterisation

The underwater channel characterisation was based on the method described in Section 1.6. By measuring the transmitted and received power,  $P_T$  and  $P_R$ , respectively, over a propagation distance  $z$ , the wavelength-dependent attenuation coefficient ( $c(\lambda)$  in  $\text{m}^{-1}$ ) can be calculated through Equation 1.10, as well as the unit-less number of ALs ( $c(\lambda) \cdot z$ ) [9]. The calculated attenuation coefficient versus Maalox content for the operational wavelength for this work (514 nm), with their first order polynomial fit, are shown in Figure 5.8. For comparison, the typical values of the attenuation coefficients for three *Jerlov* oceanic types (I-III) and four *Jerlov* coastal types (3C-9C) are also shown. These values were acquired from [10] and calculated for  $\lambda = 525 \text{ nm}$ , the closest wavelength to the Osram LD's measured peak emission wavelength.

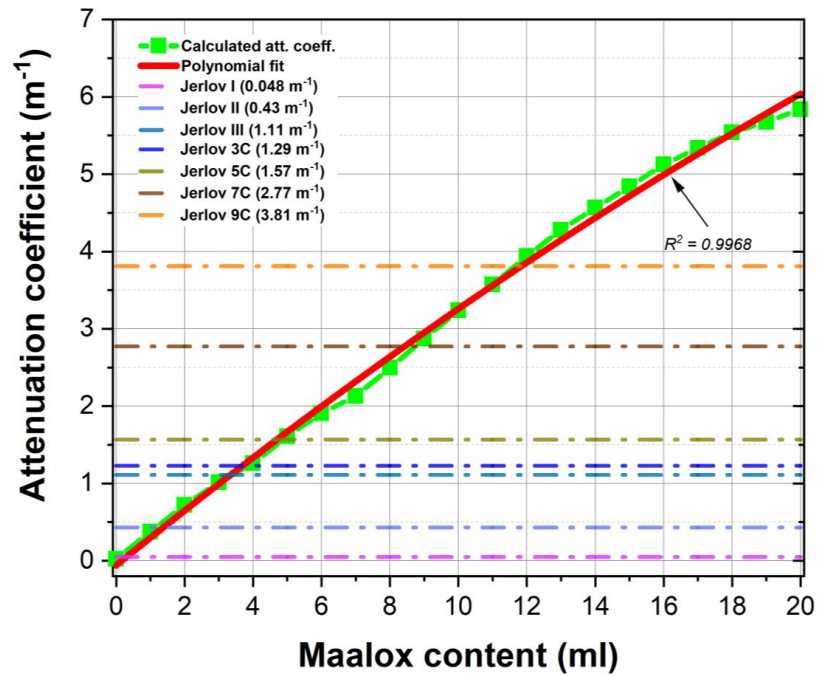


FIGURE 5.8: The calculated attenuation coefficient for  $\lambda = 514$  nm vs Maalox content with their second order polynomial fit and the values for  $c(525$  nm) of *Jerlov* water types for reference.

As seen from Figure 5.8, the content of the scattering agent started from 0 ml and ended at 20 ml (or 0.0125% in concentration) in 160 l of tap water. From the above graph, it can be deduced that light undergoes heavier attenuation as the Maalox content increases, since scattering is the dominant process which prevents photons from arriving at the power meter sensor. However, as explained in Section 1.6, for contents of the scattering agent above 16 ml (with a corresponding number of ALs = 7.7), the linearity between  $c(\lambda)$ -Maalox content breaks down as the signal (in our case the received power), attenuates at a slower rate. For Maalox contents above 16 ml (or 0.01% in concentration), the estimation for  $c(\lambda)$  and number of ALs can be derived by the second order polynomial fitting curve that describes the variation of  $c(\lambda)$  versus Maalox content (Figure 5.8 and Table 5.1).

TABLE 5.1: Values for Maalox content and concentration, and for the respective  $c(\lambda)$  and number of ALs. The values shown in this table for  $c(\lambda)$  and ALs were derived from the second order polynomial fitting curve shown in Figure 5.8.

Maalox content (ml)	Maalox conc. (%)	$c$ ( $\text{m}^{-1}$ )	ALs
18	0.0112	5.52	8.29
20	0.0125	6.04	9.06
24	0.0150	6.77	10.15
28	0.0175	7.87	11.81
35	0.0218	9.02	13.8
40	0.0250	9.98	14.97

### 5.3 Background theory and methodology

The results based on the Fibrance fibre measurements were extracted by constructing eye diagrams for each underwater channel and estimating the corresponding BERs. As such, a brief description of an eye diagram is given in the following sections. Secondly, we describe the background theory and methodology that was followed for the eye diagrams and corresponding histogram construction and the calculation of BER.

#### 5.3.1 Eye diagrams

Eye diagrams are widely used in high-speed communications and electrical engineering to assess the received signal's quality visually. They are created by repeatedly superimposing successive segments of a data stream transmitted in reference to a "master clock" signal. Ideally, an eye diagram would resemble a rectangular box as the transitions between 1's and 0's would be instantaneous and free from noise and distortion. In reality, however, these rise and fall times of signals are finite, suffer from random time jitter and noise, and thus, they do not lie perfectly on top of each other. The deviation of the digital signal is attributed, amongst other effects, to manufacturing and installation errors, or/and digital signal reflections, crosstalk and intersymbol interference (ISI), which result in the formation of an eye-shaped image, an example of which is illustrated in Figure 5.9. Binary "0" and "1" represent the mean values of logic 0's and 1's, respectively, while the amplitude shows the difference between the logic levels or the vertical opening of the eye. Based on that difference and the power (or voltage) threshold (indicated as "*Decision threshold*" in Figure 5.9), the receiver will determine whether a received bit is "0" or "1". The presence of noise or distortion causes the eye to shrink. On the other hand, an "open eye" indicates that the signal is of good quality and error-free. The optimum time to sample the bit stream is when the most open part of the eye occurs (indicated as "*Best time to sample*" in Figure 5.9), meaning

best signal-to-noise ratio (SNR). The bit period is defined as the inverse of the data rate and indicates the horizontal opening of the eye. Timing errors are also crucial in determining signal quality, mainly when high-speed signals are transmitted. One such timing error that also causes eye shrinkage is jitter, which refers to the time deviation from the periodicity of a data-bit event or the misalignment of rise and fall times.

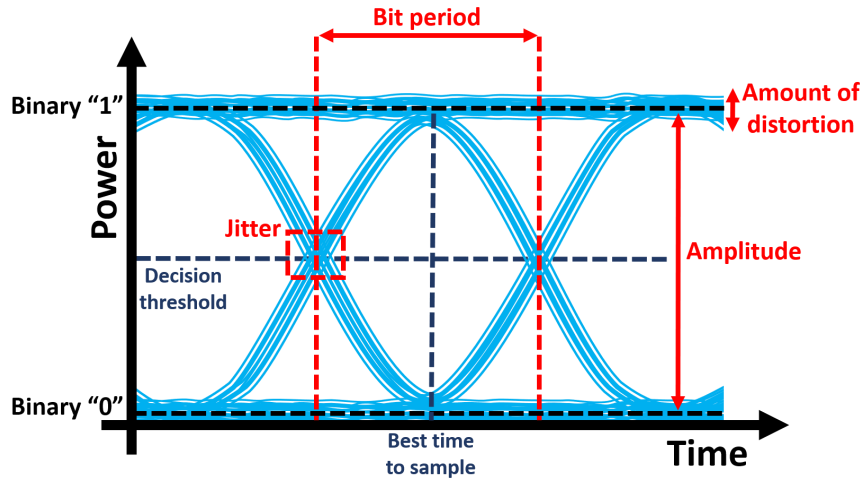


FIGURE 5.9: Graphical illustration of an eye diagram.

### 5.3.2 Methodology for calculating Bit-Error Ratios

The process for the extraction of the Fibrance fibre measurements' BERs, was based on the work from Shake and Takara (2002) [15] and is as follows. Figure 5.10 shows the constructed eye diagram from the OOK received signal at 0 ml of the scattering agent. "Upper" and "Lower" refer to the logic 1 and 0 levels. The bit stream is sampled at  $time = \tau$  where the maximum eye opening occurs, i.e. approximately at the centre of the bit period. The corresponding logic levels' voltage distributions around a voltage threshold are also depicted on the left side of the figure.

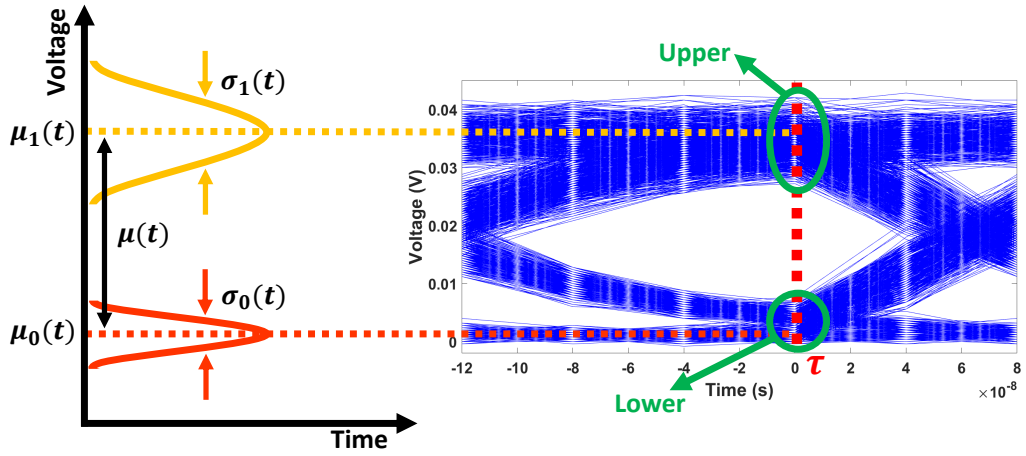


FIGURE 5.10: Constructed eye diagram at 5 Mb/s over 0.04 ALs (0 ml of Maalox) on the right and the corresponding 1's (Upper) and 0's (Lower) normal distribution on the left.

It is worth reminding here that the SiPM ( $R_x$ ) consists of an array of SPADs (see Section 2.1.6) and the photon detection follows Poissonian distribution [16]. However, for this work, it is assumed that the number of received photons is large enough such that each distribution around the logic levels can be approximated by a normalised Gaussian [17] through Equation 5.1:

$$G(t) = \frac{1}{\sqrt{2\pi}\sigma(t)} e^{-\frac{(\tau - \mu(t))^2}{2\sigma^2}}, \quad (5.1)$$

where  $\sigma(t)$  and  $\mu(t)$  are the distribution's standard deviation and mean value, respectively. Then, the  $Q$ -factor (or Quality factor) can be defined as:

$$Q = \frac{|\mu_1(t) - \mu_0(t)|}{\sigma_1 + \sigma_0}, \quad (5.2)$$

where  $\mu_1$ ,  $\mu_0$ ,  $\sigma_1$ , and  $\sigma_0$  are the mean values and standard deviations of the Upper (1's) and Lower (0's) logic levels, respectively. The  $Q$ -factor measures how clearly separated the distribution of Upper and Lower values are. A high  $Q$  indicates that the distributions are distinctly separated, making distinguishing a 1 from a 0 easy. On the other hand, a low  $Q$  shows that the distributions are wide and close together, resulting in the logic levels' overlapping, and thus, some 1's can be mistaken as 0's, and vice versa. Following Equation 5.1 and by setting the exponential's numerator as:

$$z^2 = \frac{(\tau - \mu(t))^2}{2\sigma(t)^2} \Rightarrow dz = \frac{1}{\sqrt{2}\sigma(t)} d\tau \Rightarrow d\tau = \sqrt{2}\sigma(t) dz, \quad (5.3)$$

the normalised Gaussian distribution, integrated between  $-\tau$  and  $+\tau$ , can be written as:

$$\int_{-\tau}^{\tau} G(t)dt = \frac{1}{\sqrt{2\pi}\sigma(t)}\sqrt{2}\sigma(t) \int_{-\tau}^{\tau} e^{-z^2} dz = \frac{1}{\sqrt{\pi}} \int_{-\tau}^{\tau} e^{-z^2} dz. \quad (5.4)$$

Claiming that the normalised Gaussian is symmetric around the  $y$ -axis, the Error function (erf) can be defined, and Equation 5.4 is now written as:

$$\int_{-\tau}^{\tau} G(t)dt = \frac{2}{\sqrt{\pi}} \int_0^{\tau} e^{-z^2} dz \equiv \text{erf}(t). \quad (5.5)$$

Then, the Complementary Error function (erfc) arises directly from the erf, as follows:

$$\text{erfc}(t) \equiv 1 - \text{erf}(t) = \frac{2}{\sqrt{\pi}} \int_{\tau}^{\infty} e^{-z^2} dz. \quad (5.6)$$

Practically, the Error function indicates the probability that a value of interest (that is  $\tau$ , for the above description) can be found within the range  $\pm t/(\sqrt{2}\sigma)$ . The Complementary Error function represents the probability that  $\tau$  is outside that range [18, 19]. Finally, the BER, which is the key quantity of interest for this work, is related to the erfc and can be extracted through the following equation [15]:

$$BER = \frac{1}{2} \text{erfc} \left( \frac{Q}{\sqrt{2}} \right). \quad (5.7)$$

The fitting of the Gaussian distributions on the histograms of the Upper and Lower levels (as shown in Figure 5.10) defined the mean values and standard deviations for each content of the scattering agent tested for this work. As such, the calculation of the  $Q$ -factor via Equation 5.2 was enabled, and subsequently, the BER at the fixed data rate of 5 Mb/s for every water sample was provided via Equation 5.7. The constructed voltage histograms can be seen in Section 5.4.2 where the voltage distributions (noise) for each logic level (Upper and Lower) along with the corresponding eye diagrams are depicted around a voltage threshold which was set manually to give the best BER result.

## 5.4 Results

### 5.4.1 Data streams

The 0 to 3.3 V digital PBRS signal sent to the LD and optically transmitted through the water had the form as shown in Figure 5.11 (top). As mentioned, the PRBS is 127

bits long and was transmitted at a fixed data rate of 5 Mb/s. For comparison, along with the digital signal, the received signal through clear tap water (no scattering agent added) over 0.04 ALs is also shown in Figure 5.11 (bottom).

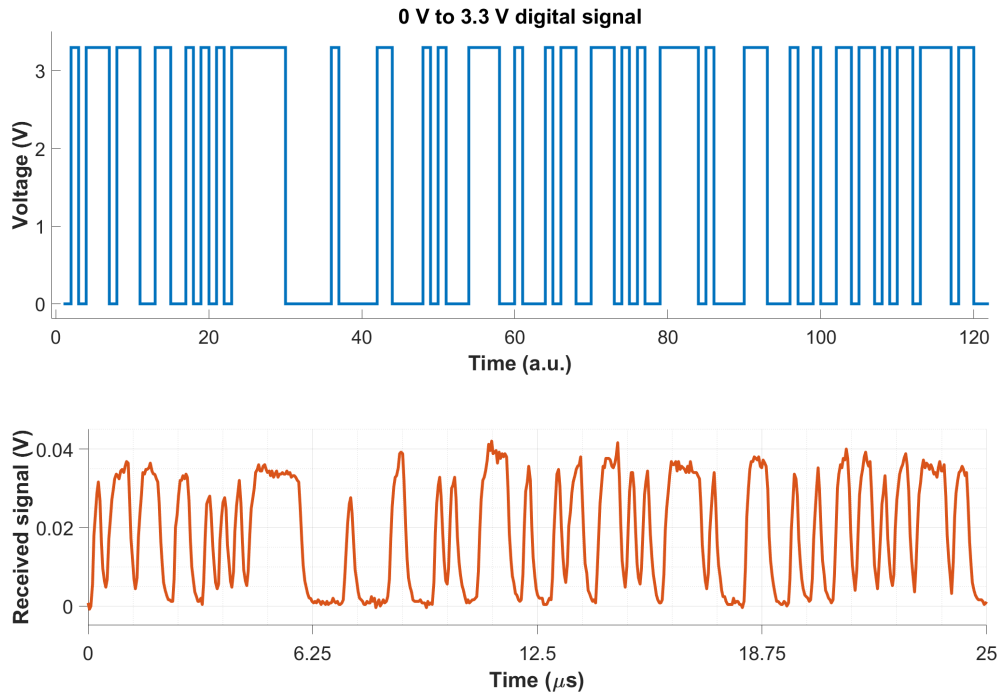
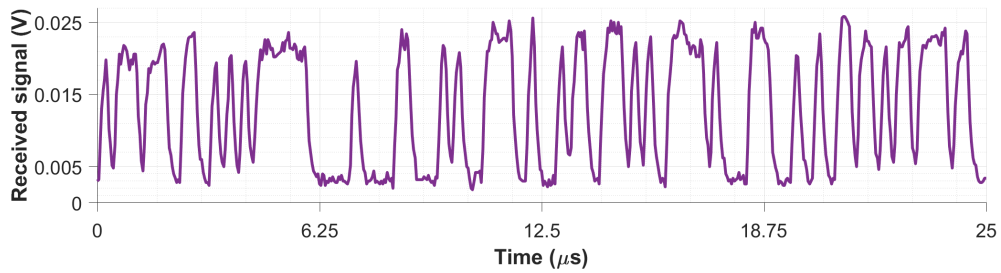
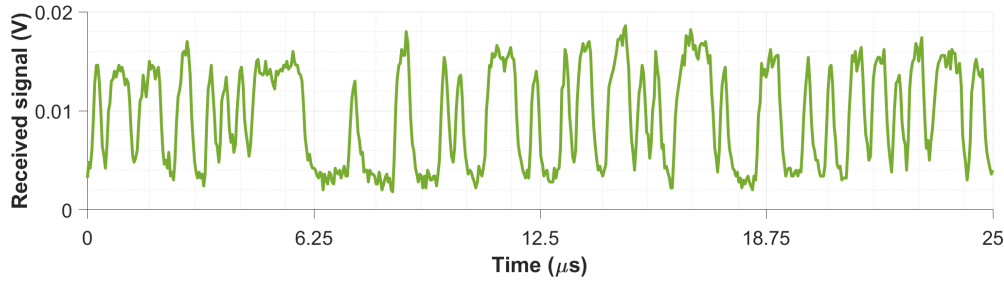


FIGURE 5.11: The forms of the digital signal (top) sent to the LD, and (bottom) the received signal at 5 Mb/s over 0.04 ALs (0 ml of Maalox).

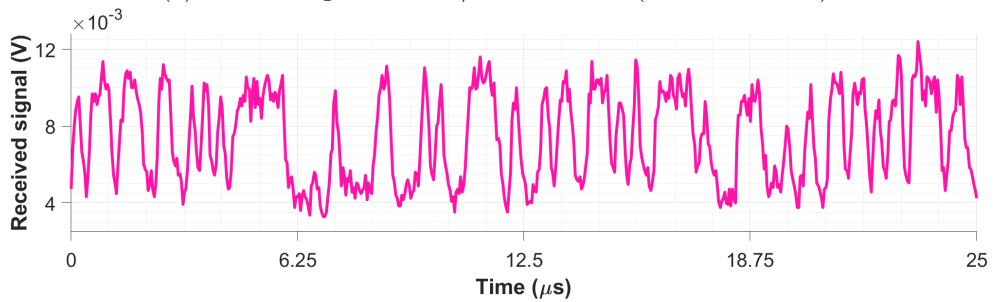
The form of the received signals over various turbidities can be seen in Figures 5.12a-5.12d. These were obtained by adding 8 ml, 16 ml, 28 ml, and 40 ml of Maalox in the water tank, while the corresponding number of ALs was 3.75, 7.7, 11.81, and 14.97. For all the received signal plots, time on the  $x$ -axis represents the time duration of a single data stream, equal to  $25.4 \mu\text{s}$  (i.e. the number of bits per bit steam  $\times$  bit period =  $127 \text{ bits} \times \frac{1}{5 \times 10^6} \frac{\text{sec}}{\text{bits}}$ ).



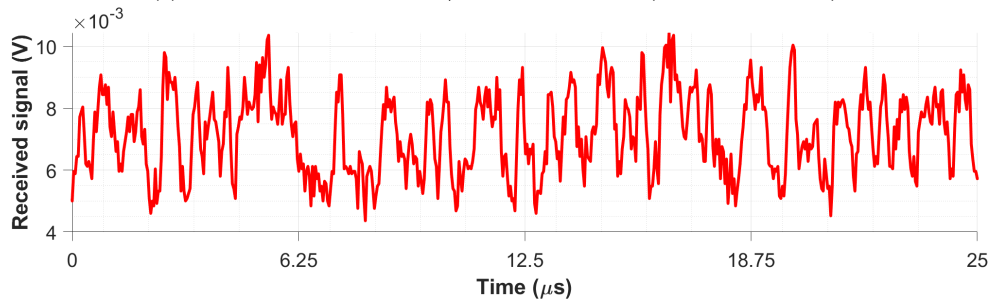
(a) Received signal at 5 Mb/s over 3.75 ALs (8 ml of Maalox).



(b) Received signal at 5 Mb/s over 7.7 ALs (16 ml of Maalox).



(c) Received signal at 5 Mb/s over 11.81 ALs (28 ml of Maalox).



(d) Received signal at 5 Mb/s over 14.97 ALs (40 ml of Maalox).

FIGURE 5.12: The forms of the received signals at 5 Mb/s over various water turbidities. As the water becomes more turbid due to the added scattering agent, the received signal experiences an attenuation of approximately 60% and becomes noisier.

Visual inspection of Figures 5.11 and 5.12 reveals an adequate similarity between the digital and the received signals, and thus, it can be assumed that the underwater beacon could support the 5 Mb/s data rate over a modest number of ALs. However, it can be observed that the received signal undergoes a decrease in the order of 60% and becomes noisier as the attenuation level increases, making the separation between logic 0's and 1's increasingly difficult. As such, further analysis is required to extract more robust



information on the feasibility of the underwater beacon concept, which will be provided in the following section.

#### 5.4.2 Eye diagram construction, histogram creation and Bit-Error Ratios calculation

The eye diagrams for the underwater Fibrance fibre measurements over clear and turbid water samples were constructed through the MATLAB<sup>®</sup> “*eyediagram*” built-in function. The input arguments included the received bit streams shown in the previous section (5.4.1) and were constructed for underwater wireless optical transmissions at the fixed data rate of 5 Mb/s as defined by the FPGA, over clear tap water and for each Maalox content (1 ml up to 40 ml). The distance between  $T_x$ - $R_x$  was fixed at 1.5 m. Following the method described in [15] and Section 5.3.2, the voltage distribution histograms around a voltage threshold were also built to acquire more precise information on signal distinguishability. Figure 5.13 shows the wide open eye diagram for clear tap water over 0.04 ALs. The water sample’s attenuation coefficient as calculated in Section 5.2.2, was  $0.02 \text{ m}^{-1}$ , a value close to *Jerlov* I ( $0.048 \text{ m}^{-1}$  for  $\lambda = 525 \text{ nm}$ ) water type. The histogram of the logic 1’s and 0’s distributions is also shown on the figure’s right. Both diagrams were constructed around a voltage threshold of 0.02 V at which the BER was lowest ( $1.38 \times 10^{-13}$ ), where it is evident that 0’s are clearly distinguished from 1’s and vice versa.

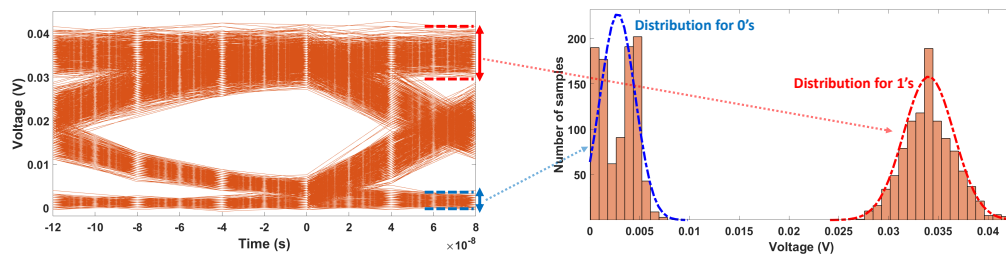
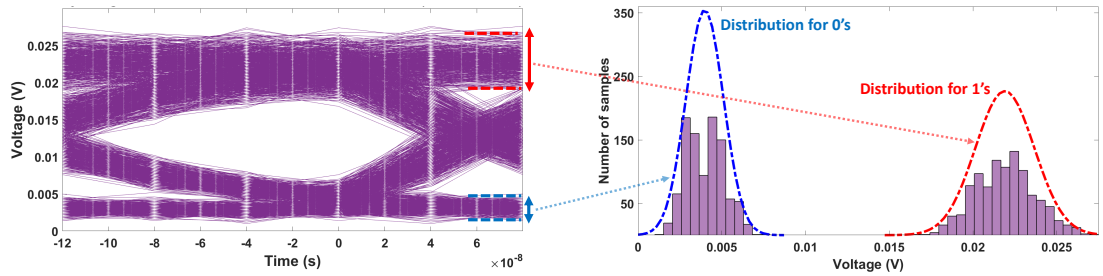


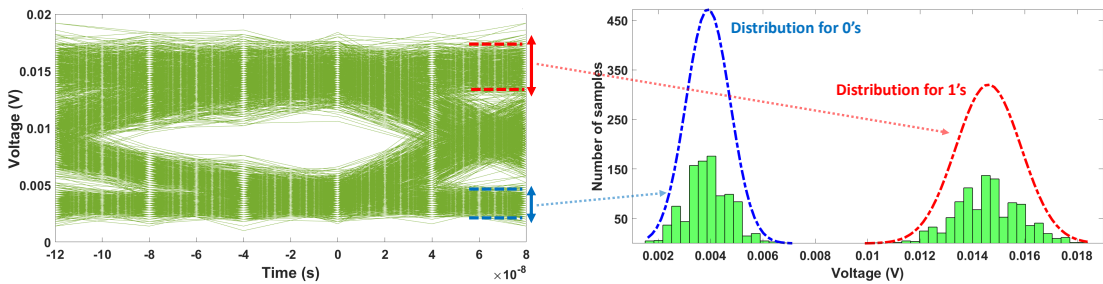
FIGURE 5.13: Constructed eye diagram at 5 Mb/s over 0.04 ALs (0 ml of Maalox) on the left and the normal distributions histogram corresponding to the 1’s (Upper) and 0’s (Lower) on the right. The corresponding received signal for both diagrams is shown in Figure 5.11b.

The resiliency of the underwater beacon concept was further examined for the same scattering agent’s contents as in the previous section (8 ml, 16 ml, and 28 ml). Figures 5.14a - 5.14c show the eye diagrams and the histograms over 3.75, 7.7, and 11.81 ALs, respectively. As before, the voltage threshold was chosen to give the lowest BER values over the above number of ALs;  $2.6 \times 10^{-10}$ ,  $1.48 \times 10^{-7}$ , and  $7.9 \times 10^{-4}$ , respectively. Visual inspection of the eye diagrams below reveals that error-free data transmissions via the underwater beacon should be achievable over 10 ALs. The BER values mentioned above are in alignment with that assumption as they are listed below the FEC threshold

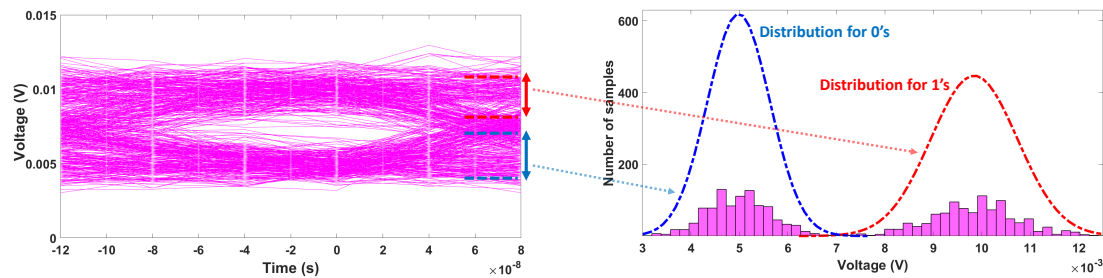
( $3.8 \times 10^{-3}$ ). In addition, it can be seen via the voltage histograms that the  $Q$ -factor (as defined by Equation 5.2) for the Maalox contents of 0 ml, 8 ml, and 16 ml is still high enough to allow a clear separation between 1's and 0's. However, a detailed look in Figure 5.14c shows an evident broadening of the voltage distributions and a slight overlapping of their tails around the voltage threshold of  $\approx 7$  mV. The increased presence of noise, attributed to the large number of scattered photons that do not reach the SiPM, results in a lower  $SNR^*$  and a higher BER.



(a) Constructed eye diagram at 5 Mb/s over 3.75 ALs (8 ml of Maalox) on the left and the corresponding to the 1's (Upper) and 0's (Lower) normal distributions histogram on the right.



(b) Constructed eye diagram at 5 Mb/s over 7.7 ALs (16 ml of Maalox) on the left and the corresponding to the 1's (Upper) and 0's (Lower) normal distributions histogram on the right.



(c) Constructed eye diagram at 5 Mb/s over 11.81 ALs (28 ml of Maalox) on the left and the corresponding to the 1's (Upper) and 0's (Lower) normal distributions histogram on the right.

FIGURE 5.14: The constructed eye diagrams and voltage distribution histograms for error-free underwater wireless optical communication by the Fibrance fibre over varied underwater conditions.

At 40 ml of Maalox and over 14.97 ALs, the eye is completely closed (see Figure 5.15), indicating that error-free data transmission is not feasible. That was also confirmed by the

\* Conventional SNR can be defined as  $SNR = 10 \log_{10} \frac{\bar{P}_{signal}}{\bar{P}_{noise}}$ , where  $\bar{P}_{signal}$  and  $\bar{P}_{noise}$  are the average received power and noise, respectively [16].

BER calculation, which stood above the FEC threshold and equalled  $4.45 \times 10^{-2}$ . Under these highly scattering conditions, photons are severely scattered from their optical path to the  $R_x$ . Furthermore, it can be seen that the tails of the voltage distributions around the logic levels are significantly overlapped. Thus, the detector cannot distinguish 1's from 0's, which results in a strongly distorted captured signal, as shown in Figure 5.12d.

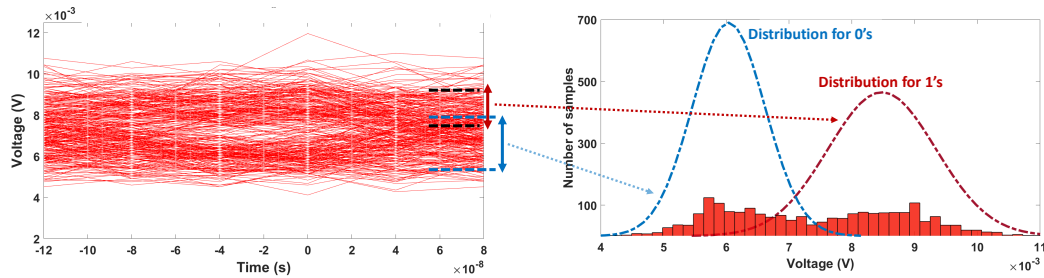


FIGURE 5.15: Constructed eye diagram at 5 Mb/s over 14.97 ALs (40 ml of Maalox) on the left and the corresponding to the 1's (Upper) and 0's (Lower) normal distributions histogram on the right.

The achieved BERs from 16 ml of Maalox and above, as derived by Equation 5.7, over 1.5 m range between beacon and SiPM, are shown in Figure 5.16 as a function of the attenuation coefficient and the number of attenuation lengths for each water sample.

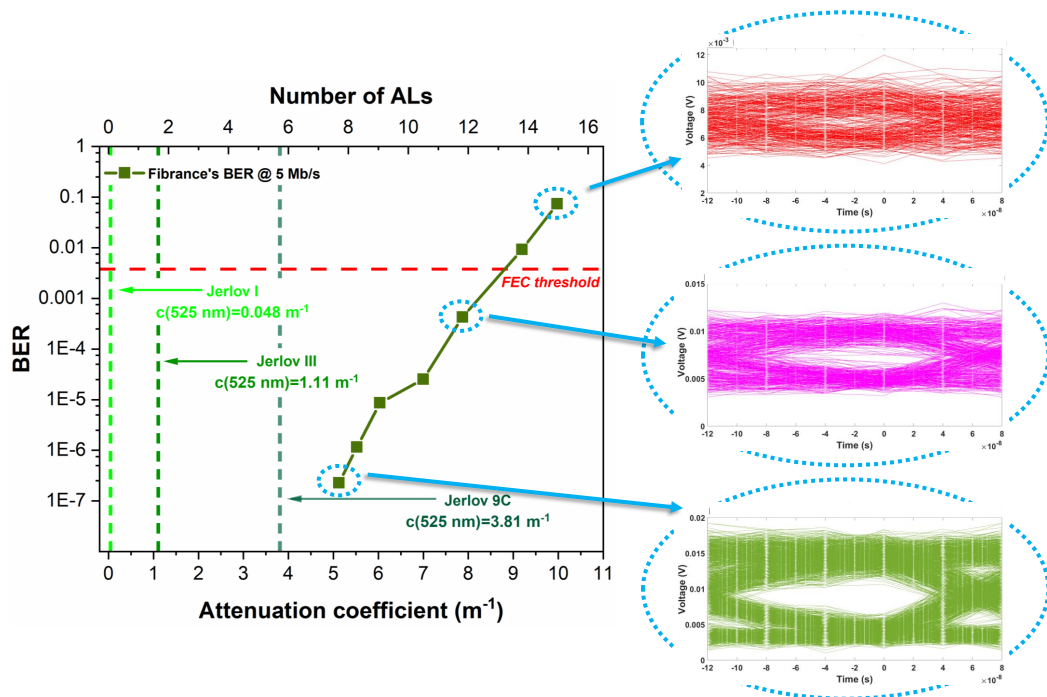


FIGURE 5.16: Achieved BERs vs attenuation coefficients and number of ALs for the Maalox contents tested for this work over 1.5 m between  $T_x$ - $R_x$ .

The first plotted data point corresponds to an achieved BER of  $2.28 \times 10^{-7}$  over a water sample of 16 ml Maalox content (or 0.01% in concentration). The attenuation coefficient and the number of ALs are  $5.13 \text{ m}^{-1}$  and 7.7, respectively. The form of that received signal is depicted in Figure 5.12b while the corresponding eye diagram can be seen for convenience on the right of the figure. The achieved BER, before the FEC threshold ( $3.8 \times 10^{-3}$ ), is  $4.26 \times 10^{-4}$  over 11.81 ALs at a water sample of  $7.87 \text{ m}^{-1}$  in attenuation coefficient and of 28 ml (0.0175% concentration) of the antacid. The reader is referred to Figure 5.12c for inspection of the form of the received signal, and the corresponding constructed eye diagram is given on the right, as before. These BER values accurately reflect the Fibrance fibre's potential to be deployed over turbid waters. For reference, in Figure 5.16, are also drawn in vertical lines the attenuation coefficients of two *Jerlov* oceanic (I-II) and one coastal (9C) type at 525 nm (calculated from [10]), which is the closest wavelength to the operational wavelength of the Osram LD ( $\approx 514 \text{ nm}$ ) coupled to the Fibrance. These waters are considered the murkiest natural water types, as classified by N. G. Jerlov [20]. Although Figure 5.16 are depicted, for convenience, data from 16 ml of the scattering agent and above, the reader is referred to Table 5.2 for a complete presentation of the achieved BERs along with the calculated  $c(\lambda)$  and ALs over 1.5 m between  $T_x$ - $R_x$ .

TABLE 5.2: Summary of all the calculated values of the Fibrance fibre at 5 Mb/s over 1.5 m between  $T_x$ - $R_x$ . Note that as the level of attenuation increases, the BER increases, as scattering prevents signal photons from reaching the  $R_x$ .

Maalox content (ml)	Maalox conc. (%)	$c$ ( $m^{-1}$ )	ALs	BER
0	0	0.02	0.04	$1.38 \times 10^{-13}$
1	0.0006	0.37	0.56	$2.80 \times 10^{-12}$
2	0.0012	0.72	1.08	$1.7 \times 10^{-9}$
3	0.0018	1.01	1.52	$3.25 \times 10^{-14}$
4	0.0025	1.26	1.89	$4.99 \times 10^{-10}$
6	0.0037	1.9	2.86	$4.35 \times 10^{-13}$
8	0.0050	2.5	3.75	$4.52 \times 10^{-10}$
10	0.0062	3.24	4.85	$1.12 \times 10^{-8}$
12	0.0075	3.94	5.9	$1.05 \times 10^{-7}$
14	0.0087	4.58	6.85	$5.47 \times 10^{-5}$
16	0.0100	5.13	7.7	$2.28 \times 10^{-7}$
18	0.0112	5.52	8.29	$1.15 \times 10^{-6}$
20	0.0125	6.03	9.05	$8.63 \times 10^{-6}$
24	0.0150	7	10.5	$2.52 \times 10^{-5}$
28	0.0175	7.87	11.81	$4.26 \times 10^{-4}$
35	0.0218	9.2	13.8	$9.2 \times 10^{-3}$
40	0.0250	9.98	14.97	$7.37 \times 10^{-2}$

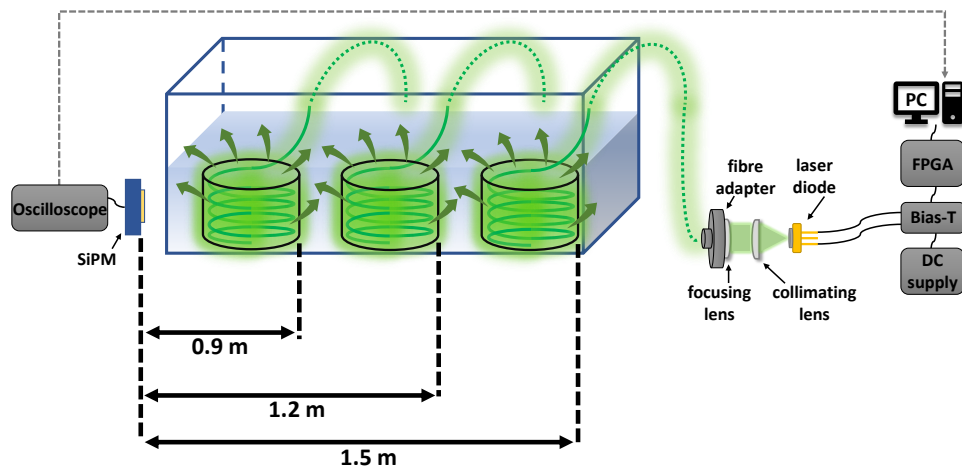


FIGURE 5.17: Depiction of the experimental set-up while moving the beaker towards the detector.

In Section 5.2.1, it was noted that for the most extreme scattering water samples, bit streams of different underwater optical ranges were captured by moving the beaker in  $\approx 30$  cm steps towards the detector (see Figure 5.17), in an attempt to improve the signal's quality. Figure 5.18 depicts, in a  $3 \times 3$  grid form, the resulting constructed eye diagrams for Maalox contents of 28 ml, 35 ml, and 40 ml, over 0.9 m, 1.2 m, and 1.5 m at 5 Mb/s. The number of ALs, along with the calculated BERs, are indicated on the top of each diagram, and it can be observed that the opening of the eye becomes more distinct as the  $T_x$ - $R_x$  distance reduces, as expected. It is important to stress that at 40 ml of the scattering agent and at 1.2 m between beacon and detector (element 2.1 of Figure 5.18's grid), the maximum number of ALs (11.97) is estimated to be achieved, over which error-free data transmission could be demonstrated ( $7.13 \times 10^{-4}$  BER). A summary of the calculated values for the various distances between the underwater beacon and the SiPM is given in Table 5.3.

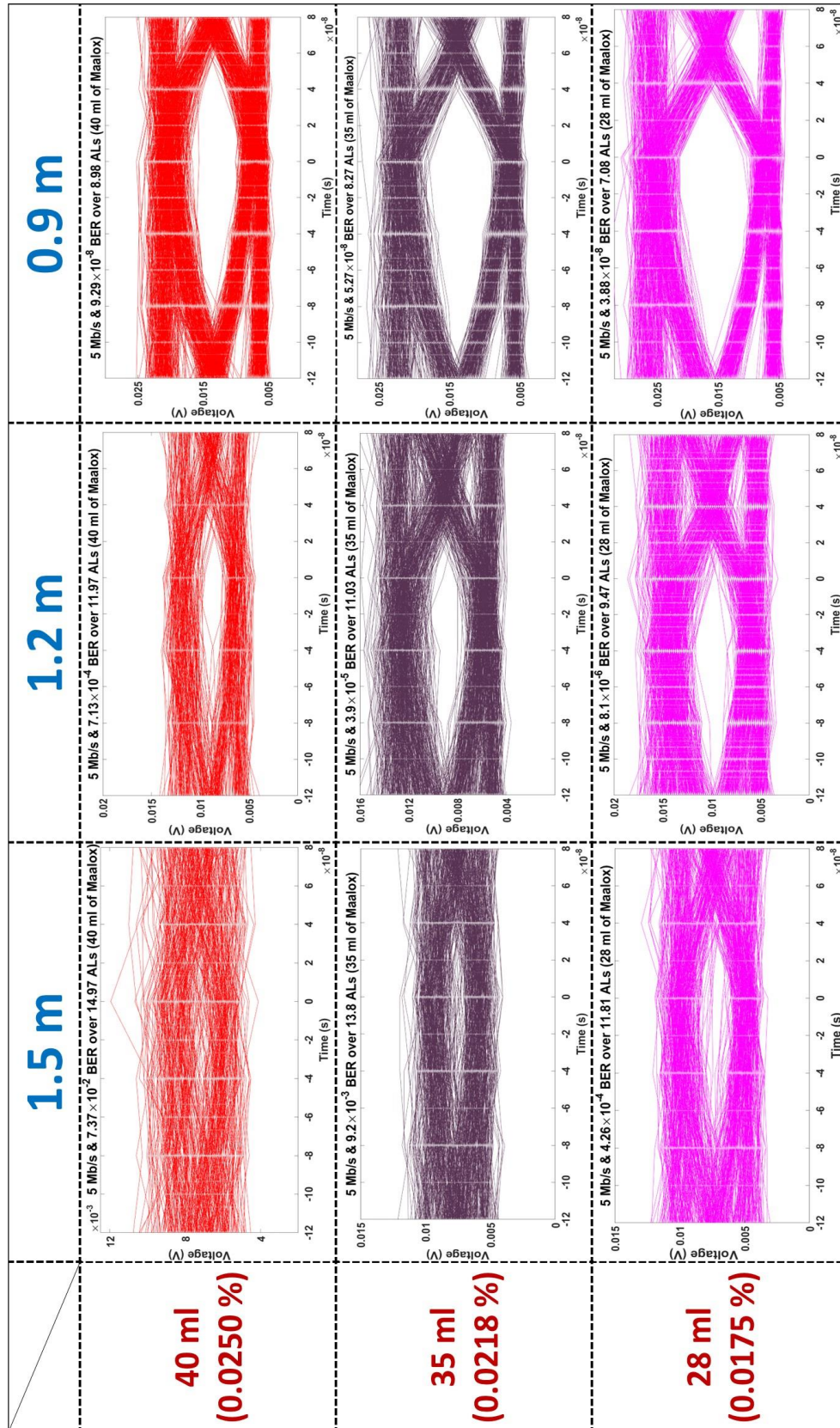


FIGURE 5.18: The constructed eye diagrams for the highest contents of the scattering agent over 1.5 m, 1.2 m, and 0.9 m between  $T_x$ - $R_x$ .

TABLE 5.3: Summary of the calculated Fibrance fibre values over various ranges, under extreme scattering conditions. Below are listed the Maalox content and the corresponding concentration, the water sample's attenuation coefficient, the distance between the beacon and the SiPM, the number of ALs, and the achieved BER.

Maalox content (ml)	Maalox conc. (%)	$c$ ( $m^{-1}$ )	$T_x-R_x$ (m)	ALs	BER
40	0.0250	9.98	1.5	14.97	$7.37 \times 10^{-2}$
			1.2	11.97	$7.13 \times 10^{-4}$
			0.9	8.98	$9.29 \times 10^{-8}$
35	0.0218	9.02	1.5	13.8	$9.2 \times 10^{-3}$
			1.2	11.03	$3.9 \times 10^{-5}$
			0.9	8.27	$5.27 \times 10^{-8}$
28	0.0175	7.87	1.5	11.81	$4.26 \times 10^{-4}$
			1.2	9.47	$8.1 \times 10^{-6}$
			0.9	7.08	$3.88 \times 10^{-8}$

The promising results of the underwater beacon concept have shown the potentiality of the Fibrance fibre system to be implemented over turbid waters and in real-world scenarios as 5 Mb/s were successfully transmitted over  $\approx 15$  ALs.

## 5.5 Wavelength Division Multiplexing simulation for the Fibrance fibre

In the chapter's introduction (Section 5.1), it was mentioned that the Fibrance fibre would be ideal for WDM, depending on the underwater conditions. As such, simulations based on a MATLAB<sup>®</sup> script were performed and estimated the  $T_x-R_x$  distance that the underwater beacon could support, firstly with the current configuration, secondly with increased coupled power, and thirdly at an increased data rate of 10 Mb/s. Two wavelengths were chosen for these simulations, namely 450 nm and 525 nm, both of which are obtainable from laser diodes.

The simulations were based on the work conducted by Hamza *et al.* [21] and Khalighi *et al.* [17], which examined the deployment of SiPMs for underwater wireless optical signal detection. An ideal alignment between  $T_x$  and  $R_x$  is assumed, as well as negligence of ambient light noise (i.e. the system operates in deep waters). A Poisson-based photon detection probability and the photodetector's characteristics have been considered for the signal detection. Furthermore, it is assumed that the Fibrance fibre is emitting



power isotropically; at a given propagation distance  $z$ , the surface area of the emitted light is spherical and hence equal to  $4\pi z^2$ . As mentioned in Section 5.2.2, the optical power losses can be modelled through Equation 1.10, and thus, the received power,  $P_R$ , is given as follows:

$$P_R(z) = P_T(z) \left( \frac{A_{PD}}{4\pi z^2} \right) e^{-c(\lambda)z}, \quad (5.8)$$

where  $P_T$ ,  $A_{PD}$ , and  $c(\lambda)$  are the transmitted power, the photodetector's area and the water's attenuation coefficient, respectively. Finally, the simulation calculates the BER as the transmission distance increases, i.e. the range between beacon and SiPM, over the same *Jerlov* water types as mentioned in the previous section (I, III, and 9C).

Figure 5.19 shows the modelling of the WDM Fibrance fibre link by keeping the experiment's parameters unchanged, i.e. fixed data rate at 5 Mb/s using OOK,  $\lambda_1 = 450$  nm,  $\lambda_2 = 525$  nm, and  $P_T = 5$  mW. It is worth noting that the underwater beacon would work at modest distances of  $\approx 12.4$  m (at 450 nm) and  $\approx 10$  m (at 525 nm) over *Jerlov* I water type (or over 0.27 and 0.48 ALs, respectively) and at  $\approx 2.6$  m (at 450 nm) and 2.8 m (at 525 nm) over *Jerlov* III water type through 2.84 and 3.08 ALs, respectively. These estimations align perfectly with the "real" results acquired in Section 5.4.2, where it was shown that error-free transmission is feasible through an identical number of ALs. The oscillations shown on the right side of the figure are an "artefact" of the simulation. The calculations work with an integer number of photons whose number becomes small when the received signal is weaker. Thus, any change from, e.g. 11 to 10 photons results in BER "jumps". A complete representation of the estimated values shown in Figure 5.19 is displayed in Table 5.4.

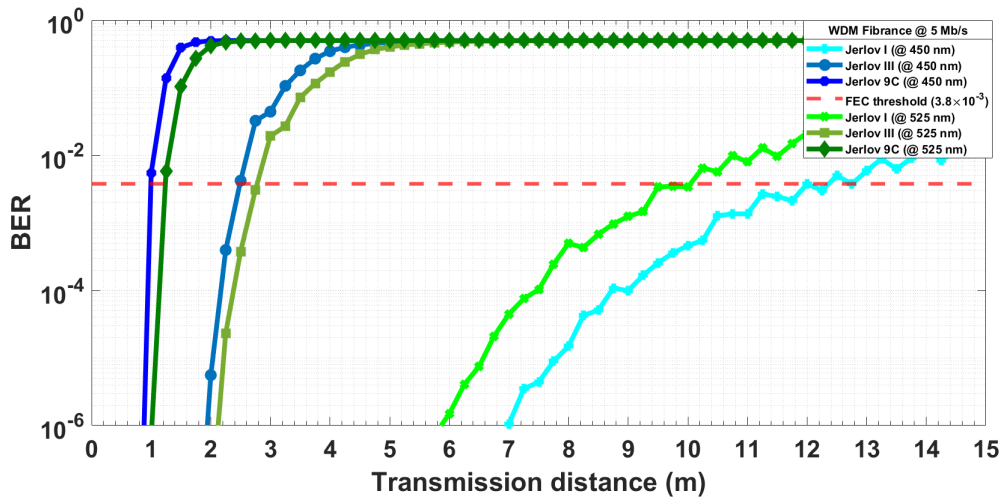


FIGURE 5.19: BER vs  $T_x$ - $R_x$  simulation, over *Jerlov* I, III, 9C water types at 450 nm and 525 nm. The modelling parameters are the same as with the experiment described in Section 5.2.1.

TABLE 5.4: Estimated values below the FEC threshold for the simulated WDM Fibrance fibre link at  $P_T=5$  mW and 5 Mb/s.

5 mW, 5 Mb/s			
$\lambda$ (nm)	<i>Jerlov</i> water type	max $T_x$ - $R_x$ (m)	ALs
450	I	12.4	0.27
	III	2	2.84
	9C	< 1	< 5.33
525	I	10	0.48
	III	2.8	3.08
	9C	< 1	< 3.81

Next, by increasing the  $P_T$  to 20 mW, via more efficient coupling between the LD and the Fibrance fibre, and keeping the rest of the parameters as before, transmission distances of  $\approx 21.2$  m (at 450 nm) and  $\approx 16$  m (at 525 nm) are estimated over *Jerlov* I water type (or 0.47 and 0.77 ALs, respectively) for error-free underwater data transfers. For *Jerlov* III, distances of approximately over 2.8 m (at 450 nm) and 3.4 m (at 525 nm) or 3.98 and 3.77 ALs, respectively, are estimated at which the achieved BER is below threshold. Furthermore, at 525 nm, error-free Fibrance communication can be achieved in *Jerlov* 9C through 4.57 ALs. These results are depicted in Figure 5.20, and a detailed representation of the error-free estimated values are shown in Table 5.5.

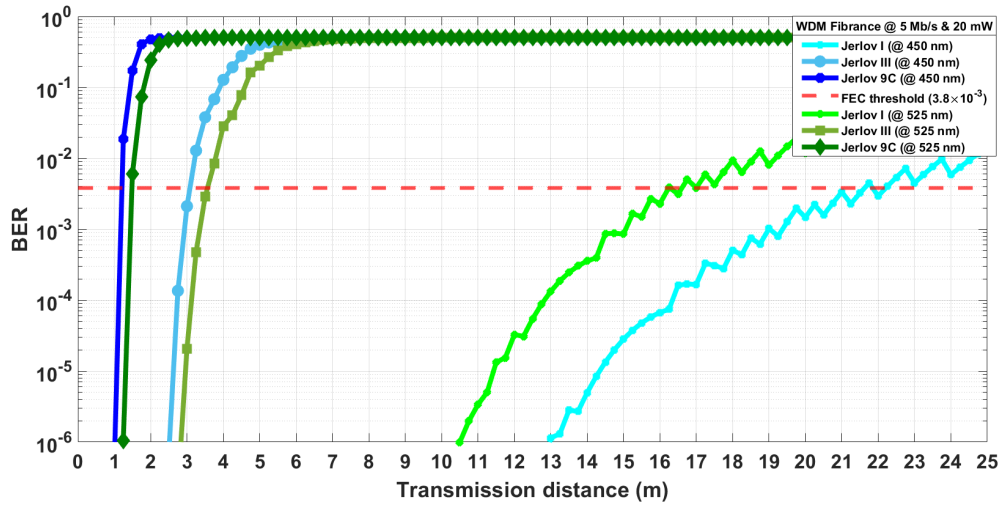


FIGURE 5.20: BER vs  $T_x$ - $R_x$  simulation, over *Jerlov* I, III, 9C water types at 450 nm and 525 nm. The modelling parameters are the same as with the experiment described in Section 5.2.1 except for the transmitted power,  $P_T$ , which was set to 20 mW.

TABLE 5.5: Estimated values below the FEC threshold for the simulated WDM Fibrance fibre link at  $P_T=20$  mW and 5 Mb/s.

20 mW, 5 Mb/s			
$\lambda$ (nm)	<i>Jerlov</i> water type	max $T_x$ - $R_x$ (m)	ALs
450	I	21.2	0.47
	III	2.8	3.98
	9C	< 1	< 5.33
525	I	16	0.77
	III	3.4	3.77
	9C	1.2	4.57

It should also be noted that between the two simulations (Figures 5.19 and 5.20), there is an increase of  $\approx 60 - 70\%$  in range for *Jerlov* I water type at both wavelengths, as the  $P_T$  increases. Conversely, over, e.g. *Jerlov* III, the increase is calculated between 21-40% despite the power difference. This can be interpreted by considering that attenuation via absorption is the dominant factor for power losses over clear waters. Indeed, for instance, the absorption coefficient for *Jerlov* I at 525 nm, is  $\alpha_I = 0.046 \text{ m}^{-1}$  whilst the much smaller scattering coefficient, is  $b_I = 2.05 \times 10^{-3} \text{ m}^{-1}$  [10]. In general, absorption can be overcome by simply increasing the output power (and, thus, the number of emitted photons) of the light source, which can result in a significant optical range improvement. On the other hand, as the turbidity of the water increases, the scattering coefficient becomes much larger than absorption's (e.g. in *Jerlov* 9C at 525 nm,  $b_{9C} = 3.38 \text{ m}^{-1}$  and  $\alpha_{9C} = 0.430 \text{ m}^{-1}$  [10]) and scattering becomes the dominant cause for power losses. A

more convenient method to compare scattering in different water types is to examine the changes in scattering albedo,  $\omega$ , as the water turbidity increases. The scattering albedo of a water sample is defined as the ratio of the scattering to the overall attenuation coefficient ( $\omega = b/c$ ) [13]. As such, at 525 nm,  $\omega_I = 0.043$  whereas  $\omega_{9C} = 0.89$  for *Jerlov* I and 9C, respectively. It can now be deduced that an increase in the  $T_x$ 's output power has an insignificant effect on the optical range improvement over turbid waters. Scattering impact on UWOC could be mitigated either by the deployment of high-sensitive receivers (SPADs or SPAD-arrays) for low-light measurements (at the order of few photons) or by the implementation of more sophisticated temporal (or spatial) modulation schemes.

Further simulation results were provided by increasing the data rate from 5 Mb/s to 10 Mb/s whilst maintaining the  $P_T$  at 5 mW. This could have been done by changing the FPGA's parameters for the real-time measurements of this work. However, at data rates  $> 10$  Mb/s, the limited bandwidth of the SiPM can affect the system's range performance [17]. Increased data rate means faster transitions between 1's and 0's which can cause ISI and, thus, lower SNR. The BERs plot at 10 Mb/s can be seen in Figure 5.21.

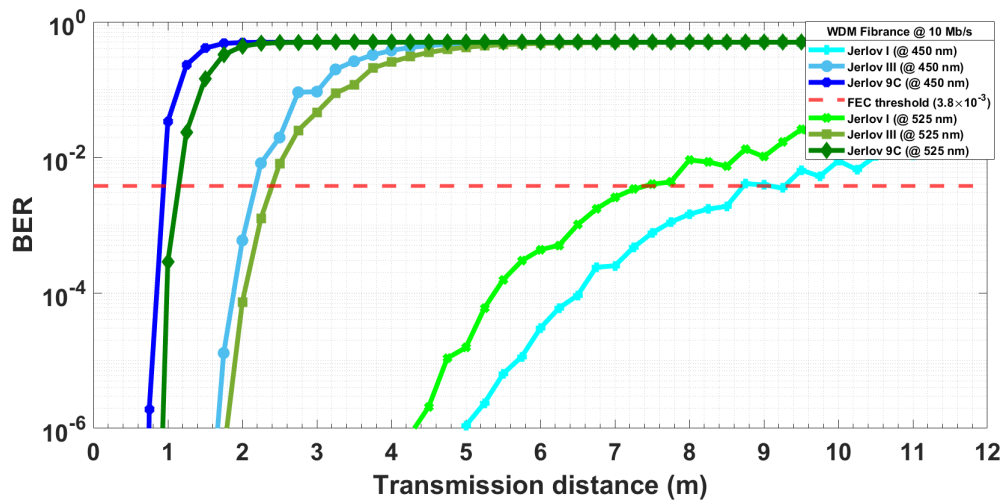


FIGURE 5.21: BER vs  $T_x$ - $R_x$  simulation, over *Jerlov* I, III, 9C water types at 450 nm and 525 nm. The modelling parameters are the same as with the experiment described in Section 5.2.1 except for the data rate,  $P_T$ , which was set to 10 Mb/s.

TABLE 5.6: Estimated values below the FEC threshold for the simulated WDM Fibrance fibre link at  $P_T= 5$  mW and 10 Mb/s.

<b>5 mW, 10 Mb/s</b>			
$\lambda$ (nm)	<i>Jerlov</i> water type	max $T_x-R_x$ (m)	ALs
450	I	8.5	0.19
	III	1.8	2.55
	9C	0.7	3.73
525	I	7.3	0.35
	III	2.2	2.44
	9C	1	3.81

In Table 5.6 are posted the below FEC estimated values for Fibrances fibre WDM at 10 Mb/s. As expected, the maximum attainable range decreases while the data rate increases, compared to the values at 5 Mb/s (see Table 5.4). Nevertheless, WDM high-speed UWOC via the Fibrance fibre over more than 3.5 ALs seem achievable, indicating the potential deployment of the Fibrance system for real-world applications.

## 5.6 Summary

This chapter presented an innovative, cost-effective and practical wireless underwater communication system that should be applicable to real-world applications in challenging underwater environments. As such, an off-the-shelf light-diffusing fibre (Fibrance) was employed as an underwater transmitter coupled to a laser diode operating at  $\approx 514$  nm. By exploiting the Fibrance fibre’s property of scattering light uniformly along its length, the fibre was used as an underwater beacon to send, in an omnidirectional way, data of 5 Mb/s over a 1.5 m water tank and through clear and turbid waters. In this way, sophisticated optical set-ups and complex mechanical components were eliminated, proving that the Fibrance fibre concept can mitigate alignment restrictions.

The turbidity of the water was varied by adding a commercial antacid in the water tank, and the eye diagrams constructed for each water sample provided visual information on the feasibility of the underwater communication link; error-free underwater data transmission was demonstrated for over 11 ALs. This deduction was confirmed by further data analysis on extracting the achieved BER for each water sample tested. Eventually, a BER of  $4.26 \times 10^{-4}$  indicating error-free data transmission over 11.81 ALs was recorded. The results show that with suitable engineering, the Fibrance concept could be adapted in an, e.g., UUV to send (or receive) data to/from a surface vessel located near the unmanned vehicle. This work can also be considered a milestone in the UWOC field due to the novelty of the  $T_x$  and its promising results on underwater

wireless optical data transmissions through an adequate number of ALs. It is worth noting that the majority of the UWOC references concern works carried out over clear (tap) waters, which, although it is helpful for the research and academic community, does not apply to realistic cases.

Future work includes the employment of the Fibrance fibre not only as a transmitter but as a receiver as well. The fibre can be coupled to a detector of high sensitivity (e.g. a SPAD). A collimated or focused light beam, incident to any point of the Fibrance fibre, can be coupled through the walls of the fibre and waveguided to the detector. Preliminary measurements over free space on this idea above showed promising results. The idea would apply to low-light level communications on the order of few photons detection and in underwater tracking or navigation as the received signal would be dependent on where the Fibrance fibre was illuminated, and thus, the locations of the  $R_x$  and  $T_x$  would be known. Furthermore, simulations conducted from the Fibrance WDM perspective showed that the underwater beacon concept could be employed using multiple fibres and/or coupling light of different wavelengths into a single Fibrance fibre, and it can support high-speed UWOC over turbid waters by choosing the optimum optical frequency according to the underwater environment.

## References

- [1] Stephan Logunov, Ed Fewkes, Paul Shustack, and Fred Wagner. Light diffusing optical fiber for Illumination. *Solid-State and Organic Lighting*, 2013.
- [2] Scott Robertson Bickham, Dana Craig, Edward John Fewkes, and Stephen Lvovich Logunov. Optical Fiber Illumination Systems and Methods, 2011. URL <https://patents.google.com/patent/US20110122646A1/un>. US 2011/0122646 A1.
- [3] Corning Inc. Corning Fibrance Light-Diffusing Fiber. <https://www.corning.com/emea/en/products/advanced-optics/product-materials/specialty-fiber/light-diffusing-fiber2.html>.
- [4] Paul J Shustack, Stephan L Logunov, Edward J Fewkes, and Paul G Dewa. Photocuring in Areas Where You Typically Cannot Get Light. *Radtech Conference*, pages 1–11, 2014.
- [5] Corning Inc. Corning ® Fibrance ® Light-Diffusing Fiber - Specification Sheet. Technical Report M1400561-Rev 1.1, August 2016.
- [6] Corning Inc. Corning ® Fibrance ® Light-Diffusing Fiber 2 - Specification Sheet. Technical Report M1400561-Rev 5, January 2020.
- [7] W. Spencer Klubben, Stephan L. Logunov, Edward J. Fewkes, Jeff Mooney, Paul M. Then, Peter G. Wigley, Horst Schreiber, Kaitlyn Matias, Cynthia J. Wilson, and Manuela Ocampo. Novel light diffusing fiber for use in medical applications. In *Optical Fibers and Sensors for Medical Diagnostics and Treatment Applications XVI*, volume 9702, pages 234 – 239. International Society for Optics and Photonics, SPIE, 2016. doi: 10.1117/12.2218267. URL <https://doi.org/10.1117/12.2218267>.
- [8] Osram Opto Semiconductors. Green Laser Diode in TO38 ICut Package. Technical Report Version 1.1, February 2016.
- [9] William Cox and John Muth. Simulating channel losses in an underwater optical communication system. *Journal of the Optical Society of America A*, 31(5):920, 2014. ISSN 1084-7529. doi: 10.1364/JOSAA.31.000920. URL <https://www.osapublishing.org/abstract.cfm?URI=josaa-31-5-920>.
- [10] Michael G. Solonenko and Curtis D. Mobley. Inherent optical properties of jerlov water types. *Appl. Opt.*, 54(17):5392–5401, Jun 2015.
- [11] Brandon M. Cochenour, Linda J. Mullen, and Allan E. Laux. Characterization of the beam-spread function for underwater wireless optical communications links. *IEEE Journal of Oceanic Engineering*, 33(4):513–521, 2008. ISSN 03649059. doi: 10.1109/JOE.2008.2005341.
- [12] Brandon Cochenour, Linda Mullen, and Alan Laux. Spatial and temporal dispersion in high bandwidth underwater laser communication links. *Proceedings - IEEE Military Communications Conference MILCOM*, 2008. doi: 10.1109/MILCOM.2008.4753048.
- [13] Brandon Cochenour, Linda Mullen, and John Muth. Effect of scattering albedo on attenuation and polarization of light underwater. *Optics Letters*, 35(12):2088–2090, 2010. ISSN 0146-9592. doi: 10.1364/OL.35.002088. URL <https://www.osapublishing.org/abstract.cfm?URI=ol-35-12-2088>.
- [14] Linda Mullen, Derek Alley, and Brandon Cochenour. Investigation of the effect of scattering agent and scattering albedo on modulated light propagation in water. *Applied Optics*, 50(10):1396–1404, 2011. ISSN 15394522. doi: 10.1364/AO.50.001396.

- 
- [15] Ippei Shake and Hidehiko Takara. Averaged Q-factor method using amplitude histogram evaluation for transparent monitoring of optical signal-to-noise ratio degradation in optical transmission system. *Journal of Lightwave Technology*, 20(8):1367–1373, 2002. doi: 10.1109/JLT.2002.800793.
- [16] Alexander D. Griffiths, Johannes Herrnsdorf, Christopher Lowe, Malcolm Macdonald, Robert Henderson, Michael J. Strain, and Martin D. Dawson. Temporal encoding to reject background signals in a low complexity, photon counting communication link. *Materials*, 11(9), 2018. doi: 10.3390/ma11091671.
- [17] Mohammad Ali Khalighi, Tasnim Hamza, Salah Bourennane, Pierre Leon, and Jan Opderbecke. Underwater Wireless Optical Communications Using Silicon Photo-Multipliers. *IEEE Photonics Journal*, 9(4):1–10, 2017. doi: 10.1109/JPHOT.2017.2726565. URL <http://ieeexplore.ieee.org/document/7981330/>.
- [18] Bart J. Van Zeghbroeck. Gaussian, Error and Complementary Error function. <https://ecee.colorado.edu/~bart/book/gaussian.htm#gaussian>, 1998.
- [19] J. R. Culham. ME755-Special Functions. [http://www.mhtlab.uwaterloo.ca/courses/me755/web\\_chap2.pdf](http://www.mhtlab.uwaterloo.ca/courses/me755/web_chap2.pdf), 2004.
- [20] N. G. Jerlov. Chapter 10 irradiance. In *Optical Oceanography*, volume 5 of *Elsevier Oceanography Series*, pages 115 – 132. Elsevier, 1968. doi: [https://doi.org/10.1016/S0422-9894\(08\)70929-2](https://doi.org/10.1016/S0422-9894(08)70929-2). URL <http://www.sciencedirect.com/science/article/pii/S0422989408709292>.
- [21] Tasnim Hamza, Mohammad Ali Khalighi, Salah Bourennane, Pierre Leon, and Jan Opderbecke. On the suitability of employing silicon photomultipliers for underwater wireless optical communication links. *2016 10th International Symposium on Communication Systems, Networks and Digital Signal Processing, CSNDSP 2016*, (1), 2016. doi: 10.1109/CSNDSP.2016.7573950.



## Chapter 6

# Conclusions

### 6.1 Summary

This thesis has presented work showing the employment of novel devices based on micro-LEDs, micro-LED arrays and laser diodes in Visible Light Communications for underwater applications. The main body of the work showed two basic ideas; firstly, the capability of these devices to transmit data at high speed using underwater wireless optical communications. Secondly, it highlighted the versatility and novelty of these devices as demonstrated not only in their implementation over transparent bodies of water but also in underwater environments that simulated natural bodies of water.

Chapter 1 introduced the reader to UWOC. An overview of the current state-of-the-art of the field was given by separately considering UWOC applications based on LED- and laser-based devices. Then, the background theory of the technologies used for underwater wireless data transmission, that is, acoustic, RF, and optical waves, was analysed, along with their pros and cons. A brief introduction to marine optics was then followed, where water's most important optical properties, such as absorption and scattering, which are the main UWOC limiters, were discussed. Chapter 1 closed by introducing the number of attenuation lengths (ALs) concept and the characterisation of the water tank used for the experiments throughout this thesis. The purpose was to determine the attenuation coefficient ( $c(\lambda)$ ) of water samples of different turbidities and match these experimental  $c(\lambda)$ 's to those of seawaters. Three off-the-shelf laser diodes of different wavelengths (violet, blue, green) were used, whose beams propagated over the water tank. The most common approach to mimic different seawaters and vary their turbidities is to add different concentrations of Maalox antacid (a scattering substance).

Chapter 2 described the underlying physics of the semiconductor-based devices used in this thesis. Fundamental concepts of solid-state physics were discussed, such as the

materials' energy band diagrams and the energy gap, the effective mass, and the carrier concentration in a semiconductor. Since p-n junctions are the basis of every LED/laser-based device and photodetectors mentioned throughout the thesis, the electrical and optical characteristics of a p-n junction were introduced. Then a brief discussion was given on the structure of multiple quantum wells and the operating principles of a laser diode, a PiN photodiode and a Single-Photon Avalanche photodiode. The chapter closed with a simple description of the modulation schemes applied in the results shown in the following chapters.

The novelty presented in Chapter 3 refers to the operation of custom-made micro-LED arrays. Two arrays operated at 450 nm and consisting of micro-LEDs of 60  $\mu\text{m}$  and 80  $\mu\text{m}$  were used to exploit **(a)** their larger output optical power when compared to a single micro-LED and **(b)** their high modulation bandwidth that is a key feature for micro-LEDs when compared to conventional LEDs. Applying OFDM and using a PiN photodiode, we demonstrated maximum data rates of 4.92 Gb/s over 1.5 m of clear tap water and 15 Mb/s over 5.33 ALs when adding the Maalox antacid that varied the turbidity of the water. These results showed the capability of micro-LED arrays in fast UWOC, even in underwater environments with high light attenuation.

Chapter 4 discussed the employment of transmitters comprising novel micro-LED arrays that were developed using a transfer-printing (TP) technique and a custom-made array of Single-Photon Avalanche Photodiodes (SPADs) as a receiver. Using TP to integrate devices on the same substrate enabled the operation of dual-colour micro-LEDs: an array comprising individually-addressable violet and blue micro-LEDs, an array comprising individually-addressable blue-green micro-LEDs and an array comprising blue-green micro-LEDs, in a  $2 \times 2$  layout and connected in series. In Chapter 1, it was discussed that as the turbidity of the water increases, the optimum wavelength for minimum error-free data transmission shifts towards red. Therefore, "adaptive" transmitters operating at multiple wavelengths depending on the underwater conditions are highly attractive for UWOC. By Wavelength Division Multiplexing (WDM) and using OOK, I showed an aggregate data rate of up to 200 Mb/s over 5.85 ALs and 100 Mb/s over 8.52 ALs.

Chapter 5 introduced the employment of a light-diffusing fibre (Fibrance fibre) as a transmitter and an off-the-shelf SPAD array (SensL) as a receiver. In a real-world scenario, the Fibrance could be used as an underwater beacon attached to an underwater vehicle emitting data omnidirectionally. In such a way, restrictions that include the maintenance of a strict alignment between the transmitter-receiver in the challenging underwater environment and employing tethered devices are mitigated. The Fibrance fibre was coupled with an off-the-shelf green laser diode (LD), operating at 514 nm, and by using OOK, a data rate of 5 Mb/s was demonstrated over highly-turbid waters

(11.81 ALs). The chapter closed with computational simulations where the output optical power of the LD increased, and so did the achievable data rate, showing the capabilities of the Fibrance concept in UWOC.

Based on the above, some broader conclusions that can be drawn are the following:

**High-speed underwater data transmission:** My research demonstrates the capability of micro-LED arrays and laser diodes to transmit data at high speeds through underwater wireless optical communications. This finding suggests promising possibilities for efficient and rapid data transfer in underwater environments.

**The versatility of devices:** The versatility and novelty of micro-LED arrays and laser diodes are highlighted in transparent bodies of water and underwater environments simulating natural bodies of water. This versatility suggests that these devices could be applied across various underwater conditions, showcasing their adaptability.

**Modulation schemes and techniques:** The discussion of modulation schemes applied in our research indicates a consideration of different techniques for optimising data transmission. Understanding and employing these modulation schemes are crucial for achieving the demonstrated high data rates in underwater communication.

**Micro-LED arrays and high modulation bandwidth:** Using custom-made micro-LED arrays operating, with larger output optical power and high modulation bandwidth, showcases their potential for achieving high data rates in underwater communication. The demonstration of 4.92 Gb/s over clear tap water and 15 Mb/s over turbid water suggests practical applications in varying underwater conditions.

**Transfer-printing for device integration:** Employing a transfer-printing technique for developing micro-LED arrays indicates a methodological advancement. This technique enables the operation of dual-colour micro-LEDs, providing adaptability to changing underwater conditions.

**Adaptive transmitters with WDM:** The concept of adaptive transmitters operating at multiple wavelengths based on underwater conditions, achieved through wavelength division multiplexing, presents a promising solution for maintaining efficient communication as water turbidity changes.

**Innovative transmitter-receiver set-up:** The use of a light-diffusing fibre (Fibrance fibre) as a transmitter or a custom-made SPAD array (Photon Torrent chip) as

a receiver showcases an innovative set-up. This approach addresses challenges related to alignment and tethered devices in challenging underwater environments.

**Real-world application considerations:** The application of Fibrance fibre as an underwater beacon attached to a vehicle, emitting data omnidirectionally, indicates a consideration for real-world scenarios and practical challenges associated with underwater communication.

## 6.2 Future work

The suggested future work within the frame work of this thesis can be summarised in the following research directions: (1) wavelength division multiplexing, (2) UV-based UWOC for the establishment of non-line of sight (NLOS) communication links, and (3) optical wireless communications in the air-water interface.

### Wavelength Division Multiplexing (WDM)

Underwater WDM was explored in Chapter 4. Two micro-LED arrays emitting at different wavelengths (violet-blue and blue-green) were used to demonstrate UWOC of an aggregate data rate of 200 Mb/s. Recent advances in VLC in air by the Institute of Photonics (IoP) at Strathclyde University have shown the demonstration of Gb/s using AlGaInP red micro-LEDs, developed by a transfer-printing (TP) technique [1]. Furthermore, a dual-colour optorode, consisting of a blue and a red micro-LED developed by TP, was used in optogenetics experiments for the excitement of different neural populations [2]. As previously discussed, in aquatic environments, a wavelength-adaptive source implemented on, e.g., an ROV would be highly practical as light attenuation underwater is wavelength-dependent. Micro-LED-based devices emitting in the red-green-blue (RGB) have already been developed at the IoP, and therefore, an underwater light source can comprise such arrays based on either micro-LEDs (developed by TP) or off-the-shelf laser diodes. In addition, underwater absorption spectroscopy in turbid aquatic environments can be enabled if the ROV is equipped with a white light source and a photodetector for detecting backscattered photons. In such a way, the minimum of water absorption can be determined (or estimated), and the optimum wavelength among the RGB array can be selected for UWOC with low attenuation.

The IoP's previous experience in hands-on UWOC experiments in real-world scenarios has shown that engineering such underwater vehicles is among the main challenges. The hardware of an ROV, including the electronic and electrical parts, has to be water sealed and everything set up to balance buoyancy issues that can be of critical importance when it comes to windy weather conditions and strong underwater currents.

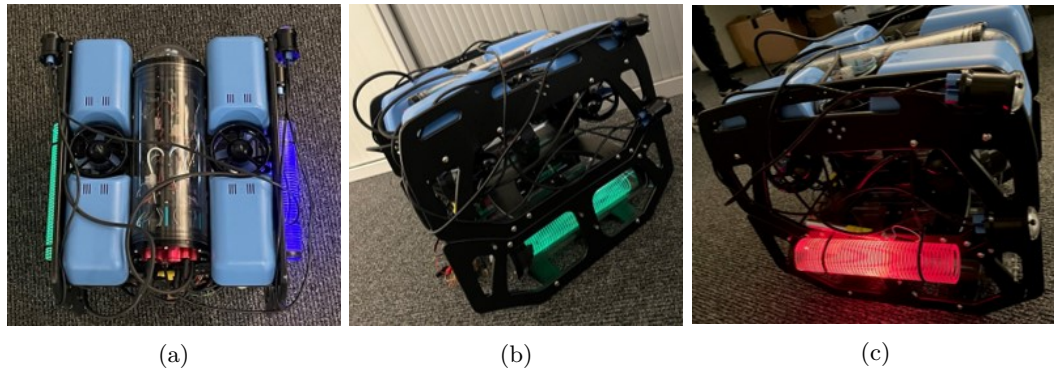


FIGURE 6.1: Images of an ROV capable of demonstrating WDM underwater. The ROV can be equipped with light sources emitting at different wavelengths and coupled with the diffusing Fibrance fibre to send data omnidirectionally as an underwater beacon (see Chapter 5). The ROV's Fibrance coupled with (a) and (b) a violet and green laser diode, and (c) with a red laser diode. Images courtesy of the Fraunhofer Centre for Applied Photonics (FCAP) in Glasgow.

An ROV example, suitable for underwater WDM, can be seen in Figure 6.1. The ROV was developed at Glasgow's Fraunhofer Centre for Applied Photonics (FCAP). As transmitters, laser diodes of three wavelengths (violet, green (Figures 6.1a and 6.1b), and red, Figure 6.1c) were used and then coupled with the Fibrance fibre, as demonstrated in Chapter 5.

### UV-based UWOC

Recently, the optical wireless communications (OWC) field has seen intense interest in utilising light sources emitting in the deep UV (DUV) region (200 nm - 315 nm) of the electromagnetic spectrum. This is because the atmosphere strongly attenuates the DUV wavelengths rendering the DUV light sources good candidates for secure inter-satellite communications as their signal is hidden from terrestrial observers. In aquatic environments, the intensity of the UV radiation varies according to  $I \sim 1/\lambda^4$  (as discussed in Section 1.4.1.2). As such, the UV wavelengths undergo the strongest scattering within the range of the optical radiation. The intensively scattered photons can pave the way for NLOS communication links where the strict alignment between transmitter and receiver has been lifted.

In terms of experimental work, little has been demonstrated in the literature; power losses due to geometry changes and water turbidity were studied for NLOS UWOC using a UV laser diode emitting at 375 nm [3]. The same group demonstrated NLOS UWOC of a maximum data rate of 80 Mb/s over 30 cm and 20 Mb/s over a maximum distance of 2.5 m, using a 377 nm laser diode and OOK [4]. Most recently, Maclure *et al.*, from the Strathclyde University's IoP demonstrated over air data transmissions of 6.94 Gb/s over 10 m and  $> 1$  Gb/s at a maximum distance of 116 m using a single DUV micro-LED

emitting at 285 nm [5]. Similar DUV microLED-based devices can be used in the near future for efficient NLOS UWOC applications.

### **Optical wireless communications in the air-water interface**

OWC in the air-water (and water-air) interface can be thought of as the next step when considering the evolution of the UWOC field and upon previous discussion of the NLOS underwater links. For instance, data exchange between multiple underwater sensors and a ship or an airborne vehicle can be established (see Figure 6.2). When compared to the former, the latter can be more practical in terms of time- and cost-efficiency. However, engineering such devices and their practical implementation can be challenging owing to the even more complex channel characteristics due to water waves, refraction index changes from one layer to the other that lead to refraction or total reflection of the optical beam, and the atmosphere's turbulence that now needs to be considered.



FIGURE 6.2: Schematic illustration of optical wireless communication links in the air-water and water-air interface. Taken from [6].

Preliminary theoretical and computational studies have shown the feasibility of communication links of vertical alignment between transmitter-receiver across the air-ocean interface when atmospheric and underwater scattering occurs as well as wind-roughened ocean surface [7]. In [8], the authors demonstrated up to 110 kb/s using a red laser diode operating at 635 nm over a “water + air” distance of less than 1.5 m. Most recently, over a total distance of 26 m (5 m over air and 21 m over water), wireless data transfer of 5.5 Gb/s using a green laser diode emitting at around 520 nm was reported [6]. These laser-based results and the emerging deployment of DUV micro-LED devices in OWC show new optical communication capabilities over the water-air (and vice versa) communication channel, either consisting of a NLOS or LOS configuration.

**End-to-end Networking**

Increasingly, multiple communication systems operating over different hardware and in different environments, including fixed and mobile infrastructure, are being considered as a “Network of networks”. Fixed and mobile underwater communication, including at visible wavelengths, is an important element in developing this integrated multi-network capability. Such consideration are included in the recently funded EPSRC “TITAN” (Platform Driving Ultimate Connectivity) programme, led by the University of Strathclyde’s Professor Harald Haas and involving 17 UK University partners.

## References

- [1] J. F. C. Carreira, E. Xie, R. Bian, J. Herrnsdorf, H. Haas, E. Gu, M. J. Strain, and M. D. Dawson. Gigabit per second visible light communication based on alga-inspired red micro-led micro-transfer printed onto diamond and glass. *Opt. Express*, 28(8):12149–12156, Apr 2020.
- [2] Jose F.C. Carreira. *Hybrid micro-LED devices enabled by elastomeric micro-transfer printing*. PhD thesis, University of Strathclyde, Department of Physics, 2020.
- [3] Xiaobin Sun, Wenqi Cai, Omar Alkhazragi, Ee-Ning Ooi, Hongsen He, Anas Chaaban, Chao Shen, Hassan Makine Oubei, Mohammed Zahed Mustafa Khan, Tien Khee Ng, Mohamed-Slim Alouini, and Boon S. Ooi. 375-nm ultraviolet-laser based non-line-of-sight underwater optical communication. *Optics Express*, 26(10):12870, May 2018.
- [4] Xiaobin Sun. *Ultraviolet Based Underwater Wireless Optical Communication*. PhD thesis, King Abdullah University of Science and Technology, 2020.
- [5] Daniel M. Maclure, Cheng Chen, Jonathan J. D. McKendry, Enyuan Xie, Jordan Hill, Johannes Herrnsdorf, Erdan Gu, Harald Haas, and Martin D. Dawson. Hundred-meter gb/s deep ultraviolet wireless communications using alga micro-leds. *Opt. Express*, 30(26):46811–46821, Dec 2022.
- [6] Yifei Chen, Meiwei Kong, Tariq Ali, Jiongliang Wang, Rohail Sarwar, Jun Han, Chaoyang Guo, Bing Sun, Ning Deng, and Jing Xu. 26 m/5.5 Gbps air-water optical wireless communication based on an OFDM-modulated 520-nm laser diode. *Opt. Express*, 25(13):14760–14765, Jun 2017.
- [7] Karl Idar Gjerstad, Jakob J. Stamnes, Børge Hamre, Jon K. Lotsberg, Banghua Yan, and Knut Stamnes. Monte carlo and discrete-ordinate simulations of irradiances in the coupled atmosphere-ocean system. *Appl. Opt.*, 42(15):2609–2622, May 2003.
- [8] R. S. Sangeetha, Ram Lochan Awasthi, and T. Santhanakrishnan. Design and analysis of a laser communication link between an underwater body and an air platform. In *2016 International Conference on Next Generation Intelligent Systems (ICNGIS)*, pages 1–5, 2016.



# List of Publications

## Refereed Journal Papers

- [1] G. N. Arvanitakis, R. Bian, J. J. D. McKendry, C. Cheng, E. Xie, X. He, G. Yang, M. S. Islim, A. A. Purwita, E. Gu, H. Haas, and M. D. Dawson, *Gb/s underwater wireless optical communications using a series-connected micro-LED array*, IEEE Photonics Journal, **12**(2), pp. 1-10 (2020), Article No. 7901210.

## Conference Proceedings

- [2] G. N. Arvanitakis, J. J. D. McKendry, H. T. Bookey, E. Gu, and M. D. Dawson, *LEDs and Lasers for high-speed underwater optical communications*, Undersea Defence Technology Conference (UDT 2018), Glasgow, UK, June 2018.
- [3] J. F. C. Carreira, G. N. Arvanitakis, A. D. Griffiths, J. J. D. McKendry, E. Xie, J. Kosman, R. K. Henderson, E. Gu, and M. D. Dawson, *Underwater Wireless Optical Communications at 100 Mb/s using Integrated Dual-Color Micro-LEDs*, pp. 1-2, 32<sup>nd</sup> Annual Conference of the IEEE Photonics Society (IPC), San Antonio, TX, USA (2019).

## Conferences

(Presenter highlighted by bold letters)

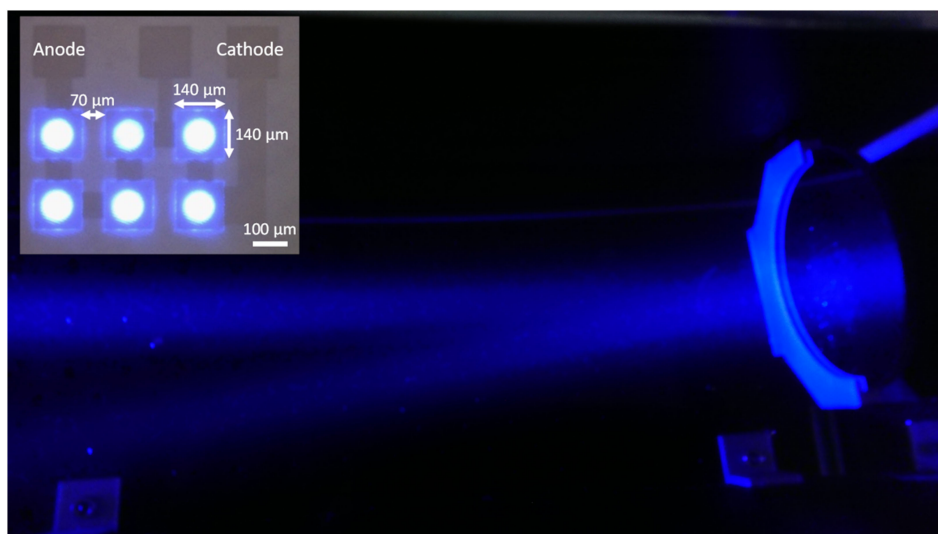
- [4] **G. N. Arvanitakis**, J. J. D. McKendry, H. T. Bookey, E. Gu, and M. D. Dawson, *LEDs and Lasers for high-speed underwater optical communications* (poster), SU2P 9<sup>th</sup> Annual Symposium, Glasgow, UK, May 2018.
- [5] **G. N. Arvanitakis**, J. J. D. McKendry, H. T. Bookey, E. Gu, and M. D. Dawson, *LEDs and Lasers for high-speed underwater optical communications* (oral), Undersea Defence Technology Conference (UDT 2018), Glasgow, UK, June 2018.
- [6] **G. N. Arvanitakis**, J. J. D. McKendry, H. T. Bookey, E. Gu, and M. D. Dawson, *LEDs and Lasers for high-speed underwater optical communications* (poster), IONS Scandinavia, Copenhagen, Denmark, July 2018.

- 
- [7] G. N. Arvanitakis, **J. Herrnsdorf**, R. Bian, C. Cheng, E. Xie, X. He, G. Yang, M. S. Islam, A. A. Purwita, E. Gu, H. Haas, and M. D. Dawson, *Advances in underwater wireless optical communications using micro-LEDs* (poster), 13<sup>th</sup> International Conference on Nitride Semiconductors, ICNS-13, Bellevue, Washington, USA, July 2019.
- [8] **J. F. C. Carreira**, G. N. Arvanitakis, A. D. Griffiths, J. J. D. McKendry, E. Xie, J. Kosman, R. K. Henderson, E. Gu, and M. D. Dawson, *Transfer-printed dual-colour micro-LEDs for underwater wireless optical communications* (oral), UK Semiconductors, Sheffield, UK, July 2019.
- [9] J. F. C. Carreira, **G. N. Arvanitakis**, A. D. Griffiths, J. J. D. McKendry, E. Xie, J. Kosman, R. K. Henderson, E. Gu, and M. D. Dawson, *Underwater Wireless Optical Communications at 100 Mb/s using Integrated Dual-Color Micro-LEDs* (oral), pp. 1-2, 32<sup>nd</sup> Annual Conference of the IEEE Photonics Society (IPC), San Antonio, TX, USA, 29 Sept. - 3 Oct. 2019.
- [10] G. N. Arvanitakis, **J. J. D. McKendry**, R. Bian, C. Cheng, E. Xie, X. He, G. Yang, M. S. Islam, A. A. Purwita, E. Gu, H. Haas, and M. D. Dawson, *Gb/s underwater wireless optical communications using micro-LEDs* (oral), UK Nitrides Consortium (UKNC), Cardiff, UK, January 2020.

# Gb/s Underwater Wireless Optical Communications Using Series-Connected GaN Micro-LED Arrays













Volume 12, Number 2, April 2020

Georgios N. Arvanitakis  
Rui Bian  
Jonathan J. D. McKendry  
Chen Cheng  
Enyuan Xie  
Xiangyu He  
Gang Yang  
Mohamed S. Islim  
Ardimas A. Purwita  
Erdan Gu, *Member, IEEE*  
Harald Haas, *Fellow, IEEE*  
Martin D. Dawson, *Fellow, IEEE*



DOI: 10.1109/JPHOT.2019.2959656

# Gb/s Underwater Wireless Optical Communications Using Series-Connected GaN Micro-LED Arrays

Georgios N. Arvanitakis <sup>1</sup>, Rui Bian <sup>2</sup>,  
Jonathan J. D. McKendry <sup>1</sup>, Chen Cheng <sup>2</sup>, Enyuan Xie <sup>1</sup>,  
Xiangyu He <sup>1</sup>, Gang Yang <sup>3</sup>, Mohamed S. Islam <sup>2</sup>,  
Ardimas A. Purwita <sup>2</sup>, Erdan Gu <sup>1</sup>, *Member, IEEE*,  
Harald Haas <sup>2</sup>, *Fellow, IEEE*,  
and Martin D. Dawson <sup>1</sup>, *Fellow, IEEE*

<sup>1</sup>Institute of Photonics, Department of Physics, SUPA, University of Strathclyde, Glasgow G1 1RD, U.K.

<sup>2</sup>Li-Fi R&D Centre, Institute for Digital Communications, University of Edinburgh, Edinburgh EH9 3JL, U.K.

<sup>3</sup>Institute of Marine Optoelectronic Equipment, Harbin Institute of Technology, WeiHai 264209, China

DOI:10.1109/JPHOT.2019.2959656

This work is licensed under a Creative Commons Attribution 4.0 License. For more information, see <http://creativecommons.org/licenses/by/4.0/>

Manuscript received September 12, 2019; revised December 6, 2019; accepted December 9, 2019. Date of publication December 13, 2019; date of current version March 18, 2019. This work was supported by the EPSRC under the “UK Quantum Technology Hub in Quantum Enhanced Imaging” Project EP/M01326X/1. Corresponding author: Georgios N. Arvanitakis (e-mail: georgios.arvanitakis@strath.ac.uk).

**Abstract:** High speed wireless communications are highly desirable for many industrial and scientific underwater applications. Acoustic communications suffer from high latency and limited data rates, while Radio Frequency communications are severely limited by attenuation in seawater. Optical communications are a promising alternative, offering high transmission rates (up to Gb/s), while water has relatively low attenuation at visible wavelengths. Here we demonstrate the use of series-connected micro-light-emitting-diode ( $\mu$ LED) arrays consisting of 6  $\mu$ LED pixels either 60  $\mu$ m or 80  $\mu$ m in diameter and operating at 450 nm. These devices increase the output power whilst maintaining relatively high modulation bandwidth. Using orthogonal frequency division multiplexing (OFDM) we demonstrate underwater wireless data transmission at rates of up to 4.92 Gb/s, 3.22 Gb/s and 3.4 Gb/s over 1.5 m, 3 m and 4.5 m, respectively, with corresponding bit error ratios (BERs) of  $1.5 \times 10^{-3}$ ,  $1.1 \times 10^{-3}$  and  $3.1 \times 10^{-3}$ , through clear tap water, and Mb/s rates through  $>5$  attenuation lengths (ALs) in turbid waters.

**Index Terms:** GaN, micro-light-emitting-diode arrays, turbid waters, underwater wireless optical communications.

## 1. Introduction

Many subsea industrial, military and scientific activities such as oceanographic surveying, or the control, monitoring and maintenance of subsea infrastructure, require the transfer of increasingly large amounts of data through high-speed communications. For example, unmanned and autonomous underwater vehicles (UUVs and AUVs) are used to capture high-resolution images or videos for applications such as assessing subsea oil and gas infrastructure. In this example,

the captured image and video data would require to be transferred back to a surface vessel for assessment, with navigation commands and instructions being sent to the vehicles. While high-speed data links can be achieved using underwater cables or tethers, this can be impractical, expensive or in some cases restrictive due to the challenging underwater environment. Therefore, high-speed underwater wireless links are greatly desirable.

Acoustic technologies are the most widely used form of underwater wireless communications due to their long range covering distances up to tens of kilometers [1]. However, they suffer from low data rates (in the order of kb/s) because of their limited bandwidth (around tens of kHz) [2]. Moreover, acoustics suffer from low speed and multipath propagation which may lead to inter-symbol interference (ISI) [3]. Radio Frequency (RF) communications, despite their widespread deployment over free-space (e.g., cell phones, TV, radio, satellite communications), are not readily deployable underwater as electromagnetic (EM) waves at these frequencies are heavily attenuated by seawater [4]. As such, underwater RF wireless communications require high transmission power and complex antenna designs [5] and yet are limited to short distances (on the order of meters) [6].

Underwater wireless optical communication (UWOC) may be considered as an alternative to acoustics and RF as the attenuation of light by water is lowest in the visible region [7]. The last 20 years has also witnessed the rapid development of efficient, compact and robust solid-state transmitters (light-emitting diodes (LEDs) and laser diodes) emitting light in the violet-blue-green region of the visible spectrum, as well as highly-sensitive photoreceivers such as single-photon avalanche diodes. Therefore, high-speed underwater optical data transmission over tens of meters using visible wavelengths is now feasible. For example, recent reports by Li *et al.* showed the demonstration of 25 Gb/s by using a vertical-cavity surface-emitting laser (VCSEL) at 680 nm for 5 m [8]. Fei *et al.*, using a blue laser diode, demonstrated 16.6 Gb/s for 5 m and 6.6 Gb/s over 55 m of clear tap water [9] while an RGB (Red Green Blue) laser was used by Kong *et al.* to achieve 9.51 Gb/s for 10 m [10].

LEDs have attracted a great deal of attention in recent years for use as light-fidelity (Li-Fi) transmitters, where LED luminaires are used to provide both general purpose lighting and mb/s or Gb/s optical wireless links. LEDs have also been demonstrated as transmitters in underwater optical links. Recent results by Shi *et al.* showed the demonstration of 15.17 Gb/s over 1.2 m of clear tap water by employing 5 LEDs of primary colors [11]. A single green LED operating at 521 nm was used by Wang *et al.* to demonstrate 2.175 Gb/s through 1.2 m of clear tap water [12]. LEDs are relatively simple, and cost-effective in comparison with other sources such as lasers, however standard off-the-shelf LEDs have limited modulation bandwidth, typically 20 MHz or so, due to the large capacitance of standard LED dies, which limits the achievable data rates. Micro-sized light-emitting diodes ( $\mu$ LEDs) on the other hand have much smaller dimensions (typically  $\leq 100 \mu\text{m}$ ) and therefore their bandwidths are not limited by device capacitance. For example, we previously reported violet-emitting  $\mu$ LEDs with modulation bandwidths up to 655 MHz, using which wireless data rates of up to 7.91 Gb/s over free-space were demonstrated [13].  $\mu$ LEDs have been employed for UWOC. For example, Tian *et al.* reported 800 mb/s over 0.6 m and 200 mb/s over 5.4 m of clear tap water [14] using a single  $\mu$ LED at 450 nm. However, the small active area of  $\mu$ LEDs results in a relatively low output power from a single  $\mu$ LED ( $< 5 \text{ mW}$ ), which may be insufficient for practical UWOC due to absorption and scattering in an underwater environment.

In order to mitigate this, here we report the deployment of series-connected  $\mu$ LED arrays operating at 450 nm for UWOC. These devices consist of 6  $\mu$ LED pixels, of either 60 or 80  $\mu\text{m}$  in diameter and connected in series. This allows the device to achieve higher optical power than a single  $\mu$ LED pixel while retaining the characteristic high modulation bandwidth of  $\mu$ LEDs. As a result, these devices offer the high output powers of a standard LED die, but with the high modulation bandwidth of  $\mu$ LEDs. Using orthogonal frequency division multiplexing (OFDM), data rates of up to 4.92 Gb/s, 3.22 Gb/s and 3.4 Gb/s over 1.5 m, 3 m and 4.5 m, respectively, with corresponding bit error ratios (BERs) of  $1.5 \times 10^{-3}$ ,  $1.1 \times 10^{-3}$  and  $3.1 \times 10^{-3}$ , of clear tap water are here demonstrated. Furthermore, by adding a scattering agent to clear tap water we explored the performance of these optical links through water of varying turbidities. Mb/s data transmission was demonstrated over 5.33 attenuation lengths. These results demonstrate that the relatively high

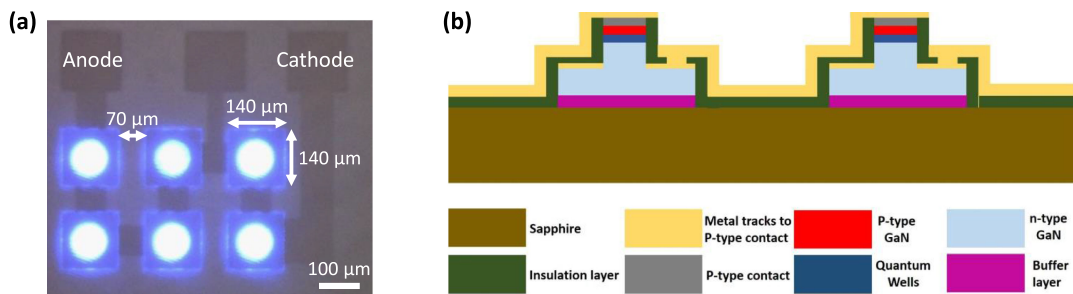


Fig. 1. (a) Planview optical image of six pixels from the  $\mu$ LED array at a DC operating current of 1 mA. (b) Schematic cross-section of two adjacent elements of the series-biased  $\mu$ LED array.

bandwidth and output power of these series-connected  $\mu$ LEDs can be used to achieve high data rates and/or mitigate the effects of signal attenuation.

## 2. $\mu$ LED Design, Fabrication and Characterization

The  $\mu$ LED devices reported here were fabricated from commercial blue-emitting III-nitride LED wafers grown on a 2" c-plane sapphire substrate with periodically patterned surfaces. The fabrication procedure is similar to that described in [15] and [16], which is summarized as follows. Standard photolithography and etching techniques were used to etch down to the n-GaN layer to define disk-shaped  $\mu$ LED pixels. A further processing step etched down to the sapphire substrate to electrically-isolate each of these  $\mu$ LEDs on individual  $140 \times 140 \mu\text{m}^2$  mesas, with a  $70 \mu\text{m}$  spacing between adjacent mesas (Fig. 1(a)). P-type and N-type contact metals (Pd and Ti/Au) were then deposited, interconnecting the  $\mu$ LEDs in series. Fig. 1(b) illustrates the simplified cross-sectional structure of the series-connected  $\mu$ LED array, where two adjacent  $\mu$ LEDs elements are shown as an example and the electrical interconnections between them are highlighted.

Each  $\mu$ LED pixel shown here is of either  $60 \mu\text{m}$  or  $80 \mu\text{m}$  in diameter while the center wavelength is approximately  $450 \text{ nm}$  for all devices. As shown in Fig. 1(a), each device consists of 6  $\mu$ LED pixels arranged in a  $3 \times 2$  array. In this work all 6 pixels were simultaneously driven together in series in order to maximize the output power.

For the series-connected devices with respectively  $60 \mu\text{m}$  and  $80 \mu\text{m}$  pixels, Fig. 2(a) presents the current versus voltage (I-V) and the output optical power versus current (L-I) while Fig. 2(b) shows the  $-3 \text{ dB}$  electrical-to-electrical (E-E) and electrical-to-optical (E-O) bandwidths versus current characteristics. Optical power is the forward detected output and was measured by placing the  $\mu$ LEDs in close proximity to a calibrated Si photodiode. The bandwidths were measured as detailed previously [15]. As shown, the turn-on voltage at  $1 \text{ mA}$  for the  $60 \mu\text{m}$  in diameter device is  $21.7 \text{ V}$  corresponding to about  $3.6 \text{ V}$  for each  $\mu$ LED element whereas for the  $80 \mu\text{m}$  device the turn-on voltage is  $20 \text{ V}$  corresponding to about  $3.3 \text{ V}$  for each  $\mu$ LED element. Additionally, both devices can be operated at a current beyond  $50 \text{ mA}$  and demonstrate an optical power before thermal rollover of over  $21 \text{ mW}$  and  $15 \text{ mW}$  for the  $80 \mu\text{m}$  and  $60 \mu\text{m}$  device, respectively.

In our previous work we have shown that in a single  $\mu$ LED emitter [16], [17] the differential carrier lifetime decreases as the current density increases and leads to an increase of the E-O bandwidth of the device [18]. As can be seen in Fig. 2(b), the E-O bandwidth for the  $60 \mu\text{m}$  in diameter series-connected  $\mu$ LED array is  $338.5 \text{ MHz}$  at  $30 \text{ mA}$  whilst for the  $80 \mu\text{m}$  device it is  $263 \text{ MHz}$  at  $50 \text{ mA}$ . These trends are in agreement with previous work [19] where it was observed that as the pixel diameter of a  $\mu$ LED element decreases, the corresponding E-O bandwidth increases.

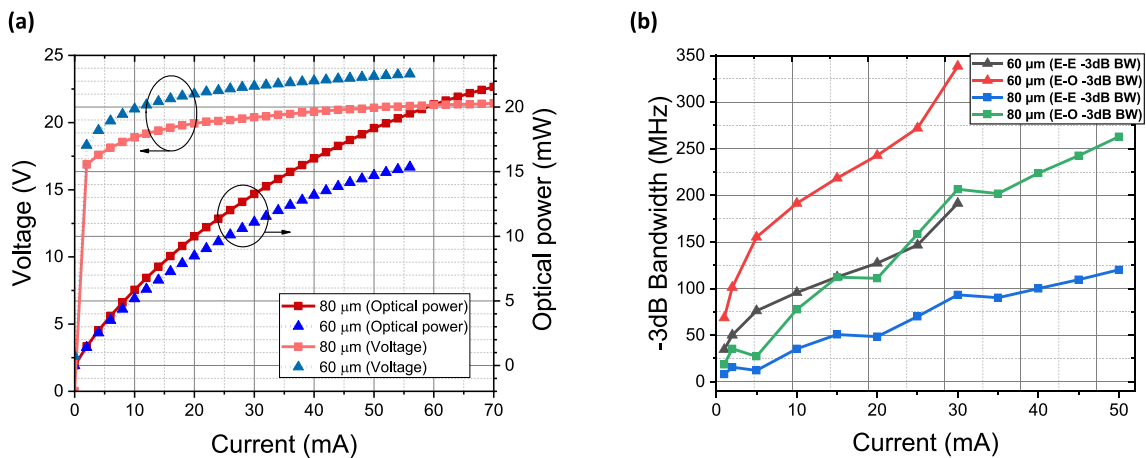


Fig. 2. (a) I-V, L-I, and (b)  $-3$  dB bandwidth plots for the two respective devices comprising six  $60 \mu\text{m}$  and  $80 \mu\text{m}$   $\mu\text{LEDs}$  in series.

### 3. Water Sample Characterization

In natural waters two fundamental wavelength dependent processes are mainly responsible for the optical attenuation of light, namely absorption and scattering, whose coefficients are denoted as  $\alpha(\lambda)$  and  $b(\lambda)$ , respectively, both with units of  $\text{m}^{-1}$ . We may then relate the attenuation of optical power to the path length  $z$  [20], [21]:

$$P_R(z) = P_T e^{-c(\lambda) \cdot z} \quad (1)$$

where  $c(\lambda) = \alpha(\lambda) + b(\lambda)$  is the overall beam attenuation and  $P_R$  and  $P_T$  are the received and transmitted powers, respectively. Eq. (1) allows the power received at a distance  $z$  to be estimated, assuming that scattered photons do not reach the receiver and thus do not contribute to the final received power. We also define the attenuation length (AL) of a water sample as the distance at which the received power in a water sample is reduced to  $1/e$  of the transmitted power, and it is equal to  $1/c(\lambda)$  [22]. The number of attenuation lengths through which transmitted light propagates is given as the unit-less product  $c(\lambda) \cdot z$  [21].

Following a method commonly reported [21], [23]–[26] in this work a mixture of aluminum and magnesium hydroxide was used as a scattering agent (Maalox antacid) and added to clear tap water to vary the level of attenuation. Increasing the concentration of Maalox increases the amount of scattering and thereby the attenuation of the optical signal as it propagates through the water. While this approach does not model affects such as turbulence, it is a simple method to mimic different natural water analogs in a laboratory setting. Detailed studies by other groups on the effect of turbulence are available elsewhere [27].

The relationship between Maalox concentration and  $c(\lambda)$  was measured as follows. Nine different concentrations of Maalox were examined, ranging from 0.000625% (1 ml of Maalox in 160 l of tap water) to 0.005625% (9 ml of Maalox). To estimate  $c(\lambda)$  at each concentration, the optical beam from a blue laser diode (Osram, PL450B) operating at the same nominal central wavelength as the  $\mu\text{LEDs}$  (450 nm), was propagated through the 1.5 m length of our water tank (dimensions 1.5 m  $\times$  0.35 m  $\times$  0.35 m). A laser was chosen for these measurements as the divergence of the  $\mu\text{LED}$  emission would make accurate estimation of  $c(\lambda)$  difficult. A plastic aspheric lens (Thorlabs, CAY033), was placed in front of the laser diode to collimate the beam which was subsequently focused onto a power meter sensor (Thorlabs, S121C), located at the other side of the tank. The received optical power,  $P_R$ , at each concentration was measured. Using these values for  $P_R$  along with Eq. (1) and the measured transmitted power of  $P_T$ , the corresponding attenuation coefficients for each water sample were calculated and are shown in Fig. 3(a). It can be seen that

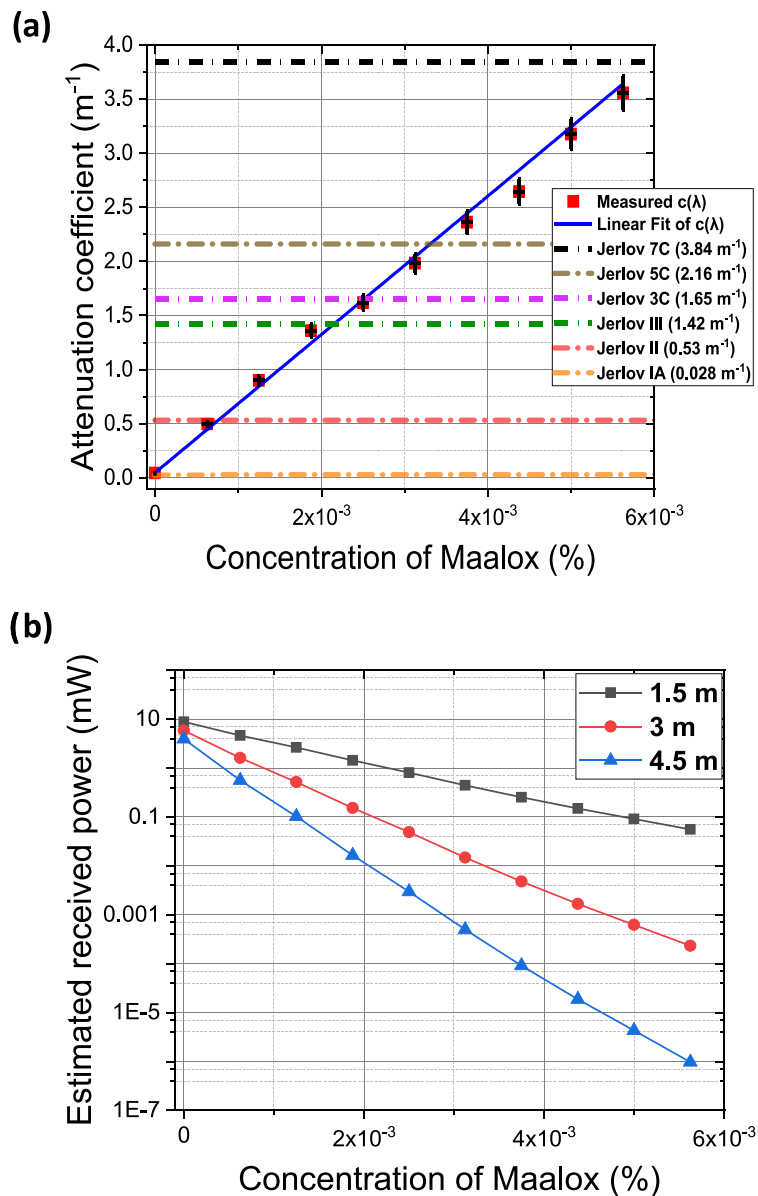


Fig. 3. (a) The calculated attenuation coefficients versus the content of the scattering agent (Maalox). For comparison, the typical values of six Jerlov ocean types are given as defined by [26], [27]. (b) The estimated received power over 1.5 m, 3 m and 4.5 m versus the Maalox concentration.

the minimum measured attenuation coefficient, which corresponds to clear tap water (no Maalox added) is  $0.05 m^{-1}$ , a value relatively close to that of Jerlov IA open ocean water type which is  $0.028 m^{-1}$  [28], [29]. For the samples with added Maalox, the maximum measured attenuation coefficient was  $3.56 m^{-1}$  for 0.005625% (9 ml) of Maalox, and is close to the Jerlov 7C coastal ocean type where  $c(450) = 3.84 m^{-1}$  [28], [29].

Fig. 3(b) illustrates the estimated received power for the  $80 \mu m$ -in-diameter series-connected  $\mu LED$  array, for each concentration of the scattering agent at 1.5 m, 3 m and 4.5 m. The estimated received power,  $P_R$ , was calculated through Eq. (1) and by taking into account that the estimated transmitted power,  $P_T$ , was 13.27 mW at 30 mA, based on the L-I measurements in Fig. 2(a).



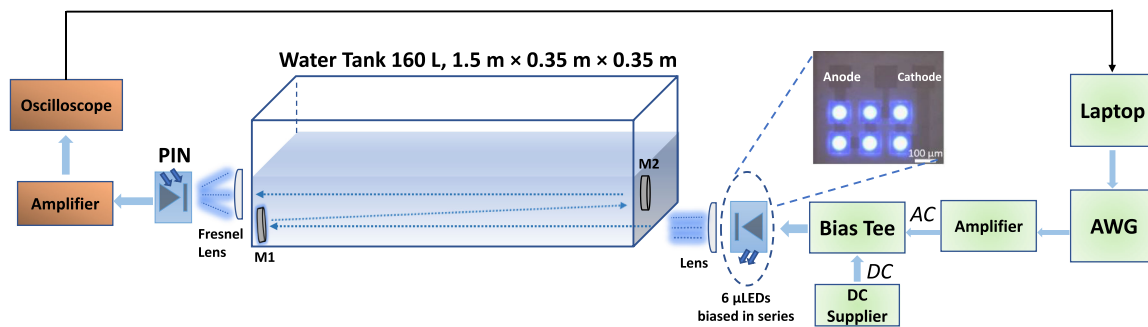


Fig. 4. Illustration of the experimental set-up used for the UWOC measurements of this work. Two mirrors (M1 and M2) were placed appropriately to increase the optical link from 1.5 m up to 3 m and 4.5 m.

#### 4. Data Transmission and Experimental Set-Up

The data transmission experimental set-up is depicted in Fig. 4. The digital data signal to be transmitted was generated and processed in MATLAB. Afterwards, this optimized signal was converted to analog through an arbitrary waveform generator (AWG, Agilent, 81180A) and amplified (amplifier SHF S126A). The signal was combined with a DC current of 30 mA through a bias tee (Tektronix, PSPL5575A) to drive the  $\mu$ LED arrays.

A condenser lens (Thorlabs, ACL50832U-A) was used to collimate the beam to be optically transmitted through the 1.5 m long water tank. For the longer range data transmissions two 100 mm diameter mirrors (M1 and M2) were mounted appropriately in the tank to increase the optical path up to 3 m and 4.5 m. At the receiver end, a 4-inch in diameter Fresnel lens (Edmund Optics, #46-614) was used to focus the collimated beam onto a PIN photoreceiver of 1.4 GHz bandwidth (Femto, HAS-X-S-1G4-SI). The amplification of the received signal was processed through an amplifier (Mini-Circuits, ZHL-6A-S+) and captured through an oscilloscope (Agilent, MSO 7104B). The received signal was processed and demodulated offline in MATLAB. At this stage, the transmitted data and received data is compared to identify any incorrectly transmitted bits, allowing the BER to be calculated. It should be noted that OFDM is robust against multi-path effects of the sort that would be experienced in underwater environments. A more detailed description of the OFDM data modulation process can be found in our previous work [13], [30].

#### 5. Communication Performance Results

As with our previous work [13], [30], an adaptive bit and energy loading scheme was used to allow different Quadrature Amplitude Modulation (QAM) levels to be loaded onto the OFDM subcarriers based on the measured signal-to-noise ratio (SNR) of each carrier. The higher the carrier SNR, the higher the QAM level that could be used and thus the more bits could be loaded onto that channel. This is illustrated in Fig. 5 where an example of the measured SNR and corresponding number of transmitted bits per OFDM carrier frequency is shown for a transmission measurement taken using a 60  $\mu$ m in diameter series-connected  $\mu$ LED device over 1.5 m of clear tap water.

Fig. 6 shows the measured BER against various transmission data rates by employing the 60  $\mu$ m in diameter series-connected  $\mu$ LEDs as transmitter, through 1.5 m of clear water. The red dashed line indicates the BER target of  $3.8 \times 10^{-3}$  [31], below which “error-free” data transmission can be achieved using Forward Error Correction (FEC) with a 7% overhead of the gross data rate. The maximum achieved data rate that met this criterion was 4.92 Gb/s which corresponds to a net data rate of 4.58 Gb/s after FEC, though it should be pointed out that FEC was not actually used in this work.

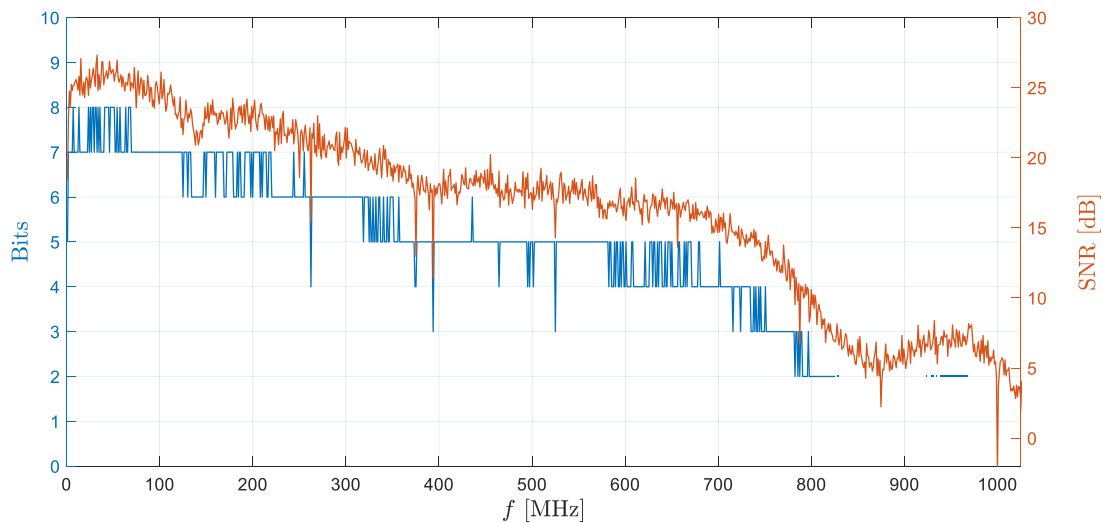


Fig. 5. Measured SNR (orange) and corresponding bit loading (blue) versus OFDM carrier frequency, obtained using a  $60\ \mu\text{m}$  in diameter series-connected  $\mu\text{LED}$  device over 1.5 m of clear tap water.

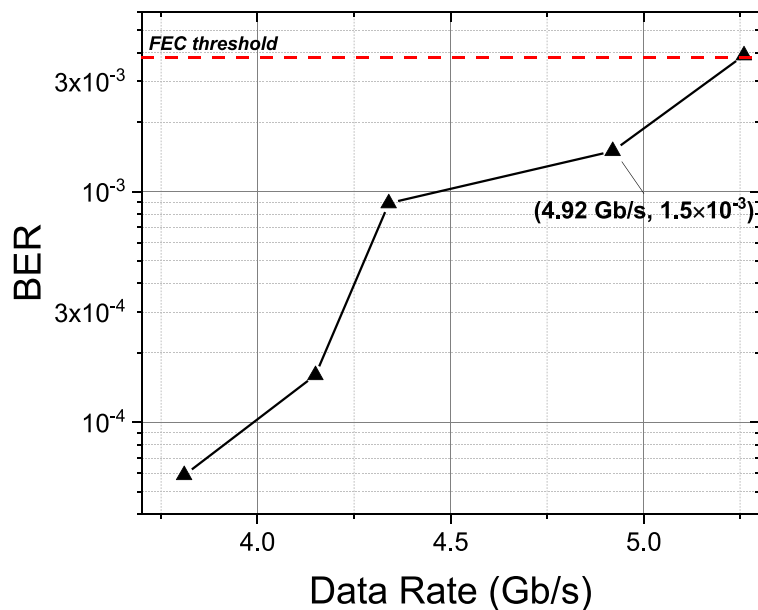


Fig. 6. BER versus data rate for the  $60\ \mu\text{m}$   $\mu\text{LED}$ s in series. Transmission is over 1.5 m of clear tap water ( $c(450) = 0.05\ \text{m}^{-1}$ ).

Fig. 7(a) shows the BER vs. data rates for the  $80\ \mu\text{m}$  in diameter series-connected  $\mu\text{LED}$ s through different water turbidities, as described in Section 3, over 1.5 m. The maximum data rate through clear tap water is  $3.78\ \text{Gb/s}$  at a BER of  $3.7 \times 10^{-3}$  and it can be shown that the increase in water turbidity, leads to attenuated transmission power levels collected by the detector and causes a lower overall signal-to-noise ratio (SNR) level. With a lower SNR level, fewer bits are loaded on each subcarrier and the achievable data rate decreases. In extreme water turbidities ( $c(450) = 3.56\ \text{m}^{-1}$ ) a data rate up to  $15\ \text{mb/s}$  was demonstrated over 5.33 ALs.

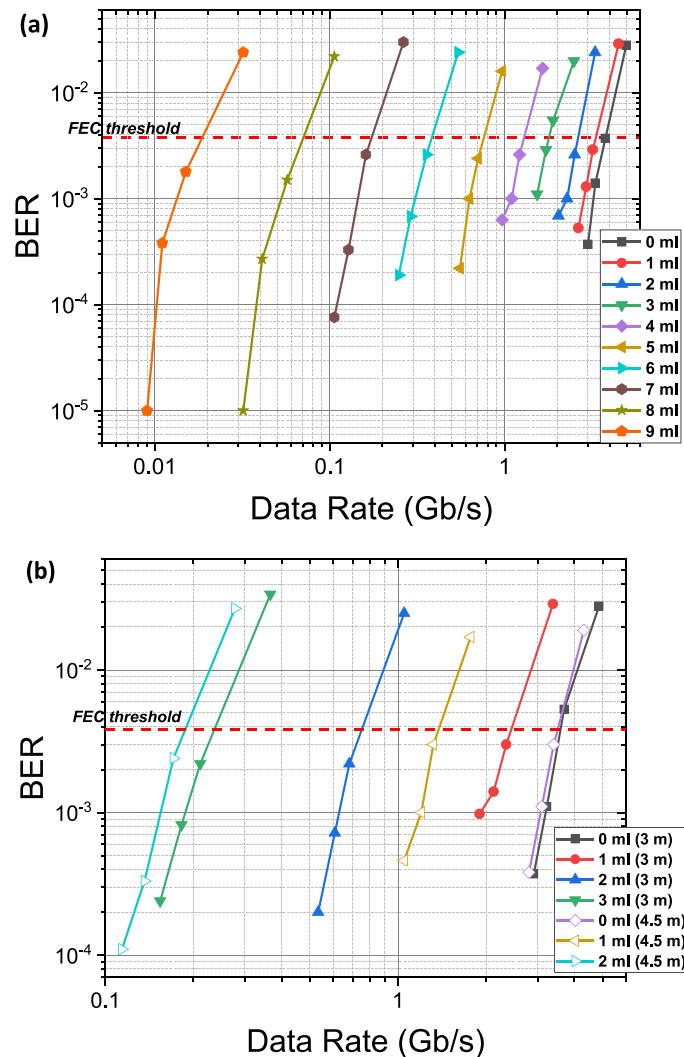


Fig. 7. (a) BER vs. data rate for the 80  $\mu\text{m}$  in diameter series-connected  $\mu\text{LEDs}$  through different water turbidities over 1.5 m. (b) BER vs. data rate for the same device through different water turbidities over 3 m and 4.5 m. Note that the maximum error-free data rates were obtained at slightly different BERs.

Fig. 7(b) presents the BER vs. data rate for the same device at the ranges of 3 m and 4.5 m through different concentrations of Maalox. At 3 m the maximum data rate through clear tap water is 3.22 Gb/s with a BER of  $1.1 \times 10^{-3}$  while at 4.5 m a larger BER of  $3.1 \times 10^{-3}$  is achieved for 3.4 Gb/s (corresponding  $c(450) = 0.05 \text{ m}^{-1}$  for both ranges). As the Maalox concentration increases, the maximum data rate drops to 211 mb/s at 3 m over 4.08 ALs with a BER of  $2.3 \times 10^{-3}$  (corresponding  $c(450) = 1.36 \text{ m}^{-1}$ ) and to 171 mb/s at 4.5 m over 4.05 ALs with a BER of  $2.5 \times 10^{-3}$  (corresponding  $c(450) = 0.90 \text{ m}^{-1}$ ).

The drop in data rate at all ranges can be explained by taking into account the Shannon-Hartley theorem [32]:

$$D = B \log_2 (1 + S/N) \tag{2}$$

where  $D$  is the maximum data transmission rate in bits/sec,  $B$  is the channel bandwidth in Hz,  $S$  is the average signal power over the entire bandwidth in W,  $N$  is the average noise power over the entire bandwidth at the Rx in W while  $S/N$  is the SNR. The degradation of the received SNR and

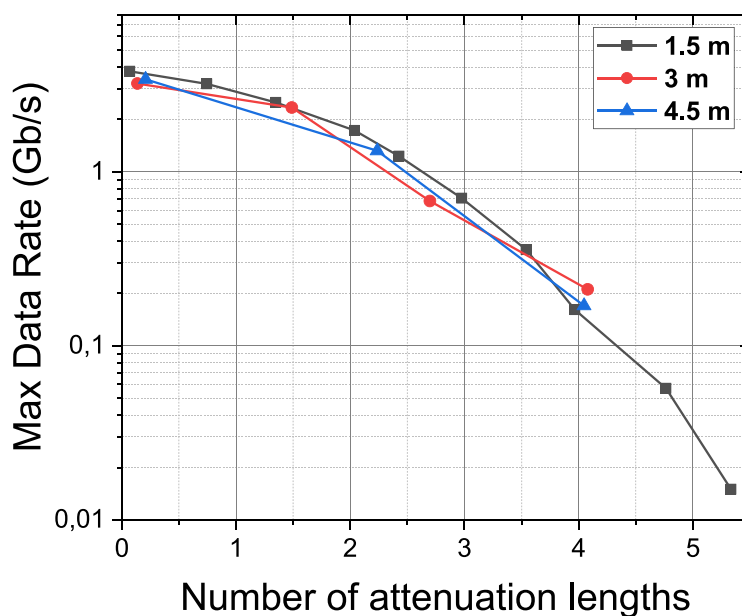


Fig. 8. The maximum data rates vs. the number of attenuation lengths for all ranges examined in this work (1.5 m, 3 m, 4.5 m).

the received optical power due to the increased attenuation result in a decrease in the achievable data rates.

Fig. 8 illustrates the error-free maximum data rates versus the number of ALs for all transmission distances. It can be seen that the maximum data rate decreases with an increase in the number of ALs, for all path lengths. This can be understood as the increased attenuation of the signal results in a lower SNR. It can also be seen that similar data rates are obtained when the number of ALs is similar, although the curves do not overlap exactly because each maximum data rate was obtained at a slightly different BER as shown in Fig. 7(a) and (b).

These results indicate that the relatively high power and bandwidth available from series-connected  $\mu$ LEDs can enable UWOC at Mb/s or Gb/s, even through turbid water samples. In future, further improvements to the achievable data rates and/or link lengths could be obtained by, for example, increasing the transmitted power by adding additional LEDs, narrowing the optical beam profile, or applying multiplexing techniques such as wavelength division multiplexing (WDM).

## 6. Conclusion

In this work, the high output power and modulation bandwidth of  $\mu$ LED arrays, consisting respectively of 6 series-connected pixels of diameter 60  $\mu$ m or 80  $\mu$ m, enabled Gb/s underwater optical wireless data transmissions using OFDM as modulation scheme, over three underwater distances of 1.5 m, 3 m and 4.5 m. A BER of  $1.5 \times 10^{-3}$  was achieved for a maximum data rate of 4.92 Gb/s through 1.5 m of clear tap water whose attenuation coefficient was  $c(450) = 0.05 \text{ m}^{-1}$ . Further underwater wireless optical transmissions were performed through different water turbidities: 2.34 Gb/s were demonstrated for an attenuation coefficient of  $0.5 \text{ m}^{-1}$  which is close to Jerlov II open ocean type ( $0.53 \text{ m}^{-1}$ ) over 3 m, whereas 1.32 Gb/s were shown over 4.5 m. With an attenuation coefficient of  $3.56 \text{ m}^{-1}$  and over 5.33 ALs, a data rate of 15 mb/s was achieved through 1.5 m. Our approach is compatible with multi-wavelength operation for WDM, and this is currently under investigation. The results of this work show the potential implementation of series-connected  $\mu$ LEDs to enable high-speed underwater wireless communications through various water turbidities.

## Acknowledgment

The data is available online at <https://doi.org/10.15129/a12fc6b9-ee8d-43d8-97e7-fd22d0009468>.

## References

- [1] E. M. Sozer, M. Stojanovic, and J. G. Proakis, "Underwater acoustic networks," *IEEE J. Ocean. Eng.*, vol. 25, no. 1, pp. 72–83, Jan. 2000.
- [2] P. Lacovara, "High-bandwidth underwater communications," *Marine Technol. Soc. J.*, vol. 42, no. 1, pp. 93–102, 2008.
- [3] M. Stojanovic, "High-speed underwater acoustic communications," in *Underwater Acoustic Digital Signal Processing and Communication Systems*, Boston, MA, USA: Springer, 2013, pp. 1–35.
- [4] J. R. Apel, *Principles of Ocean Physics*, vol. 38. New York, NY, USA: Academic, 1988.
- [5] A. I. Al-Shamma'a, A. Shaw, and S. Saman, "Propagation of electromagnetic waves at MHz frequencies through seawater," *IEEE Trans. Antennas Propag.*, vol. 52, no. 11, pp. 2843–2849, Nov. 2004.
- [6] C. Uribe and W. Grote, "Radio communication model for underwater WSN," in *Proc. 3rd Int. Conf. New Technol. Mobility Secur.*, 2009, pp. 1–5.
- [7] B. Wozniak, *Light Absorption in Sea Water*. New York, NY: Springer, 2006.
- [8] C. Y. Li *et al.*, "A 5 m/25 Gbps underwater wireless optical communication system," *IEEE Photon. J.*, vol. 10, no. 3, Jun. 2018, Art. no. 7904909.
- [9] C. Fei *et al.*, "16.6 Gbps data rate for underwater wireless optical transmission with single laser diode achieved with discrete multi-tone and post nonlinear equalization," *Opt. Express*, vol. 26, no. 26, 2018, Art. no. 34060.
- [10] M. Kong *et al.*, "10-m 951-Gb/s RGB laser diodes-based WDM underwater wireless optical communication," *Opt. Express*, vol. 25, no. 17, 2017, Art. no. 20829.
- [11] Y. Zhou *et al.*, "Common-anode LED on Si substrate for beyond 15 Gbit/s underwater visible light communication," *Photon. Res.*, vol. 7, no. 9, pp. 1019–1029, 2019.
- [12] F. Wang, Y. Liu, F. Jiang, and Nan Chi, "High speed underwater visible light communication system based on LED employing maximum ratio combination with multi-PIN reception," *Opt. Commun.*, vol. 425, pp. 106–112, 2018.
- [13] R. X. G. Ferreira *et al.*, "High bandwidth GaN-based micro-LEDs for multi-Gb/s visible light communications," *IEEE Photon. Technol. Lett.*, vol. 28, no. 19, pp. 2023–2026, Oct. 2016.
- [14] P. Tian *et al.*, "High-speed underwater optical wireless communication using a blue GaN-based micro-LED," *Opt. Express*, vol. 25, no. 2, pp. 1193–1201, 2017.
- [15] E. Xie *et al.*, "High-speed visible light communication based on a III-nitride series-biased micro-LED array," *J. Lightw. Technol.*, vol. 37, no. 4, pp. 1180–1186, Feb. 2019.
- [16] E. Xie *et al.*, "Design, fabrication, and application of GaN-based micro-LED arrays with individual addressing by N-electrodes," *IEEE Photon. J.*, vol. 9, no. 6, Dec. 2017, Art. no. 7907811.
- [17] J. J. D. McKendry *et al.*, "High-speed visible light communications using individual pixels in a micro light-emitting diode array," *IEEE Photon. Technol. Lett.*, vol. 22, no. 18, pp. 1346–1348, Sep. 2010.
- [18] S. Rajbhandari *et al.*, "A review of gallium nitride LEDs for multi-gigabit-per-second visible light data communications," *Semicond. Sci. Technol.*, vol. 32, no. 2, 2017, Art. no. 023001.
- [19] J. J. D. McKendry *et al.*, "Visible-light communications using a CMOS-controlled micro-light-emitting-diode array," *J. Lightw. Technol.*, vol. 30, no. 1, pp. 61–67, Jan. 2012.
- [20] M. N. Berberan-Santos, "Beer's law revisited," *J. Chem. Educ.*, vol. 67, no. 9, pp. 757–759, 1990.
- [21] W. Cox and J. Muth, "Simulating channel losses in an underwater optical communication system," *J. Opt. Soc. Am. A*, vol. 31, no. 5, pp. 920–934, 2014.
- [22] T. Petzold, "Volume scattering functions for selected ocean waters," *Scripps Inst. Ocean.*, no. 3, pp. 72–78, 1972.
- [23] A. Laux *et al.*, "The a, b, cs of oceanographic lidar predictions: A significant step toward closing the loop between theory and experiment," *J. Modern Opt.*, vol. 49, no. 3–4, pp. 439–451, 2002.
- [24] B. M. Cochenour, L. J. Mullen, and A. E. Laux, "Characterization of the beam-spread function for underwater wireless optical communications links," *IEEE J. Ocean. Eng.*, vol. 33, no. 4, pp. 513–521, Oct. 2008.
- [25] B. Cochenour, L. Mullen, and J. Muth, "Effect of scattering albedo on attenuation and polarization of light underwater," *Opt. Lett.*, vol. 35, no. 12, pp. 2088–2090, 2010.
- [26] B. Cochenour, S. O'Connor, and L. Mullen, "Suppression of forward-scattered light using high-frequency intensity modulation," *Opt. Eng.*, vol. 53, no. 5, 2013, Art. no. 051406.
- [27] Z. Vali, A. Gholami, Z. Ghassemlooy, M. Oomomi, and D. G. Michelson, "Experimental study of the turbulence effect on underwater optical wireless communications," *Appl. Opt.*, vol. 57, no. 28, pp. 8314–8319, 2018.
- [28] N. G. Jerlov, *Marine Optics*, vol. 14. Amsterdam, The Netherlands: Elsevier, 1976.
- [29] M. G. Solonenko and C. D. Mobley, "Inherent optical properties of Jerlov water types," *Appl. Opt.*, vol. 54, no. 17, pp. 5392–5401, 2015.
- [30] D. Tsonev *et al.*, "A 3-Gb/s single-LED OFDM-based wireless VLC link using a gallium nitride micro-LED," *IEEE Photon. Technol. Lett.*, vol. 26, no. 7, pp. 637–640, Apr. 2014.
- [31] I.-T. S. Group, "Forward error correction for high bit-rate DWDM submarine systems," ITU-T Rec. G.975.1 (02/2004), 2005.
- [32] C. E. Shannon, "A mathematical theory of communication, Part I, Part II," *Bell Syst. Tech. J.*, vol. 27, pp. 623–656, 1948.

# Underwater Wireless Optical Communications at 100 Mb/s Using Integrated Dual-Color Micro-LEDs

José F. C. Carreira<sup>1\*</sup>, Georgios N. Arvanitakis<sup>1\*</sup>, Alexander D. Griffiths<sup>1</sup>, Jonathan J. D. McKendry<sup>1</sup>, Enyuan Xie<sup>1</sup>, John Kosman<sup>2</sup>, Robert K. Henderson<sup>2</sup>, Erdan Gu<sup>1</sup>, Martin D. Dawson<sup>1</sup>

<sup>1</sup>*Institute of Photonics, Department of Physics, University of Strathclyde, Glasgow, United Kingdom*

<sup>2</sup>*Joint Research Institute for Integrated Systems, University of Edinburgh, Edinburgh, United Kingdom*

jose.correia-carreira@strath.ac.uk; georgios.arvanitakis@strath.ac.uk

\* These two authors contributed equally to this work

**Abstract** — Integrated blue-violet and blue-green micro-LED arrays, fabricated via a transfer printing method, were employed to demonstrate wavelength division multiplexing underwater data transmission at 100 Mb/s over up to 9 attenuation lengths in a 1.5 m long water tank.

**Keywords** — micro-LED, transfer printing, WDM, VLC, UWOC, turbid

## I. INTRODUCTION

The development of high-speed underwater wireless communication channels is of paramount importance for industrial, scientific, and military underwater activities [1], as tethered links can be impractical due to the challenging underwater environment. Underwater acoustics offer long range (tens of km), but suffer from high latency and limited data rates (tens of kb/s). Radio frequency communication are attenuated by seawater's conductivity resulting in data rates up to Mb/s for sub-meter ranges [2]. Optical devices operating at visible wavelengths, where water's lowest overall attenuation is exhibited, can enable high-speed transmission over tens of meters. For instance, Doniec *et al.* using an array of 18 light-emitting diodes (LEDs) demonstrated 25 Mb/s in 50 m of clear water [3]. Tian *et al.*, presented 800 Mb/s over 0.6 m of clear tap water using a single micro-LED [4]. It is worth noting, however, that as water becomes more turbid the optical window of lowest loss tends to redshift [2], thus a wavelength-adaptable transmitter is greatly desirable.

We report here the deployment of micro-transfer printing (TP) enabled hybrid blue-violet and blue-green micro-LED arrays for underwater wireless optical communications (UWOC) using a single-photon avalanche diode (SPAD) array receiver. By having two different wavelengths integrated in the same transmitter chip, the option of tuning the optimum color depending on the water conditions is enabled. Furthermore, the two chips can potentially be integrated into the same package to give 3-color output. Data transmission rates of 50 Mb/s for each single color of micro-LED over 1.5 m of highly turbid water are demonstrated. When operating in a wavelength division multiplexing (WDM) mode, with the respective pairs of colors, a 100 Mb/s link is established in each case over up to 9 attenuation lengths.

## II. DUAL COLOR MICRO-LED ARRAYS FABRICATION

Blue-violet and blue-green micro-LED arrays were fabricated by TP a blue-micro-LED platelet onto the substrate of the violet and green micro-LED, respectively. The blue-violet array follows the same fabrication process as the blue-green array which is discussed in detail in [5].

Briefly, violet (405 nm) and green (510 nm) 20  $\mu\text{m}$  diameter active area flip-chip micro-LEDs were fabricated

from commercially available InGaN epistuctures grown on c-plane sapphire by conventional photolithography techniques. Suspended flip-chip micro-LED platelets ( $6.5 \times 10^{-5} \text{ cm}^2$  active area) were then fabricated from commercially available blue emitting (450 nm) InGaN epistuctures grown on (111)-oriented silicon (Si). An elastomeric stamp was used to pick-up the blue micro-LED platelets from their Si substrate and print them onto the pre-prepared green and violet sapphire substrate micro-LED chips. The blue micro-LED platelet was then electrically insulated by parylene-C and addressed by Ti/Au (50/200 nm) metal tracks, following the process described in [5]. Fig. 1a) shows a plan view optical photograph of the resulting integrated blue-green micro-LED array (the blue-violet array shares the same layout). The micro-LEDs are individually anode-addressable sharing a common cathode. Fig. 1b) shows, by way of illustration, the blue-green device being simultaneously driven.

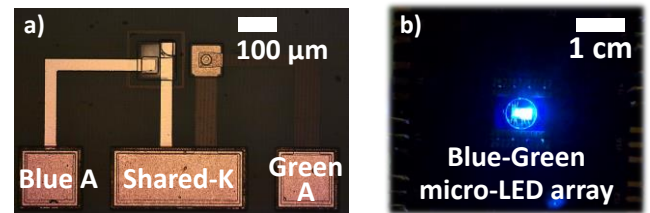


Fig. 1 – Plan view optical photographs of the blue-green micro-LED array a) magnified view; b) with both emitters simultaneously driven. Scale bars are shown inset.

## III. CHARACTERIZATION AND APPLICATION

### A. Micro-LEDs performance

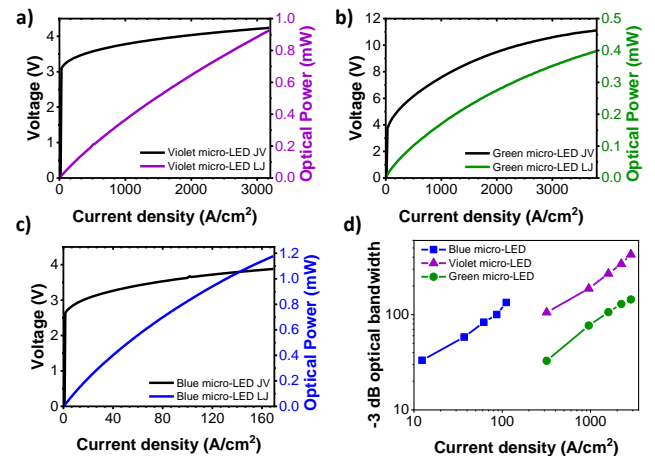


Fig. 2 – a), b) and c) current density-voltage (JV) and current density – optical power (LJ) curves of the violet, green, and blue micro-LED, respectively; d) micro-LEDs -3 dB optical bandwidth vs current density.

The individual electrical and optical performance of the chip-integrated violet, green, and blue micro-LEDs are shown

in Fig. 2 a), b), and c) respectively. The through-sapphire directed optical power output shown in Fig. 2 was measured using a calibrated Si photodiode detector butt-coupled to the device. In these conditions, the maximum optical power achieved by the violet, green, and blue micro-LED are 0.9, 0.4 and 1.2 mW, respectively. All micro-LEDs exhibit a -3dB optical bandwidth above 100 MHz (Fig. 2 d)), which renders them highly suitable for data transmission.

### B. UWOC Application

For the UWOC demonstration, an on-off keying (OOK) data signal was generated using a field-programmable gate array (FPGA, Opal Kelly XEM6310-LX45), modulating the micro-LED through a bias-tee. A sequence of length  $2^{15}$  was transmitted, consisting of a wide synchronisation pulse and a pseudo-random bit sequence. The micro-LED emission was collected and collimated by a condenser lens (Thorlabs, ACL50832U-A), propagated through a 1.5 m long water tank and then focused onto the receiver by a 4-inch diameter Fresnel lens (Edmund, #46-614). The receiver is a 64 x 64 array of Si SPADs developed by the University of Edinburgh (details found in [6]) which operates as a digital silicon photomultiplier. The photon counts are summed over a time window of 5 ns and the count values outputted through a digital-to-analog converter (DAC). The DAC signal was captured with an active oscilloscope probe and transferred to MATLAB® for offline processing to determine a bit-error ratio (BER). The turbidity of the water sample was varied by adding Maalox® antacid to tap water, a method widely used [7] to mimic different natural water analogs in a laboratory set-up. A block diagram of the experimental setup is shown in Fig. 3.

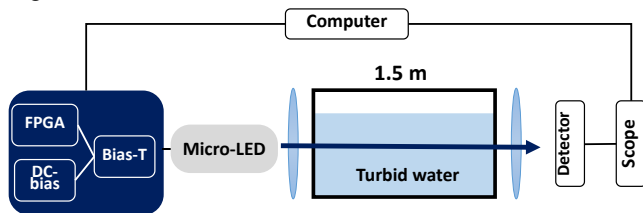


Fig. 3 – Block diagram of the experimental system.

The effect of increasing turbidity levels on the BER for individually driven micro-LEDs at the three wavelengths is shown in Fig. 4a). A 50 Mb/s communication channel, below the  $3.8 \times 10^{-3}$  forward error correction (FEC) threshold, is achieved for all the micro-LEDs for Maalox® concentration of 0.075 mL/L. For the blue and green micro-LEDs this concentration of Maalox® corresponds to a number of attenuation lengths (calculated following [8]) of 7.2 and 8.3, respectively. The operation of the integrated blue-violet and blue-green micro-LED arrays as respective dual wavelength WDM transmitters for underwater communication is shown in Fig. 4b). The blue and green micro-LED were operated simultaneously (as shown in Fig. 1b)) and each color carried a different data stream. In order to select which micro-LED was being detected bandpass filters (Laser 2000: blue FF01-445/20-25, green FF01-525-45/25) were placed in front of the detector. This results in a 100 Mb/s aggregate data rate link, below FEC, at a Maalox® concentration of 0.069 mL/L for the blue-green micro-LED array. The same measurements were repeated for the blue-violet micro-LED array, but with the use of a Laser 2000 FF01-392-23/25 bandpass filter for the

violet micro-LED. In this case, a 100 Mb/s link, below FEC, at a Maalox® of 0.075 mL/L is achieved by the blue-violet micro-LED array. It should be noticed, that used data rates are limited by the driving method, and future work could reach an aggregate data rate of several hundred Mb/s with OOK.

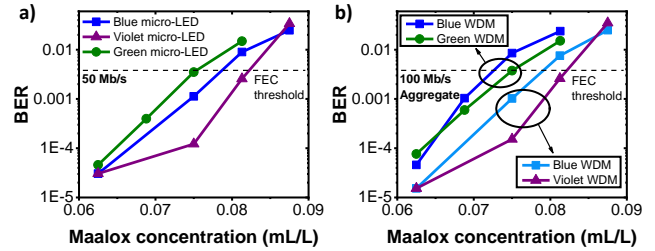


Fig. 4 – Bit-error-ratio vs Maalox® concentration a) for individually driven blue, violet and green micro-LEDs; b) Blue-green and blue-violet micro-LED arrays operated in wavelength division multiplexing mode.

### IV. CONCLUSION

By micro-TP we have fabricated on-chip dual-color (respectively blue-violet and blue-green) micro-LED arrays. The potential of these devices as a UWOC transmitter in highly turbid underwater environments has been demonstrated with 100 Mb/s data rates achieved over multiple attenuation lengths using WDM and a SPAD-based receiver.

### ACKNOWLEDGMENT

This work is funded under the EPSRC Quantic (EP/M01326X/1) and EPSRC CDT in Medical Devices & Health Technologies grant (EP/L015595/1). Plessey Semiconductors is acknowledged for providing the GaN-on-Si wafer.

### REFERENCES

- [1] H. Kaushal and G. Kaddoum, "Underwater Optical Wireless Communication," *IEEE Access*, vol. 4, pp. 1518–1547, 2016.
- [2] P. Lacovara, "High-Bandwidth Underwater Communications," *Mar. Technol. Soc. J.*, vol. 42, no. 1, pp. 93–102, Mar. 2008.
- [3] M. Doniec and D. Rus, "BiDirectional optical communication with AquaOptical II," in *2010 IEEE International Conference on Communication Systems*, 2010, pp. 390–394.
- [4] P. Tian *et al.*, "High-speed underwater optical wireless communication using a blue GaN-based micro-LED," *Opt. Express*, vol. 25, no. 2, p. 1193, 2017.
- [5] J. F. C. Carreira *et al.*, "Dual-Color Micro-LED Transmitter for Visible Light Communication," in *2018 IEEE Photonics Conference (IPC)*, 2018, pp. 1–2.
- [6] J. Kosman *et al.*, "29.7 A 500Mb/s -46.1dBm CMOS SPAD Receiver for Laser Diode Visible-Light Communications," in *2019 IEEE International Solid-State Circuits Conference - (ISSCC)*, 2019, pp. 468–470.
- [7] B. Cochenour, L. Mullen, and J. Muth, "Effect of scattering albedo on attenuation and polarization of light underwater," *Opt. Lett.*, vol. 35, no. 12, pp. 2088–2090, 2010.
- [8] W. Cox and J. Muth, "Simulating channel losses in an underwater optical communication system," *J. Opt. Soc. Am. A*, vol. 31, no. 5, p. 920, 2014.

# Light Emitting Diodes and Lasers for High-Speed Underwater Optical Communications

Georgios N. Arvanitakis<sup>1,2</sup>, Jonathan J. D. McKendry<sup>1</sup>, Henry T. Bookey<sup>2</sup>, Erdan Gu<sup>1</sup>, and Martin D. Dawson<sup>1,2</sup>

*1: Institute of Photonics, Department of Physics, University of Strathclyde, G1 1RD, Glasgow-Scotland*

*2: Fraunhofer Centre for Applied Photonics, G1 1RD, Glasgow-Scotland*

## 1 Introduction

During the last decade, a lot of research has been carried-out around Underwater Wireless Optical Communications (UWOC) as they are considered as a promising technology for high data rate transmission in underwater environments. The main application domains that require Underwater Wireless Communications include<sup>1</sup>:

- a) The military: for tactical surveillance and communications between e.g. submarines and surface vessels.
- b) Industry: e.g. for oil and gas control maintenance, underwater construction and subsea factories.
- c) The scientific community: e.g. for offshore explorations and oceanography research, pollution and climate change monitoring.

All the above activities require the deployment of sophisticated sensors and other subsea devices, such as unmanned (UUVs) and autonomous underwater vehicles (AUVs), therefore the amount of data to be transmitted and the accompanying data rates continue to rise. While data links can be achieved using underwater cables or tethers, this can be very restrictive, expensive or in some cases impractical. Therefore, underwater wireless links are greatly desirable. Underwater wireless data communications require also an environment that will support propagation of the carrier wave with low enough attenuation and background noise.

UWOC are being considered for use underwater as water exhibits a window of reduced attenuation in the visible spectrum, particularly between  $400 - 550nm^2$ . Thus, as RF signals require large antennas size, suffer from high attenuation in sea water and acoustic can provide data rate of few  $kb/s$ , the employment of light sources, such as diode lasers and GaN-based LEDs, operating in the blue-green region enable one to exceed  $Gb/s$  (e.g.  $12.4Gb/s$  for  $1.7m$  of tap water at  $450nm$  via a GaN laser diode<sup>3</sup>) at a distance of tens of meters (e.g.  $1.2Mb/s$  for  $30m$  in a pool via 6 LEDs array at  $420nm^4$ ) due to high frequency of optical carrier. Also,



they require low operating power i.e. few Watts whilst acoustic requires tens of Watts and RF tens up to hundreds of Watts, depending on the transmission distance<sup>1</sup>. To summarize the characteristics of the above-mentioned technologies that govern Underwater Wireless Communications, a table is given below (Table 1-1)<sup>1</sup>.

PARAMETERS	ACOUSTIC	RF	OPTICAL
<b>Attenuation</b>	0.1 – 4dB/km	3.5 – 5dB/m	0.39dB/m (clear ocean) – 11dB/m (turbid)
<b>Speed</b>	1500m/s	$\approx 2.55 \times 10^8$ m/s	$\approx 2.55 \times 10^8$ m/s
<b>Data rate</b>	$\sim$ kb/s	$\sim$ Mb/s	$\sim$ Gb/s
<b>Distance</b>	Up to kms	Up to $\approx$ 10m	$\approx$ 10 – 100m
<b>Frequency band</b>	10 – 15kHz	30 – 300Hz (ELF)	$10^{12}$ – $10^{15}$ Hz
<b>Transmission power</b>	Tens of Watts	Few mW to hundreds of Watts	Few Watts
<b>Antenna size</b>	0.1m	0.5m	0.1m
<b>Performance parameter</b>	Temperature, salinity, pressure	Conductivity and permittivity	Absorption, Scattering

Table 1-1 Comparison of the three dominant Underwater Wireless Communications Technologies

However, applying UWOC is not a trivial matter due to absorption and scattering effects produced by the molecular structure of water<sup>5</sup> and from substances contained within sea water such as dissolved organic materials with a diameter  $< 0.4\mu\text{m}$ <sup>6</sup> (gelbstoff), particulate organic materials (phytoplankton) and suspended inorganic particles (rocks, sands, clays)<sup>7</sup>. In general, the existence of these materials results in shifting and narrowing of the low attenuation region from the blue-green towards longer wavelengths<sup>2,5,7</sup>, as the concentration increases.

While UWOC links have been widely reported in the literature, for example 5.5Gb/s using a green Laser diode at 520nm over a 5m air channel and a 21m water channel<sup>8</sup>, these are typically “point to point” links, where a single transmitter ( $T_x$ ) addresses a single receiver ( $R_x$ ). This requires optical alignment to be maintained between  $T_x$  and  $R_x$ , which may be challenging in open waters. As such, in this paper we report the employment of the Corning® Fibrance® Light Diffusing Fiber<sup>9,10</sup> as a transmitter ( $T_x$ ). This thin, flexible optical fiber, made from glass, exhibits the property of scattering light for lighting purposes instead of delivering it from point to point over long distances. Its silica core is doped with scattering centers to scatter light continuously and uniformly along the length of the fiber.

In this way a simple and cost-effective omnidirectional “beacon” is realized with no moving or complex optical parts nor precise alignment despite the challenging underwater environment. This omnidirectional beacon could be used to establish a wireless data link within a volume of water, such as a ship broadcasting to multiple divers or, remotely-operated vehicles (ROVS) etc. that are in proximity to the ship. Another scenario could be that an ROV uses the beacon concept to communicate to a surface vessel, without the requirement to continuously track and optically align the data link. As discussed previously, optical wireless data links can remove the need for tethered communications, greatly increasing mobility, functionality and reducing costs.

## 2 Description of the Experimental Set-Up

The lab-based experimental set-up implemented in our work to date, may be seen in Figure 2.1.

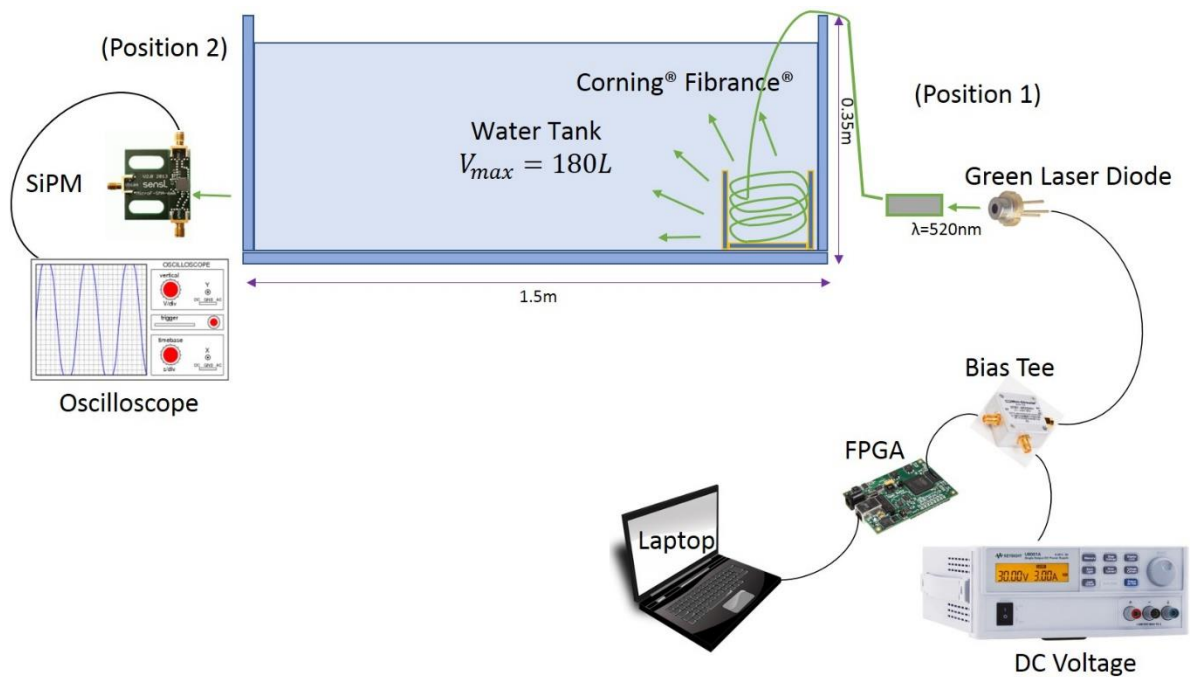


Figure 2.1 Schematic of the lab-based experimental set-up

As previously mentioned, it consists of a transmitter ( $T_x$ ) which is the Corning® Fibrance® Light Diffusing Fiber, 5m long, positioned inside a glass beaker (see Figure 2.2a).

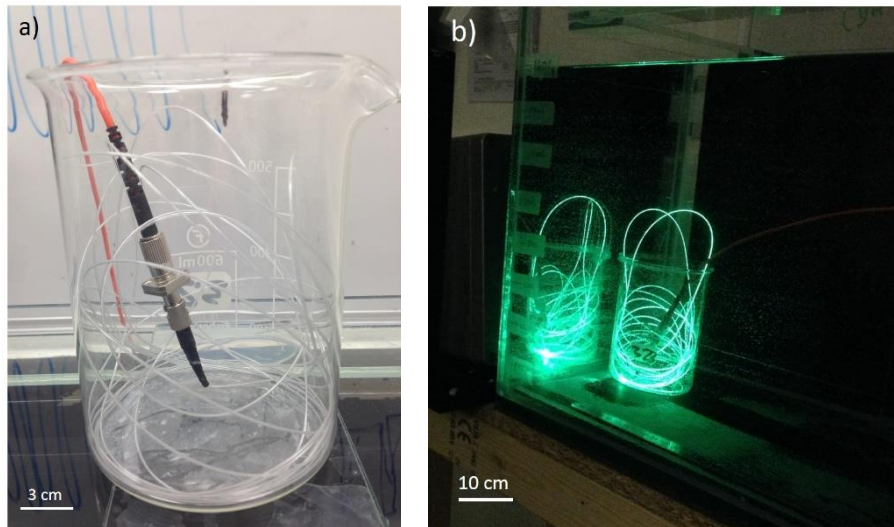


Figure 2.2 a) Photograph of the Fibrance inside the beaker and b) photograph of the Fibrance transmitter, coupled with the green Laser Diode and acting as Transmitter, inside the water tank, filled with clear tap water

The Fibrance was coupled with an off-the-shelf Osram Green Laser Diode (model PL520) operated at  $520\text{nm}$  (Figure 2.2b), supplied by a current of  $90\text{mA}$  and a forward Voltage of  $6.5\text{V}$  from a single output DC power supply. The transmitted power of the beam was  $\sim 5\text{mW}$ , measured by a THORLABS PM100A Power Meter with a S121C sensor head.

The On-Off Keying (OOK) modulation scheme was used for generating a Pseudo Random Bit Sequence (PRBS) of 127 bits via an Opal Kelly XEM3010 FPGA. The FPGA data output and the DC supply were combined and used to drive the laser diode using a bias tee. The FPGA was run by a MATLAB® script through a laptop.

The beaker containing the Fibrance transmitter fibre, was placed at the bottom of the water tank of dimensions  $1.5\text{m} \times 0.35\text{m} \times 0.35\text{m}$  and maximum volume of  $180\text{l}$  (see Figure 2.3). The tank was constructed from high transmittance<sup>11</sup> (91%) Pilkington Optiwhite™ aquarium glass to reduce optical losses. The tank was filled with  $160\text{l}$  of tap water. Moreover, to prevent reflections coming from the walls of the tank which would not occur in open water and may lead to multipath signal distortions, matt black plastic sheets were placed at the bottom of the tank and around the walls.

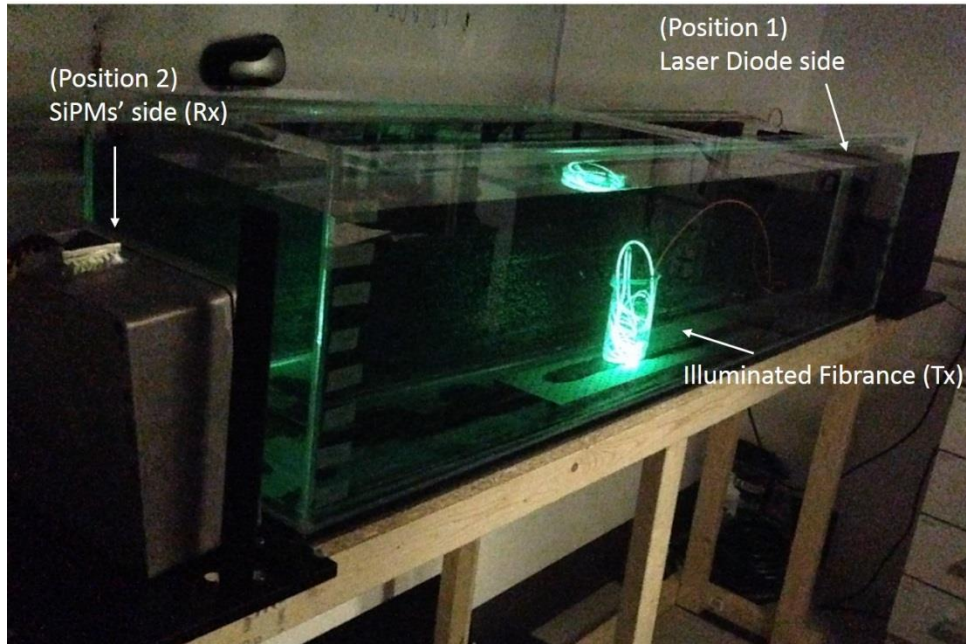


Figure 2.3 Photograph of the water tank filled with 140l of clear tap water and the Fibrance transmitter inside the beaker and placed on the bottom of the tank

As for the detector ( $R_x$ ), a  $6 \times 6\text{mm}^2$  SensL J-series 60035 Silicon Photomultiplier (SiPM) is placed at the other side of the tank (Position 2 in Figure 2.3), approximately aligned with the Fibrance transmitter and sufficient enough to collect part of the signal propagated through water, either scattered due to Maalox® (our scattering agent) or not. The SiPM, was connected to an oscilloscope for monitoring and analysing the signal.

As previously mentioned, the propagation of an optical beam underwater suffers from loss of intensity with distance due to absorption and scattering.

The optical properties of ocean water are defined by parameters such as the attenuation coefficient ( $c$  in  $\text{m}^{-1}$ ) and the single scattering albedo,  $\omega_0$ .

The attenuation coefficient describes the differential power loss per unit volume of water caused by absorption and scattering and is the sum of both the absorption  $\alpha$ , and scattering  $b$ , coefficients ( $c(\lambda) = \alpha(\lambda) + b(\lambda)$ ). It varies greatly according to the water type and is also wavelength dependent. Some typical values of the coefficients can be seen in the following table (Table 2-1), in addition to the optimum operating wavelengths for different types of water.

The scattering albedo is defined as the ratio between the amount of scattering and overall attenuation, or  $\omega_0 = b/c$ . Natural waters have single scattering albedos that range from 0.25 to  $> 0.8$  as the water becomes scattering<sup>12</sup>.

Water type	$a(m^{-1})$	$b(m^{-1})$	$c(m^{-1})$	Operating Wavelength
Clear Ocean	0.114	0.037	0.151	450 – 500nm (blue-green)
Coastal Ocean	0.179	0.220	0.339	520 – 570nm (yellow-green)
Turbid Harbour	0.366	1.829	2.195	550 – 600nm (yellow-green)

Table 2-1 Typical values of absorption, scattering and attenuation coefficients and ideal transmission wavelength for different types of water.<sup>1</sup>

In general, underwater optical propagation experiments are commonly done with simulated conditions in a laboratory water tank. In order to mimic the conditions found in natural waters, different concentrations of a scattering agent are diluted in tap water. As a scattering agent, Maalox® antacid, a mix of magnesium hydroxide ( $Mg(OH)_2$ ) and aluminium hydroxide ( $Al(OH)_3$ ), was used here. It has an albedo of  $\omega_{0, Maalox®} = 0.95^{13-15}$ .

The received power,  $P_R$ , can be found by applying the Beer's Law over a path  $d$  (Eq. 1), giving us a basic solution to the problem of determining the loss of light along a path in ocean water<sup>12</sup>.

$$P_R = P_0 e^{-cd} \quad (\text{Eq. 1})$$

Also, it is worth mentioning that we can define the attenuation length,  $d_{atten}$ , as being the distance at which  $P_R$  has fallen to  $1/e$  of  $P_0$ . Thus,  $d_{atten} = 1/c$  while the product  $cd_{atten}$  forms a unitless term which represents the number of attenuation lengths (AL)<sup>12</sup>.

### 3 Results

The main purpose of the experiment was to implement the beacon in an underwater environment and show that a data rates up to  $5Mb/s$  is achievable through different types of water, thus, different Maalox® concentrations in water.

The maximum distance between transmitter and receiver, was  $1.66m$  ( $1.5m$  through water). The  $0$  to  $3.3V$  digital Pseudo-Random Bit Sequence (PRBS) signal that was sent to the Laser Diode and was optically transmitted through water, had the form as shown in Figure 3.1. The PRBS is 127 bits long and was transmitted at a fixed data rate of  $5Mb/s$ .

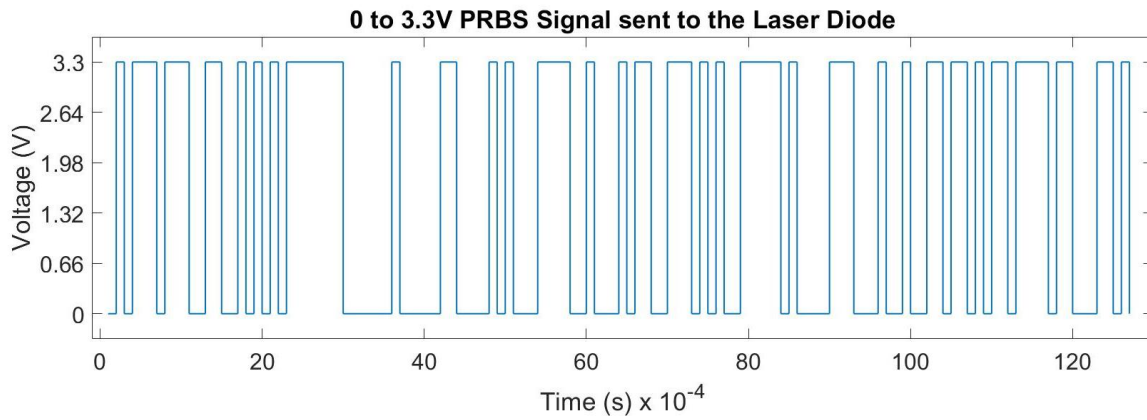


Figure 3.1 The form of the 0 to 3.3V PRBS signal that was optically transmitted through water

Different concentrations of Maalox® were tested in order to mimic three typical types of sea water (see Figure 3.2 - Figure 3.4) whose attenuation coefficients and attenuation lengths are known (see Table 2-1). As it can be seen, the underwater link based on the Fibrance transmitter, could distinctly support the  $5Mb/s$  optical signal in all types of natural water analogues, for a given distance of  $1.66m$  between transmitter and receiver which was the maximum we could set with the current set-up layout. The following graphs of the received signal present great similarity to the digital signal in Figure 3.1 and any possible distortion coming from ambient noise is negligible.

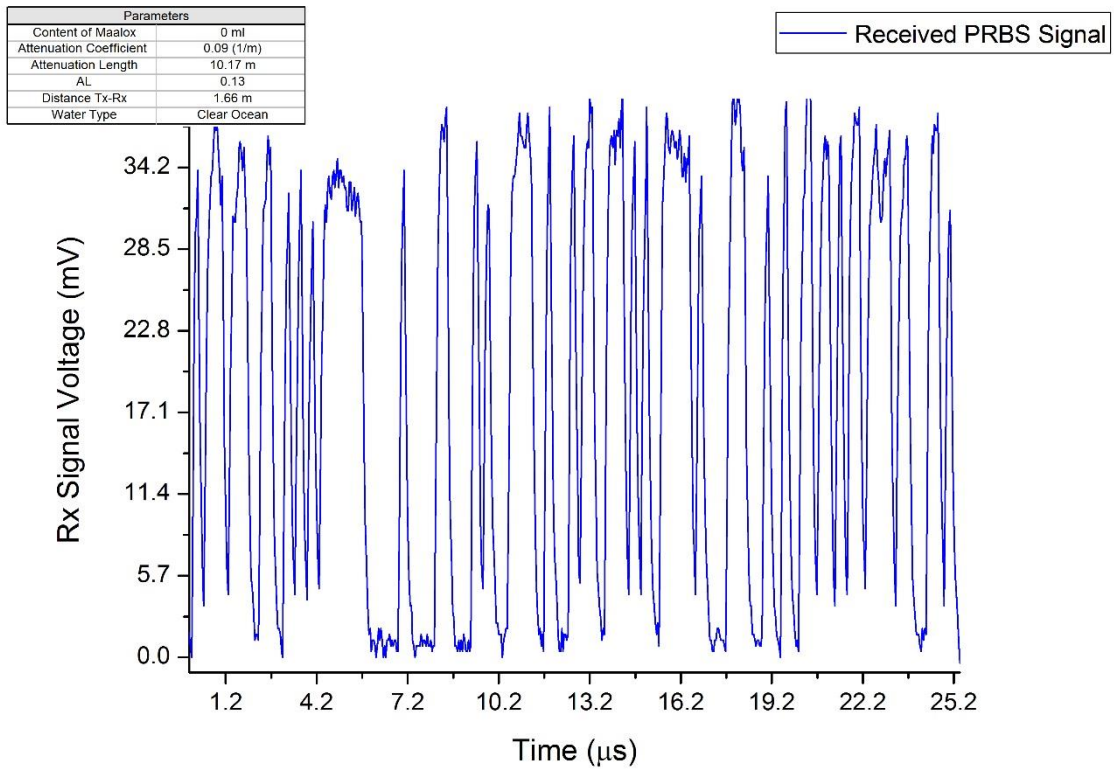


Figure 3.2 Graph of the received signal for “Clear Ocean” water and  $d_{Tx-Rx} = 1.66m$

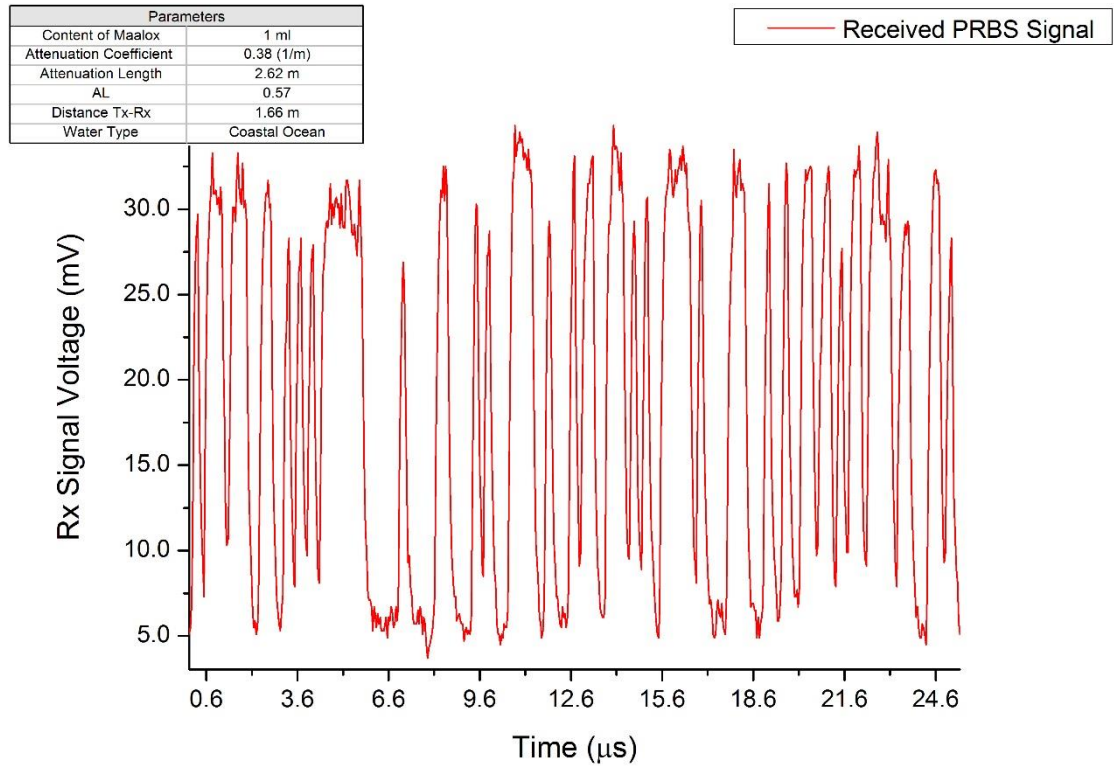


Figure 3.3 Graph of the received signal for “Coastal Ocean” water and  $d_{Tx-Rx} = 1.66m$

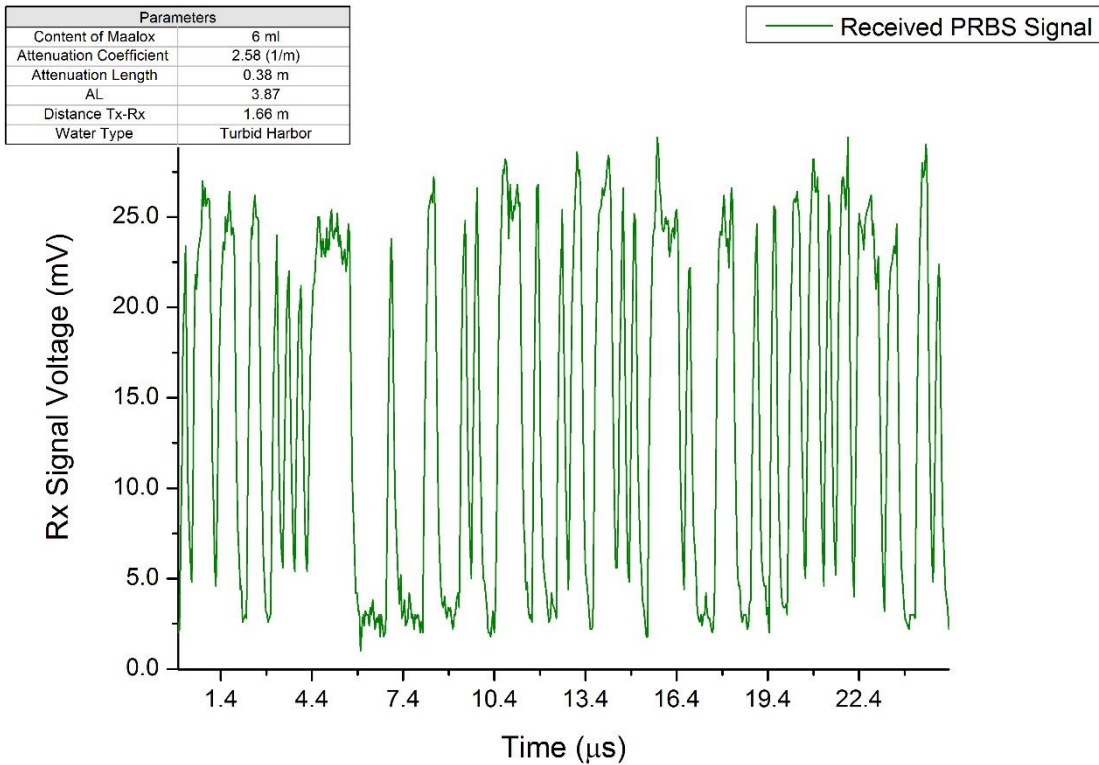


Figure 3.4 Graph of the received signal for “Turbid Harbor” water and  $d_{Tx-Rx} = 1.66m$

Moreover, the turbidity of the water was expanded in more extreme levels so as to acquire an estimation about the supporting limit of the set-up.

Three higher concentrations of Maalox® were tested, 18ml (0.0125%), 28ml (0.0175%), and 40ml (0.025%) whose attenuation lengths correspond to few centimetres. The distance between  $T_x$  and  $R_x$  remained constant (1.66m), however for the 40ml of the scattering agent two positions of the Fibrance transmitter were checked; for the closer distance to the SiPM (0.75m) the signal was clearer.

The results can be seen in Figure 3.5 - Figure 3.8. The transmittance of 5Mb/s of optical signal in a very turbid underwater environment was achieved.

These results, enable us to confirm the efficiency and cost/power-effectiveness of the Fibrance transmitter. It could be now deduced that the Fibrance concept would be rendered robust enough for the “real world” applications discussed in the Introduction section.



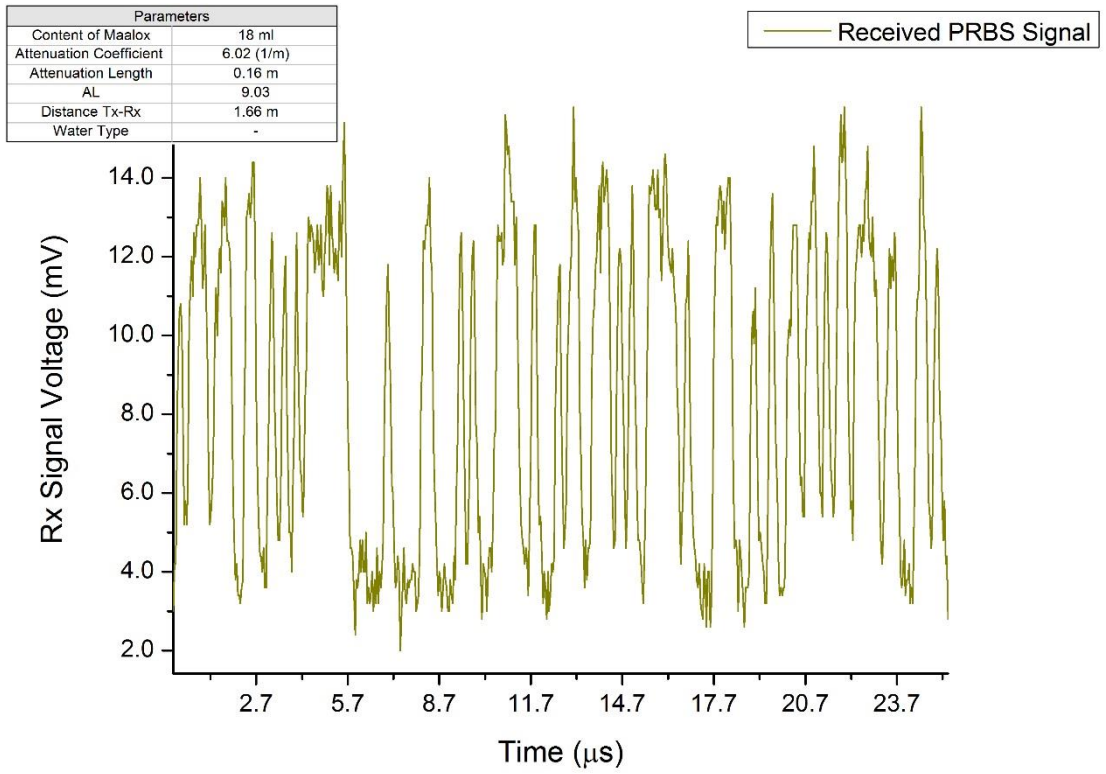


Figure 3.5 Graph of the received signal for an attenuation length of 0.16m and  $d_{Tx-Rx} = 1.66m$

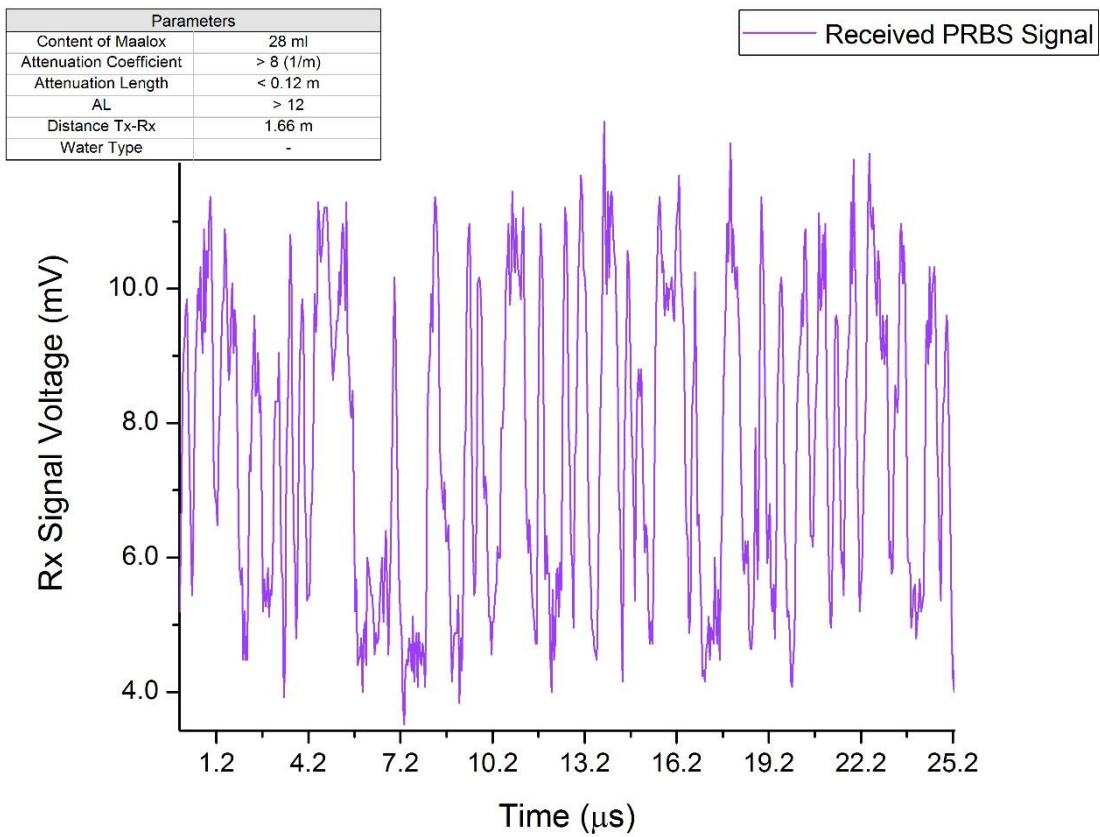


Figure 3.6 Graph of the received signal for an attenuation length smaller than 0.12m and  $d_{Tx-Rx} = 1.66m$

Parameters	
Content of Maalox	40 ml
Attenuation Coefficient	> 12.5 (1/m)
Attenuation Length	< 0.08 m
AL	> 9.37
Distance Tx-Rx	0.75 m
Water Type	-

— Received PRBS Signal

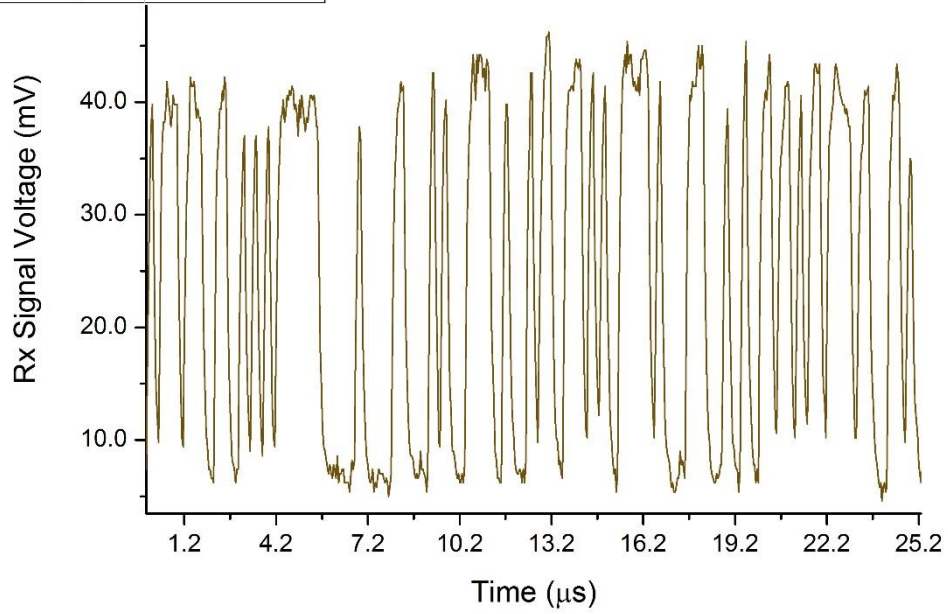


Figure 3.7 Graph of the received signal for an attenuation length smaller than 0.08m and  $d_{Tx-Rx} = 0.75m$

Parameters	
Content of Maalox	40 ml
Attenuation Coefficient	> 12.5 (1/m)
Attenuation Length	< 0.08 m
AL	> 17.25
Distance Tx-Rx	1.38 m
Water Type	-

— Received PRBS Signal

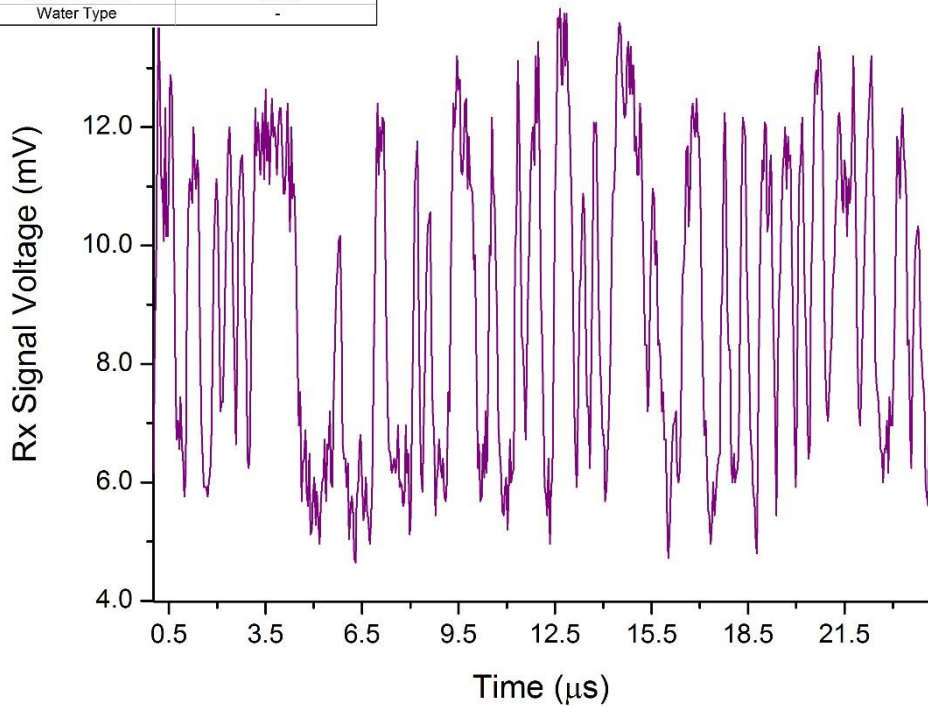


Figure 3.8 Graph of the received signal for an attenuation length smaller than 0.08m and  $d_{Tx-Rx} = 1.66m$

Regarding the distances that could be supported with the current configuration outside of the water tank, in Figure 3.9 an estimated BER versus transmission distance (the distance between the  $T_x$  and  $R_x$ ) was plotted for the three types of natural waters (Clear Ocean, Coastal Ocean and Turbid Harbor) with corresponding attenuation coefficients given in Table 2-1. These results have been calculated using the methodology given by Hamza T. et al.<sup>16</sup>, adapting the calculations such that it is assumed that the Fibrance transmitter is an isotropic emitter, emitting power equally in all directions, rather than for example a Lambertian emitter.  $5mW$  of transmitted optical power, at a wavelength of  $520nm$  is assumed, and the specifications of the SiPM used in our experiments is used as the receiver. Data is assumed to be transmitted at  $5$  Mb/s using OOK.

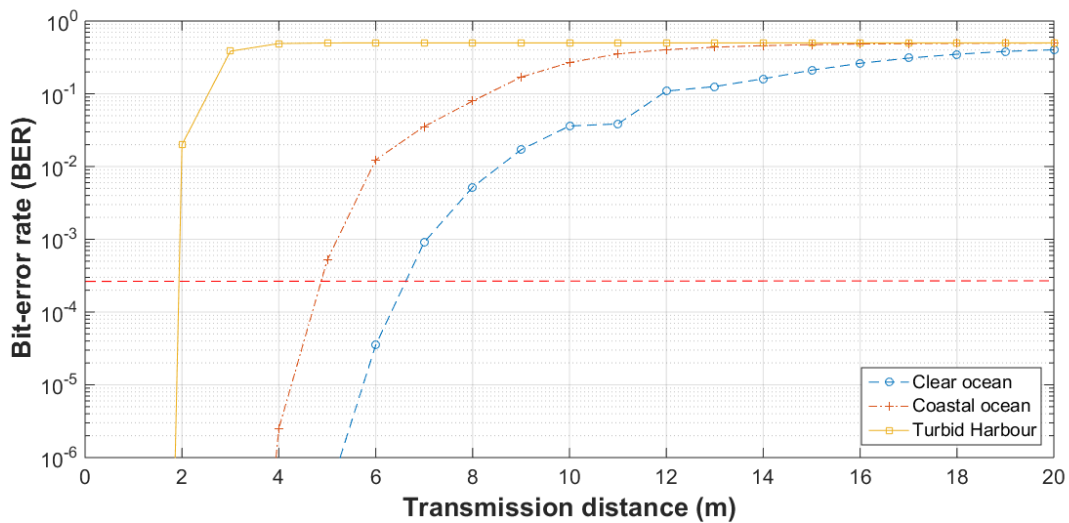


Figure 3.9 BER vs  $d_{Tx-Rx}$  for three types of natural waters

A BER of  $3 \times 10^{-3}$  is used as reference, as indicated by the horizontal red line in Figure 3.9. At this BER, data transmission can be made “error free” using forward-error correction with an overhead of 7% of the total data rate. Therefore, we define BERs below this level as “error free”. These calculations indicate that the Fibrance transmitter concept shown here would work at a distance of almost  $7m$  in clear ocean waters. This could be extended to over  $10m$  if the transmitted power was increased to  $50mW$ . These results indicate that the Fibrance “beacon” can potentially allow a unidirectional wireless optical data link with a range of several meters, using simple components and relatively modest transmitted power.

## 4 Conclusions & Future Work

In this paper, it was shown that we managed to take advantage of the special property of the Corning® Fibrance® Light-Diffusing Fiber, i.e. its core scatters light continuously and uniformly, and employ the fibre itself as transmitter in clear to turbid underwater environment.

The achieved data rate (up to 5MHz) could be increased in future measurements by employing different light sources, such as Q-Switched Laser for reaching powers up to *kWs'* or LEDs for more flexible and sophisticated modulation schemes (e.g. OFDM).

In future work we will explore the use of different light sources allowing selection of the optimum wavelength according to the type of water. Additional wavelengths would also be a method of increasing the transmitted data rate, or supporting multiple users, by using Wavelength Division Multiplexing (WDM).

We also intend to further investigate an “omnidirectional” transmission and more particularly, placing the receiver/detector in various positions around the Fibrance fibre allowing us to confirm the isotropic nature of the Fibrance fibre transmission. This will require trials of the Fibrance transmitter in a larger volume of water than that used here.

## 5 References

1. Kaushal, H. & Kaddoum, G. Underwater Optical Wireless Communication. *IEEE Access* **4**, 1518–1547 (2016).
2. Wozniak, B. *Light absorption in sea water*. (2007).
3. Wu, T.-C., Chi, Y.-C., Wang, H.-Y., Tsai, C.-T. & Lin, G.-R. Blue Laser Diode Enables Underwater Communication at 12.4 Gbps. *Sci. Rep.* **7**, 40480 (2017).
4. Doniec, M., Detweiler, C., Vasilescu, I. & Rus, D. Using optical communication for remote underwater robot operation The MIT Faculty has made this article openly available . Please share Citation Underwater Robot Operation .” IEEE / RSJ International Accessed Citable Link Detailed Terms Using Optical Comm. (2014).
5. Lanzagorta, M. *Underwater Communications. Synthesis Lectures on Communications* **5**, (2012).
6. Mobley, C. *Light and Water: Radiative transfer in natural waters*. (1994).
7. Johnson, L. J., Jasman, F., Green, R. J. & Leeson, M. S. Recent advances in underwater optical wireless communications. *Underw. Technol. Int. J. Soc. Underw.* **32**, 167–175

- (2014).
8. Chen, Y., Kong, M., Ali, T., Wang, J., Sarwar, R., Han, J., Guo, C., Sun, B., Deng, N., and Xu, J. 26 m/5.5 Gbps air-water optical wireless communication based on an OFDM-modulated 520-nm laser diode. *Opt. Express* **25**, 14760 (2017).
  9. Logunov, S., Fewkes, E., Shustack, P. & Wagner, F. Light diffusing optical fiber for Illumination. *Renew. Energy Environ. Congr.* 4–6 (2013).
  10. Corning ® Fibrance ® Light-Diffusing Fiber specification sheet. 2015–2016
  11. Nippon Sheet Glass Co., L. Pilkington Optiwhite. Available at: <https://www.pilkington.com/en-gb/uk/products/product-categories/special-applications/pilkington-optiwhite#overview>.
  12. Cox, W. & Muth, J. Simulating channel losses in an underwater optical communication system. *J. Opt. Soc. Am.* **31**, 920–934 (2014).
  13. Maccarone, A. *Single-photon detection techniques for underwater imaging*. (2016).
  14. Hanson, F. & Radic, S. High bandwidth underwater optical communication. *Appl. Opt.* **47**, 277–283 (2008).
  15. Cochenour, B., Mullen, L. & Muth, J. Effect of scattering albedo on attenuation and polarization of light underwater. *Opt. Lett.* **35**, 2088–2090 (2010).
  16. Hamza, T., Khalighi, M., Bourennane, S., Pierre, L. & Opderbecke, J. On the Suitability of Employing Silicon Photomultipliers for Underwater Wireless Optical Communication Links. *10th Int. Symp. Commun. Syst. Networks Digit. Signal Process.* (2016).